

# A $C_s$ Corrected HRTEM: Initial Applications in Materials Science

## Contents

A $C_s$ Corrected HRTEM: Initial Applications in Materials Science.....	2
Quantitative Environmental Cell - Transmission Electron Microscopy: Studies of Microbial Cr(VI) and Fe(III) Reduction.....	6
Simulations of Kikuchi Patterns and Comparison with Experimental Patterns.....	14
Experimental Atomically Resolved HAADF-STEM Imaging - A Parametric Study.....	22
Observation of Waterborne Protozoan Oocysts Using a Low-Vacuum SEM.....	26
A Possible Efficient Assay: Low-Vacuum SEM Freeze Drying and Its Application for Assaying <i>Bacillus thuringiensis</i> Formulations Quality.....	29
Observations of Algae and Their Floc in Water Using Low-Vacuum SEM and EDS.....	34
Development of Nano-Analysis Electron Microscope JEM-2500SE.....	40
Development of JSM-7400F; New Secondary Electron Detection Systems Permit Observation of Non-Conductive Materials.....	44
Applications of Image Processing Technology in Electron Probe Microanalyzer.....	48
Technology of Measuring Contact Holes Using Electric Charge in a Specimen ..	54
Organic EL Display Production Systems - ELVSS Series-.....	59
In-Situ Observation of Freeze Fractured Red Blood Cell with High-Vacuum Low-Temperature Atomic Force Microscope.....	62
Peak Deconvolution of Analysis in Auger Electron Spectroscopy.....	66
JEOL's Challenge to Nanotechnology .....	70
Progress in Development of High-Density Reactive Ion Plating .....	74
Applications of High-Power Built-in Plasma Gun.....	78
Introduction of New Products.....	81

## Cover micrograph

Experimental Kikuchi pattern (left) and simulated Kikuchi pattern (right) of MgO [100]. (See pages 14 to 21)

Courtesy of Professor Emeritus Michiyoshi Tanaka, Institute of Multidisciplinary Research for Advanced Materials, Tohoku University.

**John L. Hutchison<sup>†</sup>, John M. Titchmarsh<sup>†</sup>, David J. H. Cockayne<sup>†</sup>, Guenter Möbus<sup>†</sup>, Crispin J. D. Hetherington<sup>†</sup>, Ron C. Doole<sup>†</sup>, Fumio Hosokawa<sup>\*\*</sup>, Peter Hartel<sup>\*\*\*</sup> and Max Haider<sup>\*\*\*</sup>**

<sup>†</sup>Department of Materials, Oxford University

<sup>\*\*</sup>Electron Optics Division, JEOL Ltd.

<sup>\*\*\*</sup>CEOS GmbH

A new aberration-corrected TEM/STEM is being designed for applications in materials science. Here we describe preliminary tests of the objective lens  $C_s$  corrector, and present images showing some of the advantages in applications of  $C_s$  corrected HREM in the study of advanced materials.

## Introduction

Since the invention of the electron microscope over 60 years ago the effects of aberrations in round electromagnetic lenses have imposed fundamental limits on their performance. In the case of HREM, spherical aberration was shown by Scherzer [1] to limit interpretable resolution, although special techniques have been devised to get around this, such as "aberration-free focus" for particular crystal structures [2]. Small-probe techniques, and in particular STEM, are similarly limited by spherical aberration in the probe-forming lenses. The need for a small, well-defined probe with a high current remains a pressing need here. The recent successful development of aberration correctors for electromagnetic lenses [3, 4] will radically change this situation, as they offers dramatic improvements for direct interpretation of image contrast as well as for microanalysis with improved spatial resolution and sensitivity in materials science applications.

## A New Aberration-Corrected Microscope

In order to exploit these benefits a new TEM with aberration correction of both condenser and objective lenses is now being developed for installation at Oxford University. This instrument is based on the JEM-2010FEF instrument with a Schottky field emission source and aims to provide an HREM information limit and HAADF resolution close to 0.1 nm. Analytical features will include EELS

and energy-filtered imaging, EDS and holography. A wide objective lens pole-piece gap is possible because of the  $C_s$  correction and allows a large range of specimen tilt while retaining HREM imaging capability. In order to minimise interference and to maximise thermal stability, the microscope column, power supplies and operating consoles will all be installed in separate, adjacent rooms within a purpose-built laboratory, now under construction. Components of the new instrument are being independently developed and tested prior to final assembly.

## Assessment and Preliminary Applications of $C_s$ Corrected Objective Lens

The objective lens  $C_s$  corrector [5] has now been developed and tested on a separate JEM-2010F instrument and we illustrate here some of the initial results. Tests have confirmed the stability of the corrector over lengthy periods. This corrector is based on the design concept of Rose [6], and consist of a series of two hexapole and two transfer lenses doublets (round lenses) located between the objective and first intermediate lenses in the microscope column. This is shown in **Fig. 1**. The column height is increased by some 24 cm. The successful operation of the corrector depends upon accurate measurement of the main aberrations present, and this is done by acquiring images of an amorphous film and measuring relative changes in two-fold astigmatism and defocus with changes in incident beam tilt. This in turn is achieved by calculating Fourier transforms of the images, and displaying these as a tableau showing the variations as a function of beam tilt and azimuthal orientation.

<sup>†</sup>Parks Road, Oxford, OX1 3PH, UK

<sup>†</sup>E-mail: john.hutchison@materials.ox.ac.uk



Fig. 1. Column of JEM-2010F microscope with  $C_s$  corrector installed.

This method was first described by Zemlin and co-workers as a way of determining coma-free alignment conditions for HREM [7]. **Figure 2** shows a tableau of diffractograms from a specimen of amorphous Ge imaged in an uncorrected state: here the electron beam has been aligned approximately to the voltage axis, and two-fold astigmatism has been corrected. The inner four off-axis diffractograms represent a beam tilt of 9 mrad, the outer twelve a tilt of 18 mrad. The strong effects of axial coma, 3-fold astigmatism and spherical aberration are all evident; the tableau is evidently non-centrosymmetric. Measured aberration values are as follows:  $C_s$ : 0.59 mm, 3-fold astigmatism: 630  $\mu\text{m}$ , coma: 1.5  $\mu\text{m}$ . The aberration corrector is then used to compensate these effects, and a tableau corresponding to the corrected state is presented in **Fig. 3**. Here there are almost no changes between the diffractograms for tilted illumination; 2-fold and 3-fold astigmatism, coma and spherical aberration have all been corrected. These results demonstrate an information limit, in the corrected state, between 0.12 and 0.13 nm, verified by measurement of Young's fringes [8]. This value is consistent with the energy spread in the electron beam

(0.8 eV) and objective lens chromatic aberration coefficient of 1.2 mm for the URP pole-piece operating at 200 keV.

## Applications of $C_s$ Corrected HREM in Materials Science

### Localised contrast at boundaries

One of the major limitations in the current generation of field-emission-gun HREM instruments is the delocalisation of contrast at boundaries and interfaces [9]. This effect arises from the width of the aberration discs belonging to individual diffracted electron beams, the diameter of which increases with  $C_s$ . This may produce bands of spurious contrast up to several nm. in width, making quantitative interpretation of image contrast difficult. When  $C_s$  is fully corrected, this phenomenon disappears, and interfaces or boundaries appear atomically sharp.

The imaging of a grain boundary in a  $\langle 111 \rangle$  Au foil after aberration correction (**Fig. 4**) demonstrates the effective removal of delocalised phase contrast. This micrograph was recorded at close to Gaussian focus, with  $C_s$

very close to zero. A more detailed comparison of this image with those obtained using other techniques will be presented elsewhere [10]. It has been noted that while direct interpretation of aberration-corrected images promises to be more accurate in many applications, image simulation will still be required [11].

### Suppression of phase contrast

A new area in which aberration correction will provide further significant benefits is the characterization of nanometer-sized particles. Important parameters are microstructure, shape and size, all of which are difficult to determine accurately by conventional HREM imaging. First, in conventional HREM imaging, i.e. at Scherzer focus, the presence of a prominent Fresnel fringe around the edge of a small particle will make precise size measurement difficult. Second, delocalised contrast (see above) gives rise to "ghost images", particularly in a FEG instrument. Third, free-standing nanoparticles must be supported, usually on amorphous substrates for plan-view imaging. The immediate advantages of  $C_s$ -corrected imaging are clearly illustrated in **Fig. 5**. This shows an image of a small ( $\sim 4$  nm) CdSe quantum dot on an amorphous carbon support film. In an uncorrected image of such a small particle recorded at Scherzer defocus, the presence of strong Fresnel fringes and "ghost" images would obscure the fine scale structural features, which are further upset by strong phase contrast arising from the carbon film. The image recorded in the aberration-corrected state provides the following immediate advantages: the image is recorded at very close to Gaussian focus so that there is no Fresnel fringe around the edges of the particle; there are no ghost images present and the phase contrast from the amorphous support film has been almost completely suppressed. Under these conditions the amplitude contrast contribution is optimised, and the contribution from the more strongly scattering Cd and Se is enhanced. The size, shape and internal structure of the crystallite, only 2 nm in size, are thus revealed with much improved clarity [12].

### Atomic resolution imaging of complex oxide structures

Although high resolution images of complex oxide structures have been widely studied for many years the resolution of contrast at oxygen sub-lattice sites remains a serious challenge. High-voltage HREM has been used [13], and more recently image restoration techniques have been successfully developed to achieve this [14]. It is now clear that the enhanced high resolution capability afforded by  $C_s$  correction can produce resolution close to 0.1 nm, particularly when electron beam energy spread is reduced. **Figure 6** shows an image of a novel niobium oxide structure, where all the projected cation sites are revealed, along with visible contrast at the anion sites. We can expect even further improvements when the effects of chromatic aberration are reduced by reducing the energy spread in the incident electron beam.

## Conclusions

A  $C_s$  - corrected HREM has been built and its performance assessed as part of a major

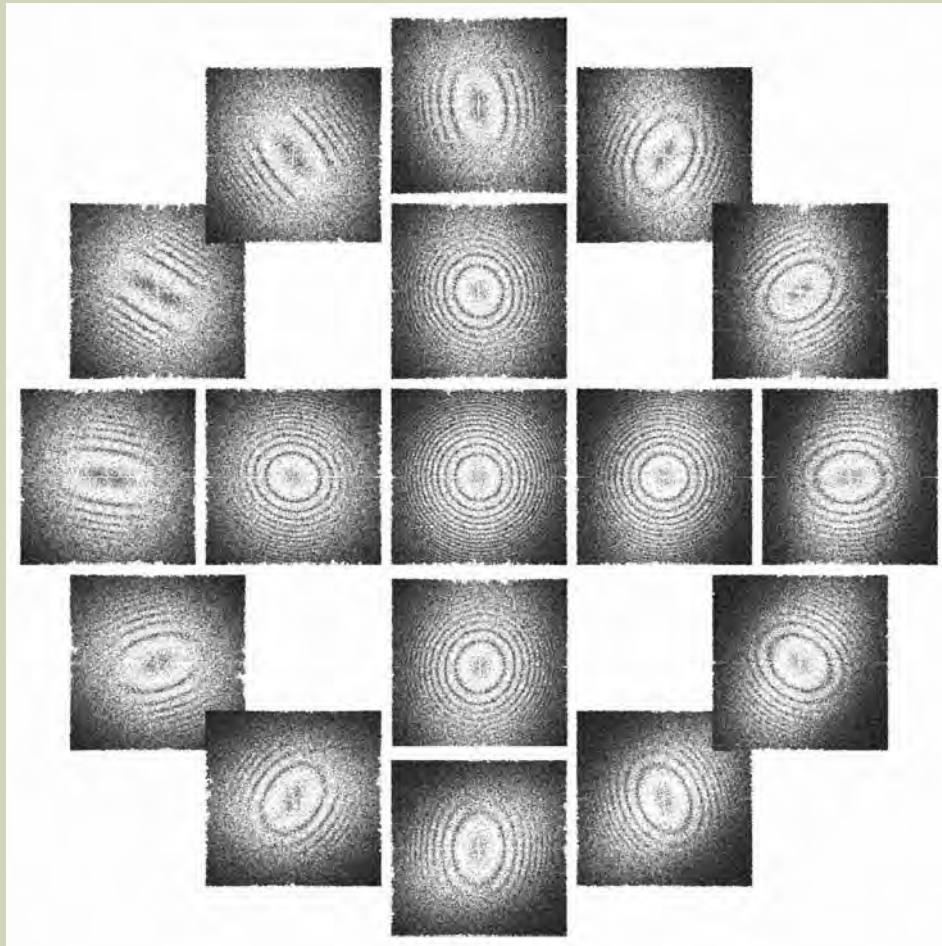


Fig. 2. Diffractogram tableau for uncorrected microscope. Outer diffractograms correspond to a beam of 18 mrad.

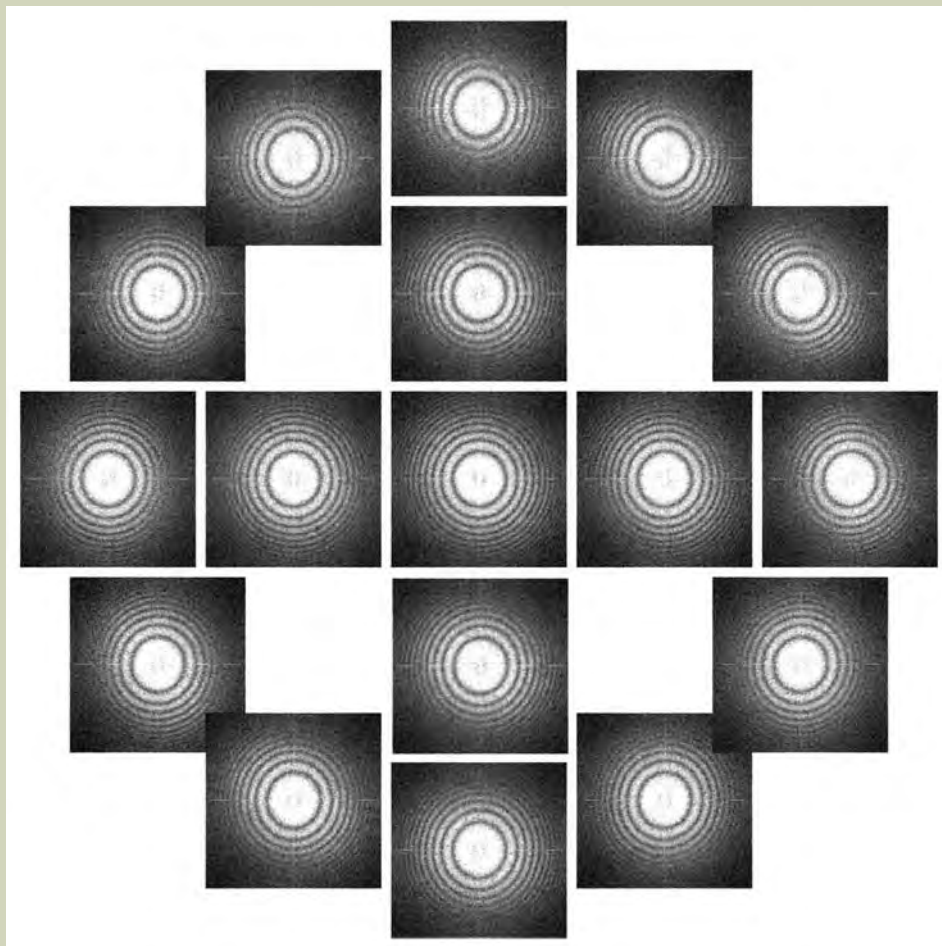


Fig. 3. Diffractogram tableau for aberration-uncorrected state.

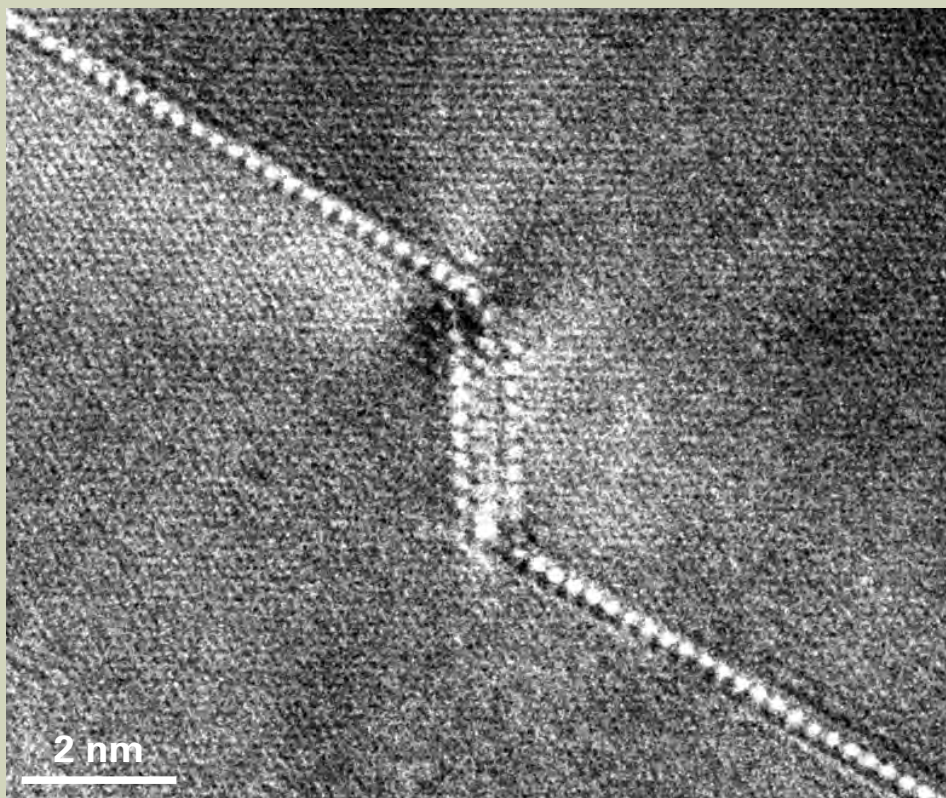


Fig. 4.  $\bullet 3$  boundary in  $\langle 111 \rangle$  gold foil, showing localised contrast.

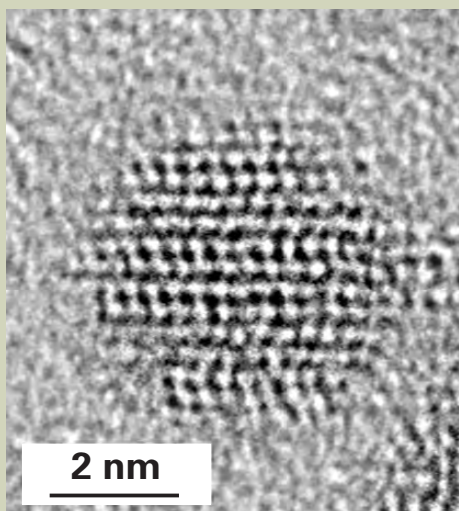


Fig. 5. Nanocrystal of CdSe, with suppressed phase contrast of supporting carbon substrate.

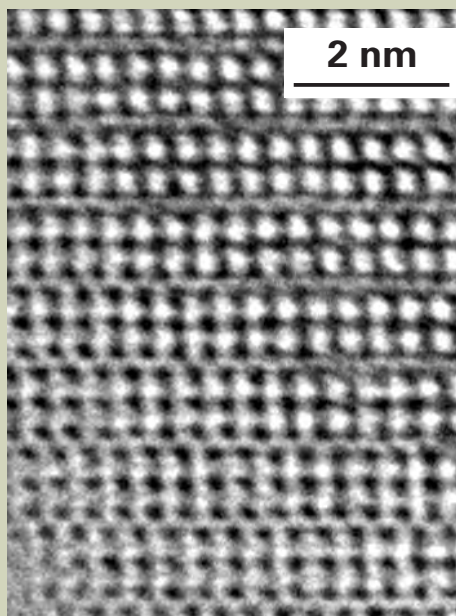


Fig. 6. Aberration-corrected image of a niobium oxide crystal, showing contrast at both cation and anion lattice sites.

project to develop a “next generation” TEM/STEM. This unique instrument will be installed in a specially built laboratory at Oxford University’s Department of Materials. We have demonstrated that the main objective lens aberrations may be fully corrected, and present examples of the main benefits to be gained by the use of  $C_s$  corrected HREM in materials science.

## Acknowledgements

This project is supported by a major JIF grant from HEFCE and EPSRC. We are also grateful to JEOL Ltd. and to JEOL (UK) Ltd. for their ongoing support.

## References

1. Scherzer O.: *J. Appl. Phys.* **20** 20 (1949).
2. Hashimoto H.: *Chemica Scripta* **14** 23 (1978-79)
3. Haider M., Rose H., Uhlemann S., Schwan E., Kabius B. and Urban K.: *Ultramicroscopy* **75**, 53 (1998).
4. Krivanek O. L., Delby N. and Lupini A. R.: *Ultramicroscopy* **78**, 1 (1999).
5. Haider M., Braunshausen G. and Schwan E.: *Optik* **99**, 167 (1995).
6. Rose H.: *Optik* **85** 19 (1990).
7. Zemlin F., Weiss P., Schiske P., Kunath W. and Herrmann K.H.: *Ultramicroscopy* **49**, 3 (1977).
8. Frank J.: *Optik* **30**, 171 (1969).
9. Thust A., Coene M., Op de Beek M. and Van Dyck D.: *Ultramicroscopy* **64**, 211 (1996).
10. Hetherington C J D *et al.* Proceedings of ICEM 15 (Durban) 2002.
11. Möbus G., Titchmarsh J. M., Hutchison J. L., Hetherington C. J. D., Doole R. C. and Cockayne D. J. H.: *Inst. Phys. Conf. Series* No. **168**, 27 (2001)
12. Allsop N. A., Hutchison J. L. and Dobson P. J.: Proceedings of ICEM 15 (Durban) 2002.
13. Horiuchi S. and Matsui Y.: *Jpn. J. Appl. Phys.* **31**, L283 (1992)
14. Kirkland A. I., Meyer R. R., Saxton O. W., Hutchison J. L. and Dunin-Borkowski R. E.: *Inst. Phys. Conf. Series* No. **161**, 291 (1999).

# Quantitative Environmental Cell - Transmission Electron Microscopy: Studies of Microbial Cr(VI) and Fe(III) Reduction

Tyrone L. Daulton<sup>†</sup>, Brenda J. Little<sup>††</sup>, Jin W. Kim<sup>†</sup>, Steven Newell<sup>†</sup>, Kristine Lowe<sup>†††</sup>, Yoko Furukawa<sup>†</sup>, Joanne Jones-Meehan<sup>†††</sup> and Dawn L. Lavoie<sup>†</sup>

<sup>†</sup>Marine Geosciences Division, Naval Research Laboratory

<sup>††</sup>Oceanography Division, Naval Research Laboratory

<sup>†††</sup>Chemistry Division, Naval Research Laboratory

Several applications of environmental cell (EC)-transmission electron microscopy (TEM) to microbial metal reduction studies are reviewed. Electron energy loss spectroscopy (EELS) techniques were used to determine oxidation state, at high spatial resolution, of Cr associated with the metal-reducing bacteria, *Shewanella oneidensis*, in anaerobic cultures containing Cr(VI)O<sub>4</sub><sup>2-</sup>. These techniques were applied to fixed cells examined in thin section by conventional TEM and unfixed, hydrated bacteria examined by EC-TEM. Measurements by EELS demonstrated that cell boundaries became saturated with low concentrations of Cr and the precipitates encrusting bacterial cells contained a reduced form of Cr in oxidation state +3 or lower. In addition, reduction by *S. oneidensis* of structural Fe(III) in nontronite, an expandable clay, was studied under anaerobic conditions. Direct observations by EC-TEM yield unambiguous measurement of layer spacings and the contraction of hydrated, clay layers upon reduction of structural Fe(III). In particular, nonreduced and Fe(III)-reduced nontronite, observed by EC-TEM, exhibit mean (001) spacings of 1.50 nm and 1.26 nm, respectively.

## Introduction

Conventional transmission electron microscopy (TEM) studies of microbial reduction of metals have provided important information. However, they are limited because the techniques of fixation, embedding, and microtoming, necessary to prepare thin specimens, are known to alter delicate cellular and abiotic microstructures. Fixation and dehydration preserve some cellular structure, but buffer and organic solvent washes remove extracellular polymers. In addition, soluble ions from extracellular and intracellular sources, such as soluble reduction intermediates, can be lost. Reduction intermediates are unstable with intermediate valence state between the valences of the stable end members of the reduction process. Dehydration causes basal layer spacings in expandable clay minerals to contract and the extracellular biopolymers produced by bacteria associated with clays to collapse into a filamentous, web-like network. In contrast, environmental cell (EC)-TEM is a powerful technique in which hydrated specimens can be examined at high spatial resolution in more or less their natural state. The purpose of this paper is to demonstrate the application of EC-TEM for the study

of microbial metal reduction mechanisms and their alteration products; two studies are reviewed.

## Microbial reduction of Cr(VI)

Hexavalent chromium species are strong oxidants which act as carcinogens, mutagens, and teratogens in biological systems [1]. The high solubility, bioavailability, and toxicity of Cr(VI) make it a particular environmental concern. Microbial mechanisms for Cr(VI) reduction are of particular technological and biological importance because they convert a toxic, mobile element into a less toxic, immobile form. The study of microbial Cr(VI) reduction, such as the identification of reduction intermediates, has been hindered by the lack of an analytical technique that can determine the oxidation state of Cr at subcellular spatial resolution. The most widely used method for following Cr(VI) reduction is the diphenylcarbazide colorimetric method [2]. Other methods used to determine oxidation state in bacterial cultures include electron spin resonance (ESR) (also called electron paramagnetic resonance (EPR) and electron magnetic resonance (EMR)) spectroscopy, and X-ray photoemission spectroscopy (XPS). These bulk techniques cannot provide detailed information at the subcellular (submicron) level necessary for understanding microbial reduction processes.

Both TEM and scanning electron microscopy (SEM) have sufficient resolution to study the spatial relationship between cells and reduction products, as well as their chemistry. For example, energy-dispersive X-ray spectroscopy (EDXS) has been used to identify elements present in reduction products associated with bacteria [3-8] and wetland plants [9]. However, EDXS is insensitive to oxidation state. Electron energy loss spectroscopy (EELS) by TEM is a direct probe of the electron configuration around atoms, and can determine the oxidation state of 3d and 4d transition metals at high spatial resolution [10, 11]. Furthermore, EELS techniques have been used to produce oxidation state maps using energy filtered imaging [12].

Determination of oxidation state by EELS is accomplished by analyzing valence induced differences in fine structure of L<sub>2</sub> and L<sub>3</sub> (or collectively L<sub>2,3</sub>) absorption edges by comparison of unknowns to standards of known oxidation state. The L<sub>2,3</sub> absorption edges arise from transitions to unoccupied d levels from two spin-orbit split levels, 2p<sub>1/2</sub> level (producing the L<sub>2</sub> edge) and the 2p<sub>3/2</sub> level (producing the L<sub>3</sub> edge). The valence of a transition metal is related to the number of holes in the d level (i.e. the 3d<sup>n</sup> or 4d<sup>n</sup>) configuration. For example, tetrahedral Cr(VI) has an empty d orbital (3d<sup>0</sup> configuration) and octahedral Cr(III) has a 3d<sup>3</sup> configuration. Since L<sub>2,3</sub>

<sup>†</sup>Stennis Space Center, MS, 39529 USA  
<sup>†</sup>E-mail : tdaulton@nrlssc.navy.mil

absorption edges are inherently dependent on the number of unoccupied  $d$  levels in  $3d$  and  $4d$  transition metals, they are sensitive to valence state. In general, oxidation state can affect the position, shape and relative intensity of  $L_{2,3}$  absorption edges. Techniques used to determine mixed/single valence states involve analysis of the following: (a) the position of the  $L_{2,3}$  absorption edges [10], (b) the ratio of the  $I(L_{3})/I(L_{2})$  integrated-peak intensity (henceforth abbreviated  $L_{3}/L_{2}$ ) [10, 11], and (c) least squares fits of summed spectra of standards or calculations to the shape of  $L_{2,3}$  absorption edges [13].

Because of difficulties in the application of EELS techniques to actual microcharacterization of mineral oxidation state, these techniques have been under utilized. For example, despite the detailed, submicron-scale information EELS techniques can provide, to our knowledge, they have never been applied in microbial reduction studies. In fact, previous TEM studies assumed microbial Cr(VI) reduction products were Cr(III) [6, 8]. Since Cr(III) is a stable and insoluble reduced form, this assumption is likely correct. However, the oxidation state of the Cr associated with bacteria has not yet been determined by direct measurement. We recently demonstrated the application of EELS techniques for the determination of oxidation state of metals associated with hydrated bacteria [14]. In particular, Cr(VI) reduction by *Shewanella oneidensis* [15] was studied.

### Basal layer contraction of expandable clays induced by Fe(III) reduction

Bacteria have been shown to effectively reduce octahedral Fe(III) in clays [16, 17]. The importance of the role of redox driven interactions between ferruginous clays and bacteria in the alteration of clays has been receiving increasingly more attention. For example, swelling pressures of ferruginous clays are related to basal layer spacing [18], which depends on the oxidation state of octahedral Fe [19]. Furthermore, reduction of Fe(III) in ferruginous clays produces decreased swelling pressures [20], increased cation fixation [21], smaller specific surface area [22], and a decrease in mean layer spacing [23]. Interlayer force is believed produced by the mutual attraction to interlayer cations by the net-negative charge of phyllosilicate layer surfaces which balances the total charge of the clay. Therefore these studies suggest, increased interlayer force may be driven by reduction-induced changes in the surface layer charge. However, this theory cannot be fully evaluated because of the lack of direct measurements. Nearly all structural data have been obtained by bulk techniques, and data available by direct measurements are inconclusive, e.g. [24].

Stuki and Tessier [24] examined chemically reduced Fe-rich smectite by high resolution (HR)-TEM. Specimens were prepared by thin section after water exchange with embedding resin. Using selected area electron diffraction (SAED), they showed the crystal stacking changed from turbostratic to a more ordered structure in the reduced state, indicating an increase of interlayer attraction due to the structural reduction of Fe(III) to Fe(II).

However, the expected contraction in clay (001) layer spacing was not found. A constant layer spacing of 1.26 nm was observed in both oxidized and reduced smectite. This measurement is in conflict with the earlier *in-situ* pressure-cell X-ray diffraction work of Wu *et al.* [23] which demonstrated a decrease in mean interlayer distance upon reduction of Fe(III) in bulk Na-nontronite. However, the effects of resin infiltration on the interlayer spacing are uncertain and, therefore, the homogeneous layer spacing observed by Stuki and Tessier [24] may be due to artifacts induced by resin infiltration. We recently demonstrated the application of EC-TEM to study the collapse of basal spacing in ferruginous-expandable clays induced by microbial Fe(III) reduction [25]. The effects of anaerobic respiration (Fe(III) reduction) by *S. oneidensis* on nontronite were examined. In particular, differences in layer spacings between nonreduced and reduced nontronite, in their 'native' hydrated state, were characterized using EC-TEM.

## Cultures, Methods, and Techniques

### Cultures

*S. oneidensis* [15] was originally isolated from the anaerobic zone of Mn-rich sediments in Oneida Lake, NY [26]. *S. oneidensis* (ATCC RF50108) is a Gram-negative bacterium capable of respiring aerobically and anaerobically using a variety of terminal electron acceptors, including:  $O_2$ , Fe(III), Mn(IV), nitrite ( $NO_2^-$ ), nitrate ( $NO_3^-$ ), sulfite ( $SO_3^{2-}$ ), thiosulfate ( $S_2O_3^{2-}$ ), tetrathionate ( $S_4O_6^{2-}$ ), trimethylamine N-oxide, fumarate, glycine, Cr(VI), U(VI), and Tc(VII) [27-29]. Complete details on the cultures and reduction experiments can be found in [14, 25], and are summarized below.

For conventional-TEM studies of Cr(VI) reduction, cells were grown anaerobically for 30 days with  $100 \mu M$   $CrO_4^{2-}$  as the sole terminal electron acceptor. Samples (1 mL) were pelleted by centrifugation, fixed in 1 mL of a 5% aqueous solution of glutaraldehyde overnight at room temperature, and embedded in Spurr's resin. The embedded specimen was sectioned to 80 nm thickness by microtome, and mounted on amorphous carbon (a-C) coated Cu TEM grids (see [14] for full description).

For EC-TEM studies of Cr(VI) reduction, cells were grown anaerobically with  $100 \mu M$   $CrO_4^{2-}$  as the sole terminal electron acceptor. A total of 0.275 moles  $K_2CrO_4$  was added to the culture over a 51-day incubation. In contrast to conventionally prepared TEM specimens, EC-TEM specimen preparation was minimal: culture was centrifuged, supernatant removed, and the pellet rinsed with distilled water to remove trace salts. An aliquot (several  $\mu L$ ) of the resuspended pellet was quickly loaded into the EC-specimen holder. Removal of trace salts from the culture circumvented salt precipitation on the EC window as the bulk of the aliquot evaporated, leaving a thin hydrated layer. The specimen was examined at 100 Torr of air (saturated with water vapor) circulating through the EC at a rate of  $\approx 2$  Torr L  $min^{-1}$ .

For studies of clay reduction, nontronite

from Uley graphite mine, South Australia (Clay Mineral Society standard (NAu-1) [30]) was used as the sole terminal electron acceptor. Samples (diameters  $< 2.0 \mu m$ ) were sterilized by exposure to microwave radiation (5 min), and sterility was confirmed from lack of bacterial growth on Luria-Bertani (LB) agar after 2 days. Cells were grown anaerobically with nontronite for 4 days, then examined by EC-TEM at 10 - 100 Torr of air (saturated with water vapor) circulating through the EC at a rate of  $\approx 2$  Torr L  $min^{-1}$ .

### Transmission electron microscopy

A JEOL JEM-3010 transmission electron microscope operating at 300 keV with a LaB<sub>6</sub> filament was used in these studies. This instrument is equipped with an EDXS system, a Gatan imaging filter (GIF200) capable of EELS, and a JEOL EC system. The EC-TEM system is of the closed cell type [31] where confinement of a pressurized environment is achieved with electron-transparent windows. The microscope is equipped with two interchangeable JEOL EC specimen holders (a two-line gas EC and a four-line gas/liquid EC) that are connected to the EC system by flexible, stainless steel lines. Both *in-situ* EC-TEM specimen holders are capable of circulating dry or water-saturated gas (using two lines) at flow rates of 0 - 15 Torr L  $min^{-1}$  through the specimen chamber at  $10^3$  to  $> 200$  Torr pressure. The four-line holder has two additional service lines which can be used to independently inject several microliters of liquids from different reservoirs. Each EC holder consists of a small cylindrical cell sealed by two electron transparent windows on the top and bottom (see Fig.1 for the 4-line cell used in this study). The windows are 15 - 20 nm thick amorphous carbon (a-C) films covering seven hexagonally arrayed, 0.15 mm apertures on a 3.5 mm diameter Cu disk (Fig. 1). Prior to use, the windowed grids were tested to withstand a pressure differential of 250 Torr for one minute. A computer controls the EC system and facilitates the operation of inserting, and removing the EC holders from the microscope column without breaching the delicate windows (Fig. 2). Higher sensitivity leak checks of the EC windows are performed automatically during the specimen insertion sequence prior to full insertion into the column. Specimens are supported on the lower a-C film window. In conventional TEM, many specimens are supported on a-C films, in this sense, there is only one additional a-C film the electron beam must pass through using EC-TEM. Resolution tests of graphite in the EC show lattice resolution of at least 0.38 nm at 60 Torr of hydrated room air. It should be noted that the EDXS system cannot be used with EC-TEM because there is no direct line of sight between the specimen and the EDXS detector.

Unlike EC systems based on the principle of differential pumping, closed-cell EC systems require absolutely no modification to the column and the transmission electron microscope can still be used for conventional TEM without compromising resolution and analytical capabilities. The microscope was also equipped with conventional single- and double-tilt specimen holders for conventional TEM. The single-tilt holder has an adapter which accepts

windowed EC grids for analysis following their use in the EC holder.

### EELS techniques for oxidation state determination

Two EELS techniques were used to identify oxidation state of Cr associated with bacteria. Oxidation state was determined by both the chemical shift of  $L_{2,3}$  edges and the ratio of  $L_{3}/L_{2}$ , integrated-peak intensities, the two most sensitive and straightforward techniques.

Results of both techniques are used in combination to yield higher confidence and accuracy. In contrast, previous EELS studies have focused on demonstrating the capability of one technique, rather than applying techniques in combination to actual microcharacterization in physical/biological systems.

### EELS experimental parameters

The following conditions were used during collection of EELS spectra under EC-TEM

and TEM conditions: an illumination angle  $2\alpha = 4 - 10$  mrad, a collection angle of  $2\beta = 10.8$  mrad, a 2 mm entrance aperture, and an energy dispersion of 0.1 eV/channel. Low-loss spectra were acquired with an integration time of 0.128 s and core-loss spectra between 0.512 and 1.02 s. For each acquisition, 10 (EC-TEM) or 25 (conventional TEM) spectra were summed. Spectra were collected in diffraction mode of the transmission electron microscope (i.e. image coupling to the EELS

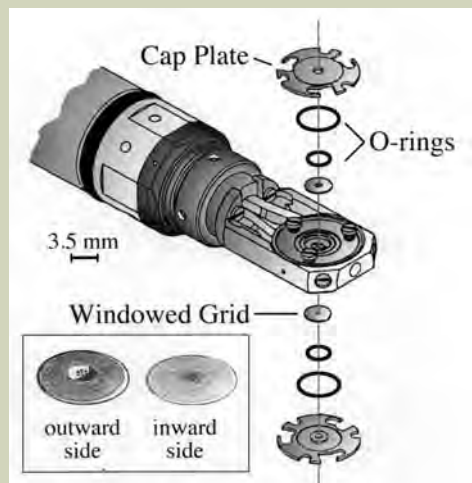


Fig. 1. Schematic illustration of the specimen chamber for the four-line EC specimen holder.

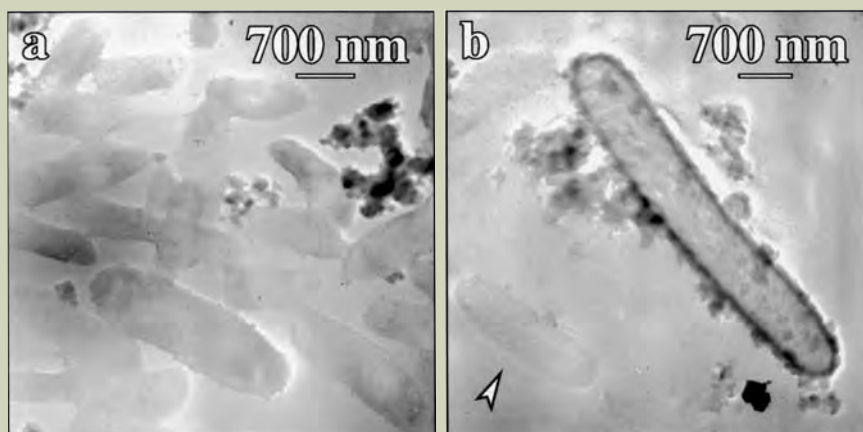


Fig. 3. *Shewanella oneidensis* imaged by EC-TEM at 100 Torr: (a) bacteria exhibiting low contrast in bright-field imaging and (b) bacteria encrusted with electron dense particulate. The arrowhead in panel (b) points to a low contrast bacterium in the same field of view as a bacterium with electron dense particulate, illustrating the dramatic contrast difference.

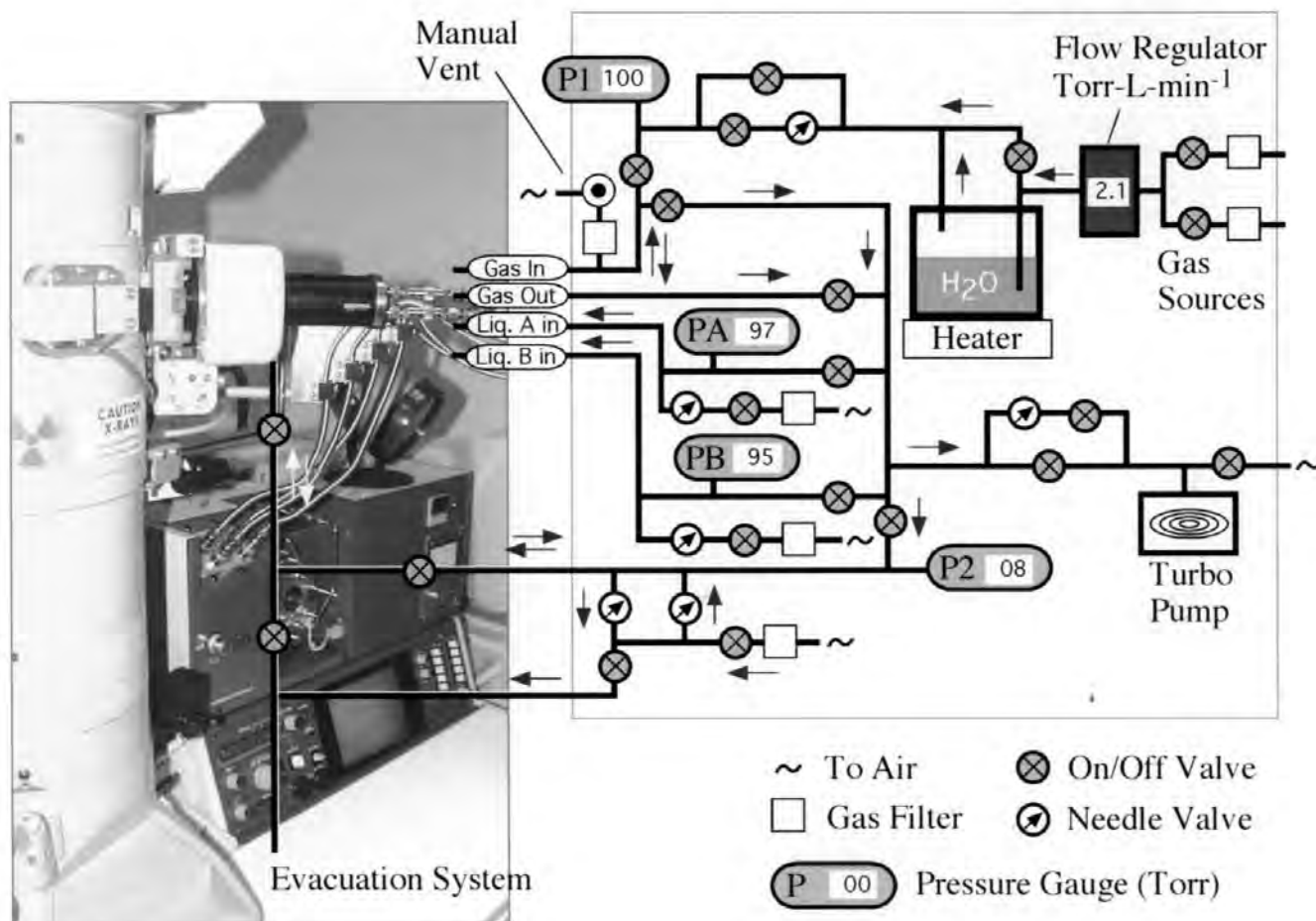


Fig. 2. Schematic illustration of the EC control system.

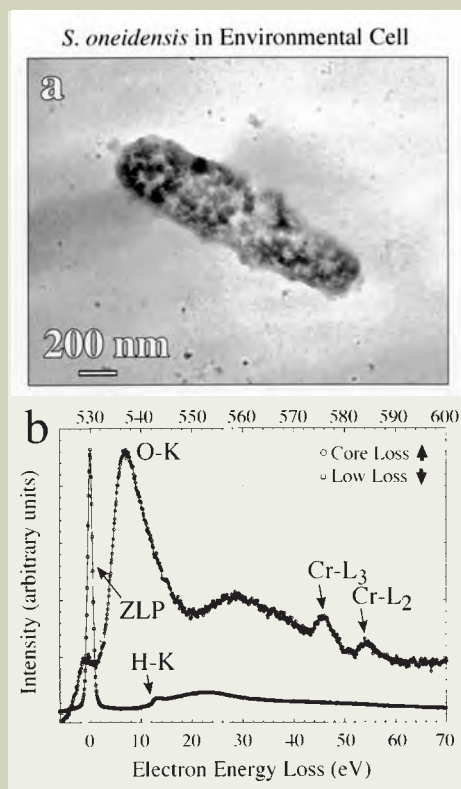


Fig. 4. *Shewanella oneidensis* imaged by EC-TEM at 100 Torr: (a) cell is encrusted with electron dense particulate. (b) EC-TEM EELS spectrum from the bacterium demonstrates the presence of Cr. Both the low-loss spectrum containing the zero-loss peak (ZLP) and the core-loss spectrum of the O-K and Cr-L absorption edges are shown. The full width at half maximum of the ZLP is a measure of the instrumental resolution, which under these EC-TEM conditions is  $\approx 1$  eV. As indicated by vertical arrows, the top abscissa corresponds to the low-loss spectrum and the bottom abscissa corresponds to the core-loss spectrum.

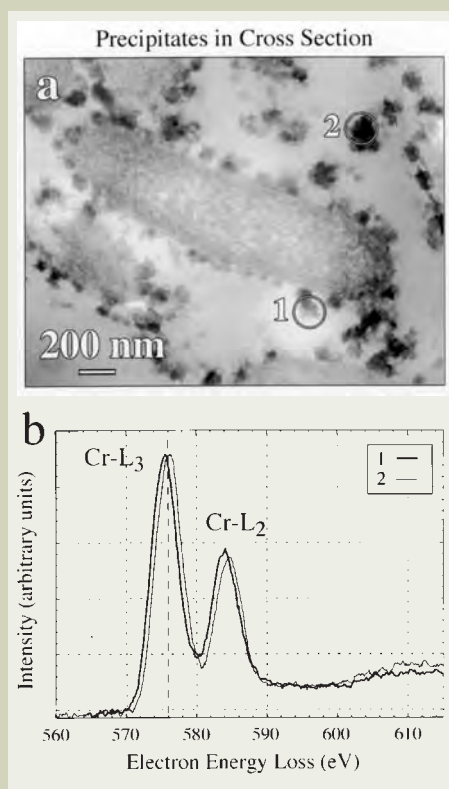


Fig. 5. *Shewanella oneidensis* imaged by conventional TEM in  $\approx 80$  nm thick, thin section: (a) cell is encrusted with electron dense particulate. The field of view displays several bacterial cells in random, oblique cross-section. Cross-sectional images show precipitates occur on the outer cell surface and no evidence of intracellular precipitates is observed. (b) EELS spectra from the isolated precipitates demonstrates the presence of Cr. The analyzed precipitates are labeled and the diameter of the circle corresponds to the electron probe diameter.

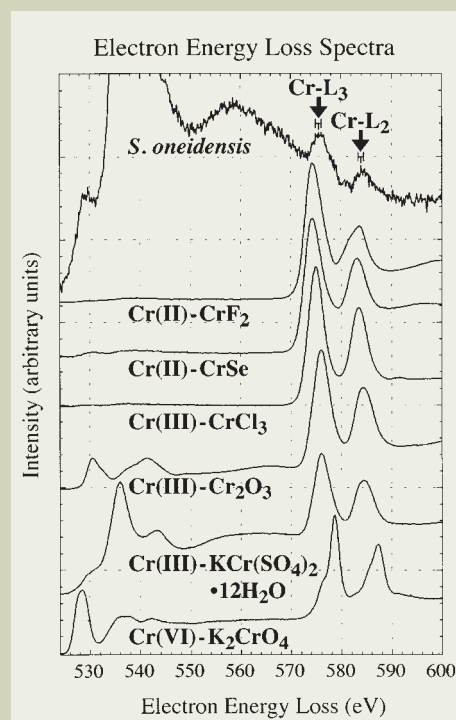


Fig. 6. A comparison of the core-loss EELS spectra of encrusted *Shewanella oneidensis* in the EC at 100 Torr and Cr standards of known oxidation state. Spectra were normalized to the intensity of the  $L_3$  peak and offset from one another. The spectra shown for the Cr standards represent the sum of twenty individual spectra. The error bars shown for *S. oneidensis* represent the error in energy loss calibration for that spectrum only. For the errors associated with other spectra, see Table 1.

spectrometer) and were corrected for dark current and channel-to-channel gain variation of the charge coupled device (CCD) detector.

Energy calibration of the core-loss regime and measurement of energy drift during data acquisition were performed by collecting zero-loss spectra before and following collection of core-loss spectra. Energy of core-loss spectra was calibrated using the average position of the two zero-loss peaks. The error in the energy calibration corresponded to the energy drift of the zero-loss peaks. In addition, a C-K edge spectrum was acquired immediately following spectrum collection from the O-K / Cr-L core-loss regime. The measured position of the C-K ( $1s$ ) peak at 284.9 eV (arising from transitions to the  $\neq^*$  molecular orbital) from the TEM a-C support film was used to evaluate the energy calibration. Either the pre-O-K edge background or the pre-Cr-L edge background (depending on the analysis to be performed) was subtracted from core-loss spectra using a power law and plural inelastic scatter-

ing was removed by Fourier deconvolution methods [32].

Chromium standards were analyzed by conventional TEM. Standards were produced by placing high purity Cr(II)F<sub>2</sub>, Cr(II)Se, Cr(III)Cl<sub>3</sub>, Cr(III)<sub>2</sub>O<sub>3</sub>, KCr(III)(SO<sub>4</sub>)<sub>2</sub>·12H<sub>2</sub>O, and K<sub>2</sub>Cr(VI)O<sub>4</sub> powders directly on Cu TEM grids coated with holey a-C. Once the standard was prepared, it was examined immediately. For each standard, 20 individual grains were analyzed by EELS. Results were averaged and reported with the statistical standard error.

## Results

### Direct imaging of Cr(VI) cultures

Examination of *S. oneidensis* in Cr(VI) cultures by EC-TEM, showed the rod-shaped morphology typical of the species (Fig. 3). The micrographs demonstrate that bacterial membranes were intact and did not show evidence of rupture from partial decompression.

Cells remained hydrated and intact while extracellular polymers surrounding the cells retained moisture. In comparison, unfixed cells deposited on a holey a-C film and examined under high vacuum by conventional TEM (not shown), exhibited ruptured cell membranes, as well as loss of both cell and extracellular polymer mass through dehydration.

Direct imaging revealed two distinct populations of *S. oneidensis* in the cultures: bacteria exhibiting low image contrast (Fig. 3a) and bacteria exhibiting electron dense, high-contrast cell boundaries often encrusted with high-contrast precipitates (Fig. 3b). Cross-sectional images of bacteria by conventional TEM showed no evidence of intracellular precipitates, suggesting precipitates are restricted to the outer surface of the bacteria. Precipitates ranged in size between  $\approx 10$  - 200 nm, and SAED indicated that the grains were predominantly amorphous perhaps due to a high degree of hydration. Often the cells exhibited a 30 - 49 nm thick, high contrast perimeter,

indicating that the cell boundary became saturated with elements of heavy mass.

## Chemical analysis by EELS of Cr(VI) cultures

**Figure 4** shows EELS low-loss and core-loss spectra collected from an encrusted bacterium examined by EC-TEM. The dominant feature in the low-loss spectrum is the zero-loss peak corresponding to electrons which escaped inelastic collisions. The width of the zero-loss peak is a measure of the energy distribution of the incident beam and corresponds to the best energy resolution of the spectrometer (energy resolution typically decreases with increasing energy loss). The narrow zero-loss peak (Fig. 4) shows energy resolution is not significantly affected by transmission through the hydrated, pressurized environment of the EC. The broad feature around 25 eV in the low-loss spectrum corresponds to plasmon excitations (i.e., collective excitations of valence electrons). The ratio of the integrated intensity under the zero-loss and plasmon peaks is related to specimen thickness. The relative height of the two peaks illustrates that multiple scattering is not severe in the EC. The total thickness traversed by the electron beam, estimated by the log-ratio technique [32], is  $1.13 \lambda$ , where  $\lambda$  is the total mean free path for inelastic scattering through the EC windows and specimen. The low-loss spectrum also exhibits a sharp feature at 13.2 eV that is only observed in EELS spectra collected in the EC. It is consistent with the EELS K-edge of hydrogen [33] which can be produced by electron beam radiolysis of water in the hydrated specimen. For example, similar EELS edges at 13 eV have also been observed concurrently with electron-beam-induced bubble formation from frozen-hydrated biological specimens and were attributed to hydrogen formation [34].

In the core-loss spectrum of encrusted *S. oneidensis* examined by EC-TEM, a strong O-K (1s) edge signal was observed at  $537.1 \pm 0.5$  eV due to H<sub>2</sub>O in the hydrated bacterium and extracellular substances. A less intense feature at  $529.2 \pm 0.5$  eV can be attributed to oxygen 2p hybridization with the Cr 3d band, while the broad feature at 558 eV can be attributed to plural (O-K core-loss plus plasmon) scattering. The characteristic pair of Cr-L<sub>2</sub> and Cr-L<sub>3</sub> edges in the EELS spectrum indicates that the precipitates are Cr-rich.

Bacterial cultures were also examined in cross-section by conventional TEM. Spectra collected from individual precipitates encrusting the outer cell boundary of *S. oneidensis* (Fig. 5) showed characteristic Cr-L<sub>2,3</sub> edges. The sectioned precipitates selected for analysis were those loosely attached to the bacterial outer surface where spectra could be collected without contributions from the bacterial cell. In addition, the electron-dense cell boundary of *S. oneidensis* cells that lacked precipitates encrusting the surface was examined by EELS in cross section. Spectra from the cell boundary revealed characteristic Cr-L<sub>2,3</sub> edges indicating the cell boundary was saturated with Cr at concentrations likely too low to be detected by EDXS.

A comparison of core-loss spectra from encrusted, hydrated *S. oneidensis* (collected by EC-TEM) and Cr standards of known oxida-

Compound	Formal Valence	Cr-L <sub>3</sub> (2p <sub>3/2</sub> ) (eV)	Cr-L <sub>2</sub> (2p <sub>1/2</sub> ) (eV)	Technique	Reference
Cr	0	573.8	583.0	XPS	[40]
		574.0	583.4	XPS	[41]a
		574.1		XPS	[42]b
		574.3	582.8	EELS	[43]c
		576.5 ± 1.0	585.0 ± 1.0	EELS	[38]d
CrP	0	574.2		XPS	[42]
Cr(CO) <sub>6</sub>	0	577.6	586.3	XPS	[40]
CrF <sub>2</sub>	II	574.2 ± 0.1	583.5 ± 0.1	EELS	This study
CrSe	II	574.2 ± 0.1	583.1 ± 0.1	EELS	This study
CrCl <sub>3</sub>	III	574.9 ± 0.1	583.4 ± 0.1	EELS	This study
		576.4	587.4	XPS	[40]
CrPO <sub>4</sub> •4H <sub>2</sub> O	III	576.4 ± 0.2		XPS	[44]b
CuCrO <sub>2</sub>	III	576.4 ± 0.2	586.2 ± 0.2	XPS	[40] [45]e
Cr <sub>3</sub> (OH) <sub>2</sub> (OOCCH <sub>3</sub> ) <sub>7</sub>	III	576.5 ± 0.2		XPS	[44]b
NaCrO <sub>2</sub>	III	577.0 ± 0.2	586.9 ± 0.2	XPS	[40] [45]e
Cr <sub>2</sub> O <sub>3</sub>	III	575.9 ± 0.1	584.3 ± 0.1	EELS	This study
		576.4	585.9	XPS	[41]a
		576.6 - 576.8		XPS	[42]
		576.8 ± 0.2	586.2 ± 0.2	XPS	[40] [45]e
		576.8	584.8	EELS	[46]
		576.8	586.7	XPS	[47]
		577.9 ± 1.0	585.8 ± 1.0	EELS	[38]d
FeCr <sub>2</sub> O <sub>4</sub>	III	576.0	584.0	XPS	[48]f
KCr(SO <sub>4</sub> ) <sub>2</sub> •12H <sub>2</sub> O	III	576.0 ± 0.1	584.5 ± 0.1	EELS	This study
		581.0	590.5	XPS	[40] [45]e
LaCrO <sub>3</sub>	III	576.1 ± 0.09	585.8 ± 0.05	XPS	[49]
LiCrO <sub>2</sub>	III	577.0 ± 0.2	586.8 ± 0.2	XPS	[40] [45]e
CrOOH	III	577.0	586.9	XPS	[47]
Cr(OH) <sub>3</sub> •0.4H <sub>2</sub> O	III	576.9	586.3	XPS	[41]a
		577.1		XPS	[42]
CrP	III	577.4		XPS	[42]
CrCl <sub>3</sub> •6H <sub>2</sub> O	III	577.5		XPS	[42]
CrPO <sub>4</sub>	III	577.8		XPS	[42]
CrBO <sub>3</sub>	III	578.0		XPS	[42]
Cr <sub>2</sub> (SO <sub>4</sub> )•15H <sub>2</sub> O	III	578.6		XPS	[42]
CrO <sub>2</sub>	IV	576.3	586.0	XPS	[47]
LaCrO <sub>4</sub>	V	578.8 ± 0.21	588.0 ± 0.22	XPS	[49]
CrO <sub>3</sub>	VI	578.3 ± 0.2	587.0 ± 0.02	XPS	[45]e
		579.0	588.2	XPS	[41]a
CaCrO <sub>4</sub>	VI	578.9 ± 0.2	588.1 ± 0.2	XPS	[40] [45]e
BaCrO <sub>4</sub>	VI	579.1 ± 0.2	588.4 ± 0.2	XPS	[40] [45]e
K <sub>2</sub> Cr <sub>2</sub> O <sub>7</sub>	VI	579.4 ± 0.2	588.8 ± 0.2	XPS	[40] [45]e
		579.8	589.1	XPS	[47]
Na <sub>2</sub> Cr <sub>2</sub> O <sub>7</sub>	VI	579.4 ± 0.2	588.5 ± 0.2	XPS	[40] [45]e
Rb <sub>2</sub> Cr <sub>2</sub> O <sub>7</sub>	VI	579.4 ± 0.2	588.7 ± 0.2	XPS	[40] [45]e
Cs <sub>2</sub> Cr <sub>2</sub> O <sub>7</sub>	VI	579.5 ± 0.2	588.7 ± 0.2	XPS	[40] [45]e
SrCrO <sub>4</sub>	VI	579.6 ± 0.2	588.6 ± 0.2	XPS	[40] [45]e
K <sub>2</sub> CrO <sub>4</sub>	VI	578.6 ± 0.1	587.2 ± 0.1	EELS	This study
		579.6 ± 0.2	588.9 ± 0.2	XPS	[40] [45]e
PbCrO <sub>4</sub>	VI	578.6	587.2	XPS	[48]f
		580.9	587.8 - 589.5	EELS	[50]
Cs <sub>2</sub> CrO <sub>4</sub>	VI	579.8 ± 0.2	588.8 ± 0.2	XPS	[40] [45]e
Li <sub>2</sub> CrO <sub>4</sub>	VI	579.8 ± 0.2	589.0 ± 0.2	XPS	[40] [45]e
Na <sub>2</sub> CrO <sub>4</sub>	VI	579.8 ± 0.2	589.1 ± 0.2	XPS	[40] [45]e

XPS studies used the Au 4f<sub>7/2</sub> line at 84.0 eV for energy calibration unless otherwise stated.

a) After recalibrating the XPS Au 4f<sub>7/2</sub> line to 84.0 eV from 84.07 eV.

b) Reported as calibrated to XPS Au 4f<sub>7/2</sub> line at 84.0 eV and C (1s) at 284.8 eV.

c) As reported in reference as binding energies.

d) EELS L-edge onsets reported in reference, however L-peak positions are shown here.

e) After recalibrating the XPS Au 4f<sub>7/2</sub> line to 84.0 eV from 82.8 eV.

f) Energy calibration not reported.

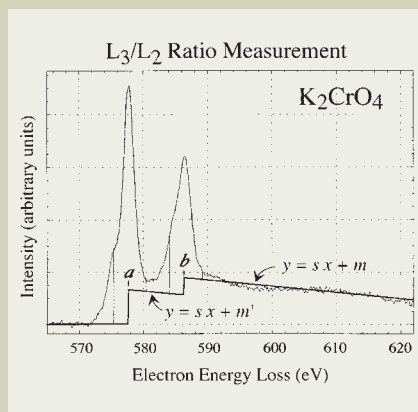


Fig. 7. Core-loss EELS spectrum for  $K_2CrO_4$  illustrating the background subtraction used in method I. The step function (bold line) used to subtract the background from the  $L_{2,3}$  edges and the areas integrated to yield peak intensities (shaded regions) are shown. The fitting parameters  $a$ ,  $b$ ,  $s$ , and  $m$  are: the  $L_3$  maximum, the  $L_2$  maximum, the slope of the linear function fitted to the 20 eV post  $L_2$  edge region (600 - 620 eV), and the intercept of the linear function. The parameter  $m'$  is given by  $m' = (2m - as)/3$ .

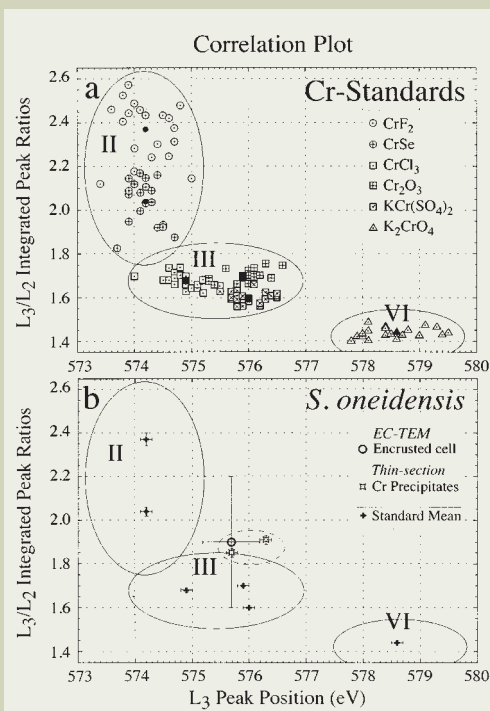


Fig. 8. The correlation between measured  $L_3/L_2$  integrated-peak intensity ratios and  $L_3$  peak positions for a) the Cr oxidation-state standards, b) bacteria and precipitates. Plotted  $L_3/L_2$  ratios were determined using background subtraction method II. The different Cr oxidation states fall within separate regions in the plot and are labeled II, III, and VI. The solid data points represent the mean of the data for a particular Cr standard.

tion state (collected by conventional TEM) is shown in Fig. 6. The spectrum of  $KCr(SO_4)_2 \cdot 12H_2O$  exhibited a peak at 535.7 eV similar to the stronger feature observed in the spectrum from hydrated *S. oneidensis*, and likely corresponds to  $H_2O$  bound in the structure. More importantly, systematic differences in Cr- $L_{2,3}$  fine structure are apparent in the spectra of standards (Fig. 6). For example, the Cr- $L_{2,3}$  lines for the standards show a systematic shift in edge-peak energy and variation in relative intensity with oxidation state (Fig. 6). In addition, the Cr- $L_{2,3}$  lines of the  $K_2CrO_4$  peaks are further differentiated in that they appear asymmetric because each is split into two separate peaks separated by  $\sim 2$  eV.

### EELS oxidation state analysis of standards

Oxidation state was identified by both the  $L_3$  peak positions and the ratio of  $L_3/L_2$  integrated-peak intensities. Measurement of the  $L_3$  peak positions is straightforward and the results for Cr standards are summarized in Table 1. For measurement of the ratio of  $L_3/L_2$  integrated-peak intensities, two methods of background subtraction were used. The first method, illustrated in Fig. 7, is similar to the double step function used by [35]. In this method, the Cr- $L_3$  pre-absorption edge was fit to a power law and subtracted. A linear function was then fit to the Cr- $L_2$  post-edge region

over a 20 eV window (extending from 600 to 620 eV). A linear step function was inserted at the  $L_2$  maximum and a straight line (of the same slope as that fitted to the Cr- $L_2$  post-edge region) was extrapolated into the  $L_3$  threshold. A second step function was inserted at the  $L_3$  maximum and set to zero below the  $L_3$  maximum. The ratio for the step heights was set at 2:1, consistent with the multiplicity of the initial states, that of four  $2p_{3/2}$  electrons and two  $2p_{1/2}$  electrons. It should be noted that the ratios of  $L_3$  to  $L_2$  intensities do not follow the expected 2:1 ratio for early 3d transition metals [36]. These anomalous ratios can be partially explained by atomic multiplet effects producing overlapping transitions from  $2p_{3/2}$  and  $2p_{1/2}$  states [37]. Nonetheless, an approximation of 2:1 is sufficient for this work.

Although the first subtraction method approximates the decreasing background, the fit of Cr- $L_2$  post-edge region was often affected by a broad post-edge feature, containing plural scattering effects not completely removed from the spectra. The post-edge feature varied with each spectrum, introducing scatter in the  $L_3/L_2$  peak ratios. To provide a more consistent background subtraction for all spectra, a second method using a flat, two-step function was applied. The second background fitting procedure is identical to the first except the slope of the linear function is set to zero and it is fit to a 2 eV wide window immediate-

ly following the Cr- $L_2$  peak, in the edge tail, prior to the post-edge feature.

Once the background was subtracted using either of the two methods, the Cr- $L$  peaks were integrated over a 5 eV window. The  $L_3/L_2$  peak ratios for the Cr standards are summarized in Table 2. The flat, two-step background subtraction method yielded the lower values, however, less relative scatter in the data. The core-loss spectra for  $K_2CrO_4$  exhibited almost no post  $L_2$  edge features and this may account for the close similarity in  $L_3/L_2$  peak ratios determined using the two background subtraction methods (Table 2). The correlation between measured  $L_3/L_2$  integrated-peak intensity ratios and  $L_3$  peak positions for the Cr oxidation-state standards is shown in Fig. 8a. Measurements of the standards demonstrate that Cr oxidation states fall within well-separated regions in the correlation plot. Since the local electronic structure of the atom is responsible for the fine structure of absorption edges, other factors in addition to valence state influence  $L_{2,3}$  fine structure. These factors include atom coordination, spin-orbit interactions, crystal field splitting, atomic coulomb repulsion, and exchange effects. For example, within a given oxidation state in Fig. 8a, spectra for the individual standards fall within separate groupings reflecting possible differences from these factors which must be considered to correctly interpret fine structure of absorption edges. The correlation plot represents a map of the possible range in fine structure (including influences from factors other than valence) that a particular Cr oxidation state can display.

### EELS oxidation state analysis of Cr(VI) cultures

The EELS measurements of the bacterium examined by EC-TEM and precipitates examined in thin section by conventional TEM are summarized in Table 3. The error reported for the precipitates represents the standard error of the mean of 10 measurements. The errors reported for the encrusted bacteria represent the drift in energy calibration of the spectrometer ( $L_3$  position) and an estimate based on counting statistics ( $L_3/L_2$  ratio).

### Direct imaging of nontronite cultures

Clay-layer structures in their hydrated state are beam sensitive. Therefore, standard procedures for imaging beam sensitive specimens were employed. Representative examples of high resolution lattice images of nontronite basal layers taken by EC-TEM are shown in Fig. 9. The EC-TEM measured distributions of (001) layer spacings in nonreduced and microbially reduced nontronite are shown in Fig. 10. Each data point in the distribution represents the mean (001) spacing of a packet of fringes within individual clay grains. Nonreduced nontronite has mean (001) spacing of  $1.50 \pm 0.08$  nm and the microbially Fe(III) reduced form has mean (001) spacing of  $1.26 \pm 0.10$  nm (the errors represent the standard deviation of the population). It is clear from Fig. 10 that the distributions differ and a standard statistical T-test for unpaired data with unequal variance confirms the difference in means is significant. Reduction of Fe(III) in nontronite over 4 days by *S. oneiden-*

sis produced a 0.24 nm contraction in mean (001) layer spacing.

## Discussion

### Oxidation state determination

It is difficult to explicitly deconvolve the influences of atom coordination, spin-orbit interactions, and crystal field splitting on fine structure from those of valence state. Nonetheless, the mean oxidation state of an unknown can be determined by plotting its  $L_{3/2}$  peak position and  $L_{3/2}$  integrated-peak intensity ratio in a correlation plot of oxidation state standards (see Fig. 8a). However, it is important that the correlation plot contain the broadest collection of standards feasible to map the full range in fine structure that a particular oxidation state can display. The better these ranges are known, the more confidence can be placed in the oxidation state determination. In this regard, the data in Table 1 supplement that of Fig. 8a. Table 1 includes published  $L_{2,3}$  peak positions (absorption edge maximums) from previous EELS studies as well as core-level (or inner-shell) binding energies measured from XPS studies. In XPS, a bulk specimen is illuminated with monochromatic X-rays and the kinetic energies of ejected photoelectrons are measured. The EELS edge onset, the sudden rise in intensity preceding each of the  $L_{2,3}$  peaks, represents the ionization threshold which approximately corresponds to the inner-shell binding energy measured by XPS. The difference in chemical shift measured by EELS and XPS for oxides has been suggested to be on the order of the band-gap energy [38], and may arise from many-body relaxation effects (more dominant in XPS) in which nearby electron orbitals are pulled towards a core hole [32]. Table 1 gives an indication of the range of  $L_{2,3}$  peak positions expected for each Cr oxidation state and their relative overlap. It is important to note that XPS values are reported as binding energies, not edge maxima. Furthermore, charging of insulating materials in XPS requires the referencing of binding energies to allow comparability of results from different specimens. However, various methods are used for this referencing which lead to binding energy differences of up to 0.5 eV [39]. Therefore, the XPS binding energies in Table 1 should be compared qualitatively.

The EELS measurements of the bacteria examined by EC-TEM and precipitates examined in thin section by conventional TEM are plotted in Fig. 8b. The correlation plot (Fig. 8b) indicates that Cr associated with *S. oneidensis* is most consistent with a mean oxidation state of +3 or lower. Measurements of hydrated bacteria in the EC are in good agreement with the analysis of isolated precipitates measured in cross section by conventional TEM. These results illustrate EELS techniques yield accurate data even under the more onerous experimental conditions of the EC.

### Collapse of nontronite layers by Fe(III) reduction

We report the first accurate TEM measurements of nontronite layer contraction induced by the reduction of structural Fe(III). A contraction of 0.24 nm in mean (001) layer spacing was observed. Our measurement is consistent with previous *in-situ* X-ray diffraction studies

Compound	Formal Valence	$L_{3/2}$ Integrated Ratio	
		Background Method I Pearson <i>et al.</i> (1993)	Background Method II Flat Two Step
CrF <sub>2</sub>	II	2.97 ± 0.07	2.37 ± 0.03
CrSe	II	2.60 ± 0.06	2.04 ± 0.02
CrCl <sub>3</sub>	III	1.75 ± 0.03	1.68 ± 0.01
Cr <sub>2</sub> O <sub>3</sub>	III	1.81 ± 0.01	1.70 ± 0.01
KCr(SO <sub>4</sub> ) <sub>2</sub> •12H <sub>2</sub> O	III	1.77 ± 0.02	1.60 ± 0.01
K <sub>2</sub> CrO <sub>4</sub>	VI	1.42 ± 0.01	1.44 ± 0.01

Specimen	Cr-L <sub>3</sub> (2p <sub>3/2</sub> ) (eV)	Cr-L <sub>2</sub> (2p <sub>1/2</sub> ) (eV)	$L_{3/2}$ Integrated Ratio	
			Background Method I	Background Method II
<i>Encrusted S. oneidensis</i>	575.7 ± 0.5	584.5 ± 0.5	2.75 ± 0.30	1.90 ± 0.30
Isolated precipitates	575.7 ± 0.1	584.3 ± 0.1	1.72 ± 0.02	1.85 ± 0.02
	576.3 ± 0.1	584.7 ± 0.1	1.77 ± 0.02	1.91 ± 0.02

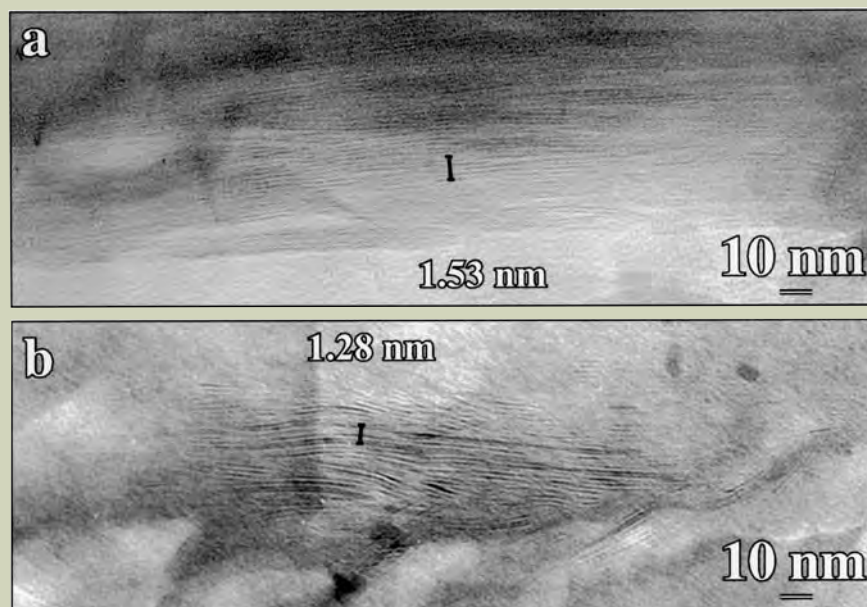


Fig. 9. High resolution lattice images of basal layers of nontronite imaged by EC-TEM at 10 - 100 Torr: (a) nonreduced control and (b) microbially Fe(III) reduced form. The bar illustrates five consecutive basal layer fringes and their average (001) spacing is indicated. There is a range of (001) layer fringe spacings in any one nontronite image. However, the mean spacing is generally smaller for Fe(III)-reduced nontronite than the nonreduced nontronite control (see Fig. 10). The layer fringes annotated by the bars were chosen to contrast the difference in (001) spacings for fringes near the means of the distributions shown in Fig. 10.

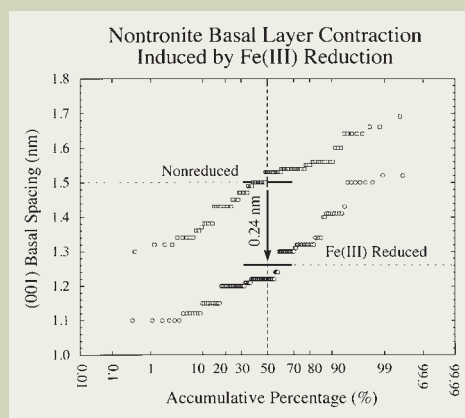


Fig. 10. Distribution of (001) layer spacings in nonreduced and microbially reduced nontronite as measured by EC-TEM. The horizontal bar represents the mean of the distribution.

which observed an interlayer contraction of  $0.28 \pm 0.04$  nm in Na-nontronite after  $\approx 85\%$  of the Fe(III) was reduced (based on Fig. 8 of [23]). Our TEM measurement was possible because clays were examined in their 'native' hydrated state in an EC. Previous TEM reduction studies used water exchange with methanol and infiltration with L.R. White resin in attempts to preserve the layer spacings of hydrated clay [24]. However, our EC-TEM results suggest the homogeneous layer spacing observed in both reduced and oxidized smectite by Stucki and Tessier [24] results from the interaction between the non-polar methanol and clay interlayer surfaces. In comparison to EC-TEM results, the observation that a homogeneous 1.26 nm (001) layer spacing is produced in the methanol-clay system regardless of Fe(III)/Fe(II) content [24] suggest interlayer forces are affected by the presence or lack of polar water molecules.

We show that established embedding techniques used to study clay reduction do not accurately preserve basal spacings of expandable clays. At least for L. R. White, solvent exchange and resin infiltration contract layer spacings, and therefore cannot be used to study, for example, the correlation between layer spacing and local Fe(III)/Fe(II) composition. In fact, conventional TEM has been unable to even image conclusively the contraction of clay layers induced by Fe(III) reduction. As demonstrated here, conventional TEM specimen preparation artifacts such as clay layer contraction arising from solvent exchange, dehydration, and resin infiltration are avoided by using EC-TEM.

## Summary

We demonstrate quantitative EELS oxidation state measurements can be performed using EC-TEM which could provide data lost by conventional specimen preparation. To our knowledge, this is the first demonstration of EELS microanalysis by EC-TEM. We further demonstrate, for the first time using TEM, the collapse of (001) layers of nontronite induced by Fe(III) reduction. This is possible because the clays were examined in their 'native' hydrated state using an EC. The technique of EC-TEM, especially together with EELS, can provide data on mineralogy, spatial distribution, and speciation of metals, necessary for determining the mechanism (s) of microbial metal reduction/oxidation.

## Acknowledgements

This work was supported by ONR program element 0602233N, NRL/ONR Core 6.1 Funding, CORE/NRL Postdoctoral Fellowship (J. Kim), and ONR-ASEE Postdoctoral Fellowship (K. Lowe). We thank Dr. K. Nealson (University of Southern California) and Dr. J. Kostka (Florida State University) for kindly providing specimens of *S. oneidensis*. We thank Dr. W. Straube (Geo-Centers, Inc.) for fixing and embedding Cr-cultures for TEM analysis. We thank Dr. A. Neal (Montana State University) for comments.

## References

- Cieslak-Golonka, M., *Polyhedron*, **15**, 3667 (1995).
- Clesceri, L. S., Greenberg, A. E., and Eaton, A. D. (Eds) *Standard Methods for the Examination of Water and Wastewater*, American Public Health Association, Washington, DC (1999).
- Hill R. R. H. and Cowley H. M., *S. Afr. J. Sci.*, **82**, 595 (1986).
- Fude, L., Harris, B., Urrutia, M. M., and Beveridge, T. J., *Appl. Environ. Microbiol.*, **60**, 1525 (1994).
- Badar, U., Ahmed, N., Beswick, A. J., Pattanapitpaisal, P., and Macaskie, L. E., *Biotech. Lett.*, **22**, 829 (2000).
- McLean, J. S., Beveridge, T. J., and Phipps, D., *Environ. Microbiol.*, **2**, 611 (2000).
- Smith, W. L. and Gadd G. M., *J. Appl. Microbiol.*, **88**, 983 (2000).
- McLean, J. and Beveridge, T. J., *Appl. Environ. Microbiol.*, **67**, 1076 (2001).
- Lytle, C. M., Lytle, F. W., Yang, N., Qian, J. H., Hansen, D., Zayed, A., and Terry, N., *Environ. Sci. Technol.*, **32**, 3087 (1998).
- Paterson, J. H., Krivanek, O. L., *Ultramicroscopy*, **32**, 319, (1990).
- van Aken, P. A., Liebscher, and B., Styrsa, V. J., *Phys. Chem. Min.*, **25**, 323 (1998).
- Wang, Z. L., Bentley, J., and Evans, N.D., *J. Phys. Chem. B*, **103**, 751 (1999).
- Cressey, G., Henderson, C. M. B., and van der Laan, G., *Phys. Chem. Miner.*, **20**, 111 (1993).
- Daulton T. L., Little B. J., Lowe K., and Jones-Meehan J., *Journal of Microbiological Methods*, in press (2002).
- Venkateswaran, K., Moser, D. P., Doilhopf, M. E., Lies, D. P., Saffarini, D. A., MacGregor, B. J., Ringelberg, D. B., White, D. C., Nishijima, M., Sano, H., Burghardt, J., Stackebrandt, E., and Nealson, K. H., *Int. J. Syst. Bacteriol.*, **49**, 705 (1999).
- Stucki, J. W., Komadel, P., and Wilkinson, H. T., *Soil Science Society of America Journal*, **51**, 1663 (1987).
- Kostka, J. E., Stucki, J. W., Nealson, K. H., and Wu, J., *Clays & Clay Minerals*, **44**, 522 (1996).
- Ravina, I. and Low, P. F., *Clay & Clay Minerals*, **20**, 109 (1972).
- Kohyama, N., Shimoda, S., and Sudo, T., *Clay & Clay Minerals*, **21**, 229 (1973).
- Stucki, J. W., Low, P. F., Roth, C. B., and Golden, D. C., *Clays & Clay Minerals*, **32**, 357 (1984).
- Chen, S. Z., Low, P. F., and Roth, C. B., *Soil Sci. Soc. Amer. J.*, **51**, 82 (1987).
- Shen, S., Stucki, J. W., and Boast, C. W., *Clays & Clay Minerals*, **40**, 381 (1992).
- Wu, J., Low, P. F., and Roth, C. B., *Clays & Clay Minerals*, **37**, 211 (1989).
- Stucki, J. W. and Tessier, D., *Clays & Clay Minerals*, **39**, 137 (1991).
- Kim, J., Daulton, T., Furukawa, Y., Lavoie, D., and Newell, S., *Geology*, submitted (2002).
- Myers, C. R. and Nealson, K. H., *Geochim. Cosmochim. Acta*, **52**, 2727 (1988b).
- Myers, C. R. and Nealson, K. H., *Science*, **240**, 1319 (1988a).
- Lovley, D. R., Phillips, E. J. P., Gorby, Y. A., and Landa, E. R., *Nature*, **350**, 413 (1991).
- Llyod, J. R. and Macaskie, L. E., *Appl. Environ. Microbiol.*, **62**, 578 (1996).
- Keeling, J. L., Raven, and M. D., Gates, W. P., *Clays and Clay Minerals*, **48**, 537 (2000).
- Fukami, A., Fukushima, K., and Kohyama, N., In: Bennett R. H., Bryant W. R. and Hulbert M. H. (Eds.), *Microstructure of Fine-grained Sediments from Mud to Shale*, Springer-Verlag, New York, pp. 321 (1991).
- Egerton, R. F., *Electron Energy-loss Spectroscopy in the Electron Microscope*, Plenum, New York (1996).
- Geiger, J., Schmoranzler, H., *J. Mol. Spectrosc.*, **32**, 39 (1969).
- Leapman, R. D. and Sun, S., *Ultramicroscopy*, **59**, 71 (1995).
- Pearson, D. H., Ahn, C. C., and Fultz, B., *Phys. Rev. B*, **47**, 8471 (1993).
- Leapman, R. D. and Grunes, LA., *Phys. Rev. Lett.*, **45**, 397 (1980).
- Zaanen, J., Sawatzky, G. A., Fink, J., Speier, W., and Fuggle, J. C., *Phys. Rev. B*, **32**, 4905 (1985).
- Leapman, R. D., Grunes, LA., and Fejes, P.L., *Phys. Rev. B*, **26**, 614 (1982).
- Swift, P., *Surf. Interface Anal.*, **4**, 47(1982).
- Allen, G.C. and Tucker, P.M., *Inorg. Chim. Acta.*, **16**, 41 (1976).
- Asami, K. and Hashimoto, K., *Corrosion Science*, **17**, 559 (1977).
- Moffat, T. P., Latanision, R. M., and Ruf, R. R., *Electrochim. Acta*, **40**, 1723 (1995).
- Fink, J., Müller-Heinzerling, T., Scheerer, B., Speier, W., Hillebrecht, F. U., Fuggle, J. C., Zaanen, J., and Sawatzky, G. A., *Phys. Rev. B*, **32**, 4899 (1985).
- Neal, A. L., Lowe, K., Daulton, T. L., Jones-Meehan, J., and Little B. J., *Journal of Applied Surface Science*, submitted (2002).
- Allen, G. C., Curtis, M. T., Hooper, A. J., and Tucker, P. M., *J. Chem. Soc., Dalton Trans.*, **16**, 1675 (1973).
- Krivanek, O. L. and Paterson, J. H., *Ultramicroscopy*, **32**, 313 (1990).
- Ikemoto, I., Ishii, K., Kinoshita, S., Kuroda, H., Alario-Franco, M. A., and Thomas, J. M., *J. Solid State Chem.*, **17**, 425 (1976).
- Kendelewicz, T., Liu, P., Doyle, C. S., Brown, G. E., Nelson, E. J., and Chambers, S. A., *Surf. Sci.*, **424**, 219 (1999).
- Konno, H., Tachikawa, H., Furusaki, A., and Furuichi, R., *Anal. Sci.*, **8**, 641 (1992).
- Brydson R., Garvie, L. A. J., Craven, A. J., Sauer, H., Hofer, F., and Cressey, G., *J. Phys.: Condens. Matter*, **5**, 9379 (1993).

# Simulations of Kikuchi Patterns and Comparison with Experimental Patterns

Kazuya Omoto<sup>†</sup>, Kenji Tuda and Michiyoshi Tanaka

Institute of Multidisciplinary Research for Advanced Materials, Tohoku University

## Introduction

Since the energy filtering technique for electron microscopy was established, it has already been a common sense that rocking curves of diffraction patterns (CBED patterns) formed by elastically scattered electrons are reproduced very well by the dynamical calculations of electron diffraction. It is high time to study inelastic scattering quantitatively. There exist three major fundamental inelastic scattering processes: plasmons (5 to 30eV), core-excitations (> 50eV) and phonons (thermal diffuse scattering, TDS) (< 0.1eV). The cross section of the core-excitations is small but that of plasmons is very large. Inelastic scattering due to plasmons is harmful to the quantitative analysis of the rocking curves of the diffraction patterns. In order to remove the background intensities of these inelastically scattered electrons, various energy-filtering techniques have been developed. We have developed, in collaboration with JEOL, the JEM-2010FEF field-emission electron microscope equipped with a new  $\Omega$  filter, which enables us to remove the plasmon-loss and core-loss intensities over the entire CBED patterns. However, inelastic (quasi-elastic) scattering due to phonons (TDS) is difficult and impractical to remove at present. TDS is known as the major origin of the anomalous absorption effect. In contrast to plasmon scattering, TDS extends to large scattering angles and forms Kikuchi bands and Kikuchi lines, which are impedimental to the accurate analysis of the rocking curves of CBED patterns.

Omoto et al. [1], derived a comprehensive theoretical expression for inelastic scattering of fast transmission electrons from a perfect crystal. Their expression includes both elastic and inelastic multiple scatterings and is regarded as an extended form of Fujimoto's expression for elastic scattering [2]. When the approximation of single inelastic scattering is applied to the expression, it becomes equivalent to the formula of Rez et al. [3]. When TDS is considered with the use of the Einstein model or the scattering factor for TDS given

by Hall and Hirsch [4], the expression of Rossouw and Bursill [5] is derived. This expression is used here in computer simulations of TDS intensity distributions (Kikuchi patterns). We will show several results of the simulations for MgO and compare them with experimental results.

Before showing the simulation results of Kikuchi patterns, we briefly describe the theory of inelastic scattering and quote the important equations, which are the basis of the present calculations.

## Theoretical

A comprehensive expression of the scattering amplitude for elastic and inelastic scattering of fast transmission electrons from a perfect crystal is given as

$$|\phi(t)\rangle = \exp[it\hat{M}]|a_0\rangle|\mathbf{O}\rangle, \quad (1)$$

where  $|a_0\rangle$  and  $|\mathbf{O}\rangle$  are the initial states of the crystal and the incident plane wave of an electron,  $\hat{M}$  is the elastic and inelastic scattering operator and  $t$  is the thickness of a specimen.

The scattering amplitude in direction  $\mathbf{K}_i + \mathbf{G}$  to excite the crystal from the 0th state to the  $i$ th state, where  $\mathbf{G}$  is the reciprocal lattice vector, is obtained by multiplying (1) by  $\langle \mathbf{G} | \langle a_i |$  from the left side.

$$\langle \mathbf{G} | \langle a_i | \phi(t) \rangle = \langle \mathbf{G} | \langle a_i | \exp[it\hat{M}] | a_0 \rangle | \mathbf{O} \rangle \quad (2)$$

If we consider only elastic scattering ( $i = 0$ ), eq.(2) is reduced to

$$\langle \mathbf{G} | \langle a_i | \phi(t) \rangle^{(0)} = \langle \mathbf{G} | \exp[it\hat{M}_{00}] | a_0 \rangle | \mathbf{O} \rangle, \quad (3)$$

where the superscript (0) implies elastic scattering. The expression (3) is exactly Fujimoto's equation. Thus, equation (1) including inelastic scattering is regarded as a natural extension of Fujimoto's equation.

The amplitude of single inelastic scattering  $\langle \mathbf{G} | \langle a_i | \phi(t) \rangle^{(i)}$  is expressed in the following way,

$$\langle \mathbf{G} | \langle a_i | \phi(t) \rangle^{(i)} = \int_0^t \underbrace{\langle \mathbf{G} | \exp[i(t-\xi)\hat{M}_{i0}] | a_0 \rangle | \mathbf{O} \rangle}_3 \underbrace{i d\xi \hat{M}_{i0}}_2 \underbrace{\exp[i\xi\hat{M}_{00}] | a_0 \rangle | \mathbf{O} \rangle}_1 \quad (4)$$

As illustrated in **Fig. 1(a)** on the right-side page, the incident electron is scattered elastically in slice 1 of thickness  $\xi$ , scattered inelas-

tically in slice 2 of infinitely small thickness  $d\xi$  and again scattered elastically in slice 3 of thickness  $(t - \xi)$ .

Let us consider only thermal diffuse scattering (TDS). When the atom vibrations are approximated by the Einstein model, the intensity of TDS electrons in direction  $\mathbf{p} + \mathbf{G}$  per a solid angle is expressed as

$$\frac{dI_p^G}{d\Omega} = t \sum_{\lambda\lambda'} \sum_{\mu\mu'} \langle \mathbf{G} | p\lambda \rangle \langle p\lambda' | \mathbf{G} \rangle \langle 0\mu | \mathbf{O} \rangle \langle \mathbf{O} | 0\mu' \rangle \times \frac{T_{\mu\mu'}^{\lambda\lambda'} \exp[it\gamma_{p\lambda\lambda'}] - \exp[it\gamma_{0\mu\mu'}]}{it(\gamma_{p\lambda\lambda'} - \gamma_{0\mu\mu'})}, \quad (5)$$

where

$$T_{\mu\mu'}^{\lambda\lambda'} = \sum_{gh} \sum_{\mathbf{h}} \langle p\lambda | \mathbf{g} \rangle \langle \mathbf{g} | p\lambda' \rangle T(\mathbf{Q}, \mathbf{Q}') \langle \mathbf{h} | 0\mu \rangle \langle 0\mu' | \mathbf{h} \rangle, \quad (6)$$

$\mathbf{Q} = \mathbf{p} + \mathbf{g} - \mathbf{h}, \mathbf{Q}' = \mathbf{p} + \mathbf{g} - \mathbf{h}$

$\gamma_{p\lambda\lambda'} = \gamma_{p\lambda} - \gamma_{p\lambda'}^*$  and  $\gamma$  and  $\mu$  denote indices of the Bloch states.  $T_{\mu\mu'}^{\lambda\lambda'}$  stands for inelastic scattering and other terms stand for elastic scattering.  $T(\mathbf{Q}, \mathbf{Q}')$  is the following function

$$T(\mathbf{Q}, \mathbf{Q}') = \frac{1}{V_c} \sum_{\alpha} f_{\alpha}(\mathbf{Q}) f_{\alpha}(\mathbf{Q}') \exp[-i(\mathbf{Q} - \mathbf{Q}') \cdot \mathbf{r}_{\alpha}] \times \{\exp[-U_{\alpha}(\mathbf{Q} - \mathbf{Q}')] - \exp[-U_{\alpha}(\mathbf{Q}) - U_{\alpha}(\mathbf{Q}')]\}, \quad (7)$$

which is the TDS scattering factor given by Hall and Hirsch.  $T(\mathbf{Q}, \mathbf{Q}')$  for MgO is shown in **Fig. 1(b)**.

In the limiting case  $t \rightarrow \infty$ , only the terms  $\lambda = \lambda'$  and  $\mu = \mu'$  remain, the TDS intensity or eq.(5) becomes

$$\lim_{t \rightarrow \infty} \frac{1}{t} \frac{dI_p^G}{d\Omega} = \sum_{\lambda\mu} \langle \mathbf{G} | p\lambda \rangle^2 \langle p\lambda | \mathbf{G} \rangle \langle 0\mu | \mathbf{O} \rangle^2, \quad (8)$$

where

$$T_{\mu}^{\lambda} = T_{\mu\mu}^{\lambda\lambda} = \sum_{gh} \sum_{\mathbf{h}} \langle p\lambda | \mathbf{g} \rangle \langle \mathbf{g} | p\lambda \rangle T(\mathbf{Q}, \mathbf{Q}') \langle \mathbf{h} | 0\mu \rangle \langle 0\mu | \mathbf{h} \rangle. \quad (9)$$

This is equivalent to Takagi's expression [6]. In this expression, the cross terms of the transition probabilities (**Fig. 1(c)**) are omitted and the absorption effect in the elastic scattering process cannot be taken into account. As a result, the thickness dependence, the asymmetry features, the accurate intensity distribution along the band, the accurate incidence-orient-

2-1-1 Katahira, Aoba-ku, Sendai 980-8577 Japan  
E-mail:tanakam@tagen.tohoku.ac.jp

<sup>†</sup>He now works for JEOL Ltd.

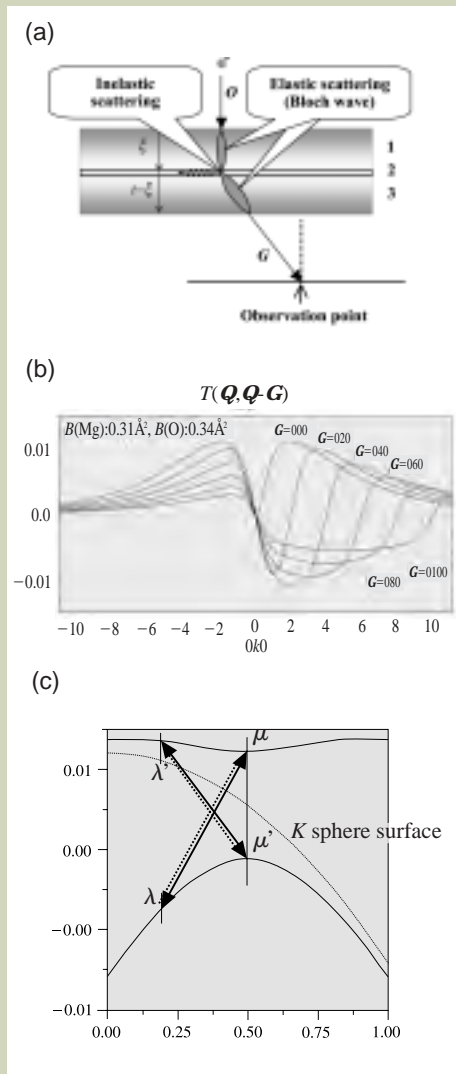


Fig. 1 (a). Schematic diagram of elastic and inelastic scattering.  
 (b). TDS scattering factors for MgO.  
 (c). Dispersion surface and transitions between branches.

tation dependence and the interference fringes of Kikuchi patterns cannot be discussed.

The thickness dependence, the incidence-orientation dependence and  $B$ -factor dependence of zone-axis Kikuchi patterns are displayed for MgO. The contributions from constituent elements to Kikuchi patterns are shown for the [100] and [110] incidences. Simulated Kikuchi patterns are compared with experimental patterns.

## Simulations

### Thickness dependence

We firstly show in **Fig.2** how the [100] zone-axis Kikuchi patterns of MgO change with the specimen thickness. Kikuchi patterns are weak and vague for thin specimens. As the thickness increases, clear Kikuchi bands appear and fine interference fringes are created. The simulations were carried out at an accelerating voltage of 100kV with 357 beams for  $B(\text{Mg}) = 0.31\text{\AA}^2$  and  $B(\text{O}) = 0.34\text{\AA}^2$ , the number of pixels being  $281 \times 281$ .

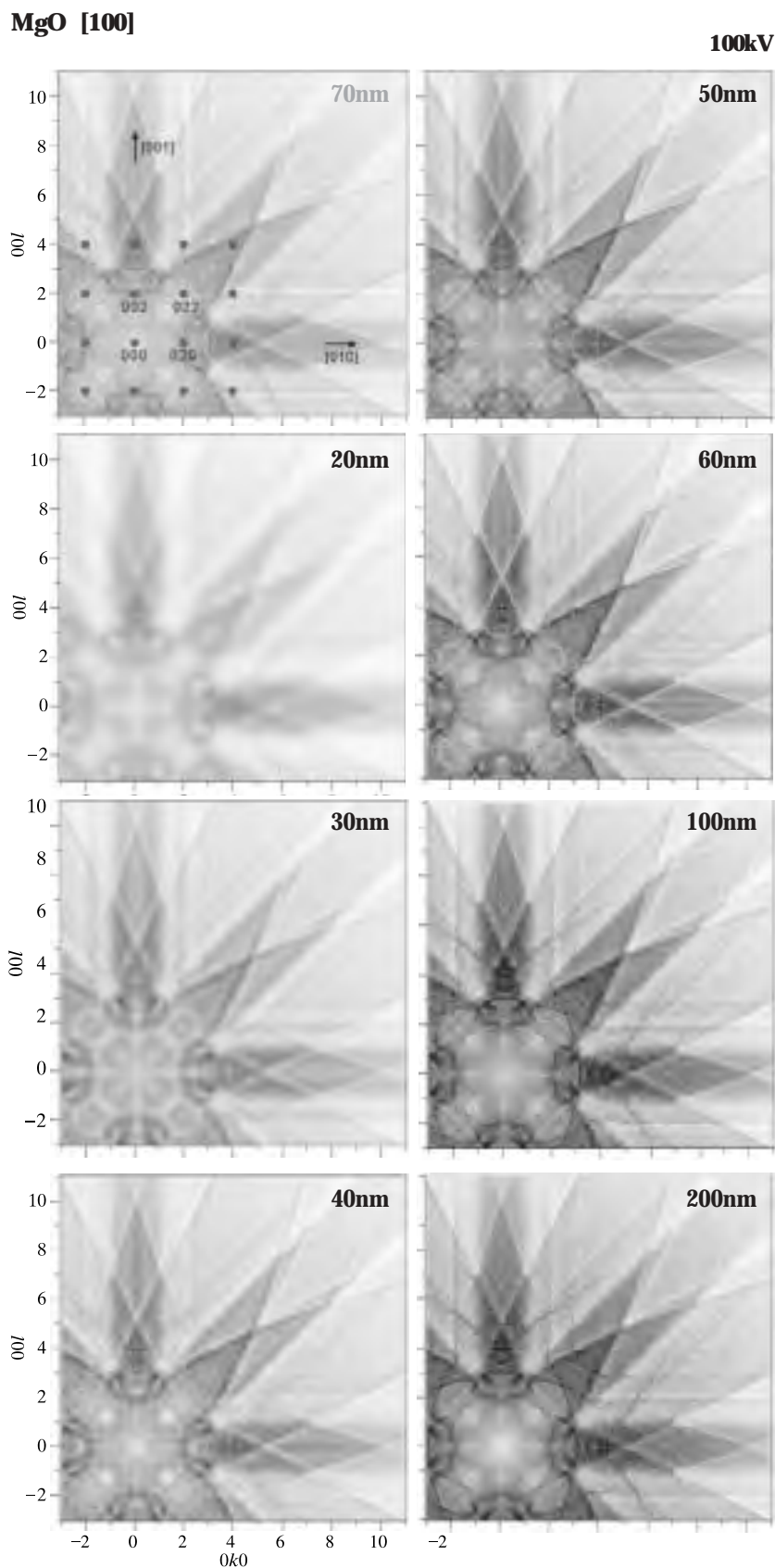


Fig. 2. Intensity changes of the simulated Kikuchi patterns of MgO with the specimen thickness (at the [100] zone-axis incidence).

### Incidence-orientation dependence

It is shown how the Kikuchi patterns of MgO at the [100] zone-axis incidence change with the orientation of the incident beam. The incidence orientation is changed from (a) (zone axis) to (f) in the [010] direction as shown in Fig. 3. All the patterns in Fig. 4 are similar but their intensities decrease with the increase of the tilt angle from the zone axis. This is understood by the fact that the excitation of branch 1 of the Bloch states, from which most part of the Kikuchi band is originated, decreases with the tilt angle.

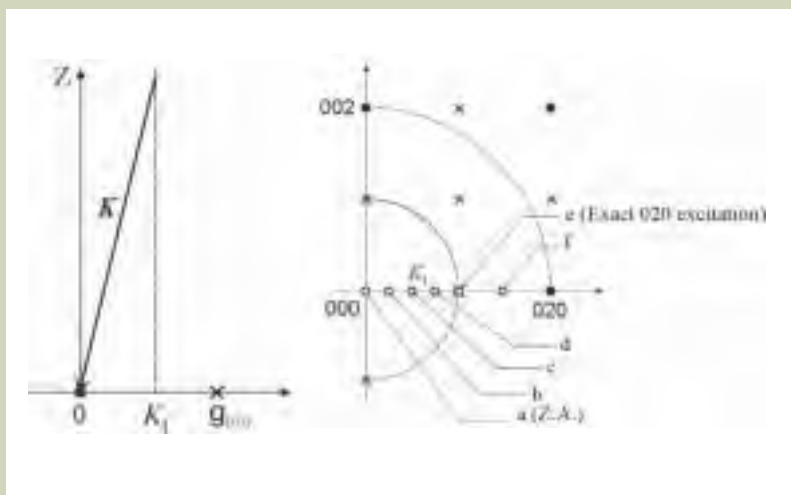


Fig. 3. Changes of the incidence orientation in the [010] direction.

### MgO [100]

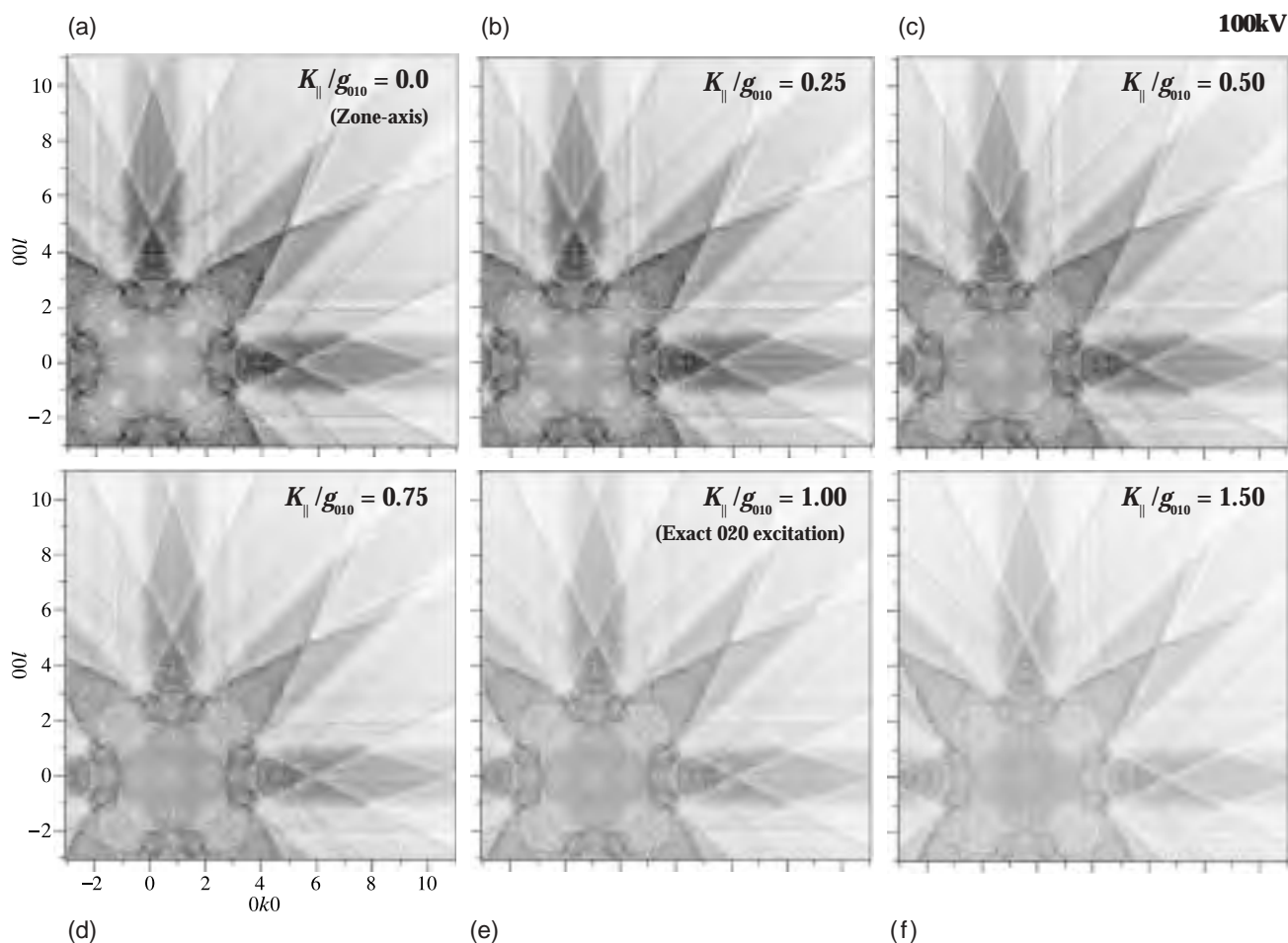


Fig. 4. Intensity changes of the simulated Kikuchi patterns of MgO with the orientation of the incident beam (in the [010] direction from the [100] zone-axis incidence).

### B-factor dependence

It is shown how the Kikuchi patterns of MgO at the [100] zone-axis incidence change with the Debye-Waller factors ( $B$  factors). Simulations were performed for five cases (a to e in Fig.5). The values of the  $B$  factors and the corresponding TDS scattering factors  $T(Q, Q)$  are given in the figure. It is seen in Fig.6 that the intensities of the Kikuchi patterns increase with the increase of the  $B$  factors, or with the increase of the thermal motions of atoms.

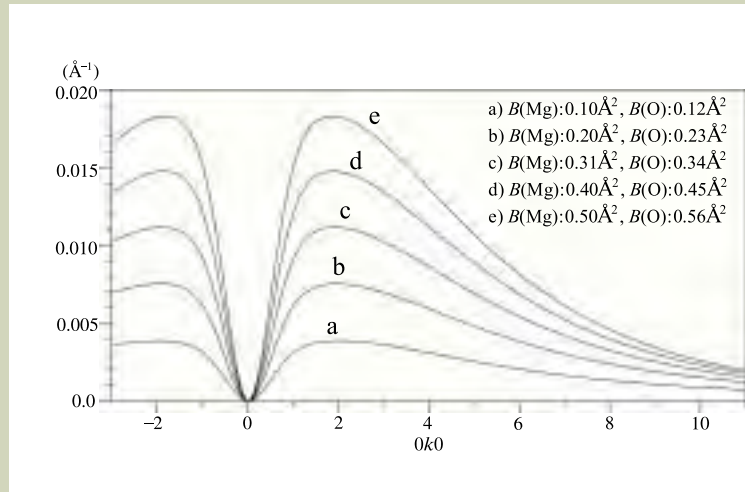
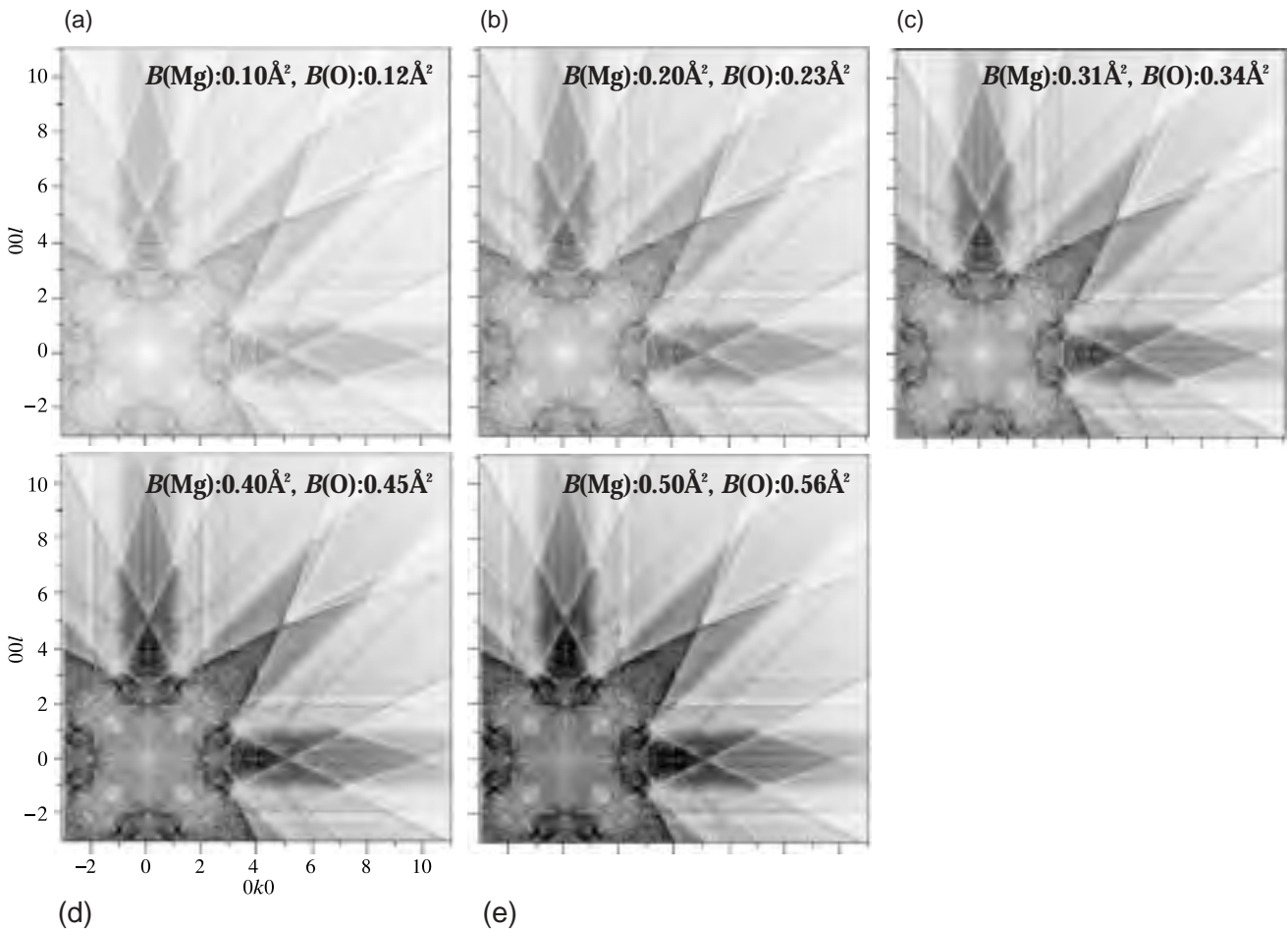


Fig. 5. Dependence of TDS scattering factors for MgO on  $B$  factors.

### MgO [100]



Accelerating voltage : 100kV  
 Thickness : 70nm  
 Number of beams : 357  
 Number of pixels : 281 × 281

Fig. 6. Intensity changes of the simulated Kikuchi patterns of MgO with the  $B$  factors (at the [100] zone-axis incidence).

## Contributions from constituent elements

$T(\mathbf{Q}, \mathbf{Q})$  contains the sum of atom species. If summation is carried out only for a definite atom species, the contributions from different atom species can be separately calculated. A similar simulations can also be carried out by selecting a certain branch of the initially excited Bloch states because a Bloch state often

forms its intensity maximum at the rows consisting of atoms of one kind.

In the case of the [100] incidence for MgO, Mg atoms are located on top of O atoms (Fig.7). Thus, the Kikuchi patterns produced by both atoms are the same but their intensities are different according to the difference of their atomic scattering factors (Fig.8). In the case of the [110] incidence for MgO, the branches 1 and 2 form high electron concen-

trations on Mg and O atom rows, respectively (Fig.9). The Kikuchi bands running in the upper-right direction have different intensity distributions between the patterns of Mg and O (Fig.10). That is, owing to the difference of the excitations of the branches (the sites of inelastic scattering) concerned, the innermost band is weaker than the next band in the pattern of O but the innermost band is stronger than the next band in the pattern of Mg.

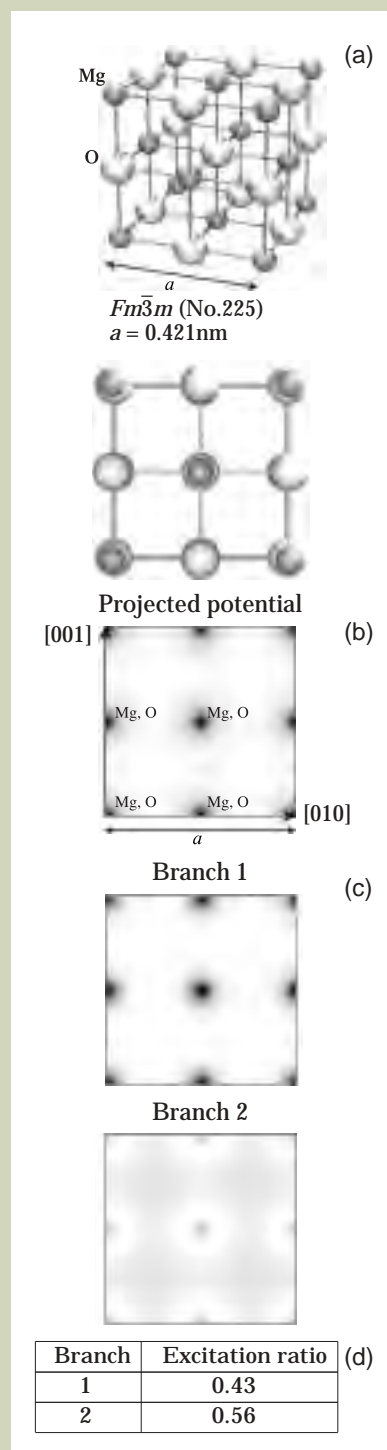


Fig. 7. (a) Crystal structure of MgO. (b) Projected potential of MgO. (c) Bloch states for branches 1 and 2. (d) Excitation ratios of branches 1 and 2.

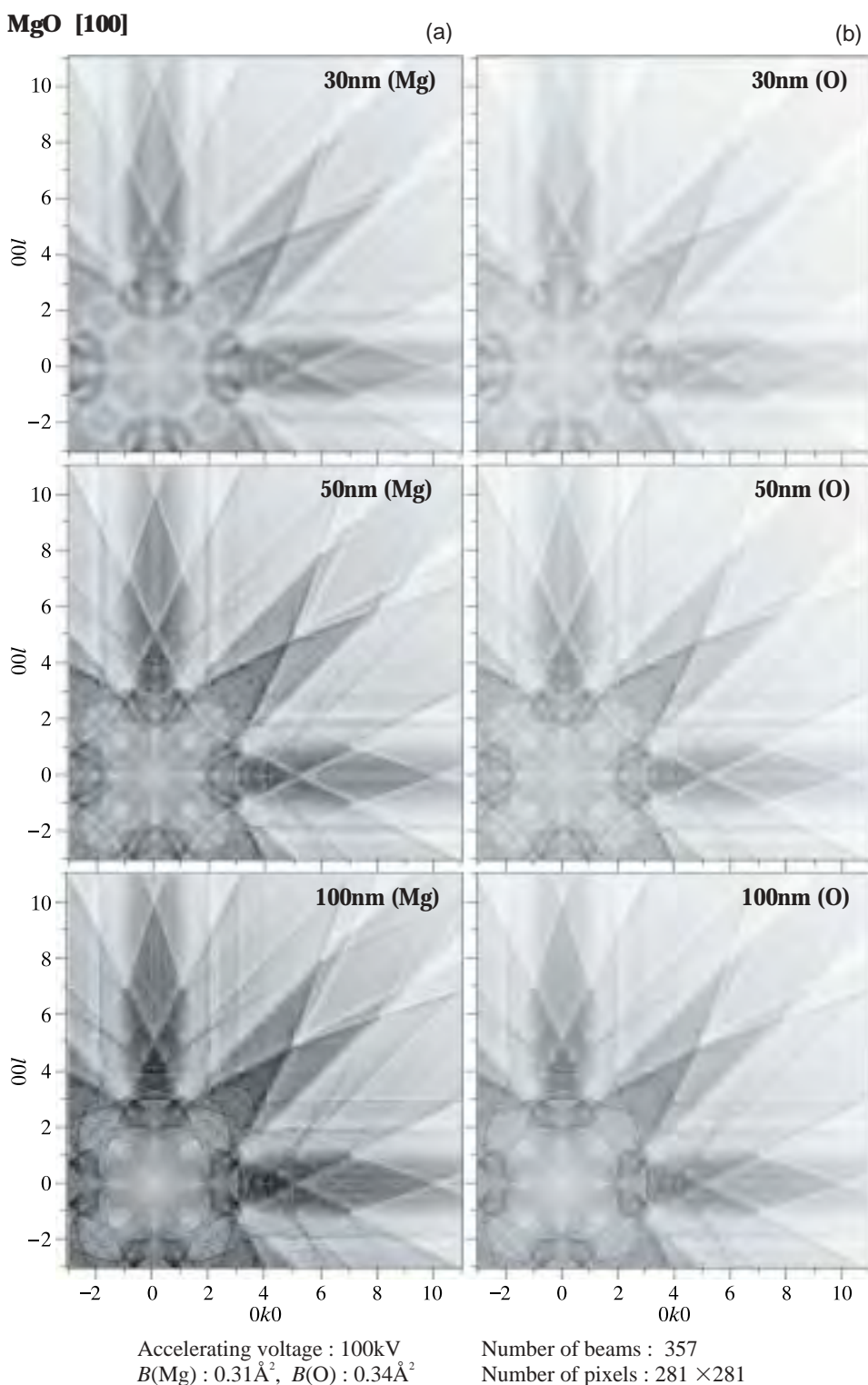


Fig. 8. Intensity changes of the simulated Kikuchi patterns of MgO with the specimen thickness for (a) branch 1 and (b) branch 2 (at the [100] zone-axis incidence).

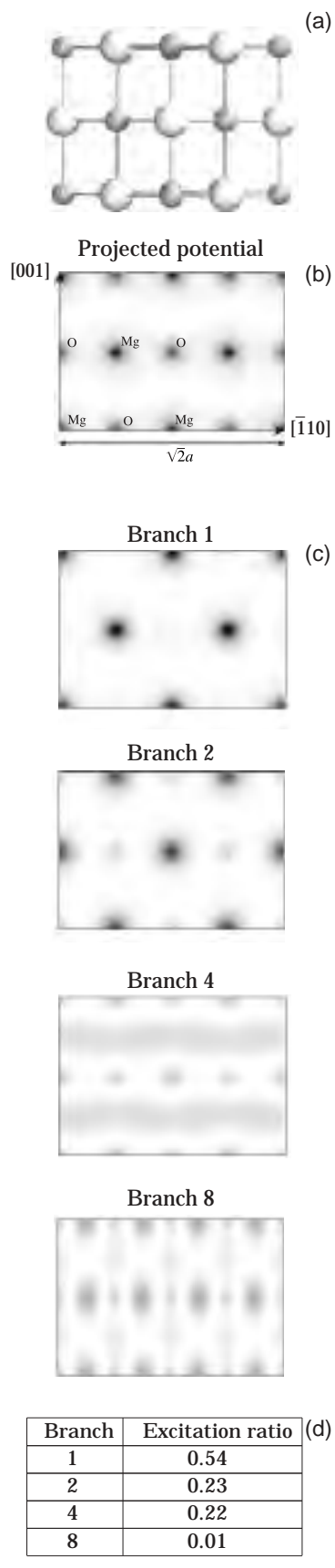


Fig. 9. (a) Crystal structure of MgO. (b) Projected potential of MgO. (c) Bloch states for branches 1, 2, 4 and 8. (d) Excitation ratios of the branches.

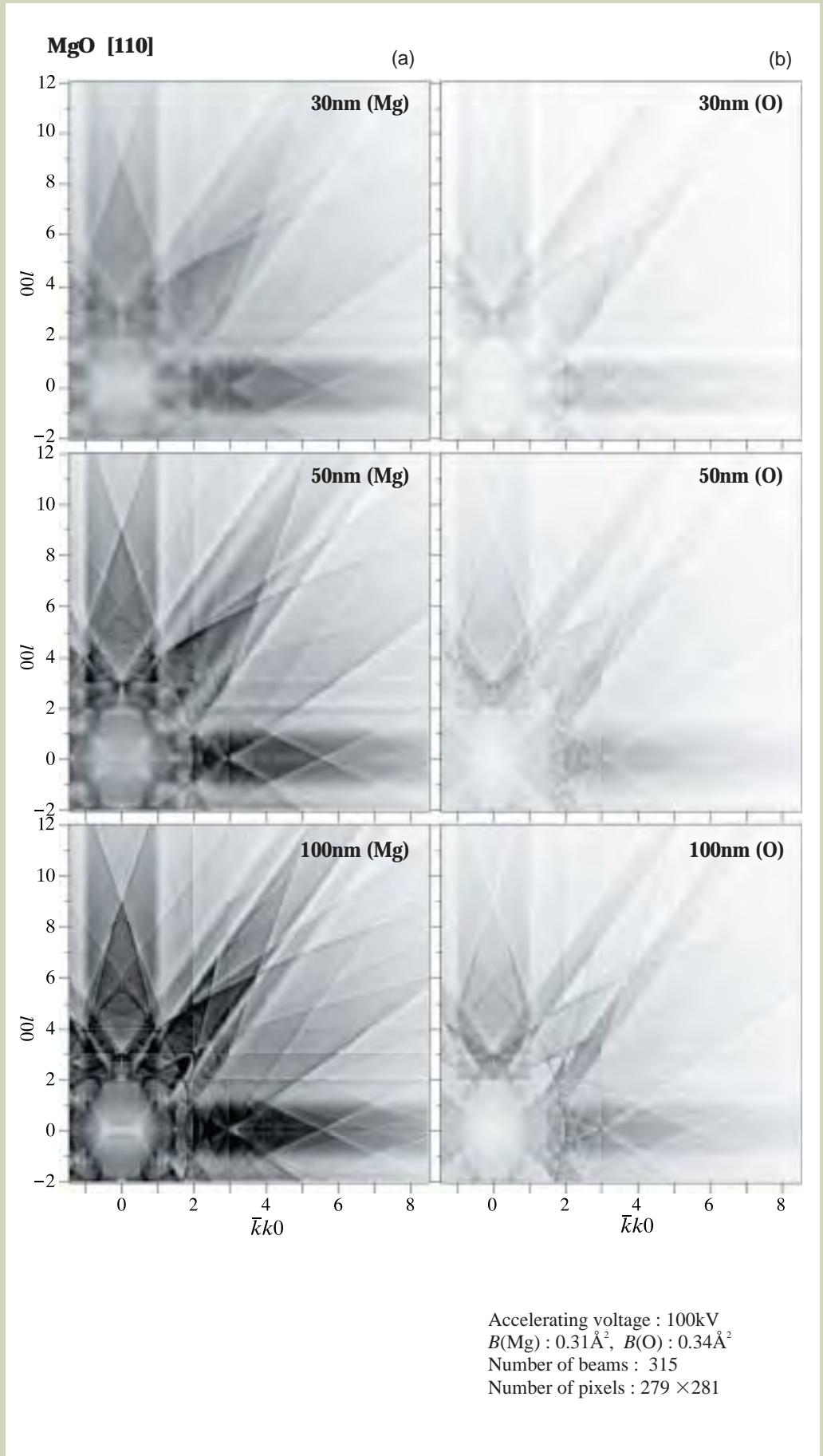


Fig. 10. Intensity changes of the simulated Kikuchi patterns of MgO with the specimen thickness for (a) branch 1 and (b) branch 2 (at the [110] zone-axis incidence).

## Comparison Between Experimental and Simulated Patterns

Simulated zone-axis Kikuchi patterns are compared with experimental patterns for MgO [100]. The experimental diffraction patterns are energy-filtered zero-loss patterns taken with the JEM-2010FEF at an accelerating voltage of 100kV. The simulations agree very well with the experiments (Fig.11). That is, not only the Kikuchi lines and bands at high angles but also the detailed patterns at the central area are reproduced very well. It is seen that the thickness dependence (Fig.12) and incidence-orientation dependence (Fig.13) are also reproduced well by the simulations.

## Conclusion

To carry out computer simulations of Kikuchi patterns, we derived a comprehensive theoretical expression for inelastic scattering of fast transmission electrons from a perfect crystal. The simulations for MgO based on this expression showed good agreement with experimental CBED patterns taken with the JEM-2010FEF energy-filtering TEM.

The results presented here have brought us to a first step for studying TDS intensities quantitatively. We will continue this study aimed at quantitative analysis of inelastic scattering in electron microscopy.

Detailed studies of Kikuchi patterns are referred to in our latest book "Convergent-Beam Electron Diffraction IV" published in 2002 by JEOL.

## References:

1. K. Omoto, K. Tsuda and M. Tanaka: *J. Electron Microsc.*, **51** (2002) 67.  
M. Tanaka, M. Terauchi, K. Tsuda and K. Saitoh: *Convergent-Beam Electron Diffraction IV*, JEOL, Tokyo, 2002.
2. F. Fujimoto: *J. Phys. Soc. Jpn.*, **14** (1959) 1558.
3. P. Rez, C. J. Humphreys and M. J. Whelan: *Phil. Mag.*, **35** (1977) 81.
4. C. R. Hall and P. B. Hirsch: *Proc. R. Soc. London Ser. A*, **286** (1965) 156.
5. C. J. Rossouw and L. A. Bursill: *Acta Cryst.*, **A41** (1985) 320.
6. S. Takagi: *J. Phys. Soc. Jpn.*, **13** (1958) 287.

### MgO [100]

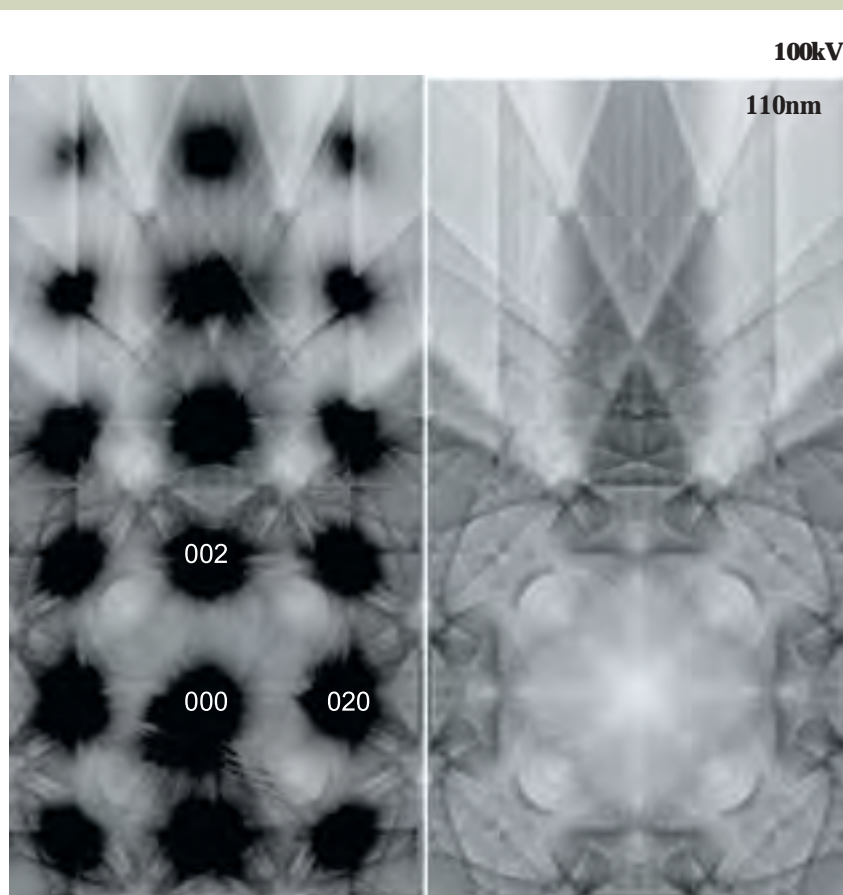


Fig. 11. Experimental Kikuchi pattern of MgO taken with the JEM-2010FEF (left) and its simulated pattern (right) (at the [100] zone-axis incidence).

### Thickness dependence

#### MgO [100]

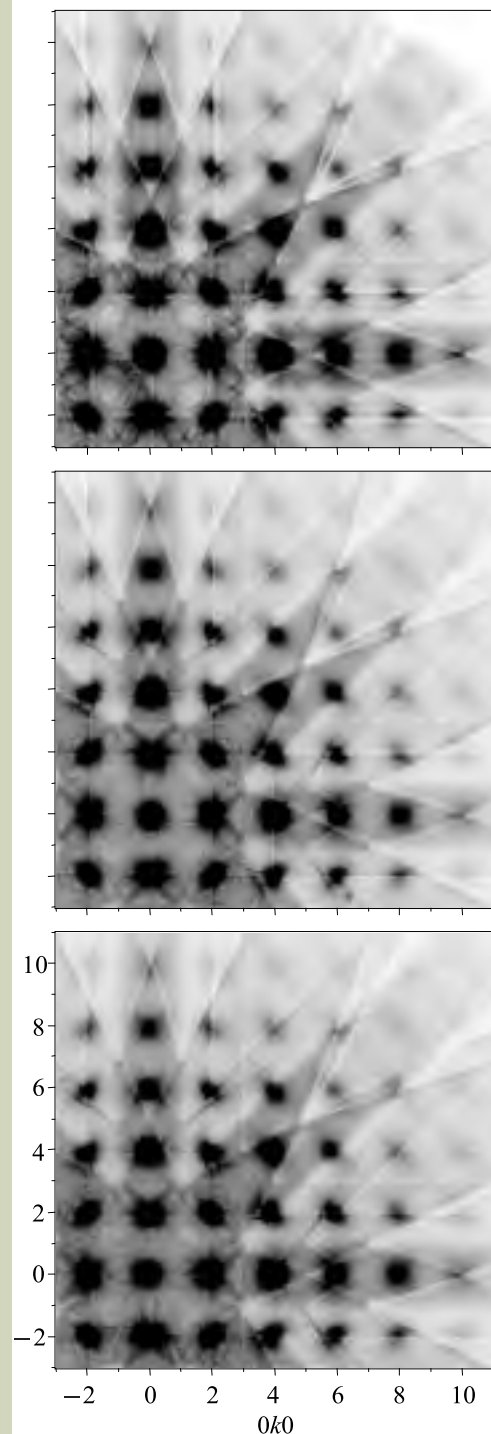
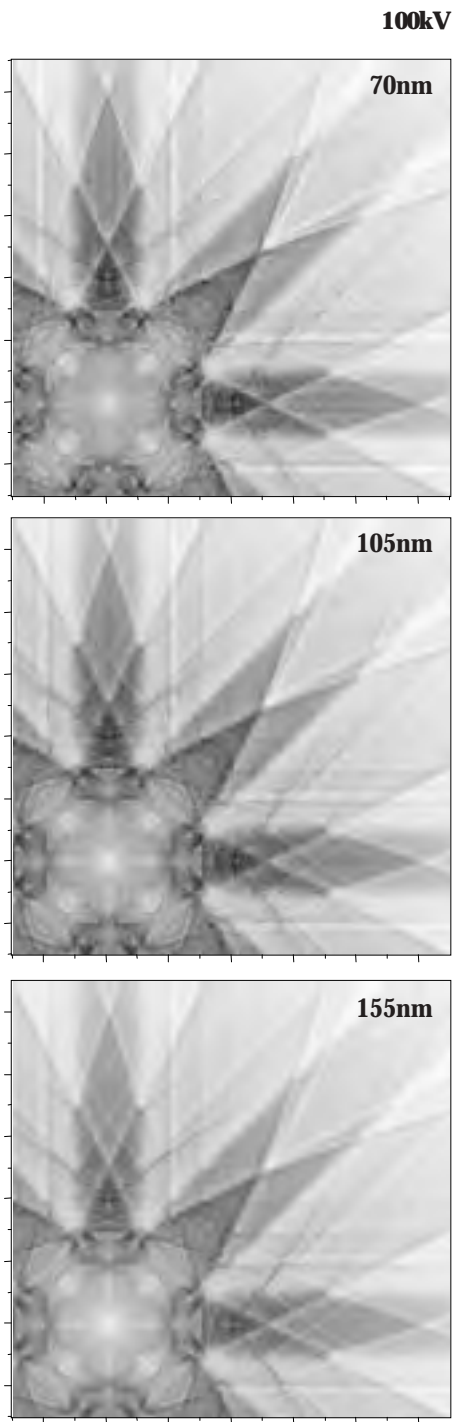
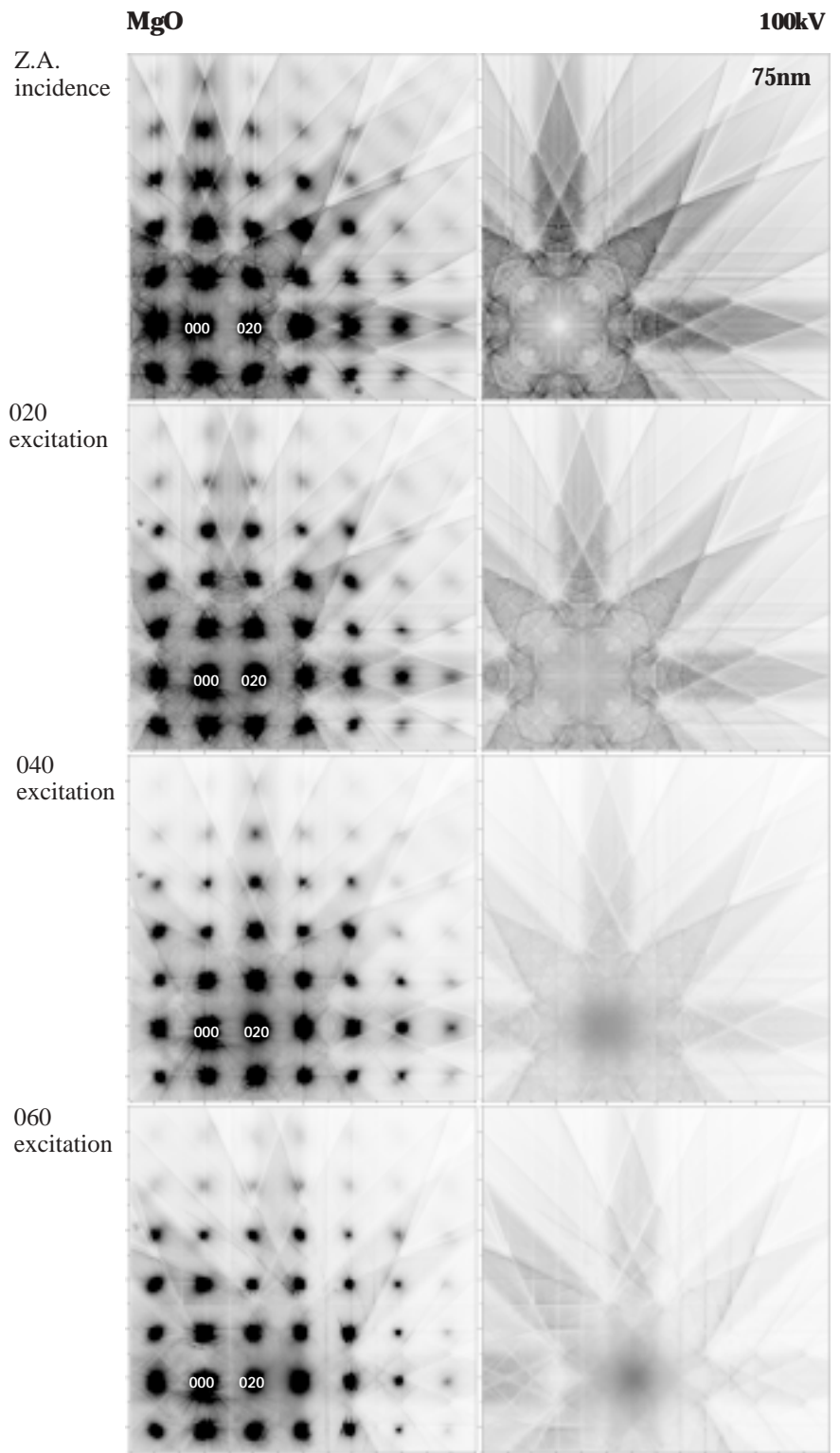


Fig. 12. Thickness dependence: Experimental and their simulated patterns (right).



$B(\text{Mg}) : 0.31\text{\AA}^2$ ,  $B(\text{O}) : 0.34\text{\AA}^2$   
 Number of beams : 277  
 Number of pixels :  $281 \times 281$

**Incidence-orientation dependence**



$B(\text{Mg}) : 0.31\text{\AA}^2$ ,  $B(\text{O}) : 0.34\text{\AA}^2$   
 Number of beams : 277  
 Number of pixels :  $281 \times 281$

patterns (left)

Fig. 13. Incidence-orientation dependence: Experimental patterns (left) and their simulated patterns (right).

# Experimental Atomically Resolved HAADF-STEM Imaging-A Parametric Study

Sašo Šturm<sup>†</sup>, Aleksander Rečnik<sup>†</sup>, Masahiro Kawasaki<sup>\*\*</sup>, Takashi Yamazaki<sup>\*\*\*</sup>, Kazuto Watanabe<sup>\*\*\*\*</sup>, Makoto Shiojiri<sup>\*\*\*\*\*</sup> and Miran Čeh<sup>†</sup>

<sup>†</sup>Department for Nanostructured Materials, “Jožef Stefan” Institute

<sup>\*\*</sup>JEOL USA Inc.

<sup>\*\*\*</sup>Department of Physics, Science University of Tokyo

<sup>\*\*\*\*</sup>Tokyo Metropolitan College of Technology

<sup>\*\*\*\*\*</sup>Department of Anatomy, Kanazawa Medical University

<sup>†††††</sup>Kyoto Institute of Technology

---

The influence of defocusing conditions and thickness changes on the experimental HAADF-STEM image was examined. For this study we used various materials.  $\text{CaTiO}_3$  was used to demonstrate sensitivity of experimental HAADF-STEM to relatively small difference in average atomic number ( $Z$ ), which is when the perovskite structure is viewed along the [001] axis 23.4 for Ti-O columns and 20.0 for Ca atomic columns. Compositional sensitivity was additionally evaluated by studying the intensity variations along the planar Ruddlesden-Popper faults in non-stoichiometric AO-doped  $\text{SrTiO}_3$  ( $A = \text{Ca, Sr, Ba}$ ) and  $\text{Sb}_2\text{O}_3$ -doped ZnO where we studied ordering of Zn and Sb atoms in the inversion boundary. In both cases the HAADF STEM images clearly indicate compositional changes along the internal interfaces.

## Introduction

In recent years a number of analytical techniques involving transmission electron microscopy have been employed in the field of materials science in order to study the structure and chemistry of both the perfect crystals and their interfaces at the atomic level. In spite of this there are only two widely accepted atomic-resolution methods that can actually help us visualize the atomic structures: high-resolution transmission electron microscopy (HRTEM) and high-resolution scanning-transmission electron microscopy (STEM). HRTEM images are mainly sensitive to the changes in a phase of the incoming parallel electron wave as it passes through the specimen. Such images provide very reliable information about the crystallography of the specimen in chosen crystallographic orientation while they suffer from limitations regarding the information on the chemical composition. The local structure can be obtained from HRTEM images only by image simulation including all the parameters that influence the final HRTEM images, such as lens aberrations, defocus value and thickness of the specimen [1]. Although the reciprocity theorem of scattering theory for electron microscopy states that a HRTEM and a bright-field (BF) high-resolution STEM should provide the same information [1, 2], basic difference between HRTEM and STEM is that in STEM the image is formed with no refocus of

the scattered electrons. The STEM image is produced by detecting the intensity of the electron flux in a convergent-beam electron diffraction pattern that is integrated over the detector geometry as a function of the scanning electron probe position. In the case where low-order or Bragg-diffracted beams hit the BF detector the image is dominated by coherent scattering and can suffer contrast reversal in the similar fashion as in HRTEM. Due to possible instabilities of the scanning unit and low signal-to-noise ratio of the BF detector there is no justified reason for choosing such an imaging technique over conventional HRTEM.

With increasing the scattering angle the intensity of the STEM image is dominated by thermal diffuse scattering (TDS), which is due to random thermal vibrations of the atoms. TDS is exposed as a low-intensity diffuse background in between the Bragg diffraction peaks over a large angular range [3-6]. The TDS arises from tightly bound  $s$ -states localized at atomic position, which implies that an annular-dark-field (ADF) detector could serve as a Bragg filter where the integrated intensity over a high-angle angular range will peak at the atomic columns, and the intensity of the signal is proportional to the average atomic number, hence  $Z$ -contrast [7]. Due to highly focused sub-nm probe localized at the atomic column the intensity, which is detected by the annular detector is a thickness-integrated  $s$ -state density at the site of the atom [8]. This imaging technique that enables atomically resolved compositional sensitivity in STEM is

called HAADF-STEM or  $Z$ -contrast imaging, and it is performed by detecting incoherent scattered electrons with an annular dark-field (ADF) detector at high angles and over a large angular range. The incoherent nature of  $Z$ -contrast images also means that changes of thickness and defocus should not cause a contrast reversal and so they can be interpreted more directly [9, 10]. However, recent studies have shown that focus, thickness and inner detector angle affect the contrast of a HAADF-STEM image and that proper image calculations are also necessary [11-14].

Until recently, there have been very few HAADF-STEM experiments to show the influence of the focus, thickness and inner detector angle on experimental image. To evaluate these effects we performed a systematic study of the influence of focusing conditions and thickness changes at given HAADF detector angles on atomic resolution experimental HAADF-STEM images. For the parametric study we used perfect crystal of  $\text{CaTiO}_3$ , with a relatively small difference in average atomic number ( $Z$ ) between the Ti-O (23.4) and Ca (20.0) atomic columns [15, 16]. In addition we investigated the compositional sensitivity of experimental, atomically resolved,  $Z$ -contrast images. Two systems that exhibit a defect atomic structure were used for these experiments. We investigated a non-stoichiometric  $\text{SrTiO}_3$  with an excess amount of AO ( $A = \text{Ca, Sr, Ba}$ ); this excess is normally accommodated via the formation of rock-salt-type planar faults, also known as Ruddlesden-Popper (RP) faults [17, 18]. These faults can

---

<sup>†</sup>Jamova 39, SI-100 Ljubljana, Slovenia  
<sup>†</sup>E-mail: saso.sturm@ijs.si

be described as an antiphase translation of the cation sub-lattice in two neighboring perovskite blocks with a translation vector of  $\mathbf{R}_{RP} = \frac{1}{2}[110]_{per}$ , with a RP fault actually consisting of two AO-rich atomic planes. Finally, in order to reveal the changes in chemistry along a single atomic column we performed Z-contrast imaging of an Sb-rich inversion boundary (IB) in a ZnO sample along the  $\langle 2\bar{1}10 \rangle$  projection.

## Experimental Procedures

Analytical grade starting materials were used to prepare the samples.  $\text{CaTiO}_3$  was produced by pressing the pellets and sintering in air at  $1350^\circ\text{C}$  for 10 hours. Non-stoichiometric  $\text{SrTiO}_3$  containing RP-faults was prepared by mixing  $\text{SrTiO}_3$  with 10 mol%  $\text{CaO}$ ,  $\text{SrO}$  or  $\text{BaO}$  and then sintering in air for 10 hours at  $1450^\circ\text{C}$ . ZnO with Sb-rich IBs was prepared with the addition of 0.1 mol%  $\text{Sb}_2\text{O}_3$  and sintered for 16 hours at  $1200^\circ\text{C}$ .

The specimens for transmission electron

microscopy observations were prepared by ion-beam milling using  $\text{Ar}^+$  ions at 4 kV, at an incident angle of 10 degrees. STEM images were obtained in a JEM-2010F TEM/STEM, equipped with a Schottky-type field-emission gun, ultra-high resolution pole-piece ( $C_s = 0.5$  mm), and fitted with a scanning image observation system with bright-field (BF) and an annular dark-field (ADF) STEM detectors. The collection angle can be controlled by changing the camera length in TEM/STEM systems for these detectors. In order to discard the elastically diffracted beams the HAADF collection range was set to 100 and 174 mrad for HAADF, while the probe semi-angle used was 10 mrad.

## Results and Discussion

STEM image distortions caused by possible mechanical vibrations, instabilities of the scanning coils or any other external interferences during STEM image acquisition may seriously hinder a proper quantification of experimental

STEM images. In such a case, valuable information about the intensity distribution located at atomic columns, which is masked by the distortions and noise, can be reconstructed in several ways. For the image processing we used the IMAGE-WARP procedure [19], which is based on real-space corrections of scanning artifacts on experimental STEM images. With an accurate atomic model of the analyzed region IMAGE-WARP is able to provide geometrically corrected HAADF-STEM images that can be used for matching with the HAADF-STEM simulations after they are filtered using conventional image-processing techniques.

### The influence of focus and thickness on the contrast of the experimental atomic-resolution HAADF-STEM images

Compared to HRTEM images, atomic resolution HAADF-STEM images are less sensitive on defocus and thickness, however their influence may be important for an accurate determination of the compositional variations. In order to evaluate the influences of defocus and thickness on the experimental atomically resolved HAADF-STEM image of  $\text{CaTiO}_3$  viewed along the  $\langle 001 \rangle$  axis we performed two sets of experiments: we varied the defocus of the objective lens and the thickness of the sample at a fixed focus value.

The starting defocus value was set close to the condition of the maximum information transfer (which may be regarded as Scherzer focus). The experimental HAADF-STEM images taken at different defoci were first processed using the IMAGE-WARP procedure. The processed images are presented in Fig. 1a-c. Warped experimental images were additionally processed with average filtering and polynomial smoothing. In the final images, shown in Fig. 1d-f, the atomic columns of Ti-O and Ca are readily distinguished by a relative difference in the intensities. Despite a different probe shapes at different focus values (insets in images d-f) the relative differences in the contrast seem to be insignificant, however, if we compare the intensity profiles across the atomic columns these small variations become visible (Fig. 1g).

Two major differences are observed from the intensity profiles. First, by decreasing the focus value the spots corresponding to Ca columns become smaller, indicating that the point-to-point resolution is improved. Second, the ratio between the intensities of the mixed Ti-O and Ca atomic columns varies with focus value by approximately 10%. The improvement in the resolution is consistent with the shape of the probe profile for the corresponding foci. It is, however, surprising that we did not observe any artifacts in the experimental images due to the tails that were found in images of Si [20], indicating that there must be additional effects that alter the image contrast, such as spread of focus and/or damping effects due to absorption. The fact that the Ti-O vs. Ca intensity ratio is focus dependent is very important and should be thoroughly considered in the STEM image calculations when using HAADF-STEM imaging for quantitative composition analysis.

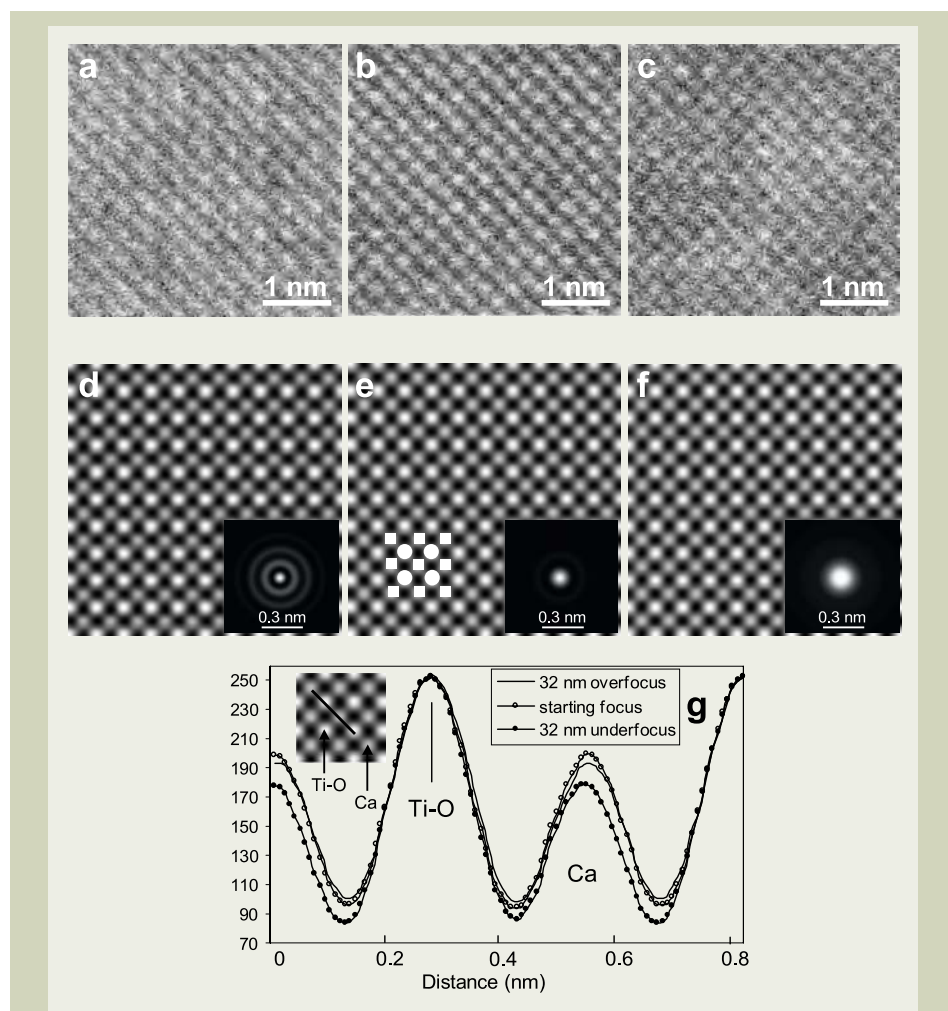


Fig. 1. (a-c) Warped experimental HAADF-STEM images of  $\text{CaTiO}_3$  crystal in the  $[001]$  zone axis. (a) 32 nm underfocus from the starting focus, (b) starting (Scherzer) focus, and (c) 32 nm overfocus from the starting focus. (d-f) Average and polynomial processed HAADF STEM images with the corresponding scaled calculated beam profiles. (d) 32 nm underfocus, (e) starting (Scherzer) focus, and (f) 32 nm overfocus. In the middle image (e) positions of Ti-O (full circles) and Ca (full squares) columns are indicated. (g) Intensity profiles across Ti-O and Ca atomic columns along  $[110]$  direction. Relative intensity of Ca columns varies for approx. 10% within the focus range of 64 nm. The starting focus was set close to the condition of the maximum information transfer.

These results also suggest that in image calculations the experimentally evaluated probe function should be used, rather than the calculated one. Quite different results were observed in atomically resolved HAADF-STEM images recorded at different thickness of a specimen and at the same focus value. Processed STEM images taken from 85, 45 and 25 nm thick single  $\text{CaTiO}_3$  crystal regions are shown in Fig. 2a-c. Again, the subtle differences in images are only resolved from the corresponding intensity profiles across Ti-O and Ca atomic columns in the  $\langle 110 \rangle$  perovskite direction (Fig. 2d). For all thicknesses the Ti-O vs. Ca intensity ratio remains the same, which confirms that the thickness does not significantly influence the STEM image. However, according to intensity profiles, the best point-to-point resolution and signal to noise are obtained for 45 nm thick region of the specimen. Thicker region of the specimen (85 nm) yielded worse resolution while the thinner region of the specimen (25 nm) exhibited much poorer signal to noise ratio, which can be attributed to fewer atoms in the atomic columns but probably also to loss of coherency along atomic columns due to amorphous layer, which is probably comparable in thickness to the thickness of crystallized  $\text{CaTiO}_3$  at this overall thickness. The influence of present amorphous layer on signal to noise ratio and resolution certainly needs to be incorporated in future into image calculations. Finally, our experimental evidence show that atomically resolved HAADF STEM images of 40 to 60 nm thick specimens provide the best point-to-point resolution and signal to noise ratio.

### The chemistry of planar faults in AO-doped $\text{SrTiO}_3$ (A = Ca, Sr, Ba) resolved by HAADF STEM imaging

Atomically resolved, Z-contrast images were acquired in the  $\langle 001 \rangle_{\text{per}}$  zone axis for all three samples: CaO-, SrO-, and BaO-doped  $\text{SrTiO}_3$ . The final results of the image processing are shown in Fig. 3. In the case of SrO-excess  $\text{SrTiO}_3$  we observe a typical four-fold perovskite pattern where the large bright dots represent Sr columns ( $Z_{\text{Sr}}=38$ ) and smaller dots in-between represent mixed Ti-O columns ( $Z_{\text{Ti-O}} = 23.4$ ) (Fig. 3a). A single RP fault is visible as a vertical zig-zag of large dots in the image. In the case of CaO- and BaO-doped  $\text{SrTiO}_3$  (Fig. 3b, c) the dots in the fault appear darker than the corresponding A-site dots in the perovskite ( $Z_{\text{Ca}} = 20$ ,  $Z_{\text{Ba}} = 56$ ). To clarify the intensity variations between the RP fault and the bulk we averaged equivalent atomic columns along the fault by applying line scans over the maximum intensity of the corresponding bright dots. Intensity profile diagram in Fig. 3 shows that the maximum intensity in the line scans for the A columns (A-A') and the Ti-O (B-B') columns in the  $\text{SrTiO}_3$  matrix is similar in all systems, whereas the intensity of the line scan along the RP fault alters, depending on the different AO dopant (F-F').

Figure 3a shows no significant differences between the A-A' and F-F' line scans, which clearly indicates that the RP fault in the SrO-excess  $\text{SrTiO}_3$  comprises only Sr ions. In contrast, for the case of CaO-excess  $\text{SrTiO}_3$  the line scans from the RP fault show a lower

intensity than the corresponding scans from the matrix, suggesting that the fault planes are preferentially occupied by Ca ions. Finally, a similar effect can be observed in the case of BaO-doped  $\text{SrTiO}_3$  where line scans taken from the fault planes have a lower intensity than the corresponding line scans in the bulk, therefore indicating that the RP fault consists of elements with a lower atomic number (Z) than the A sites in the perovskite matrix. Our results suggest that Ba ions prefer A sites in the perovskite by forming a  $\text{Ba}_x\text{Sr}_{1-x}\text{TiO}_3$  solid solution, while the surplus Sr ions segregate to RP faults. The suggested compositional models are in agreement with previous results on the structural compensation of RP faults, where cations with smaller ionic radii preferentially occupy the RP fault, thus minimizing the lattice mismatch between the rock-salt structure of the fault and the perovskite matrix.

### The ordering of Zn and Sb atoms in the inversion boundary in $\text{Sb}_2\text{O}_3$ -doped ZnO resolved by HAADF-STEM imaging

The Sb-rich basal plane inversion bound-

aries (IBs) in zinc oxide were analyzed using various quantitative transmission electron microscopy techniques. HRTEM was used to resolve the crystallography and the atomic structure of IBs along the zone axes  $\langle 2\bar{1}\bar{1}0 \rangle$  and  $\langle 01\bar{1}0 \rangle$  while HAADF-STEM was used to determine the exact amount and the arrangement of Sb in the IB plane. Owing to the non-centrosymmetric structure of ZnO, polar c-axes across IBs are head-to-head oriented forming a  $\dots A\beta\gamma - B\alpha\delta - A \rightarrow \beta_{\text{oct}} \leftarrow C - \gamma_{\text{II}} A - \alpha_{\text{II}} C \dots$  stacking sequence where O layers are denoted by Roman, and Zn layers by Greek letters (with subscripts indicating type-I and type-II tetrahedral and octahedral sites). The displacement vector of the O sub-lattice at the IB, as measured by an iterative HRTEM analysis, is  $\mathbf{R}_{\text{IB}} = 1/3 \cdot \langle 01\bar{1}0 \rangle - 0.102 \cdot \langle 0001 \rangle$ , while the width of octahedral IB layer is  $0.398 \cdot \langle 0001 \rangle$  [21]. HRTEM observation of the IB in the two zone axes indicated a perfect ordering of Sb atoms in the octahedral IB plane. However, the periodic contrast in the IB plane, in spite of HRTEM image simulations, does not reliably provide an information whether the rest of octahedral sites is occupied by Zn or

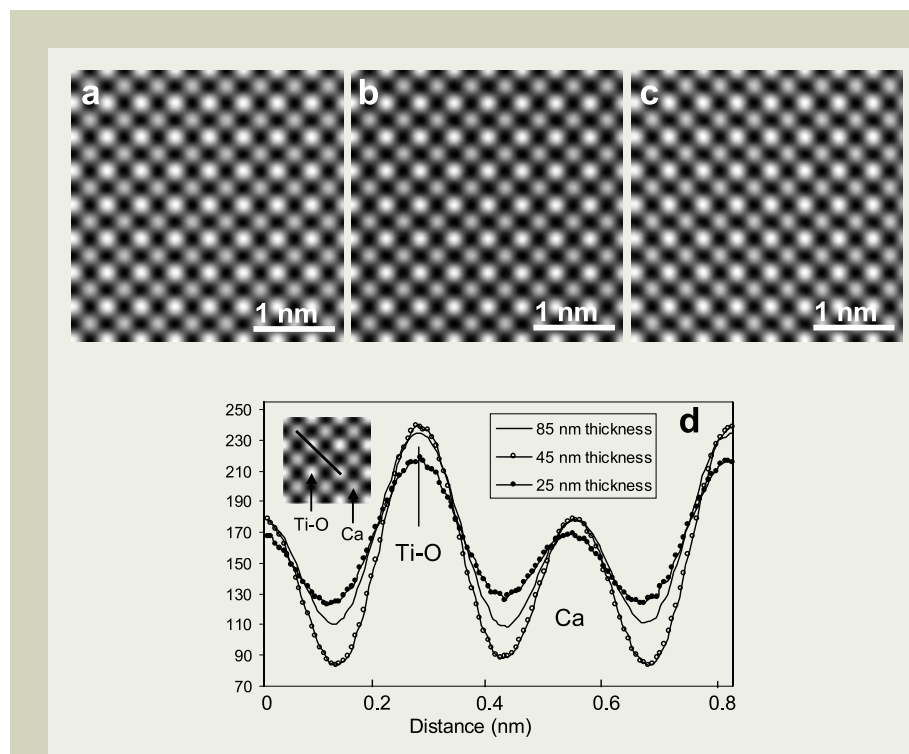


Fig. 2. (a-c) Processed HAADF-STEM images of  $\text{CaTiO}_3$  crystal in the  $[001]$  zone axis taken from regions with different thickness. (a) 85 nm, (b) 45 nm, and (c) 25 nm. (d) Intensity profiles across Ti-O and Ca atomic columns along  $[110]$  direction. Point-to-point resolution and signal to noise ratio are best for 45 nm thick specimen. The starting focus was set close to the condition of the maximum transfer.

they are vacant. Using experimental high-angle annular dark-field (HAADF) scanning transmission electron microscopy (STEM) we could clearly show that the relaxation normal to the IB plane as measured by HRTEM actually exists. It appears as expansion of the cation sub-lattice, as reported by Rečnik *et al* [20]. In addition to the translations HAADF-STEM revealed that the IB interfaces are periodic. In the  $\langle 2\bar{1}\bar{1}0 \rangle$  view every atomic column in the IB plane has a similar intensity (Fig. 4a), but slightly higher than the intensity of Zn atomic columns in the fault-free ZnO crystal, while in the  $\langle 01\bar{1}0 \rangle$  projection we resolved an *ABB* period in the IB plane where atomic columns of higher intensity are separated by two columns of lower intensity, which are comparable to that of Zn atomic columns in the fault-free ZnO crystal (Fig. 4c). The periodicity of HRTEM and HAADF-STEM images clearly indicates that the octahedral IB plane is occupied by Sb and Zn atoms. They produce a honeycomb arrangement with the three-fold symmetry where every Sb atom is enclosed by 6 Zn atoms and every Zn atom is surrounded by 3 Sb atoms and 3 Zn atoms

[21]. The resulting composition of the IB layer is  $\text{SbZn}_2$  and the average oxidation state per octahedral site is +3 (Fig. 4b). This is consistent with the charge compensation in similar systems such as Sn- and In-doped IBs in ZnO [22, 23].

## Conclusions

Our results on HAADF STEM imaging have clearly demonstrated the unique capabilities of Z-contrast imaging when it comes to studying compositional phenomena on the atomic level in oxide materials. The point-to-point resolution we achieved in the HAADF-STEM imaging was quite similar to that for HRTEM, *i.e.* below 0.2 nm. We were able to show that the defocus value and the thickness have definite influence on the intensity of the chemically different atomic columns of Ca ( $Z=20$ ) and mixed Ti-O ( $Z=23.4$ ). Despite the fact, that the differences are far smaller compared to the corresponding HRTEM images, they should be thoroughly considered when using HAADF-STEM imaging for quantitative compositional analysis and should be properly

taken into account in the STEM image calculations. Nevertheless, the semi-quantitative interpretation of the composition of planar defects in non-stoichiometric  $\text{SrTiO}_3$  and ZnO has clearly shown that geometrically corrected, experimental HAADF-STEM images can provide reasonable chemical information that can be further improved when matched with simulated HAADF-STEM images, thus making the Z-contrast technique a unique and powerful nanoanalysis tool.

## References

1. L. Reimer, *Transmission Electron Microscopy*, Springer-Verlag, Berlin (1997)
2. J. M. Cowley, *Appl. Phys. Lett.*, **15**, 58 (1969)
3. D. A. Muller, B. Edwards, E. J. Kirkland, J. Silcox, *Ultramicroscopy*, **86**, 371 (2001)
4. Z. L. Wang, J. M. Cowley, *Ultramicroscopy*, **32**, 275 (1990)
5. Z. L. Wang, J. M. Cowley, *Ultramicroscopy*, **31**, 437 (1989)
6. A. Howie, *Journal of Microscopy*, **117**, Pt 1, 11 (1979)
7. S. J. Pennycook, D. E. Jesson, *Ultramicroscopy*, **37**, 14 (1991)
8. P. D. Nellist, S. J. Pennycook, *Ultramicroscopy*, **78**, 111 (1999)
9. J. Silcox, P. Xu, R. F. Loane, *Ultramicroscopy*, **47**, 173 (1992)
10. M. M. J. Treacy, J. M. Gibson, *Ultramicroscopy*, **52**, 31 (1993)
11. T. Plamann, M. J. Hytch, *Ultramicroscopy*, **78**, 153 (1999)
12. K. Watanabe, T. Yamazaki, I. Hasimoto, M. Shiojiri, *Physical Review B*, **64**, 115432 (2001)
13. T. Yamazaki, K. Watanabe, A. Rečnik, M. Čeh, M. Kawasaki, M. Shiojiri, *J. Electron Microscopy*, **49** (6), 753 (2000)
14. T. Yamazaki, M. Kawasaki, K. Watanabe, I. Hashimoto, M. Shiojiri, *J. Electron Microscopy*, **50** (6) 517 (2001)
15. M. Čeh, *Acta chim. slov.*, **48**, 63 (2001)
16. M. Čeh, A. Rečnik, S. Šturm, Proceedings of 5th Multinational Congress on Electron Microscopy, September 20-25, 2001, Lecce, Italy. Princeton, Rinton, 453 (2001)
17. S. Šturm, A. Rečnik, C. Scheu, M. Čeh, *J. Mater. Res.*, **15**, 2131 (2000)
18. S. Šturm, A. Rečnik, M. Čeh, *J. Eur. Ceram. Soc.*, **21**, 2141 (2001)
19. A. Rečnik, G. Möbus, M. Kawasaki, *ICEM-15* (Durban 2002), in print
20. K. Watanabe, T. Yamazaki, Y. Kikuchi, Y. Kotaka, M. Kawasaki, I. Hasimoto, M. Shiojiri, *Physical Review B*, **63**, 085316 (2001)
21. A. Rečnik, N. Daneu, T. Walther, W. Mader, *J. Am. Ceram. Soc.*, **84**, 2657 (2001)
22. N. Daneu, A. Rečnik, S. Bernik, D. Kolar, *J. Am. Ceram. Soc.*, **83**, 3165 (2000)
23. A. Rečnik, N. Daneu, W. Mader, A. Loewe, M. Kawasaki, 4<sup>th</sup> German-Slovenian Seminar on Joint Proj. in Mat. Sci. and Technology, in Berlin 2000, 48 (2000)

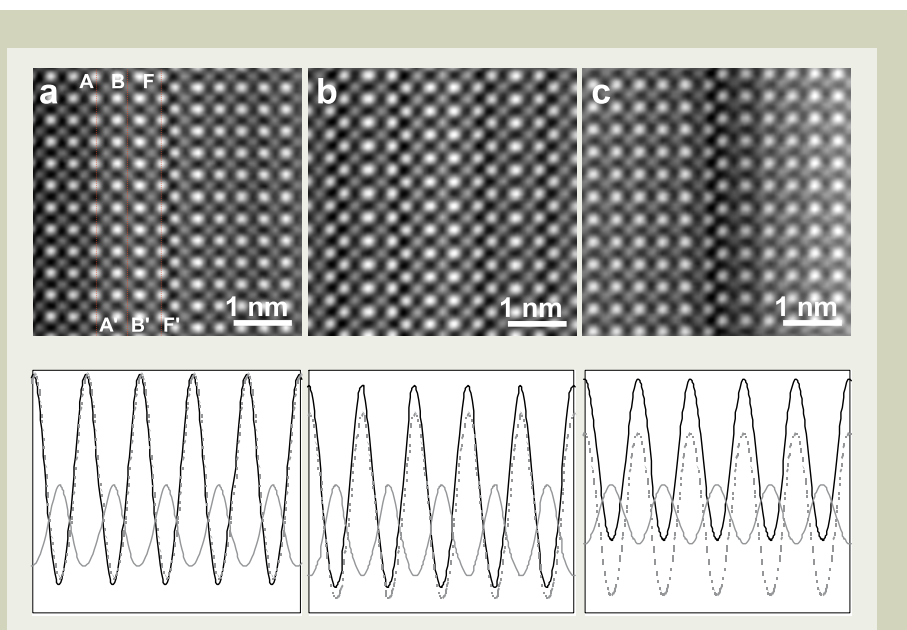


Fig. 3. Processed HAADF-STEM images of RP planar faults in [001] perovskite zone axis of (a) SrO-excess, (b) CaO-excess and (c) BaO-excess  $\text{SrTiO}_3$ , with corresponding average line scans for A-site (A-A' solid black line) columns and Ti-O (B-B' solid grey line) columns in bulk and columns located at RP-faults (F-F' dashed line). Lines are indicated in Fig. 3(a).

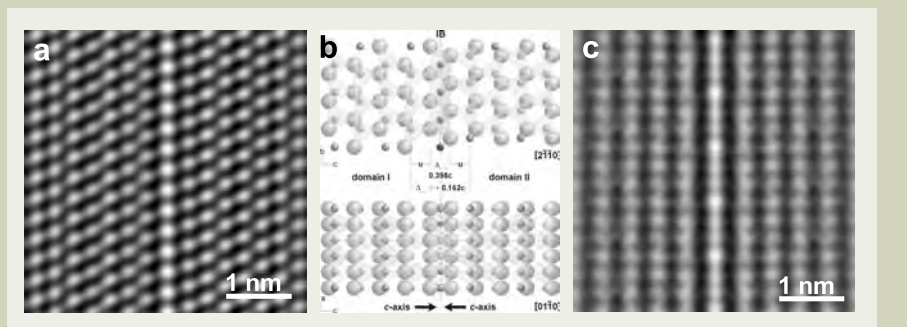


Fig. 4. (a) Processed HAADF-STEM images of IB plane in  $[2\bar{1}\bar{1}0]$  zone axis suggests equal distribution of Sb in the IB plane. (b) Reconstructed atomic model of Sb-rich IB in ZnO. Views  $[2\bar{1}\bar{1}0]$  and  $[01\bar{1}0]$ . (c) Processed HAADF-STEM images in  $[01\bar{1}0]$  zone axis suggests  $\text{SbZnZn}$  ordering in the IB plane.

# Observation of Waterborne Protozoan Oocysts Using a Low-Vacuum SEM

Jun Suzuki<sup>†</sup>, Rie Murata<sup>†</sup>, Takeo Suzuki<sup>††</sup> and Iwao Murata<sup>†</sup>

<sup>†</sup>The Tokyo Metropolitan Research Laboratory of Public Health

<sup>††</sup>Electron Optics Division, JEOL Ltd.

*Cryptosporidium parvum* (*C. parvum*), *Cryptosporidium muris* (*C. muris*), *Cyclospora cayetanensis* (*Cyclospora*) and *Isospora belli* (*Isospora*) are well known as the pathogenic protozoa of the waterborne-outbreak of diarrhea.

Three species of protozoan oocysts infect and amplify into the epithelial cells of the small intestine and only the *C. muris* oocyst infects and amplifies into the gastric mucosal epithelial cells. *C. parvum* and *C. muris* oocysts are spherical with diameters of 4-10 µm. *Cyclospora* oocysts are spherical with diameters of 8-10 µm. On the other hand *Isospora* oocysts are elliptical 20-33 µm long and 10-19 µm wide. It is especially difficult and important to observe the microstructures, such as sporozoites, of *C. parvum* and *C. muris* with an optical microscope, because of a very robust oocyst wall that protects the four sporozoites in the environment for a very long time without their losing infectivity.

In this study, the shapes of oocyst walls and inner microstructures, such as sporozoites, were clearly observed with the low-vacuum scanning electron microscope (LV-SEM) without coating and with the samples of protozoan oocysts, prepared using the simple freeze-drying method. As a result of observations with LV-SEM, the oocyst walls of four species of oocysts could be observed at a magnification >1,000× and their microstructures such as sporozoites were clearly visible at 10,000×. It was concluded that the LV-SEM using our method is useful for observation of these protozoan oocysts.

## Introduction

*Cryptosporidium parvum* oocyst (*C. parvum*) was well known protozoan parasite that was first discovered in the gastric mucosa of a mouse in 1907 [1]. The pathogenicity of *C. parvum* against human was not known early time, but since infection to immunocompromised persons was reported in 1976 [2], it has been described the attention in Europe and America as a cause of serious diarrhea symptoms to immunocompromised persons. Now *C. parvum* is recognized as one of the most commonly identified intestinal pathogens even to persons with healthy immune systems [3]. And the infection to healthy infant of *Cryptosporidium muris* oocyst (*C. muris*) was reported in Indonesia in 1996 [4]. In Japan, as the first case of infection with *C. parvum*, more than 400 persons were reported in Kanagawa Prefecture in 1993. Then as the second case, about 8,000 people with diarrhea by waterborne infection of *C. parvum* were reported in Saitama Prefecture in 1996 [5]. In genus *Cryptosporidium*, it has been observed four sporozoites in the oocyst. *C. parvum* is parasitized in the mucosal epithelial cells of the small intestine and *C. muris* is parasitized in the gastric mucosal epithelial cells.

*Cyclospora cayetanensis* oocyst (*Cyclospora*) is a protozoa that parasitizes in mucosal epithelial cells of the human small intestine and causes diarrheal symptoms. Organisms of the genus *Cyclospora* have an oocyst with two sporocysts, each of which contains two sporozoites. In 1996, the largest diffuse outbreak of

cyclosporiasis ever reported, affecting about 1,500 persons in North America [6], was associated with eating fresh raspberries; trace-back data indicated that the source of the berries was Guatemala.

On the other hand, *Isospora belli* oocyst (*Isospora*) is a protozoa that parasitizes in the mucosal epithelial cells of the human small intestine. It causes acute diarrheal symptoms against immunocompromised persons, including those infected with HIV [7].

In this study, we observed these four types of protozoan oocysts through a low vacuum scanning electron microscope (LV-SEM). We then compared this method and microscopic method according to the guideline set forth by the Ministry of Health, Labour and Welfare [8].

## Material and Method

### Collection of protozoan oocysts

We isolated protozoan oocysts by the centrifugal floating method using sucrose solution (specific gravity, 1.2) from the stool of patients, infected with *C. parvum*, *Cyclospora* and *Isospora*. Three species of protozoan oocysts as specimens were used for observation after fixing them with 10 % neutral formalin aqueous solution. We also used a specimen isolated from the bovine stool infected with *C. muris* in the same way.

### Observation of *C. parvum*, *C. muris*, *Cyclospora* and *Isospora* through optical microscope

The four samples each of *C. parvum*, *C. muris*, *Cyclospora* and *Isospora* were dispensed onto the slides and dried at 55 to 60°C.

The slides of *C. parvum* and *C. muris* were observed under B excitation, after staining them with the FL-Crypto-a-Glo kit (Waterborne Inc.) that is monoclonal antibody, which have been labeled directly with FITC, specific to the oocyst wall of *Cryptosporidium*.

*Cyclospora* and *Isospora* were observed directly through a fluorescence microscope, because their oocyst walls emit blue auto-fluorescences under UV excitation (330-380nm). We then switched to a differential interference microscope to observe their oocysts and took micrographs.

### Method of observing protozoan oocysts through low-vacuum SEM

Observation was conducted according to the following procedure using the method of observing and identifying *C. parvum* that was earlier reported by J. Suzuki *et al.* [9].

- (1) A concentrated specimen was filtered through the SEM's special-purpose specimen stage with an average pore diameter of 0.6 µm (JEOL Datum, Ltd.), depositing oocysts on the specimen stage of the SEM.
- (2) 2 mL distilled water was dropped onto the specimen set on the specimen stage and the specimen was cleaned twice while aspirating it with a syringe attached under the specimen stage.
- (3) The specimen stage was mounted on a specimen holder and was placed in an insulating container made of styrofoam; then liquid nitrogen was slowly poured around the specimen stage to freeze the specimen. The cooling time was about 40 seconds after the specimen had been frozen.
- (4) The frozen specimen was quickly mounted on the specimen stage of a low-vacuum

<sup>†</sup>3-24-1 Hyakunin-cho shinjuku-ku Tokyo 169-0073

<sup>†</sup>E-mail: suzukij@tokyo-eiken.go.jp

### Photomicrograph of *Cryptosporidium parvum*

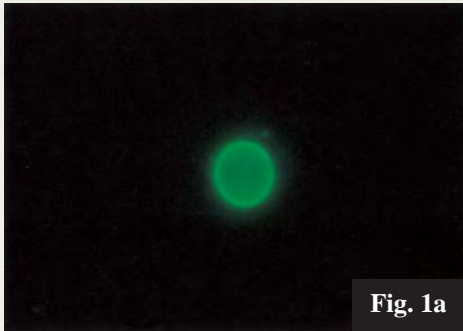


Fig. 1a. By direct immunofluorescence assay ( $\times 1,000$ ).



Fig. 1b. By Normarski differential interference contrast microscopy ( $\times 1,000$ ).

### LV-SEM image of *Cryptosporidium parvum*

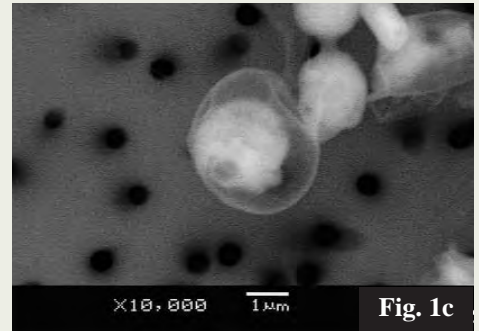


Fig. 1c. Accelerating voltage: 15 kV  
Vacuum pressure: 20 Pa.

### Photomicrograph of *Cryptosporidium muris*

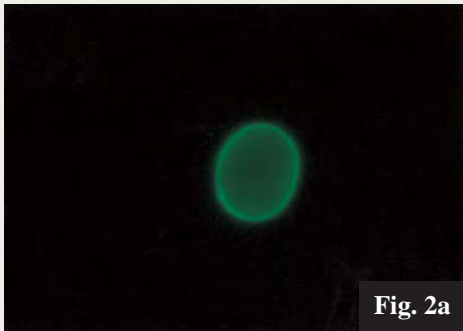


Fig. 2a. By direct immunofluorescence assay ( $\times 1,000$ ).



Fig. 2b. By Normarski differential interference contrast microscopy ( $\times 1,000$ ).

### LV-SEM image of *Cryptosporidium muris*

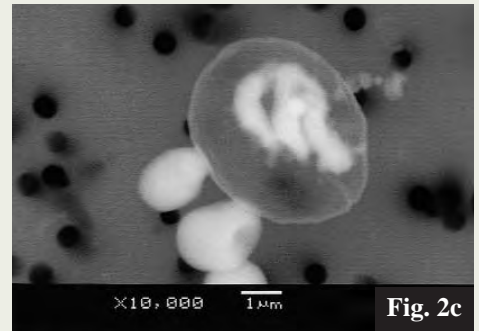


Fig. 2c. Accelerating voltage: 15 kV  
Vacuum pressure: 20 Pa.

SEM (JEOL Model JSM-5600LV), the specimen chamber was evacuated to 60 Pa, and the ice of the specimen in the LV-SEM was slowly and completely sublimated for about 60 minutes.

- (5) After sublimating the specimen ice in the LV-SEM completely, the specimen chamber was evacuated to a pressure of 20 to 30 Pa and the accelerating voltage was set at 10 to 25 kV, and *C. parvum*, *C. muris*, *Cyclospora* and *Isospora* were searched for within a magnification range of  $500\times$  to  $1,000\times$ . The overall image and the internal structure of each oocyst were observed within a range of  $5,000\times$  to  $10,000\times$ .

## Results and Considerations

### Results of observation through Fluorescence Microscope

Monoclonal antibody kits for *C. muris* are not commercially available. We then stained *C. muris* using the monoclonal antibody kit for FITC marker anti-*C. parvum* and obtained an image on which the oocyst wall emits light-green fluorescence under B excitation as does the small *C. parvum* (Fig. 1a, 2a). We also observed *Cyclospora* and *Isospora* through a

fluorescence microscope under UV excitation and obtained the images on which the oocyst wall emits light-blue fluorescence, as shown in Figs. 3a and 4a.

We observed the same field of view using a differential interference microscope and observed the stereoscopic structure of the four types of protozoan oocysts at a magnification of  $1,000\times$ , and identified sporozoites clearly in *C. muris* (Fig. 2b), but could not obtain a clear image of the sporozoite in *C. parvum* (Fig. 1b). Two sporocysts formed in a relatively thick oocyst (Fig. 3b) and the oocyst wall and internal cystoblast of *Isospora* could be observed through an optical microscope (Fig. 4b).

Therefore, of the four types of morphological protozoan oocysts observed through an optical microscope, the oocyst wall and internal structure of *C. muris*, *Cyclospora* and *Isospora* could be observed, but it was difficult to identify the internal sporozoites in *C. parvum*.

### Results of observation of protozoan oocysts through low-vacuum SEM

The existence of *C. parvum* and *C. muris*

could be confirmed through a low-vacuum SEM at a magnification of  $1,000\times$  or more (Fig. 1c, 2c). At a magnification of  $10,000\times$ , we could observe and identify the internal and external fine structures of sporozoites and oocyst walls that are difficult to observe through an optical microscope or a conventional scanning electron microscope that requires metallization with coating. Unlike *C. parvum*, which is small in size, *C. muris* is large and elliptical, but we could observe long and narrow sporozoites.

The existence of *Cyclospora* could be confirmed at a magnification of  $500\times$  or more and the oocyst wall could be clearly observed at a magnification of  $8,000\times$  (Fig. 3c). The internal structure of *Cyclospora* could be identified even by increasing the accelerating voltage to 25 kV and decreasing the pressure in the specimen chamber to 30 Pa, probably because the oocyst wall of *Cyclospora* is thick. However, observation for an extended time revealed that the specimen tends to become charged, and so, the observation conditions need to be corrected.

The existence of *Isospora* could easily be confirmed at a magnification of  $500\times$  or more, while oocyst wall and the internal structure

### Photomicrograph of *Cyclospora cayetanensis*

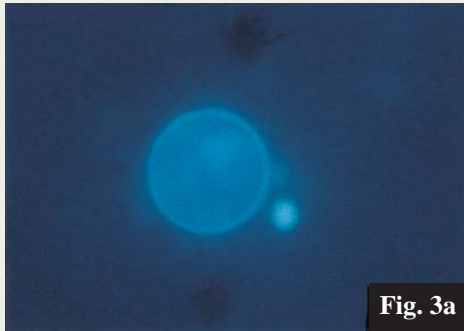


Fig. 3a. By direct immunofluorescence assay ( $\times 1,000$ ).



Fig. 3b. By Normarski differential interference contrast microscopy ( $\times 1,000$ ).

### LV-SEM image of *Cyclospora cayetanensis*

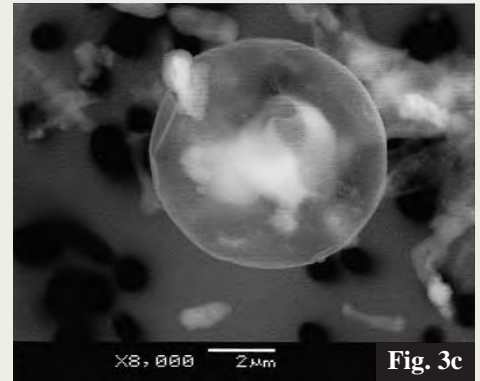


Fig. 3c. Accelerating voltage: 25 kV  
Vacuum pressure: 30 Pa.

### Photomicrograph of *Isoospora belli*

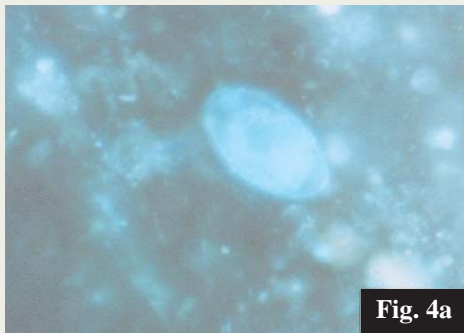


Fig. 4a. By direct immunofluorescence assay ( $\times 400$ ).



Fig. 4b. By Normarski differential interference contrast microscopy ( $\times 400$ ).

### LV-SEM image of *Isoospora belli*

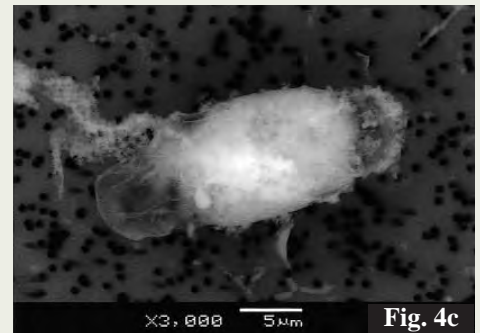


Fig. 4c. Accelerating voltage: 10 kV  
Vacuum pressure: 20 Pa.

sporoblast could be observed at a magnification of  $3,000\times$  (Fig. 4c).

Observation of four types of protozoa oocysts of *C. parvum*, *C. muris* and *Isoospora* through a low-vacuum SEM revealed that the LV-SEM is very useful in observing the minute internal structure of oocysts and that the size and morphology of oocysts and sporozoites can be compared and examined relatively easily using the images stored in a computer, especially for two types of *Cryptosporidium*. Furthermore, even the internal structure of *Cyclospora* with a thick oocyst wall could be observed by increasing the accelerating voltage.

## Conclusion

Specimens of four types of protozoan oocysts: *C. parvum*, *C. muris*, *Cyclospora* and *Isoospora* were prepared by the freeze-drying method without coating within a short time and were observed within a magnification range of  $500\times$  to  $10,000\times$ . The results showed that even the internal structure of *Cyclospora* oocyst with a thick oocyst wall

can be observed by increasing the accelerating voltage to 25 kV and decreasing the pressure in the specimen chamber to 30 Pa. On the other hand, a problem was found in that the specimen tends to become charged during prolonged observation. The walls and internal structures of *C. parvum*, *C. muris* and *Isoospora* oocysts could be observed at the accelerating voltage of 10 kV to 15 kV. Thus we found that protozoa oocysts can be observed efficiently and effectively through a low-vacuum SEM using the freeze-drying method.

## References

1. Tyzzer, E. E.: *Soc. Exp. Biol. Med.*, **5**, 12-13 (1907).
2. Nime, F. A., Burek, J. D., Page, D. L., Holscher, M. A., Yardley, J. H.: *Gastroenterology*, **70**, 592-598 (1976).
3. Navin, T. R., Juranek, D. D.: *Reviews on Infected Disease*, **6**, 313-327 (1984).
4. Katsumata T., Hoesea D., Wastlto EB., Kohno S., Hara K., Soeparto P., Ranuh ING.: *Cryptosporidiosis in Surabaya Indonesia*, VXIth International Congress for

Tropical Medicine and Malaria, Nagasaki, 390, 1996.

5. Hirata T.: Outbreaks of waterborne Cryptosporidiosis transmitted by supplied water, *J. Food Hyg. Soc. Japan*, **38** (2), 153-157 (1997). (in Japanese)
6. Omar M. Amin: Seasonal prevalence and host relationships of *Cyclospora cayetanensis* in North America during 1996, *Parasitology International*, **47**, 53-58 (1998).
7. Sakamoto M., Adachi T., Sagara H., Izeki M.: A case of AIDS complicated with *Isoosporiosis* as initial manifestation, *J. J. A. Inf. D.*, **72** (6), 643-646 (1998). (in Japanese)
8. The Ministry of Health, Labour and Welfare, Water Supply Division: Provisional detection method of *Cryptosporidium* oocysts, Eisui 49, Oct. **19**, 1998. (in Japanese)
9. Suzuki J., Murata I., Murata R., Morozumi S., Suzuki T.: A method for identification of *Cryptosporidium parvum* from river water using low-vacuum SEM, *Jpn. J. Food Microbiol.*, **14** (4), 187-191 (1998).

# A Possible Efficient Assay: Low-vacuum SEM Freeze Drying and Its Application for Assaying *Bacillus thuringiensis* Formulations Quality

Nobuhiro Matsumoto<sup>†</sup> and Takeo Suzuki<sup>††</sup>

<sup>†</sup>Institute of Agriculture and Forestry, University of Tsukuba

<sup>††</sup>Electron Optic Division, JEOL Ltd.

A new preparation method for examining the microstructures of *Bacillus thuringiensis* formulations, low-vacuum SEM freeze drying, is described through its application to observations of the formulation sample. Scanning electron micrographs revealed that the drying method preserved the microstructures of BT formulation granules intact condition well. Dehydration in a graded ethanol series is not necessary in this new method. Low-vacuum SEM freeze drying is, therefore, a simple, time-saving and reproducible method for scanning electron microscopy that is applicable to check various commercial BT formulations quality.

\*Key word: *Bacillus thuringiensis*; BT formulation; quality check; low-vacuum SEM.

## Introduction

*Bacillus thuringiensis* (BT) formulations are microbial insecticide commonly used worldwide. Their active ingredients are known to be insecticidal crystalline proteins (ICPs) produced during spore formation. The crystalline protein ( $\delta$ -endotoxin) is believed to be a protoxin because it is only highly toxic when ingested in susceptible insects midguts [1]. The potency of BT formulation indicates the dose-dependent, lethal activity of the product as compared to that of an accepted standard BT [2]. About 50 years ago, that were appearance of the first commercial products based on BT created a need for methods to compare products in various countries. The first protocols were based on spore counts, but because the number of spores did not reflect the number of crystals present in the bacteria, this method was unreliable and resulted in some major product failures in the field [2]. With the development of commercial BT products in France [3, 4], a titration method based on comparison of the LC<sub>50</sub>s of a product and standard material was developed. This method led to rapid improvements not only in product reliability, but also in increased biological activity of the products. The new technique became an instrument for industrial fermentation and formulation development.

In Japan, the silkworm bioassay has been used to determine lepidopteran BT product potency [5, 6]. Several bioassay methods have been examined for determination of the potency of BT formulations. For example, two methods are generally used in Japan to examine the oral toxicity of BT formulation; a) mixing with the diet (diet feeding method) [5 to 11], and b) injection into the mouth with a syringe (force-feeding method) [8].

Several insect species have been used for in bioassays for lepidopteran BT formulations for

<sup>†</sup>Tennodai 1-1-1, Tsukuba Ibaraki 305-8572, Japan

<sup>†</sup>E-mail: nobu-matsumoto@mue.biglobe.ne.jp

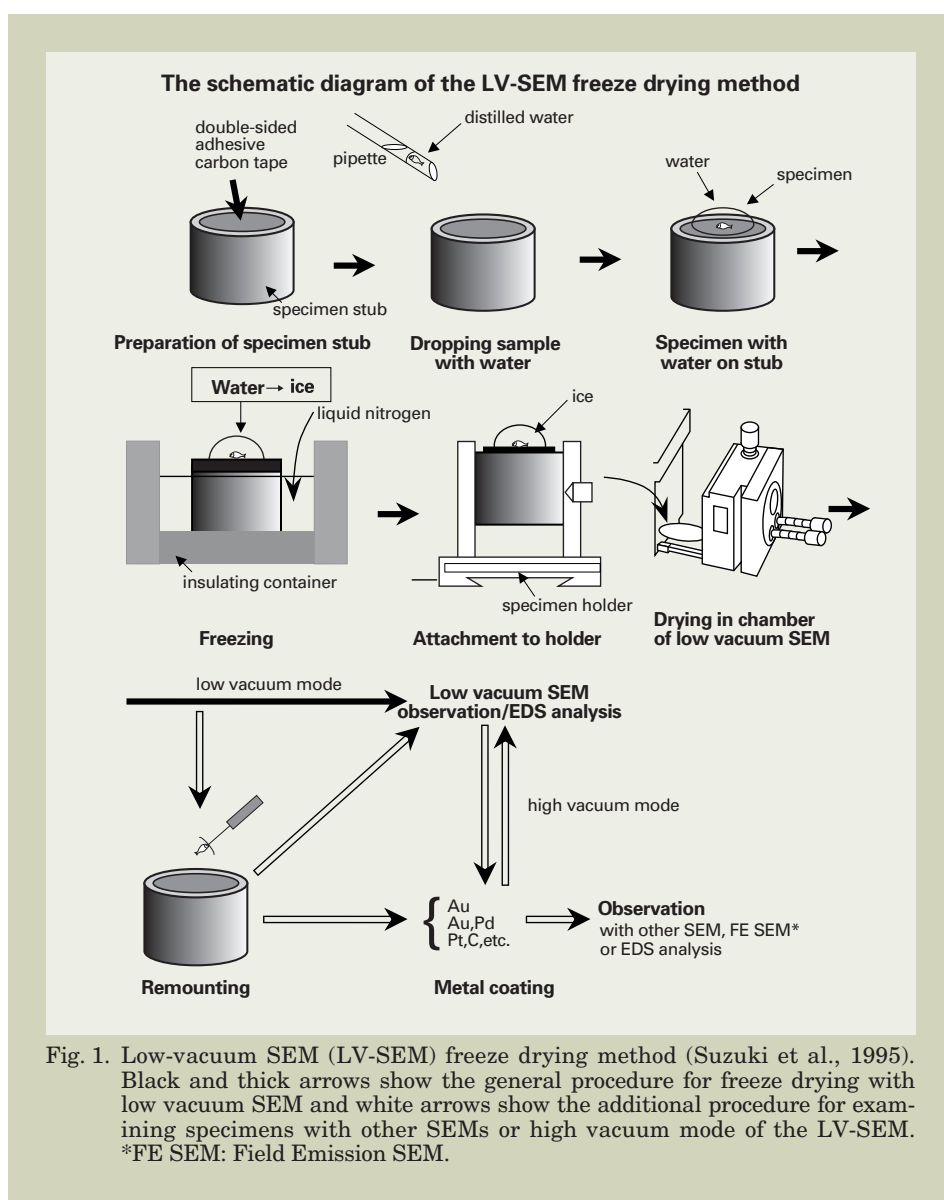


Fig. 1. Low-vacuum SEM (LV-SEM) freeze drying method (Suzuki et al., 1995). Black and thick arrows show the general procedure for freeze drying with low vacuum SEM and white arrows show the additional procedure for examining specimens with other SEMs or high vacuum mode of the LV-SEM. \*FE SEM: Field Emission SEM.

example; the silkworm, *Bombyx mori* [6, 9 to 13], diamondback moth, *Plutella xylostella* [11], small white butterfly, *Pieris rapae* [12] and common cutworm, *Spodoptera litura* [14].

Heimpel [15] has discussed the merits of using *Bombyx mori* as an internationally standardized test insect species for the assay of insecticidal activity in a lepidopteran BT formulation, where *Pieris brassicae* is not available because of quarantine regulations.

In recent years, a Low-vacuum scanning electron microscope (LV-SEM) has been developed, which allows specimen observation without the preparations needed for conventional SEM, such as chemical fixation, dehydration, drying, and coating. In the present study, we attempted, through LV-SEM observation, to compare and discriminate and control the qualities of several commercial BT formulations. Thus the degradation sample of insecticidal activity of BT formulations after long-term preservation was examined by the LV-SEM for this purpose. The results show that BT-insecticidal activity and several indicators of physical degradation can be detected with this new method. Freeze-drying method in a LV-SEM has been found to be a method suited for observing several commercial BT products such as different manufacturer samples and registration products. We introduce here this new simple method for assaying BT formulations quality.

## Materials and Methods

### Principle of LV-SEM and SEM/EDS

LV-SEM neutralizes the charge of nonconductive specimens by utilizing ions generated by the interaction between residual gas molecules in the specimen chamber and the electrons used for observation. For this purpose, the pressure of the specimen chamber can be raised to 270 Pa by using differential pumping. The use of backscattered electrons for imaging allows not only sample surfaces of BT granule structures to be observed.

The schematic diagram of the LV-SEM freeze drying method is shown in Fig. 1. The LV-SEM is a SEM that is equipped with an electron gun that generates an electron beam and a different evacuation system that allows pressure adjustment of the specimen chamber to a low vacuum range (6 to 270 Pa), while the lens system to condense the electron beam is kept at a high vacuum [16].

### BT formulation samples

Commercial BT formulations, servers and main  $\delta$ -endotoxin proteins were as follows:

- No. 1. Selectzin® (Kyowa Hakko Kogyo Co. Ltd., Tokyo, serovar *aizawai*, Cry1C) : **A**.
- No. 2. Bacilex® (Shionogi & Co. Ltd., Osaka: two-strain formulation of serovar *kurstaki* and *aizawai*, Cry1Aa and Cry1C) : **B**.
- No. 3. Dipole® (Sumitomo Chemical, Tokyo, serovar *kurstaki*, Cry1Aa) : **C**.
- No. 4. Thuricide® (SDS Bio-tech K. K., Tokyo, serovar *kurstaki*, Cry1Aa) : **D**.
- No. 5. Xentary® (Tomen Co., Tokyo, serovar *aizawai*, Cry1C) : **E**.

### Silkworm bioassay

Insecticidal activities shown in the present study were from the original data [17]. The

method of bioassay was the same as Matsumoto [10, 18].

### Observation in the solution of BT formulation by light microscopy

Prepared BT solution (ten times) samples were observed by a light microscopy. The light micrographs was taken by an Olympus bright-field microscope.

### Observation in the solution of BT formulation by electron microscope (Suzuki Method, Suzuki et al., 1995)

A scanning electron microscope (JSM-5300LV, JEOL) was used to observe the BT formulations. The colony specimen of *B. thuringiensis* on culture medium and BT formulation samples were prepared by the method of Suzuki et al. [16]. Namely, each BT formulation was prepared by dissolving it

in ten times of solute water (DW).

The BT solutions were dropped onto a specimen stub, which a piece of double-side adhesive carbon tape had been attached. These specimens on the stub were then rapidly frozen using liquid nitrogen. The formulation samples were left until they are completely frozen and frost covered them (Fig. 4a). The stub was then attached to a specimen holder for use in the LV-SEM, and freeze-dried in the specimen chamber. As needed, samples were sputter-coated with Pt-Pd alloy with an ion sputter before SEM-observation (Fig. 1).

### Observation on the surface of BT formulation granules by electron microscope (Improved Suzuki method, Matsumoto et al., 2002b, in press)

A scanning electron microscope (JSM-5300LV, JEOL) was used to observe the sur-

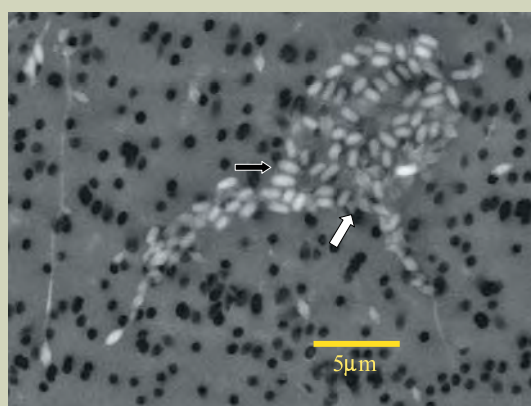


Fig. 2. Shape of the *aizawai* colony of *Bacillus thuringiensis* on a culture medium, spore and insecticidal crystal proteins (ICPs) obtained by Scanning Electron Microscope (SEM) (reflected wave). Specimen was applied for observed by low-vacuum SEM freeze drying method (Suzuki et al., 1996 : Fig.1).  
 ◼: spore; ◻: ICPs.

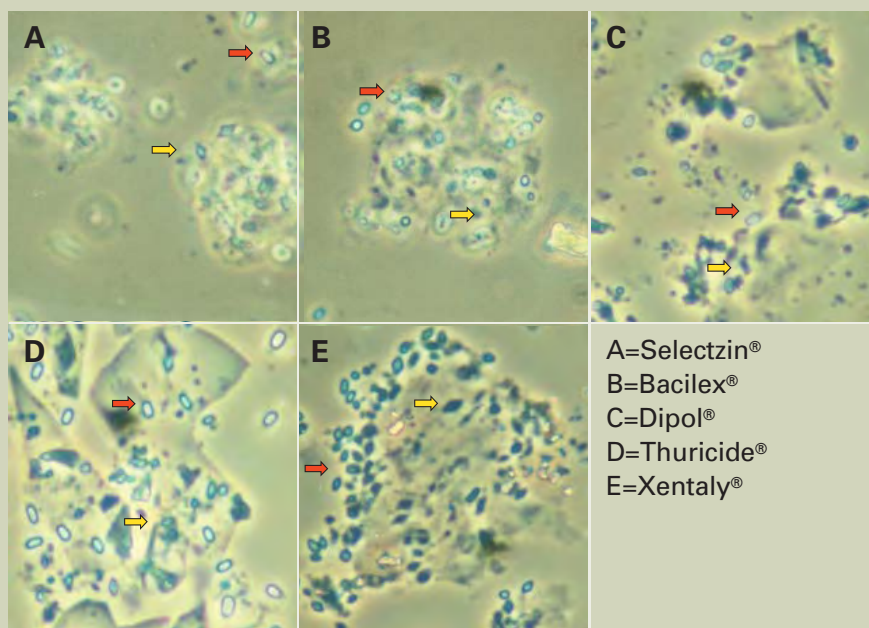


Fig. 3. Microscopic views of five formulations of *Bacillus thuringiensis* in water ( $\times 1000-1500$ ). Although spore and ICPs can be observed, discrimination of the respective BT formulations is impossible.  
 ◼: spore; ◻: ICPs.

face of the BT formulation granules. The specimens were prepared by the Improved Suzuki method [17]. Namely, each BT formulations were prepared as it is, but the dissolving step was omitted (see Fig. 5a).

### Analysis of BT formulation sample with LV-SEM/EDS

The studies on the electrolyte composition of BT granule surface have been attempted using SEM and energy dispersive X-ray analysis (EDS) based on Gould et al. [19]. An atomic element analyzer JED-2140 (JEOL) was used for this analysis. As the electron beam of SEM is exposed on samples and penetrated, it generates characteristic X-ray from the atoms in its path (Fig. 7; upper left). The EDS microanalysis system collects the X-ray, spots them by energy, and automatically identifies and labels the elements responsible for

the peaks in this energy distribution [20]. Scanning electron micrograph show the point X-ray analysis of BT formulation granules. EDS analyses of points A and B are provided in this figure (Fig. 7 upper right).

## Result

Suzuki Method was used at first to observe BT formulation samples simply and rapidly (Fig. 4a). One minute after the start of vacuum evacuation, it was possible to observe ice sublimation [16, 21]. BT spores and crystals, in the BT solution with cultivated specimen (with *B. thuringiensis* colony on medium) exposed during ice sublimation, appeared to be similar to observations by light microscope (Fig. 2 and Fig. 3). However, BT formulation samples and toxin proteins underwent obvious gelatins so we were unable to observe the

spores and crystals in the solution of BT formulation (Fig. 4b). This is like of gelation in protein solution (e.g. soybean 7S globulin [22]).

SEM observation of intact Bacilex® formulation granule revealed wall-like envelope on the surface of a normal active BT formulation (Improved Suzuki Method [17]) (Fig. 5a). Five kinds of BT formulations by the scanning electron micrographs are shown in Fig. 5b. In this method spores and crystalline protoxins were not observed as same as a light microscope, but the surface of BT formulation granules were observed without any collapses of surface on the granules (Fig. 5b, Fig. 6). This suggests the shapes of the granules are characteristic to BT formulations.

Scanning electron micrographs show the point X-ray analysis of BT formulation granules. EDS analyses of point A and B, respectively in Fig. 7 upper right. Recognition of individual components in the BT sample (e.g. Organic components (with C atoms; originated from BT  $\delta$ -endotoxins) and other additive inorganic components (with Si atoms; diatomaceous earth) patterns was simple (Fig. 4b) in visible and EDS permitted rapid identification of these component of BT samples observed (Fig. 7 lower).

## Discussion

Freeze-drying in a low-vacuum SEM has been found to be a method suited for observing the characteristic structures of commercial BT formulations. LV-SEM provided satisfactory results by the conventional methods in both the total images and microstructures of BT formulations (Fig. 5b). The most important point of this method is high preservation on BT granule surface of SEM specimens. Namely, quality of specimen was not influenced by the preparation procedure of each BT sample. Furthermore, the preparation procedure has the advantage that it drastically reduces labor and time required, because no dehydration process with a graded ethanol series is needed. All normal BT formulation has a steady characteristic surface on their granules in intact observation by LV-SEM (Fig. 5b). The surface of such BT granules is easily damaged by contraction or dissolution, especially during fixation with solutions or dehydration. Special care is needed; to avoid such damage, such specimens should be examined without troublesome processing as in the present study.

When checking BT formulations, it is essential to discriminate the target formulation and other formulations. Discrimination of BT formulations is needed for BT formulation quality control. With the advantage of this new method, it becomes possible to observe the microstructure and surface of BT formulation granules and small-sized granules which has so far been hard to observe without a LV-SEM. Namely, it was shown that by using this LV-SEM observation method, the possibility for discriminating the respective BT formulations was opened through obtaining the differences in structures on surfaces of BT formulation granules, which have fine and unique morphology.

In order to achieve much more detailed observation of BT granule surface structure, it is highly advisable to sputter-coat the specimen dried by the improved method, and then observe it at the high vacuum mode of a LV-SEM and by

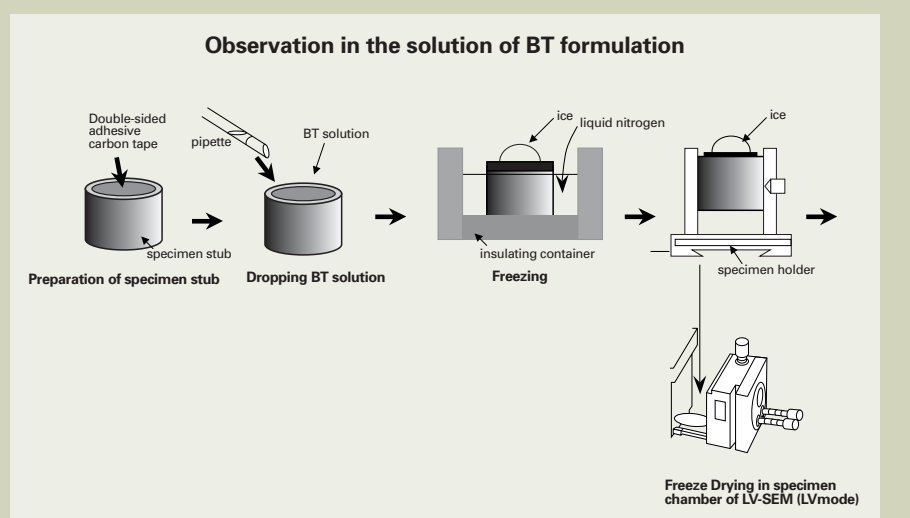


Fig. 4a. We show the procedure for specimen preparation when the LV-SEM observation of the specimen shown in Fig. 4b was performed. The method was applied to BT formulation by the method of Suzuki et al., (1995).

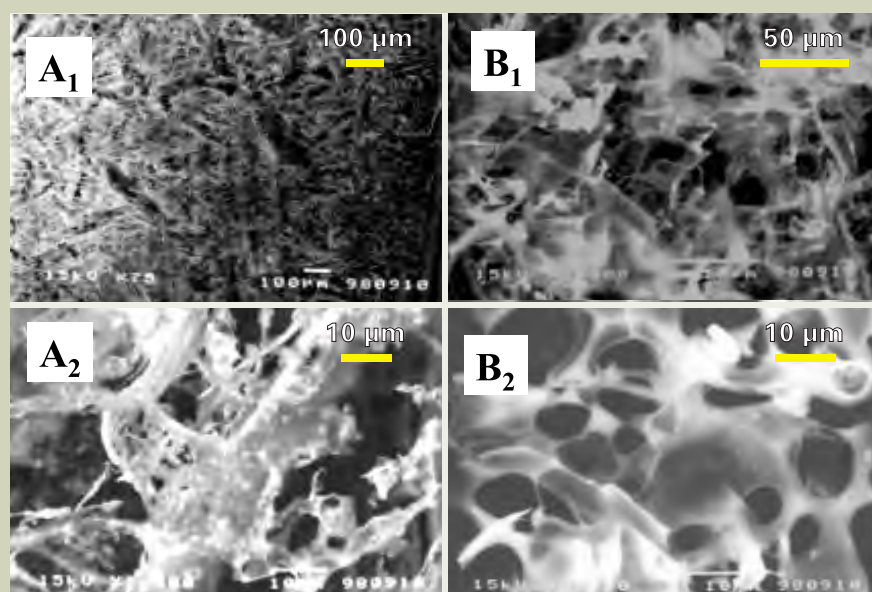


Fig. 4b. Scanning electron micrographs of BT formulations. A<sub>1</sub>: Selectzin®. A<sub>2</sub>: Same specimen with higher magnification. B<sub>1</sub>: Bacilex®. B<sub>2</sub>: Same specimen with higher magnification. In all BT solutions, unambiguous gelation occurs; thus, no spore and crystal protein are seen.

an atomic element analyzer (e.g. JSM-5410) (Fig. 7). BT  $\delta$ -endotoxin is a crystalline glycoprotein. Thereby, we tried to study more by the atomic element analyzer the components on surface of the formulation granules (Fig. 7 upper right). The result showed that the ratios of Carbon atoms (C) to Silicon atoms (Si) in different parts of BT granule are dramatic change (Fig. 7 lower). Namely, the large ratio of C to Si means that the BT granule includes much glycoprotein serving as active ingredients. And molecular component C amounts of the degraded BT sample have been rapidly decreased (Matsumoto, Data not shown). This method may applicable not only to discrimination of commercial formulations, but also to use for quality check of them (e.g. active degradation of BT after long-term storages) [17].

The new method can be useful not only for observing BT to discriminate but also detec-

tion of degradation in BT formulations. The mechanisms of deterioration of BT are still not completely elucidated. Further study on the mechanisms of inhibition and deterioration of the BT insecticidal activity are needed.

## Acknowledgements

The author would like to express heartfelt thanks to Professor Dr. Y. Kono, Assistant professor Dr. H. Honda (University of Tsukuba), and Dr. K. Nagata (RIKEN) and K. Takagi (JEOL). We are deeply indebted to Dr. D. Taylor (University of Tsukuba) for his critically reading of the manuscript.

## References

1. Angus, T. A.: Similarity of effect of valinomycin and *Bacillus thuringiensis* parasporal protein in larvae of *Bombyx mori*. *J. Invert. Pathol.*, **11**, 145-146 (1968).

2. Skovmand, O., I. Thiéry and G. Benzon.: Is *Bacillus thuringiensis* standardization still possible? Update and improvement of Bt titration over 20 years. J.-F. Charles et al., (eds.), *Entomopathogenic Bacteria: From Laboratory to Field Application.*, Kluwer Academic Publishers, Netherland, 275-295 (2000).

3. Bonnefoi, A., A. Burgerjon and P. Grison.: Titration biologique des préparations de spores de *Bacillus thuringiensis*. *C. R. Acad. Sci.*, **27**, 1418-1420 (1958).

4. Burgerjen, A. and H. Dulmarge.: Industrial and international standardization of microbial pesticides-1. *Bacillus thuringiensis*. *Entomophaga.*, **22**, 121-129 (1977).

5. Aizawa, K.: Proceedings of the first International Colloquium (colloquy) on Invertebrate Pathology and IX th Annual Meeting, *Society for Invertebrate pathology*. Queen's University at Kingston,

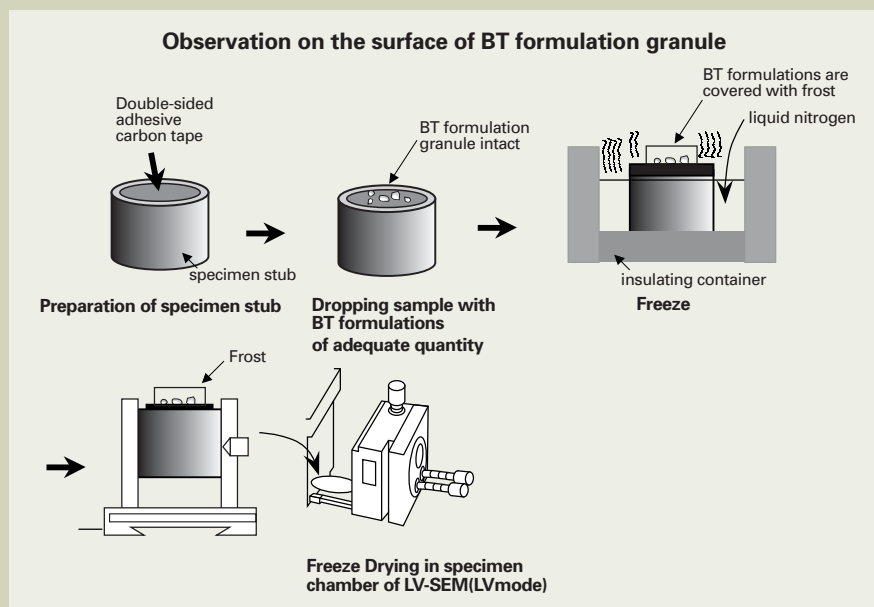


Fig. 5a. We show the procedure for specimen preparation when the LV-SEM observation of the five BT formulation granules shown in Fig. 5b was performed. Improved Suzuki method (2002b, Matsumoto et al, *in press*), which was reviewed by the method of Suzuki et al., (1995), (Fig. 1).

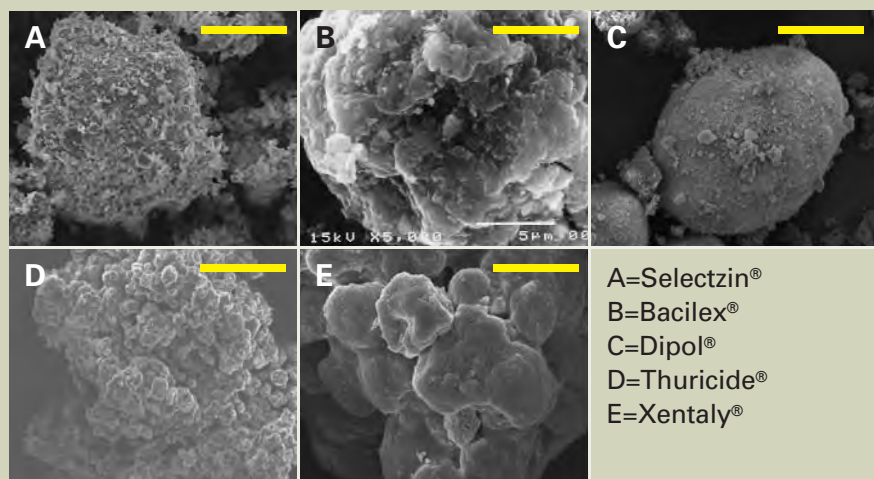


Fig. 5b. LV-SEM views of five formulation granules of *Bacillus thuringiensis* by the new method by the Improved Suzuki method (Matsumoto et al, 2002b, *in press*) ( $\times 5000$ ).  $\text{—|—}$  5  $\mu\text{m}$

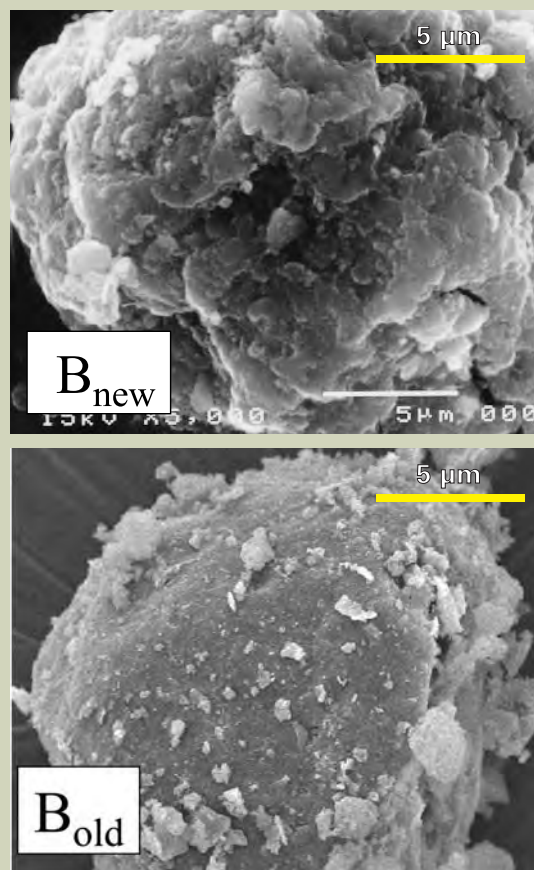


Fig. 6. Scanning electron micrographs of outer surface of envelope at a higher magnification ( $\times 5000$ ), showing the wall-like envelope. Scale bars = 5  $\mu\text{m}$ . Comparison of scanning electron micrographic observations of the granule surfaces of BT powders.  $B_{\text{new}}$  means new sample. And  $B_{\text{old}}$  means the old sample with degradation (Bacilex®, Fig. 5b-B) after 21 years preservation at 5°C under dark conditions.

Canada., pp. 59-272 (1976).

6. Matsumoto N.: Inhibition effect of propionates on the insecticidal activity of BT (*Bacillus thuringiensis*) formulations. *J. Seric. Sci. Jpn.*, **68**, 333-338 (1999) (in Japanese with English summary).
7. Okada, T., Imamura, K., Matsutani, S. and H. Sone.: Effect of the particle size of mulberry leaf powder in an artificial diet on the potency of formulation of *Bacillus thuringiensis*. *Bull. ACIS.*, **17**, 28-33 (1977) (in Japanese with English summary).
8. Asano, S., Iwasa, T. and A. Seki.: Silkworm Assay for *Bacillus thuringiensis* formulations using diet incorporation methods: (1) Evaluation Based on larval mortality. *J. Appl. Entomol. Zool.*, **41**, 187-194 (1997) (in Japanese with English summary).
9. Matsumoto N.: Effect of three soybean meals on the insecticidal activity of *Bacillus thuringiensis* formulation. *Jpn. J. Appl. Entomol. Zool.*, **44**, 113-118 (2000) (in Japanese with English summary).
10. Matsumoto, N.: Effect of light condition on the insecticidal activity of BT (*Bacillus thuringiensis*) formulations to the silkworm, *Bombyx mori* (L.). *Appl. Entomol. Zool.*, **36**, 373-376 (2001).
11. Tsuchiyama, A.: Bioassay of *B. thuringiensis* formulation using larvae of Diamondback Moth, *Plutella xylostella* L. *Jpn. J. Appl. Entomol. Zool.*, **22**, 234-237 (1978) (in Japanese with English summary).
12. Nishitsutsuji-Uo, J. and Y. Endo.: Mode of action of *Bacillus thuringiensis*  $\delta$ -endotoxin: Relative roles of spores and crystals in toxicity to *Pieris*, *Lymantria* and *Ephestia* larvae. *Appl. Entomol. Zool.*, **15**, 416-424 (1980).

13. Ishiguro, T. and M. Miyasono.: A Bioassay for toxicity of *Bacillus thuringiensis* insecticide using the force-feeding method applied to the Silkworm, *Bombyx mori* L. *Jpn. J. Appl. Entomol. Zool.*, **23**, 141-150 (1979) (in Japanese with English summary).
14. Asano, S. and N. Suzuki.: Bioassays of *Bacillus thuringiensis* formulation using diet incorporation methods with Common cutworm, *Spodoptera litura* (Lepidoptera: Noctuidae). *Jpn. J. Appl. Entomol. Zool.*, **39**, 135-141 (1995) (in Japanese with English summary).
15. Heimpel, A. M. (1967) A critical review of *Bacillus thuringiensis* var. *thuringiensis* Berliner and other crystalliferous bacteria. *Ann. Rev. Entomol.*, **12**, 287-322.
16. Suzuki, T., M. Shibata, K. Tanaka, K. Tsuchida and et al.: A new drying method: Low-vacuum SEM freeze drying and its application to plankton observation. *Bul. Plankton Soc. Jpn.*, **42**, 53-62 (1995).
17. Matsumoto, N. and T. Suzuki. An efficient assay of *Bacillus thuringiensis* by Low-vacuum SEM freeze drying. *J. Pesticide Science (in press)*, (2002b).
18. Matsumoto, N.: *In vivo* inhibitory effect of carbonic anhydrase on the insecticidal activity of *Bacillus thuringiensis*. *J. Insect Biotechnol. Sericol.*, **71**, 65-67 (2002a).
19. Gould K. G., D. E. Martin and C. E. Graham.: *Scanning electron Microscopy/1976* (Part VI). Proceedings of workshop on SEM in reproductive biology IIT Reserch Institute Cicago, Illinois., 335-341 (1976).
20. Shinno I. and K. Ishida.: Quantitative electron microprobe analysis of silicates and sulfides using energy-dispersive X-ray spectrometry. *The report on earth science, department of general education, Kyushu university.*, **23**, 25-33 (1983) (in Japanese with English summary).
21. Suzuki, J., I. Murata, R. Murata, S. Morozumi and T. Suzuki.: A method for identification of *Cryptosporidium parvum* from river water using Low-Vacuum SEM. *Jpn. J. Microbiol.*, **14**, 187-191 (1998) (in Japanese with English summary).
22. Ishino, K. and S. Kudo.: Conformational transition of alkali-denatured soybean 7s and 11s globulins by ethanol. *Agric. Biol. Chem.*, **44**, 537-543 (1980).

#### Analysis of BT formulation sample with LV-SEM/EDS

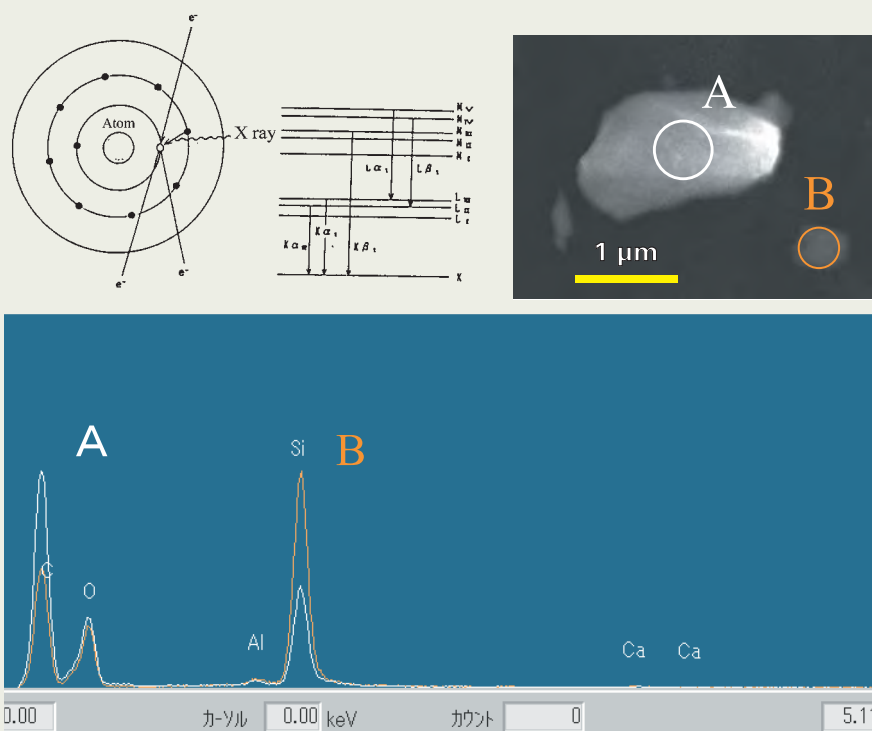


Fig. 7. The micrograph at the upper right of Fig. 7 shows a granule formed after a BT formulation was dissolved. Points A and B in the micrograph are analysis points where element analysis was performed using the EDS. We presume that the reason why the EDS signal from carbon was strong at point A is due to the granule at point A being large and ICP (insecticidal crystal proteins), an insecticidal component of the BT formation, remaining on the surface in abundance. In contrast, we consider that the reason why the signal of silicon (from a diatom), which is used as an additive to BT formulations, was stronger at point B than the carbon signal is probably due to point B being in an area consisting of residual components where ICP was completely dissolved out.

Figure 1, 4a and 5a are excerpts from Bulletin of the Plankton Society of Japan, Vol. 42, Separate volume 1, 1995 by Toda, T., Department of Bioengineering, Faculty of Engineering, Soka University.

# Observations of Algae and Their Floc in Water Using Low-Vacuum SEM and EDS

Hiroshi Konno<sup>†</sup>, Takeo Suzuki<sup>\*\*</sup>, Masato Mizushiri<sup>†</sup> and Hideharu Kashiwakura<sup>†</sup>

<sup>†</sup>Department of Civil Engineering, Tohoku Institute of Technology

<sup>\*\*</sup>Electron Optics Division, JEOL Ltd.

Algae and their floc and the effects of chlorine treatment were observed using SEM and EDS. These observations revealed that ① samples like algae and their floc can be held firmly by making the SEM pore filter surface adhesive using poly-L-ricin, ② chlorine treatment causes cracks in the end and center of *Nitzschia*, allowing observation of how the entire surface is fractured, though morphological changes with the number of days of culturing algae are not known exactly, and ③ the floc of two types of coagulants-aluminum sulfate and ferric chloride- is taken into suspending hydroxide and turned into an aggregate of silica and phosphorus in water, combined with aluminum (or iron) in the coagulant and algae, in addition to carbon and oxygen.

## Introduction

Humankind have been using water in their daily life and have gradually increased this consumption volume over many years. Now, this volume has reached a great extent, close to the limitation on water capacity. We can say that humankind have been taking advantage of the potential power of water. In that sense, they have enhanced the utility value of water, but the use of water by humankind is only momentary when viewed from the standpoint of the water circulating cycle that will last for an indefinite time. Humankind have been using water by borrowing it temporarily from nature. If they cannot stop discharging entropy into water [1] through their social activities, then they have to regenerate water, in particular, water quality. Here arises the need of wastewater treatment and water purifying techniques for utilization of water.

Activities of humankind in daily life have increased and discarded entropy, which has directly or indirectly given rise to a wide variety of substances with diversified types and concentrations, including suspended substances, melting substances, organic substances, organisms, toxic substances, viruses, and furthermore, those substances at molecular level. In recent years, the progress in the environment measurement technology has revealed new substances, which have been unknown to us and have to be eliminated from the earth. These include combined products that contaminate the environment and man-made substances that have not existed in nature. These environmental contaminants are increasingly drawing our attention as serious obstacles to the earth.

Here lies an indispensable need for conservation of water environment and research on water purification treatment. These tasks are part of risk assessment and risk management for the earth environment. We must continue monitoring, locating their

sources and determining the amount, while conserving water environment and continuing use of water by using wastewater treatment and water purifying techniques.

However, more serious and important issues are the assessment and management of aquatic biota, which is more complex than aquatic inorganic substances and of which unknown field is expanding. Aquatic plankton had existed in water before humankind lived on the earth and should have been able to coexist with humankind that utilized water. However, it so happened that aquatic plankton stank and produced toxic substances. Whether or not such a cycle is attributed to the result of life struggle in nature will be clarified by biological research sooner or later, but such a process is deemed a sort of risk. The elucidation of the mechanism and development of techniques related to this mechanism are awaited.

Water purification treatment is greatly affected by the existence of algae when the water supply source is eutrophic. They include coagulation interference [2-7], abnormal smell/taste, filter clogging [8-15], toxic substances, residue of soluble metals [3, 9], and generation of trihalomethane (THM). Algae are often pretreated with chlorine for the reason that coagulation treatment is not easy, but its treatment is limited by generation of THM. There are several reports that chlorine treatment improves the sedimentation of algae, but this reported method is not regarded good, in terms of the improvement of coagulation. On the other hand, there is no report about how the algae treated with chlorine will change. According to comparative experiments of aluminum-based coagulant and iron-based coagulant about the generation of algae floc, it is reported that aluminum-based coagulant is better than iron-based coagulant.

In this paper, we discuss the coagulation mechanism of algae based on the observations of algae and their floc formed by two types of coagulant, using a scanning electron microscope (SEM) and an energy dispersive X-ray spectrometer (EDS). Also, the results of our examinations, which cover how the

cells of algae are fractured and how the algae change morphologically in the multiplication period, are discussed.

## Cultivation of Algae, Experimenting Conditions, and Method of Sample Preparation

### Cultivation of algae and experimenting conditions

Algae were collected from Lake Kamafusa, Miyagi Prefecture, Japan, using plankton net. They were concentrated by a centrifugal separator and then were isolated in agar medium. The medium used for isolation was *Nitzschia* of algae, and BG-11 was used as medium, except for EDTA. Cultivation conditions were 18°C and 2000 Lx [7]. Coagulants used in examining the algae floc were aluminum sulfate as aluminum-based coagulant and ferric chloride as iron-based coagulant. The coagulation conditions were such that pH was 7.0, alkalinity was 50 mg/L and the coagulant was 12 mg/L at each concentration of aluminum and iron. Incidentally, the chlorine demand of the raw water was 0.2 mg/L.

### Method of preparing sample t-butyl alcohol freeze-drying method

While the critical point drying method is conducted at a pressure of about 100 atm using liquefied carbon dioxide, the conventional freeze-drying method has some disadvantages. That is, it takes time because it freezes a sample containing solution with liquid nitrogen and then is left in a high vacuum ( $10^{-4}$  Pa or less) for several to several tens of hours, while being kept at a cryogenic temperature of 80K to 190K. As a result, the sample may be adversely affected by cryohydrate when frozen. However, the t-butyl alcohol freeze-drying method, in which the freezing temperature of t-butyl alcohol is high, has become popular as a method that permits drying at a temperature relatively close to

<sup>†</sup>35-1 Yagiyama-Kasumicho, Taihaku-ku, Sendai, Miyagi, 982-8577, Japan

<sup>†</sup>E-mail: hkonno@tohotech.ac.jp

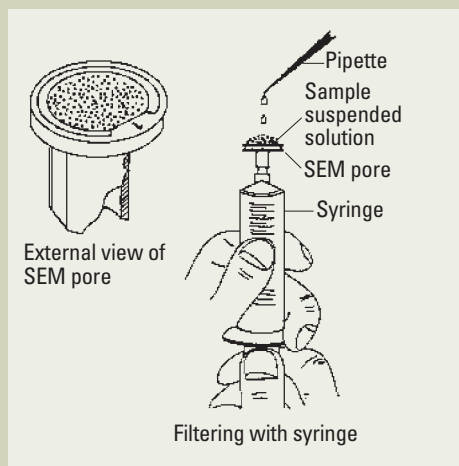


Fig. 1. SEM pore filter and sampling.

Table 1 Procedure for preparing the sample for SEM	
1	Set the SEM pore filter to the syringe
2	Drop poly-L-ricin over the entire surface of the filter (0.1 w/v%) and allow it to stay on the filter for one minute
3	After the sample is left for one minute, poly-L-ricin (0.1 w/v%) is injected to the sample, and it is left for two minutes
4	Place a sample on the SEM pore filter, and aspirate unnecessary substances using a syringe
5	Clean the SEM pore filter top surface with distilled water
6	Introduce t-butyl alcohol onto the SEM pore filter
7	Leave the sample with the SEM pore filter set in position
8	Remove the SEM pore filter from the syringe
9	Place the sample on the special-purpose sample stage and freeze-dry it

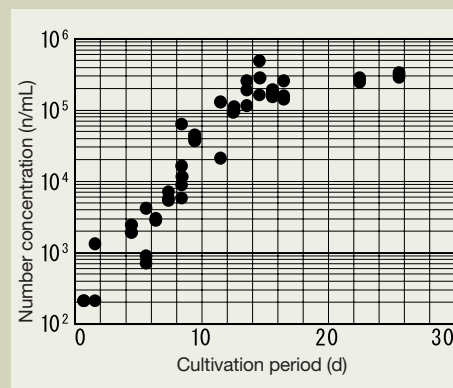


Fig. 2. Cultivation curve of *Nitzschia*.

room temperature within a short time.

A fixed, dehydrated sample is substituted in t-butyl alcohol and is placed on the sample stage of a freeze-drying unit, then the stage temperature is lowered to about 5°C (or may be left in a refrigerator for several tens of minutes). When t-butyl alcohol is frozen, water is discharged by using a vacuum pump to sublimate frozen t-butyl alcohol. When sublimation is completed and pressure starts lowering abruptly, the stage temperature is restored to room temperature, thereby a dry sample being completed with restoration of atmospheric pressure.

### SEM pore

The SEM pore is mounted on the sample stage to filter and trap particles floating in liquid. It is a polycarbonate milli-pore filter (10 μm thick, 0.6 μm pore diameter) supported with a hard conductive resin frame and is attached to a syringe when used for aspiration. It can trap particles in liquid effectively within a short time. Also the special-purpose adapter for the SEM pore allows the SEM pore to be easily installed on the sample holder. (Fig. 1)

### Preparation of sample for SEM

Table 1 shows the procedure for preparing the sample for SEM. First, a syringe was set to the SEM pore filter, the sample was fixed, and poly-L-ricin (0.1 w/v%) was injected to the sample, and the sample was left for two minutes.

If the sample were not prepared in this way, the sample would have been scattered into air when the sample chamber was in vacuum after injecting coagulant to observe the algae floc.

Then, the sample was placed on the SEM pore filter to absorb moisture. Distilled water was dropped to clean the sample with the SEM pore filter, then t-butyl alcohol was introduced onto the SEM pore filter to immerse the sample in it. Upon completion of the process above, the SEM pore filter was removed from the syringe, and it was set on the special-purpose sample stage, then it was freeze-dried with liquid nitrogen. The sample was set in the SEM within 15 seconds after freeze-drying, and observation was made in the low

vacuum (LV) mode.

## Algae *Nitzschia* and Changes in Shape with Number of Culturing Days

In this study, we used a JEOL low-vacuum scanning electron microscope (LV-SEM). It permits observation of a sample freeze-dried with liquid nitrogen simply by sublimating moisture in low vacuum without complex pretreatment nor coating the sample with platinum.

Figure 2 shows the cultivation curve of *Nitzschia*. *Nitzschia* enters a logarithmic multiplication period, when the multiplication rate is high, about one week after starting cultivation, followed by a static period when concentration is constant, and reaches the extinction period when the number concentration decreases about four weeks later.

Figures 3(a) to 3(g) show the results of observations of algae *Nitzschia* using an LV-SEM with elapse of cultivation days. Although distinctive changes in the shape of *Nitzschia* are not observed, portions that look partially dense depending on the length of cultivation period can be observed sometimes distinctively and sometimes not distinctively. Changes depending on the length of cultivation period could not be identified on the micrographs.

Figures 4(b) and 4(c) show the results of EDS analysis of Fig. 4(a) of algae *Nitzschia* that was taken several tens of days later. It can be seen that the surface material of *Nitzschia* is covered with silica peculiar to algae. It seems that in this period, a large portion often looks white on the photograph as if the cell interior has been condensed. Analysis of element distribution by EDS strongly suggests that it is the distribution of phosphorus. Assuming that the portion is an aggregate of phosphorus, it can be identified as a cell nucleus. In this portion, the activity of algae is high depending on the length of cultivation period and cell division takes place actively when it is frequently observed. But when the number of algae, in which cell

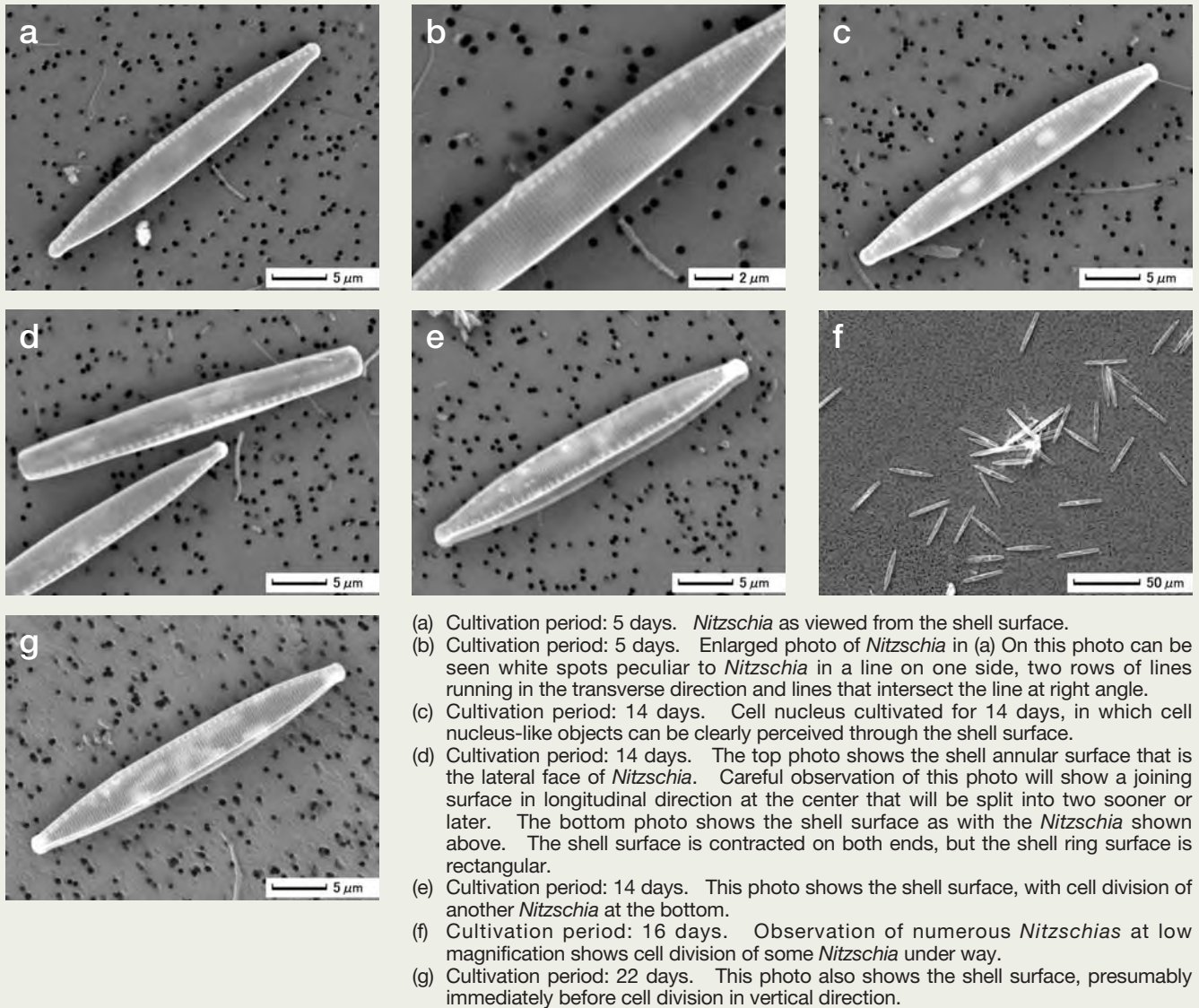
nucleus is not clearly observed, the activity lowers. Also, the number concentration does not increase, and that of algae only with shell increases. However, the cell division of this type of algae takes place separately as if the upper half and lower half of a box come apart. It is said that the cell nucleus is divided before cell division takes place, so that the biological activity of algae cannot always be evaluated by whether cell nucleus can be observed well or not.

In addition, observations of algae using an LV-SEM revealed that the size of *Nitzschia* that could be separated in the observation of algae was 20 to 30 μm, but the conditions of *Nitzschia* in each cultivation period could not be characterized by shape or other information.

## Changes in Shape and Other Parameters of Algae by Chlorine Treatment

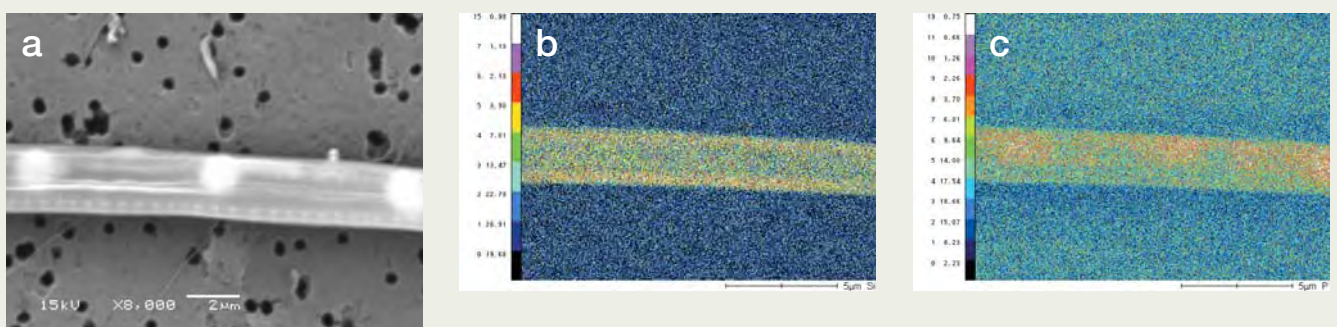
In this study, we conducted chlorine treatment of normal *Nitzschia* and observed how the algae change morphologically. We used sodium hypochlorite solution as chlorine. To prepare sample before injecting chlorine, we placed a sample on the SEM pore filter according to the ordinary sample preparation process and then injected chlorine onto the filter with adequate care not to allow the surface to dry. The concentration of chlorine at this time was 10 mg/L. Then, we left the sample for 60 minutes while taking care not to allow it to dry up. In the meantime, the filter was kept covered with chlorine. Then the sample was cleaned in the same manner as in ordinary sample preparation, and freeze-dried, then observed in low vacuum. Figure 3(a) shows needle algae *Nitzschia* on the fifth day after start of cultivation. We observed how chlorine treatment changed it morphologically from this standard form.

Figures 5(a) to 5(e) show the results. It was made clear that injection of chlorine causes cracks in the end and center, and that it differs widely from the ordinary *Nitzschia*. Thus, the cells of algae that had been treated with chlorine was fractured and the glassy portion was crushed later or simultaneously



- (a) Cultivation period: 5 days. *Nitzschia* as viewed from the shell surface.
- (b) Cultivation period: 5 days. Enlarged photo of *Nitzschia* in (a) On this photo can be seen white spots peculiar to *Nitzschia* in a line on one side, two rows of lines running in the transverse direction and lines that intersect the line at right angle.
- (c) Cultivation period: 14 days. Cell nucleus cultivated for 14 days, in which cell nucleus-like objects can be clearly perceived through the shell surface.
- (d) Cultivation period: 14 days. The top photo shows the shell annular surface that is the lateral face of *Nitzschia*. Careful observation of this photo will show a joining surface in longitudinal direction at the center that will be split into two sooner or later. The bottom photo shows the shell surface as with the *Nitzschia* shown above. The shell surface is contracted on both ends, but the shell ring surface is rectangular.
- (e) Cultivation period: 14 days. This photo shows the shell surface, with cell division of another *Nitzschia* at the bottom.
- (f) Cultivation period: 16 days. Observation of numerous *Nitzschias* at low magnification shows cell division of some *Nitzschias* under way.
- (g) Cultivation period: 22 days. This photo also shows the shell surface, presumably immediately before cell division in vertical direction.

Fig. 3. *Nitzschia* (LV-SEM observation).



- (a) This photo shows the shell annular surface. What element the *Nitzschia* and the white object represent on the photo is yet to be examined.
- (b) Silica distribution. EDS detected silica and phosphorus as well as carbon and oxygen with exceedingly high concentration. This photo shows the elemental distribution of silica, which indicates that the surface of *Nitzschia* is covered with silica peculiar to algae.
- (c) Phosphorus distribution. This photo shows the elemental distribution of phosphorus. Aggregation of phosphorus in the white, round portion suggests that the central portion like the cell shell of algae exists in this white portion.

Fig. 4. *Nitzschia* (LV-SEM observation and EDS analysis).

with it, losing its original shape. Even if shells remained after the cells had been fractured, they cannot be identified as algae after elapse of a certain period of time. Thus, we may say that chlorine treatment destroys shells like hyalin of algae considerably, leaving no form of algae.

## Observation of Algae Floc

### Aluminum-based coagulant

As mentioned earlier, coagulation conditions were such that pH was 7.0 and alkalinity was 50 mg/L. 12 mg/L of aluminum sulfate was injected as coagulant and the floc was prepared for observation after two minutes of quick agitation with a jar tester, followed by slow agitation for 15 minutes, as shown in Table 2.

Figures 6(a), 6(b) and 6(c) show the SEM micrographs of aluminum sulfate floc. These photos show how some of the algae *Nitzschia* are taken into whitish suspended matter and that 20 to 30µm *Nitzschia* aggregate to form a block. The field-of-view of the micrograph is about 200 × 300 µm, but the floc appears much larger than this.

This was analyzed by the energy dispersive X-ray spectrometer (EDS). It can measure X-rays generated from the sample surface by acquiring them using a semiconductor detector and converting them into electrical signals, thus analyzing constituent elements of the sample from the area displayed on the entire screen of an SEM image. The elemental-distribution display function includes elemental distribution and elemental mapping.

Elemental distribution is to display the intensity counts (concentrations) of each element as peak. Element map, which is obtained by elemental mapping, displays the respective constituent elements separately and quantitatively, by selecting the peaks of the respective elements. Element map is color-displayed, where a portion that contains elements in high concentration can be seen by the comparison of the relative changes in colors presented in each element map. The color order is black, blue, green, yellow, red, and white. Black indicates the lowest concentration region and white is the highest in the map.

EDS analysis shows that elements that are shown distinctively on the SEM micrograph are aluminum, silica, phosphorus, etc. in addition to carbon and oxygen.

Figure 7(a) shows an SEM micrograph, on which the element map shows silica and aluminum. This micrograph shows that the higher the intensity of white, the higher the concentration of the constituent element, while Fig. 7(b) suggests that silica is adsorbed to the floc portion though *Nitzschia* contains much silica, as a matter of course. This can be considered the silicon contained in the culture medium. Comparison of aluminum in Fig. 7(c) and the elemental distribution of phosphorus in Fig. 7(d) show high distribution in nearly the same position, and the white portion in Fig. 7(a) is the aluminum hydroxide, which is a phenomenon of phosphorus in the culture medium being adsorbed by it. It is well known that phosphorus is adsorbed to the floc and undergoes coprecipitation. This is a

good proof that indicates its coprecipitation.

### Iron-based coagulant

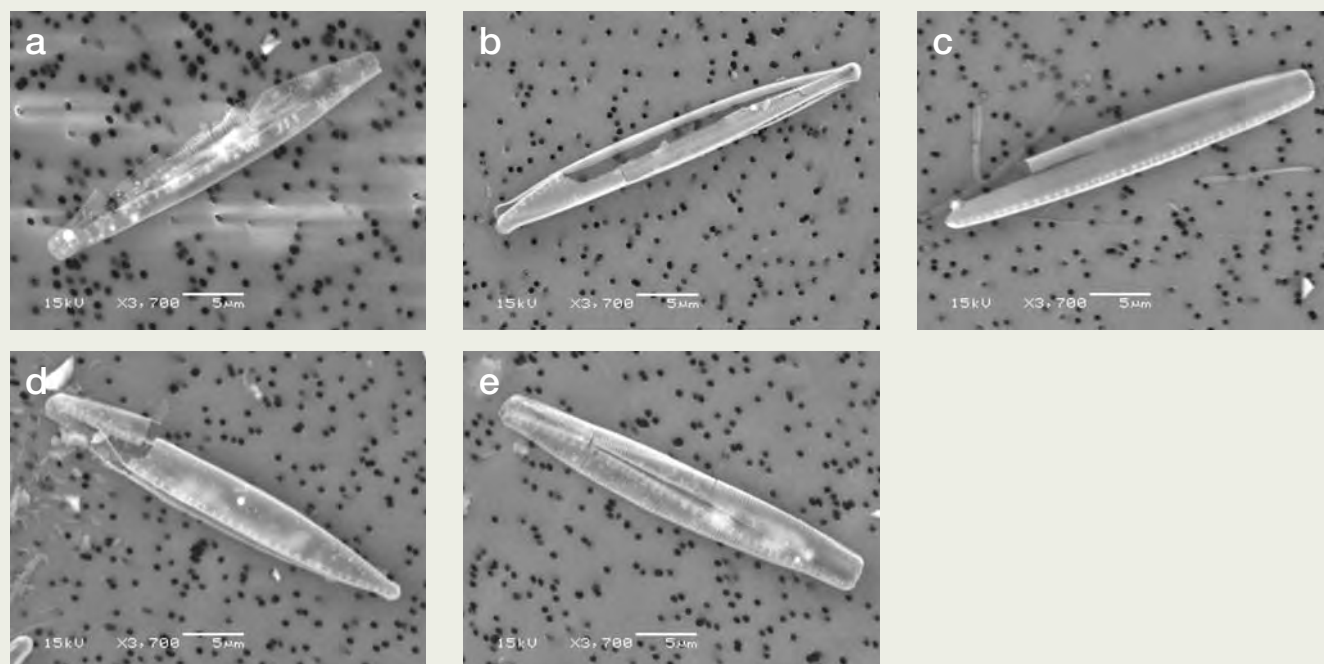
Figures 8(a), 8(b) and 8(c) are the SEM micrographs of ferric chloride floc. It can be assumed that as seen in the case of aluminum sulfate, numerous algae *Nitzschia* acquired into suspended component constitute a floc. EDS analysis of this sample in these micrographs display distinctive elements, and high concentration of silica, phosphorus, iron and calcium are detected, in addition to carbon and oxygen.

Figures 9(a), 9(b), 9(c) and 9(d), which show the SEM micrographs of the floc, reveal the same fact as seen in the case of aluminum sulfate. That is, by observing a series of element maps (silica, iron, phosphorus), it can be found that numerous *Nitzschia* of algae is acquired into ferric hydroxide floc and a new floc that is seemed to be strong is formed, and that phosphorus is strongly adsorbed to the ferric hydroxide floc and will undergo coprecipitation.

## Conclusion

Algae, floc and the effects of chlorine treatment were observed by means of SEM imaging and EDS analysis.

- The analysis results revealed the following:
- 1) In SEM observation, samples like algae floc can be supported firmly by making the SEM pore filter surface adhesive using poly-L-ricin.
  - 2) Chlorine treatment causes cracks in the end and center of *Nitzschia* and destroys cells,



- (a) This photo shows the state where cells and shell surface were fractured by chlorine treatment.
- (b) This photo shows that chlorine treatment fractured cells in the direction of shell annular surface.
- (c) This photo shows how chlorine treatment causes cracks in the shell surface of glass.
- (d) This photo shows how chlorine treatment caused cracks in the glassy shell surface in the transverse direction.
- (e) This photo shows how chlorine treatment caused cracks in the shell annular surface in the transverse direction.

Fig. 5. *Nitzschia* subjected to chlorine treatment (LV-SEM observation).

allowing easy observation of how the shell surface and shell annular surface are fractured.

- 3) The flocs of two types of coagulant - aluminum sulfate and ferric chloride - are acquired into suspended hydroxide, and are turned into an aggregate of silica and phosphorus in water that is combined with coagulant aluminum (or iron) and algae, as well as carbon and oxygen. This could be observed well.

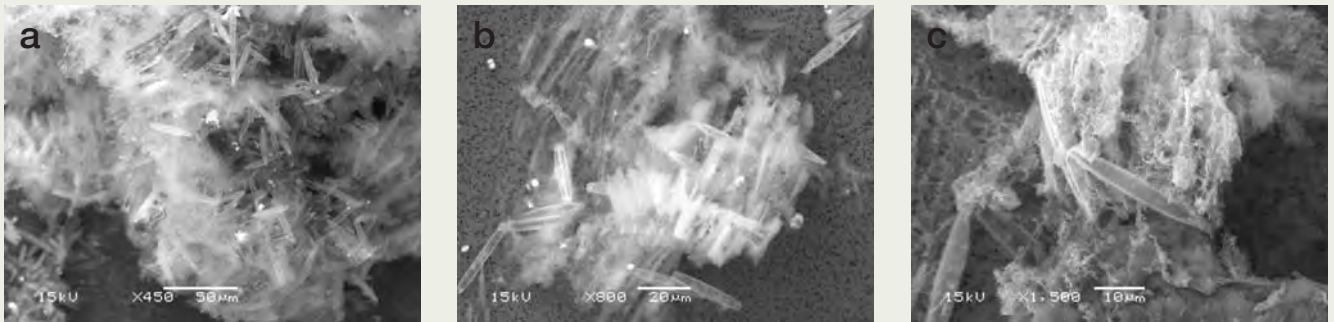
These observations greatly contributed to the clarification of the mechanisms of coagulation treatment and chlorine treatment of algae. This means that such techniques can

greatly contribute to the clarification of these phenomena. We will continue further study of these mechanisms.

## References

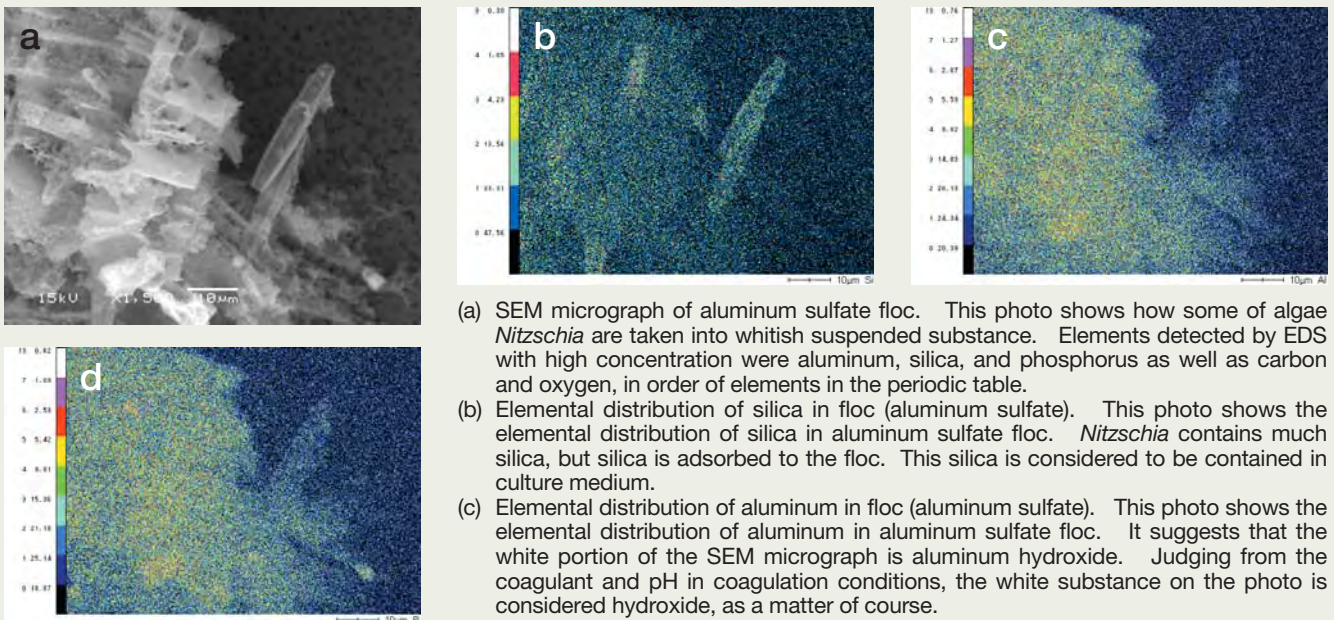
1. Asano T and Tambo N (supervising editors): Mizukankyo no kougaku to sairyou, Hokkaido University Academic Publishers, 1999.
2. Astride, V.: Advanced Coagulation of Natural Organic Matter Mechanism of Interaction between NOM and Al and Fe. AWWA Annu. Conf., pp. 403-412, 1997.

3. Okamoto R: Study on remaining of soluble iron of coagulant and influence of organic substances, Master's thesis for Tohoku Institute of Technology, 2001.
4. Bernhardt, H., Schell, H. and Hoyer, O.: Influence of algal organic substances on flocculation and filtration, WISA, 1, pp. 41-57, 1991.
5. Bernhardt, H., Hoyer, O., Lusse, B. and Schell, H.: Investigation of algal born organic substances and their effects on water treatment, Proceedings of the Japanese-German Workshop on Waste Water and Sludge Treatment, pp. 583-637, 1982.
6. Mitachi K: Effects of Aggregation



- (a) *Nitzschia* floc by coagulant (aluminum sulfate). This photo clearly shows how *Nitzschia* of 20 to 30 μm aggregates into a floc. The field-of-view of the entire photo is about 200 x 300 μm. The size of the floc greatly exceeds this field-of-view.
- (b) It appears that the *Nitzschia* floc by coagulant (aluminum sulfate) is bonded very firmly.
- (c) Floc by coagulant (aluminum sulfate). This photo clearly shows that aluminum hydroxide acts as a bridge between *Nitzschia* assuming that the white portion is aluminum hydroxide.

Fig. 6. *Nitzschia* floc by coagulant (aluminum sulfate). (LV-SEM observation)



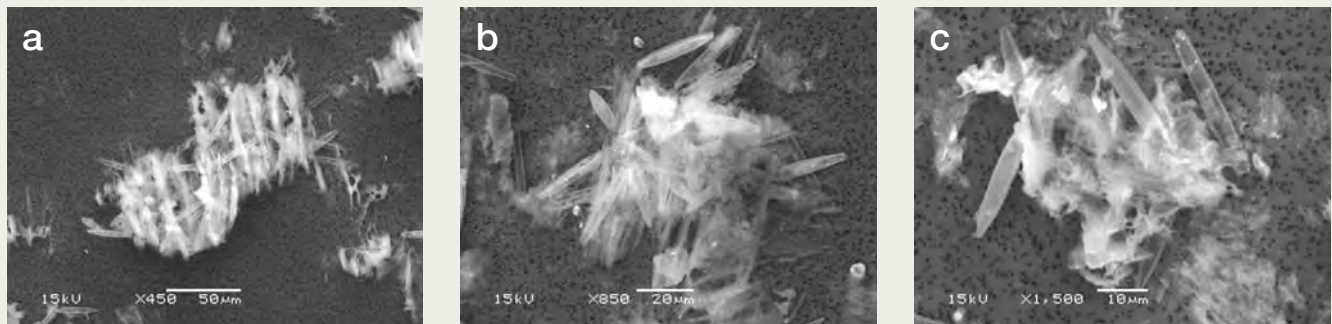
- (a) SEM micrograph of aluminum sulfate floc. This photo shows how some of algae *Nitzschia* are taken into whitish suspended substance. Elements detected by EDS with high concentration were aluminum, silica, and phosphorus as well as carbon and oxygen, in order of elements in the periodic table.
- (b) Elemental distribution of silica in floc (aluminum sulfate). This photo shows the elemental distribution of silica in aluminum sulfate floc. *Nitzschia* contains much silica, but silica is adsorbed to the floc. This silica is considered to be contained in culture medium.
- (c) Elemental distribution of aluminum in floc (aluminum sulfate). This photo shows the elemental distribution of aluminum in aluminum sulfate floc. It suggests that the white portion of the SEM micrograph is aluminum hydroxide. Judging from the coagulant and pH in coagulation conditions, the white substance on the photo is considered hydroxide, as a matter of course.
- (d) Elemental distribution of phosphorus in floc (aluminum sulfate). This photo shows the elemental distribution of phosphorus in aluminum sulfate floc. Comparison of phosphorus and aluminum shows that there are distributions in nearly the same position. This is a phenomenon of phosphorus in the culture medium being adsorbed to the floc. This photo shows a good example of the well-known phenomenon that the phosphorus is adsorbed to the floc and underwent coprecipitation.

Fig. 7. Aluminum sulfate floc (LV-SEM observation and EDS analysis)

- conditions on the formation of soluble aluminum, Master's thesis for Tohoku Institute of Technology, 2001.
7. Iino S: Study on flocculation of slender type diatoms and influence of algal organic substances, Master's thesis for Tohoku Institute of Technology, 1998.
  8. Konno H *et al*: Characteristics of deposit in filter using model materials for slender type diatoms and effective parameters to clogging of rapid sand filter, *Proc. of Environmental Engineering Research*, vol. 31, pp. 11-18, 1994.
  9. Konno H *et al*: Influence of ratio of grain size of filter to length of slender type diatoms on deposit in rapid sand filter,

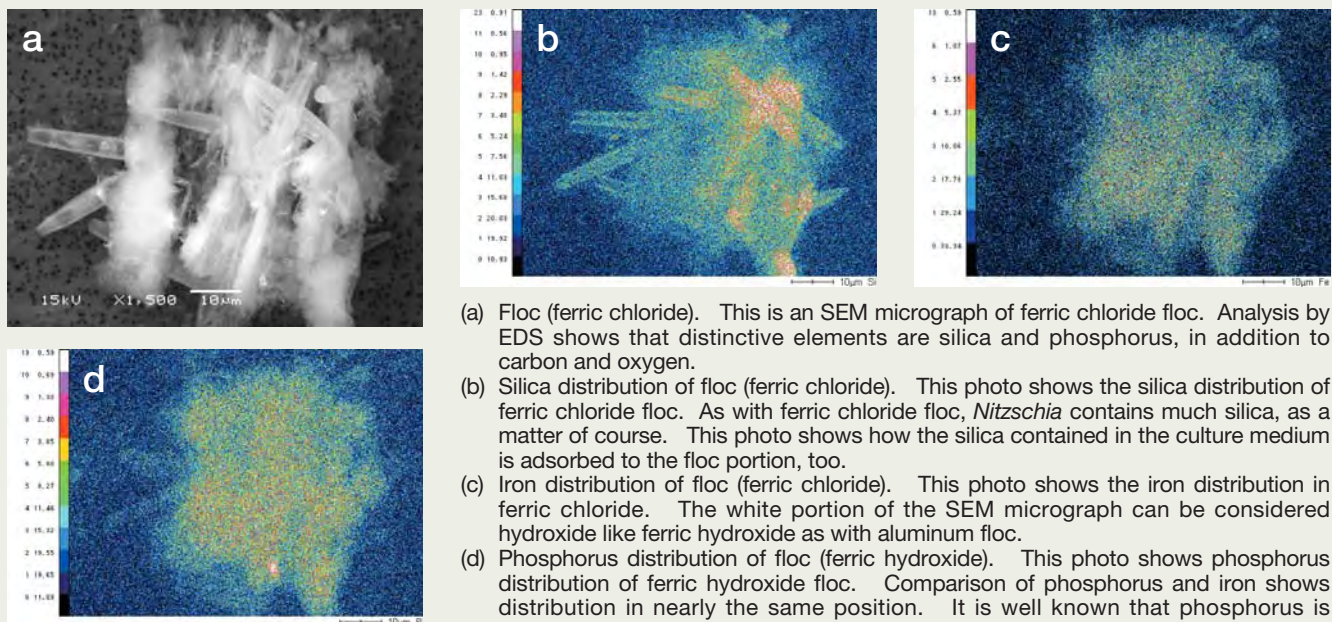
- Proc. of Environmental Engineering Research*, vol. 32, pp. 1-8, 1995.
10. Konno H., Sato A. and Magara Y.: Characteristics of Deposit of Diatom in Filter and Effective Factors to Filter Clogging, *Proc. of the IWSA Specialized Conference*, pp. 103-108, 1995.
  11. Konno H., Sato A. and Magara Y.: Study on Influence of Length of Diatom and Filter Grain to Filter Clogging Problem in Rapid Sand Filtration Process for Drinking Water, *Proc. of the 7th World Filtration Congress*, 7 (1), pp. 243-247, 1996.
  12. Konno H *et al*: Effect of double layer filter for protection of clogging of rapid sand filter by slender type diatoms, *Proc. of*

- Environmental Engineering Research*, vol. 34, pp. 371-379, 1997.
13. Konno H: Rational Depth of Anthracite Layer on Sand Layer for Protection of Filter Clogging Caused by Diatom in Rapid Filtration Process, *Proc. of 7th IAWQ Asia-Pacific Regional Conference*, pp. 765-770, 1999.
  14. Konno H *et al*: Operation of double-layer against filter clogging by diatom, *Proc. of Filtration and separation symposium*, pp. 55-59, 1999.
  15. Iwama T: Study on double-layer rapid filtration for eutrophicated raw water, Master's thesis for Tohoku Institute of Technology, 2001.



- (a) *Nitzschia* floc by coagulation (ferric chloride). On this photo, the *Nitzschia* floc is about 100 x 200 µm, which is smaller than that by aluminum sulfate.
- (b) *Nitzschia* floc by coagulation (ferric chloride).
- (c) *Nitzschia* floc by coagulation (ferric chloride). This photo shows the bridging action between *Nitzschias*, assuming that the white portion represents hydroxide.

Fig. 8. *Nitzschia* floc by coagulation (ferric chloride). (LV-SEM observation)



- (a) Floc (ferric chloride). This is an SEM micrograph of ferric chloride floc. Analysis by EDS shows that distinctive elements are silica and phosphorus, in addition to carbon and oxygen.
- (b) Silica distribution of floc (ferric chloride). This photo shows the silica distribution of ferric chloride floc. As with ferric chloride floc, *Nitzschia* contains much silica, as a matter of course. This photo shows how the silica contained in the culture medium is adsorbed to the floc portion, too.
- (c) Iron distribution of floc (ferric chloride). This photo shows the iron distribution in ferric chloride. The white portion of the SEM micrograph can be considered hydroxide like ferric hydroxide as with aluminum floc.
- (d) Phosphorus distribution of floc (ferric hydroxide). This photo shows phosphorus distribution of ferric hydroxide floc. Comparison of phosphorus and iron shows distribution in nearly the same position. It is well known that phosphorus is adsorbed to floc and undergoes coprecipitation. This photo shows a good example of coprecipitation.

Fig. 9. Floc (ferric chloride). (LV-SEM observation and EDS analysis).

# Development of Nano-Analysis Electron Microscope JEM-2500SE

Mitsuaki Ohsaki, Mituhide Matsusita and Yukihiro Kondo

Electron Optics Division, JEOL Ltd.

## Introduction

With advances in miniaturization and multi-layer wiring technologies, semiconductor devices are evolving toward much higher integration and performance. The International Technology Roadmap for Semiconductor [1], which specifies the requirements for future technologies, indicates that it will be necessary to develop materials and manufacturing processes that make a breakthrough in conventional technologies, in order to achieve the minimum feature size below 100 nm. Progress is therefore seen in the development of devices using copper wiring, low-dielectric-constant (low-k) materials, and new gate insulating films.

Inspections have so far been conducted by carrying out various tests on manufactured devices, cutting off any defective parts during their morphological observations using focused ion beam (FIB) equipment, and observing and analyzing them using a scanning electron microscope (SEM). However, as miniaturization progresses and one needs to observe the crystal morphology of the thin-film interface and routinely analyze its texture on the atomic level, one can no longer make observations only with the resolution and functions offered by SEM.

To provide a solution to these limitations, the authors developed a nano-analysis transmission electron microscope, the JEM-2500SE (Fig. 1). Described below are the features of the novel instrument.

## Features of the JEM-2500SE

This new instrument is an electron microscope designed to evaluate semiconductors. To meet its requirement, which is to obtain results quickly and feed them back quickly to the manufacturing process, or to achieve a high throughput, the JEM-2500SE achieves the following three features:

(1) ease of operation, (2) high resolution, (3) high-sensitivity analysis

## Ease of Operation

Since the SEM is widely used as a morphological observation instrument for semiconductor devices, the JEM-2500SE is also designed to be as operable as a SEM.



Fig. 1. External view of the JEM-2500SE.

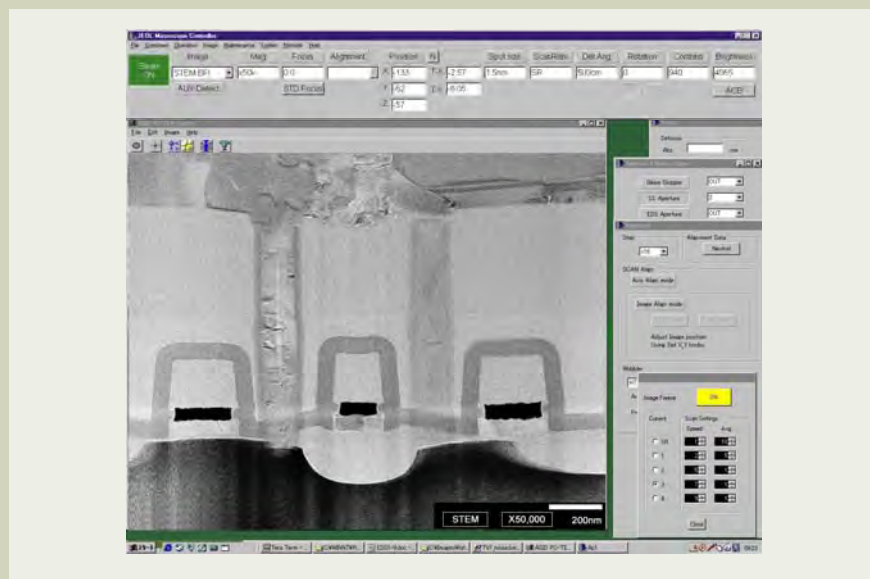


Fig. 2. Graphical user interfaces (GUIs) displayed on the LCD. Operation switch boxes displayed on the top of the selected image can be controlled with a mouse.

## Simplified operation

The LCD (Liquid Crystal Display) shows three Graphical User Interfaces (GUIs) to enable different levels of operators (user, expert, and engineer) to use this instrument with ease. Operators can easily control the microscope using a mouse (Fig. 2). A combination system is used: focusing, magnification changing, and other frequently used operations can be conducted either directly or from the control panel (Fig. 3). Detailed lens data for each image mode and preset alignment values have been stored on the PC, which makes it possible to display a variety of images such as scanning transmission electron microscope (STEM) images, scanning secondary-electron images (SEI), transmission electron microscope (TEM) images, and electron diffraction (DIFF) patterns on the LCD with very simple operation. All aperture operations are motor-

driven. As for positional alignment, optimal sizes and positions are stored on the PC in advance for each image mode. For these reasons, operators no longer have to adjust the apertures.

## Using high-brightness FEG

A thermal field-emission electron gun (FEG) has been selected because it remains stable for a long time, is bright, and also can produce a small probe. This achieves a high sensitivity for EDS (Energy Dispersive X-ray Spectroscopy) analysis and data reliability. Furthermore, the valve between the column and electron-source chamber can be opened using the GUI, so that one can obtain an electron beam instantaneously and use this microscope immediately.

## No need for a darkroom

Despite its capability to observe transmission

electron microscope (TEM) images, the JEM-2500SE does not incorporate a sheet-film camera chamber or fluorescent screen, which are provided on ordinary TEMs. Instead, this microscope comes with TV detectors for a wide field of view and for high resolution TEM observation (Fig. 4). Also, the JEM-2500SE can be equipped for an optional slow-scan CCD detector for recording high-resolution images. TEM images are displayed on the LCD just like other images. These features eliminate the need for a darkroom in which to operate the JEM-2500SE. As a result, there is no need to develop films. The detection monitor for wide field of view or for high resolution is automatically selected depending on the magnification setting.

## Suited for clean-room environment

The microscope is 2.1 m in height. It can be incorporated in a room with a 2.5 m ceiling



Fig. 3. Control panel. Knobs on the panel are used for frequently used operations such as setting of magnifications and focusing.

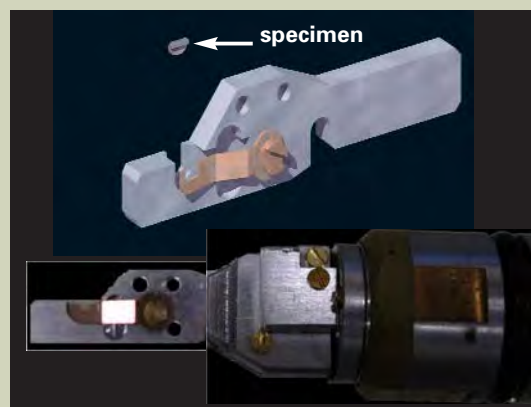


Fig. 5. Tip-on-cartridge specimen holder. The cartridge can be removed for installing a shuttle retainer used in an FIB system. Also, this holder can be used with the JEM-9310FIB that comes with a same-type goniometer stage for the JEM-2500SE.

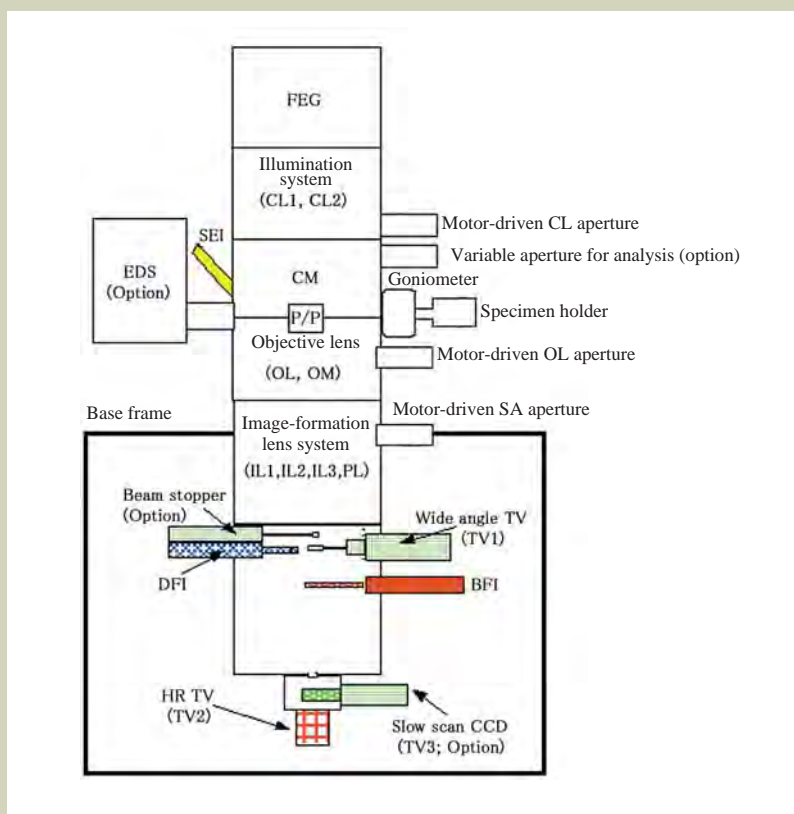


Fig. 6. High-resolution STEM image. Specimen: Silicon (111). A lattice fringe of 0.192 nm can be clearly observed.

Fig. 4. Schematic diagram of the column part. The column incorporates various image detectors. (a) SEI detector (b) TEM image detectors: wide angle TV, high resolution TV, slow-scan CCD (c) STEM image detectors: BFI, DFI.

height, which includes enough space for instrument maintenance in a clean room. The installed pneumatic dampers greatly reduce mechanical vibration of the microscope. A top-supporting system that supports the microscope at a position close to the specimen holder ensures high resistance to vibration.

As mentioned above, all apertures are controlled by motor drive and adjusted from the PC. This makes it possible to cover the entire equipment with sheet metal or something similar, thus preventing noise and protecting against pressure changes.

### Compatible with FIB with the use of a tip-on-cartridge holder

The specimen holder is based on a tip-on-cartridge design, which enables one to remove the tip on which to install a specimen (Fig. 5). For this reason, one can remove the cartridge from the specimen holder and install it on the stage for FIB for specimen preparation, thus making it possible to prepare the various specimens with all FIBs. The JEM-9310FIB focused ion beam system for specimen preparation offered by JEOL comes with a goniometer stage of the same type as the JEM-2500SE. This enables one to use the specimen holder both on the JEM-9310FIB and on the JEM-2500SE, thus shortening specimen-preparation time.

### Film-thickness measurement

STEM, SEI, and TEM images, along with DIFF patterns, displayed on the LCD, all of which are digital signals, can be stored on a PC. One can easily measure thickness of objects from the obtained images. One can determine target thicknesses based on high-resolution lattice-fringe images obtained with a TEM image or STEM image as a reference.

## High Resolution

The electron microscope must achieve high-resolution imaging of atomic-level regions in semiconductor devices. The JEM-2500SE can provide high-resolution images quickly and easily.

### STEM image and SEI

The resolution of a STEM image is 0.2 nm (Fig. 6), while the SEI has a resolution of 1.0 nm (Fig. 7). Both images are obtained by scanning an electron beam over the specimen. This procedure for obtaining these images is familiar to people who have so far been operating a SEM.

When conducting a morphological observation, the first step is to find the observation position of the section made thin by an FIB system, with the JEM-2500SE. Using an observed SEI, one can find the FIB-milled location quickly. Secondary electron images produced by highly accelerated 200 kV electrons include depth information, which is not offered by secondary electron images at low accelerating voltages. This can be a guide in thinning the specimen. The STEM can offer easy identification of the analysis points during a high-resolution observation and EDS analysis. To conduct focusing easily with the STEM, this microscope has adopted the Ronchigram method, which allows one to observe the beam-spot shapes on the specimen surface directly (Fig. 8). Furthermore, the

STEM comes with detectors to produce both bright-field images (BFI) and dark-field images (DFI). The DFI capability is particularly notable. It produces high-contrast images based on the Z (atomic number) contrast effect arising from the difference in scattering angle of the constituent elements in a semiconductor device (Fig. 12).

### TEM function

Lattice images of Si substrates in semiconductor devices are the reference in film-thickness measurement. The TEM function, which easily offers lattice images, is indispensable to atomic-level observation of semiconductors. This function is therefore adopted in the JEM-2500SE.

To reduce the height of the instrument nearly to 2 m, the JEM-2500SE's image-forming lenses, like those in ordinary TEMs, are installed below the base frame. The resolution of a TEM image is 0.14 nm (Fig. 9).

We know well that the well-aligned TEM can produce high-resolution images easily. As described above, the JEM-2500SE stores the alignment values and astigmatism-correction values for TEM in the PC memory. Therefore, one has only to set the image-selection switches on a GUI screen to the TEM mode to acquire high-resolution TEM monitor images on the LCD. As described above, the JEM-2500SE comes with TV detectors for a wide field of view and for high resolution TEM observation, as standard configurations. TEM images obtained by the detectors can be displayed on the LCD just like other images. The detection monitor for the above two modes is automatically selected depending on the magnification setting. In addition, an optional slow-scan CCD is available for the use of recording high-resolution TV images. All TEM images are digitally photographed and processed. Thus, these images can be stored in a PC, thus eliminating the need for developing films.

### Alignment of crystal orientation by diffraction (DIFF) patterns

In TEM high-resolution observation and EDS analysis, one must adjust crystal orientation correctly. Even if a specimen has been reduced to a thin film by FIB, its thickness is 10 to 30 nm and one cannot safely say that observation and EDS analysis produce exact results when crystal orientation is not exactly adjusted. The JEM-2500SE comes with image-forming lenses similarly to those in ordinary TEMs. Diffraction patterns are acquired with a detection monitor and displayed on the LCD (Fig. 10). The operator can adjust the crystal orientation by tilting the specimen while checking the diffraction pattern. To simplify the operation, an experiment is under way in which software has been incorporated for automatically tilting the specimen on the basis of information about the diffraction pattern obtained with the JEM-2010F.

## High-Sensitivity Analytical Functions

### High-sensitivity EDS

We needed to maintain a high spatial resolution while achieving a high acceptance

solid angle in X-ray analysis with the JEM-2500SE. To this end, we created a new design for an objective-lens polepiece and a collimator-equipped EDS detector (Fig. 11). This has made it possible to install an X-ray detector with a detected solid angle of 0.3 sr, which means about 2.5 times sensitivity of conventional EDS models. This has then made it possible to detect trace materials, make an EDS map in a short time, and conduct point and line analyses. The microscope also incorporates a drift-free system, which is needed in EDS mapping, as a standard feature of the EDS system (Fig. 12).

### Capability to incorporate imaging PEELS (parallel electron energy loss spectroscopy), and PEELS

This microscope can be equipped for imaging PEELS, and PEELS, which are designed to analyze the chemical bonding states of semiconductor materials. These systems add only 170 mm to the height of the JEM-2500SE.

## Summary

People who have been working on SEMs may be unfamiliar with the TEM and STEM. However, along with the increasing miniaturization of semiconductor devices, the TEM and STEM are now indispensable for observing high-resolution images. Conventional TEM and STEM instruments were used at research laboratories and operated only by specialists. However, the JEM-2500SE is a new, versatile electron microscope designed for evaluating semiconductor devices in order to achieve high throughput, which means obtaining the results quickly and feeding them quickly back to the manufacturing process. With these features, the JEM-2500SE enables anyone to obtain high-resolution TEM, SEI and STEM images with very simple operation and also to acquire high-sensitivity analysis results.

## References

1. ITRS: International Technology Roadmap for Semiconductor (Nov.1999)



Focused Ion Beam System for Specimen Preparation  
JEM-9310FIB

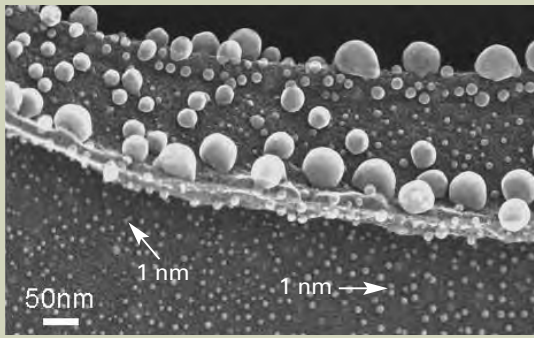


Fig. 7. High-resolution SEI. Specimen: Evaporated gold particles on carbon film. This SEI clarifies that signals are generated from the edge of the gold particles. This image can be obtained by highly accelerated 200 kV electrons, thus offering depth information on the specimen.

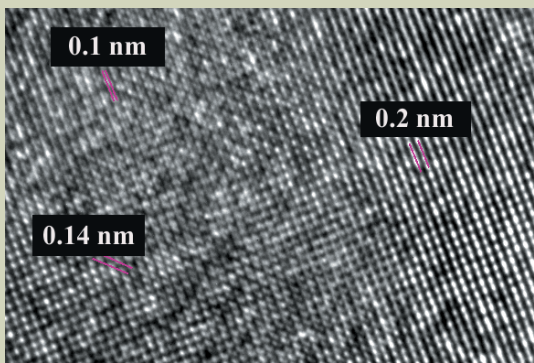


Fig. 9. High-resolution TEM image. Specimen: Single crystal gold. Lattice fringes of 0.2 nm and 0.14 nm can be clearly observed. Also, it is possible to image a 0.1 nm lattice fringe.

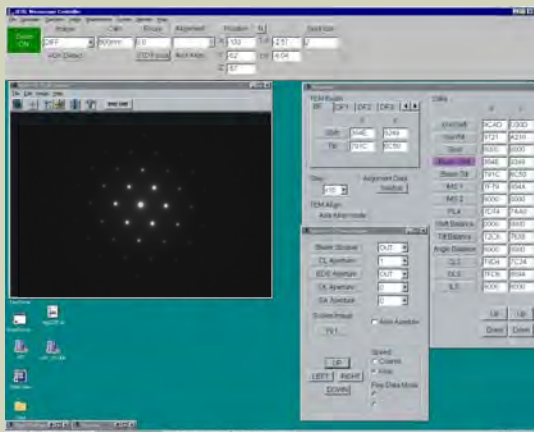


Fig. 10. Diffraction pattern displayed on the GUI screen. Crystal orientation can be adjusted correctly.

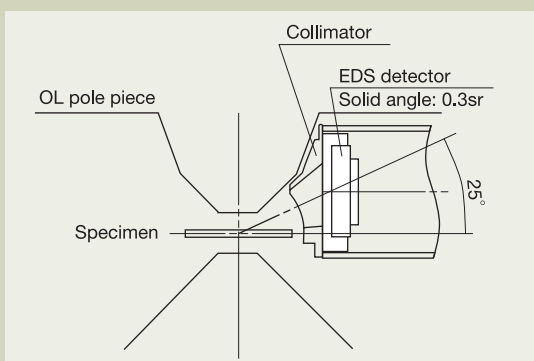


Fig. 11. The vicinity of the objective-lens polepiece. For installing an EDS detector with a detected solid angle of 0.3 sr, a new design for the objective-lens polepiece is made.

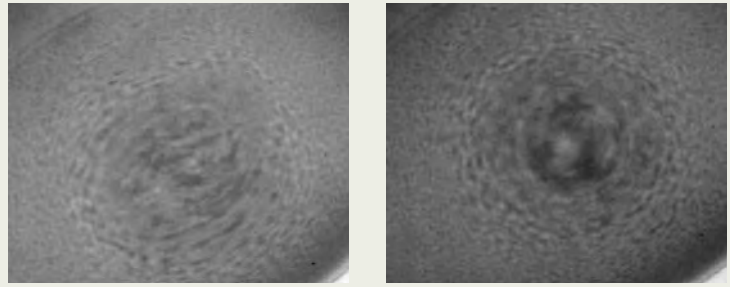


Fig. 8. Ronchigram pattern. This pattern shows the beam-spot shapes on the LCD using the image-forming lenses. When the beam shape is minimum-sized, the focus value for the exact focal point is obtained. If the shape is a perfect circle, it is shown that astigmatism correction is optimally conducted.

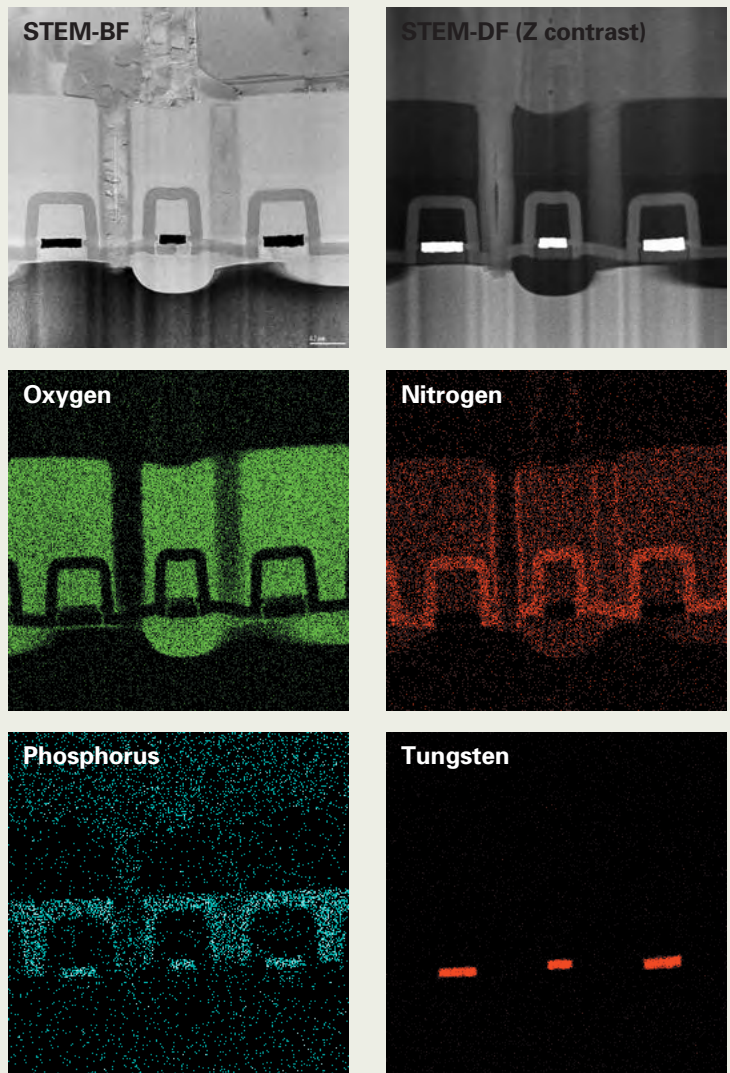


Fig. 12. Comparison of STEM images and EDS mapping. (STEM images: BFI and DFI. EDS mapping: elemental mapping images.) Specimen: 64 Mbit DRAM. The contrast of DFI depends on the atomic number. A heavy element of tungsten (W) can be clearly observed in this image. Using the EDS mapping method, elemental distribution of trace elements can be obtained.

# Development of JSM-7400F: New Secondary Electron Detection Systems Permit Observation of Non-Conductive Materials

Hiroyoshi Kazumori

Electron Optics Division, JEOL Ltd.

The JSM-7400F Field Emission Scanning Electron Microscope (FE SEM) comes with a newly developed FE electron gun that features large current and low emission noise, a strongly excited conical lens, and new secondary-electron detection systems, permitting large specimens (up to 200 mm in diameter) to be observed at a resolution surpassing that of an in-lens FE-SEM, at accelerating voltages of up to 15 kV.

The combination of a strongly excited conical lens (semi-in-lens) and retarding method has dramatically improved the guaranteed resolution, from 2.2 nm previously to 1.5 nm, at an accelerating voltage of 1 kV. It also achieves image observation at a low accelerating voltage of 100 V on the specimen, which has been difficult up to now.

## Introduction

The JSM-7400F is used for evaluating artificially constructed super-lattices and semiconductor materials, performing high-resolution microstructure observation in various specimens such as medical/biological specimens and observation of interfaces of metallic materials, and analyzing constituent elements in specimen surfaces. In these applications, there are demands for high-resolution observation of the nano-regions of specimens that include parts with low or no electrical conductivity, and observation of the surface of specimens that are easily damaged by a high energy primary electron beam, without coating the specimen surfaces.

In order to meet these demands, JEOL has developed a field-emission scanning electron microscope (FE SEM) that features the following:

- ① r-filter: An energy-selective secondary electron detection system.
- ② Gentle Beam: An objective lens that can retard a primary electron beam, which works together with a specimen stage.

## Features of the Electron Optics System of the JSM-7400F

### Field-emission electron gun

This electron gun has a construction to achieve a good vacuum in the vicinity of the emitter and low emission noise, even when the emission current is increased. It is thus possible to observe noise-free images and perform highly precise energy-dispersive X-ray spectrometry (EDS) over at least 10 hours (Fig. 1).

### Condenser lens

The condenser lens, which has been designed to consist of a single stage, is incorporated in the ultrahigh vacuum side, reducing the distance between the emitter and the face of the condenser lens by about 50 mm. As a result, aberration of the condenser lens at a large probe current is reduced, and also the probe current can be sequentially varied over a wide range from 1 pA to 1 nA without changing the diameter of the objective lens aperture. Consequently, even when a large-current electron probe is used to irradiate the specimen, the probe size will not increase, making it possible to observe low-noise images.

### Strongly excited conical objective lens

This objective lens has been made further conical in shape compared with the conical lenses of JEOL conventional FE SEMs. Thus, this new conical lens permits observation of specimens up to 150 mm in diameter tilted up to 42° at a working distance (WD) of 8 mm. The range of accelerating voltages that can be used at a WD of 3 mm is 0.5 to 16 kV, and the spherical aberration coefficient and the chromatic aberration coefficient of this lens are 2.2 mm and 1.8 mm, respectively. Particularly, at an accelerating voltage of 1 kV, observation can be performed at a shorter WD, with the respective aberration coefficients of 1 mm or less.

### Aperture angle control lens (ACL)

Previously, when an ACL was not used, if the probe current was made large, the diameter of the objective lens aperture must have been changed so as to obtain a near-optimum angle.

However, the use of an ACL permits the optimum aperture angle to be obtained at all times, regardless of changes in the probe current. Consequently, the probe diameter does not increase even if the probe current is changed.

## Influence of Charge-up on Non-Conductive Specimens

Figure 2 shows the energy distribution of electrons emitted from the specimen when irradiated by the primary electron beam. When the energy of the emitted electrons is less than 50 eV, these electrons are called secondary electrons, and when the energy is 50 eV or higher, they are called backscattered electrons. The area in which the electrons emitted from a non-conductive material are readily affected by charge-up is shown in pale green. The influence of charge-up can be eliminated by removing this area prior to the image-forming process.

## Conventional Secondary Electron Detection System

Figure 3 shows the secondary-electron detection system normally used to observe an electrically conductive specimen. It shows typical paths of the secondary electrons emitted from a specimen at a ground potential. The difference in color represents the difference in the energy of the emitted electrons. The energy increases going to the left, in the sequence yellow-green, blue, brown, and so on.

A positive voltage of several volts exists at the cylindrical electrode shown in pink. This voltage suppresses the secondary electron emission when the secondary electrons emitted

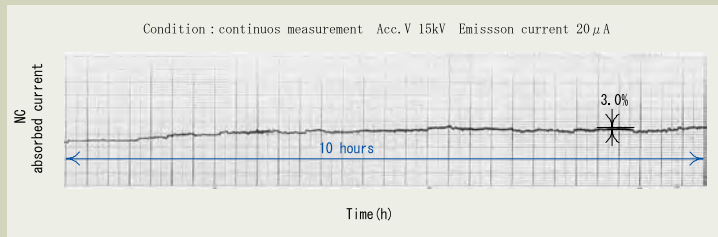


Fig. 1. Change in the NC (noise canceller) current.

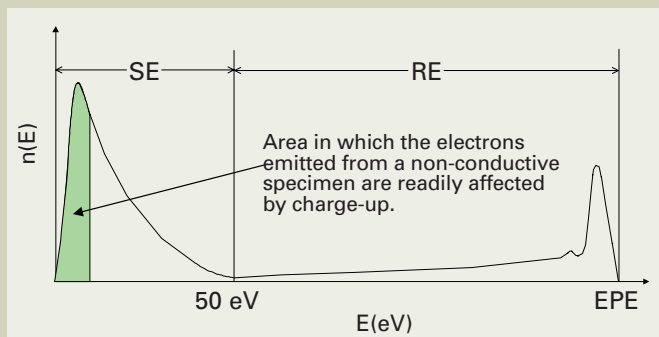


Fig. 2. Energy distribution of electrons emitted from the specimen when irradiated by the primary-electron beam.

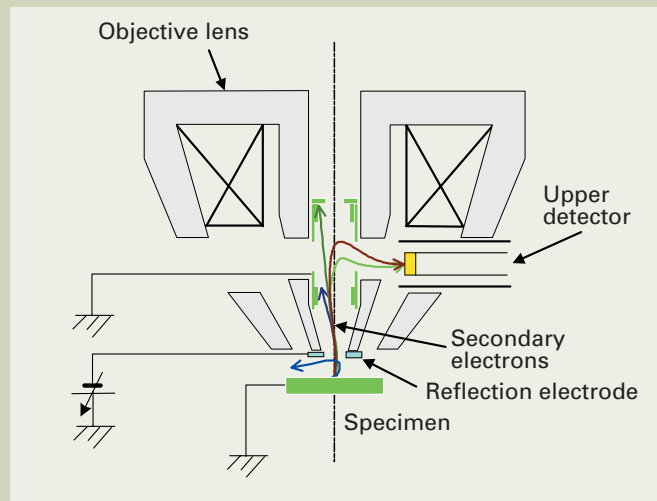


Fig. 4. Secondary-electron detection system used with a reflection electrode.

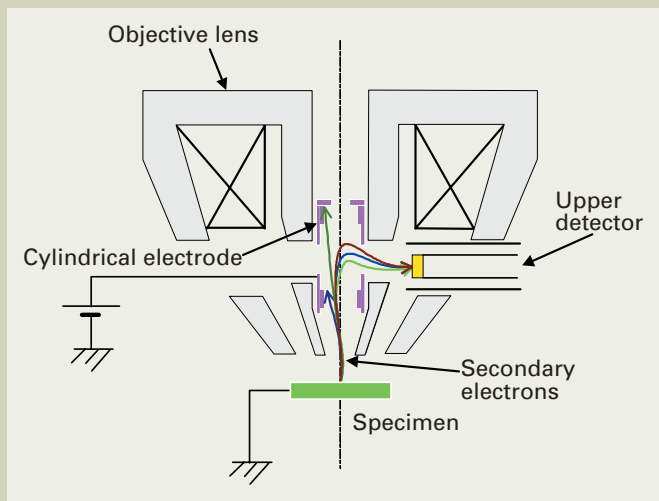


Fig. 3. Secondary-electron detection system used for normal observation (mode 2).

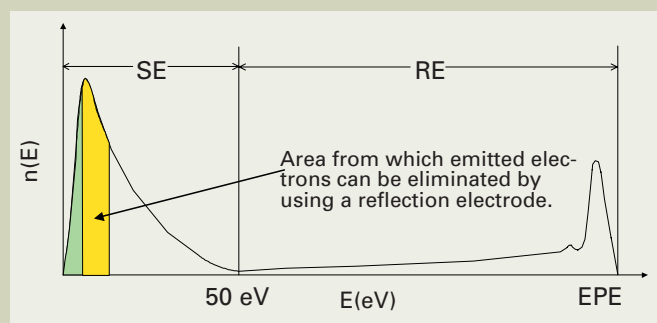


Fig. 5. Effect for removing charge-up using the reflection electrode.

from the specimen collide with the cylindrical electrode. The upper detector of this system detects a large number of low-energy secondary electrons.

Next, **Fig. 4** shows the secondary electron detection system where a reflection electrode with a negative voltage is used to eliminate the influence of charge-up of a non-conductive specimen. In the figure, the secondary electrons that follow the blue path are removed by the negative-voltage electrode.

However, secondary electrons that have an energy of 1 eV or less (shown in yellow-green) rise to the upper detector because the trapping force of the magnetic field is larger than that of the electric field for these electrons.

In **Fig. 5**, the area from which the emitted electrons can be eliminated by using a reflection electrode is shown in yellow. It is not possible to eliminate the pale green area using a reflection electrode, so the influence of charge-up remains.

## New Secondary Electron Detection System

**Figure 6** shows the r-filter secondary-electron detection system, which is one of new detection methods used in this FE-SEM. The electrodes shown in red and blue in the figure are at a positive and a negative potential of several tens of volts, respectively. The resulting electric field deflects the secondary-electron paths, causing low-energy secondary elec-

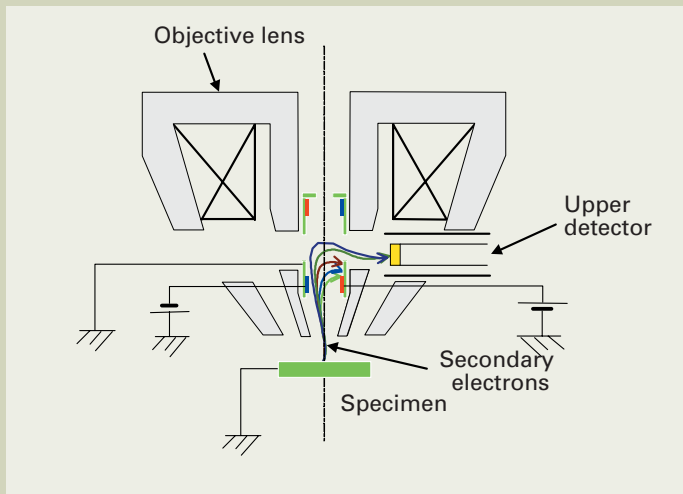


Fig. 6. r-filter secondary-electron detection system.

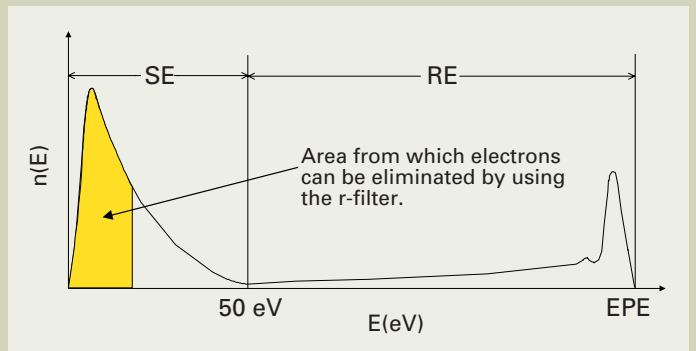
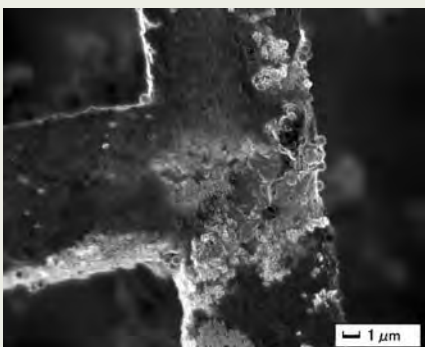
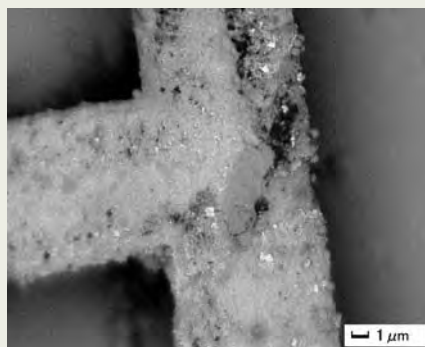


Fig. 7. Effect for removing charge-up using the r-filter.



Mode 2: Accelerating voltage 1 kV



r-filter: Accelerating voltage 1 kV

Fig. 8. Comparison of SEM images: Image obtained through normal observation (mode 2) (left) and image obtained using a detector with the r-filter (right). Magnification:  $\times 5,000$

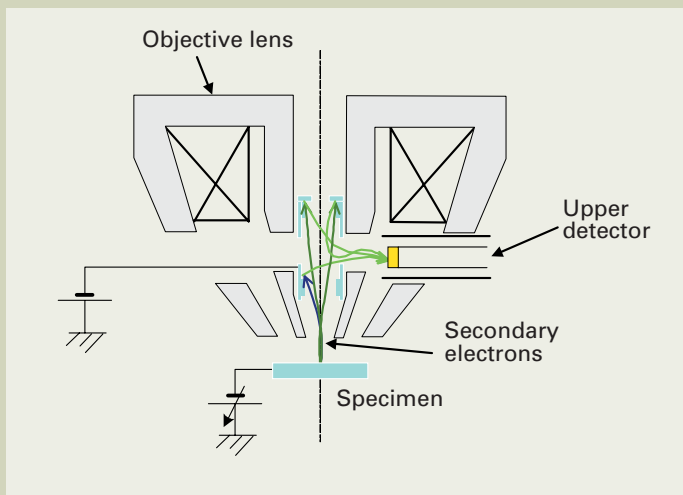
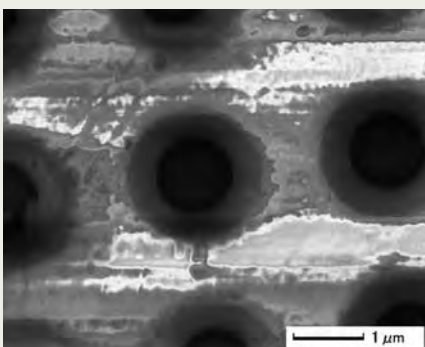
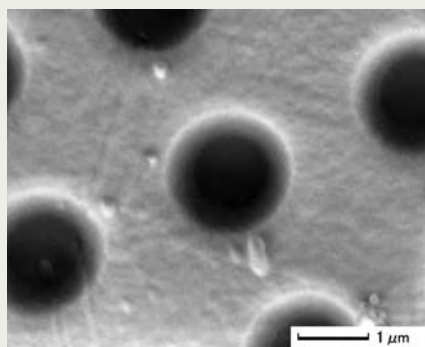


Fig. 9. Gentle Beam secondary-electron detection system.



Mode 2: Accelerating voltage 1 kV



Gentle Beam: Accelerating voltage 0.1 kV

Fig. 10. Comparison of SEM images (contact holes): Image obtained through normal observation (mode 2) (left) and image obtained using the Gentle Beam secondary-electron detector (right). Magnification:  $\times 20,000$

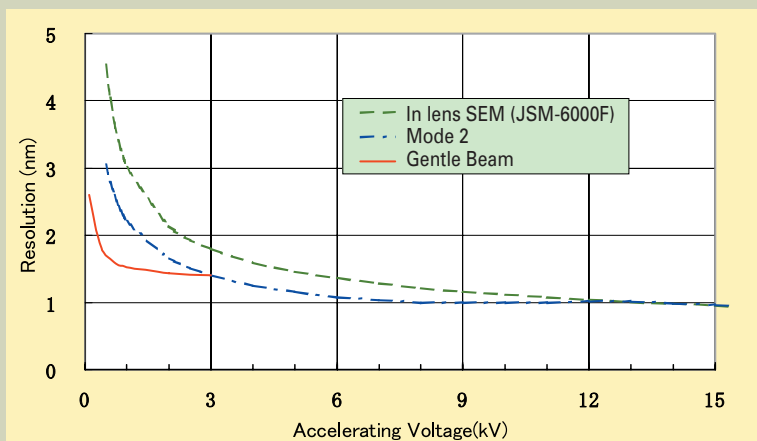


Fig. 11. Accelerating voltage versus resolution.

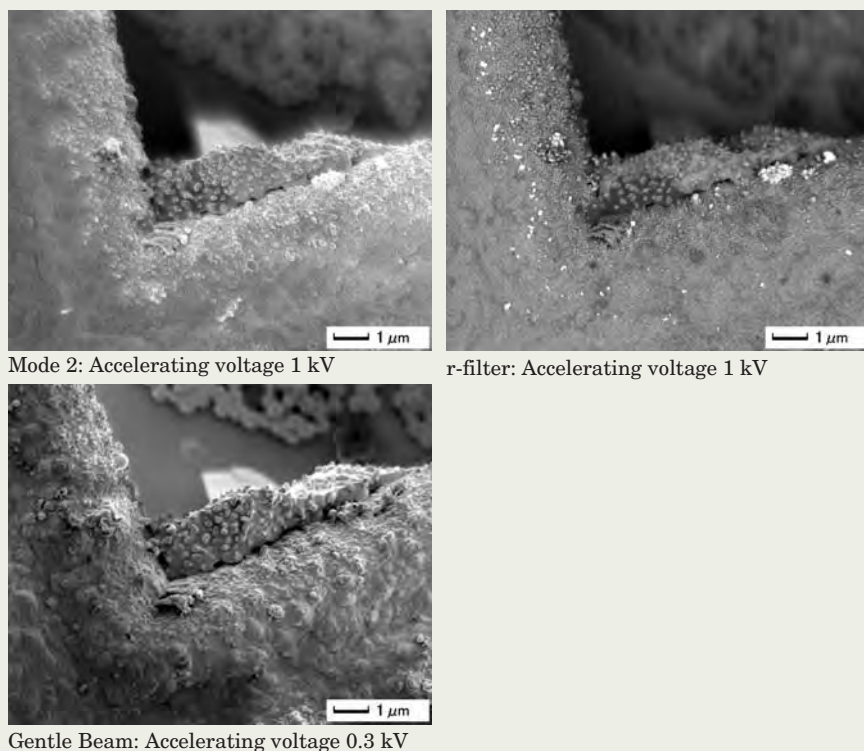


Fig. 12. Comparison of SEM images (mesh). Image obtained through normal observation (mode 2) (top left) and images obtained using the new secondary electron detection systems (top right and bottom). Magnification:  $\times 10,000$

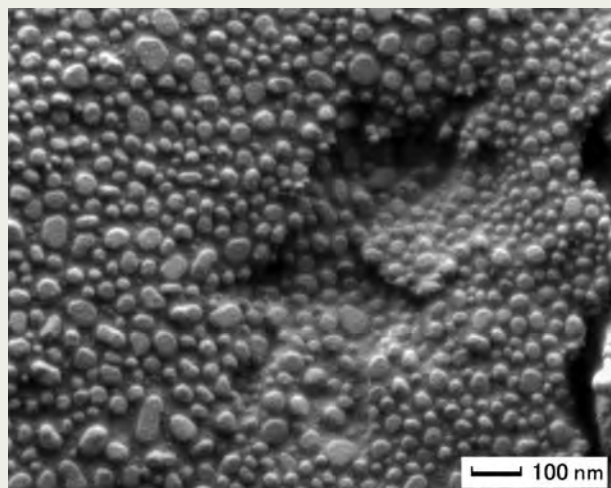


Fig. 13. Secondary-electron image of evaporated gold at an accelerating voltage of 100 V.

trons in particular to collide with the inside wall of the cylindrical electrode to eliminate them.

In Fig. 7, the area from which electrons can be eliminated by using the r-filter is shown in yellow. The pale green area is included in the yellow area, so the influence of charge-up is adequately removed.

Figure 8 shows the effectiveness of the r-filter. The use of the r-filter eliminates the accentuation of light and dark due to the influence of charge-up, and also enables the surface composition information to be seen.

Next, Fig. 9 shows the Gentle Beam secondary-electron detection system, which utilizes the primary electron-beam retarding method (Retarding method: A method of reducing the energy of the electron beam near the specimen that irradiates the surface of the specimen using a decelerating electric field.).

A negative voltage of about 1 to 2 kV is applied to the specimen. Consequently, the secondary electrons are accelerated by the potential of the specimen, and as a result, secondary electrons emitted at low energy do not exist. The electrons emitted from the specimen collide with the cylindrical electrode shown in pale blue, causing them to be multiplied to be detected by the upper detector.

Figure 10 shows the effectiveness of this method. Whereas previously observation was impossible due to the influence of charge-up, the use of the Gentle Beam system makes observation of the surface and bottom of contact holes possible.

Figure 11 shows the relationship between accelerating voltage and resolution. As indicated by the red line, degradation of resolution at low accelerating voltages is greatly reduced.

Figure 12 shows comparison of images between an image obtained through normal observation (mode 2) and those obtained using the new secondary-electron detection systems. All three images show the same area of a contaminated mesh. It can be seen that the images obtained using the three detection methods are quite different from each other.

In mode 2, halation occurs in a part of the image due to the effect of charge-up. In the case of the r-filter method, there is a lot of information on the composition of the surface, while in the case of the Gentle Beam method, surface topographic information similar to the information obtained by the lower backscattered electron detector, can be visualized.

## Summary

As described above, the JSM-7400F comes with two new secondary-electron detection systems, the r-filter and the Gentle Beam, in addition to the conventional detection system. The innovative detection systems make observation of non-conductive specimens possible, by eliminating the influence of charge-up occurring. Finally, Fig. 13 shows a SEM image of evaporated gold at a low accelerating voltage of 100 V and magnification of 100,000. This image verifies that our new FE-SEM, the JSM-7400F offers clear images even at low accelerating voltages.

# Applications of Image Processing Technology in Electron Probe Microanalyzer

Norihisa Mori, Masaru Takakura and Hideyuki Takahashi

Application & Research Center, JEOL Ltd.

The X-ray image in EPMA does not always show an ideal appearance. In this report, three kinds of image processing to improve the image quality are introduced together with some examples.

## 1. Introduction

Previously, X-ray images in electron probe microanalysis were recorded on a photographic film as a group of white dots, each of which has the X-ray intensity over a certain X-ray count. Along with the progress of computer technology, the X-ray count has now been accumulated and displayed on a CRT as an image. Accordingly, the researcher can use various types of image processing for the image display.

The most popular processing of an X-ray image is to modify the signal level and to display the data in pseudo-colors. When the signal level is modified, the image is significantly improved as a result of a visibility increase in the contrast intensification. In addition, by the color-coding of the image with pseudo-colors the regions with the same level of X-ray counts are found at a glance. Moreover, an electron probe microanalyzer (EPMA) is furnished with a variety of image-processing functions such as the particle measurement function for measuring the shape of a binary image, composite mapping function for combining two or more maps color-coded in red, blue and green gradations, smoothing, bird's-eye view display function, and contour map display function, for user's convenience.

Raw data is most important because it carries original information. However, when the researcher tries to explain a data to another person, the use of image-processed data emphasizing significant information or weakening insignificant information is quite helpful.

This paper introduces the following image-processing methods, which are effective for displaying X-ray images, secondary-electron images (SEI) and backscattered-electron images (BEI), together with actual examples of processed images.

- Emphasizing significant information by superimposing a BEI on an X-ray image (Section 2: Synthesis of images)
- Splining thinly dotted data due to insufficient number of analysis points (Section 3: Data interpolation)

- Sharpening a blurred image (Section 4: Sharpening SEI and BEI, and Section 5: Reduction of X-ray image blur due to electron scattering in the sample)

By the use of these types of image processing, measured data becomes to show more natural appearance and the image quality becomes higher. As a result, we obtained various merits, such as the acquisition of data in a shorter time and the enhancement the quality of an image obtained using a tungsten filament to a level comparable to that obtained using a LaB<sub>6</sub> tip. We will report these effects in this paper.

## 2. Synthesis of Images (masking and accumulation of images)

A BEI provides a contrast corresponding to the average atomic number, and therefore it is similar to the X-ray image reflecting the composition distribution (Fig. 1).

The BEI has advantages over an X-ray image as it has a higher spatial resolution and shows clearer outlines. However it is not easy to identify elements distributed in an observed area only from the contrast of the composition image. On the other hand, the X-ray image provides information on the distribution of specific elements in spite of its low spatial resolution.

The X-ray image and the BEI are different in their advantages. Therefore, if we superimpose these two kinds of images arithmetically, the synthesized image may show their respective advantages.

### Purpose

To make conspicuous the outline of element distribution in an X-ray image using the BEI.

### Principles

**A part of the X-ray image corresponding to the specific phase in the BEI (masked) is displayed.**

The outlines of X-ray image can be made conspicuous by binarizing or multilevel-cod-

ing of the BEI. A mask is made to display only a part possessing desired information, and then this mask is applied to the X-ray image (Fig. 2).

**An image intermediate between the X-ray image and the BEI is synthesized by multiplying the X-ray image and the BEI or dividing the former by the latter (arithmetic of images).**

The bright parts of the BEI are in a high signal level and the dark parts are in a low signal level. Numerically, the brighter part is larger in the count number than the darker part. Using this property, if the X-ray image is multiplied by the BEI, the brighter part of BEI becomes higher in the signal level and darker part becomes lower in the signal level. This emphasizes the bright parts. On the other hand, when the X-ray image is divided by the BEI, the dark part in the composition image is emphasized as shown in Fig. 3.

### Effects

By applying a mask based on the BEI to an X-ray image blur by scattered electrons, it is possible to make the outlines of X-ray image conspicuous. This contributes to the clarification of the correspondence between the X-ray image and the BEI. On the other hand, since this method uses a simple mask, the X-ray count at the masked part becomes zero, and so the outline does not change smoothly, showing sometimes an unnatural appearance.

By comparing the X-ray image with the BEI arithmetically, we have succeeded in changing the outlines to show their natural appearance. Though this arithmetic has a disadvantage that only the brightest or the darkest part of the BEI is emphasized, this technique is effective to make the image outlines conspicuous.

## 3. Data Interpolation (bi-cubic method)

Often, because of the limitation of measurement time, the researcher cannot obtain a suffi-

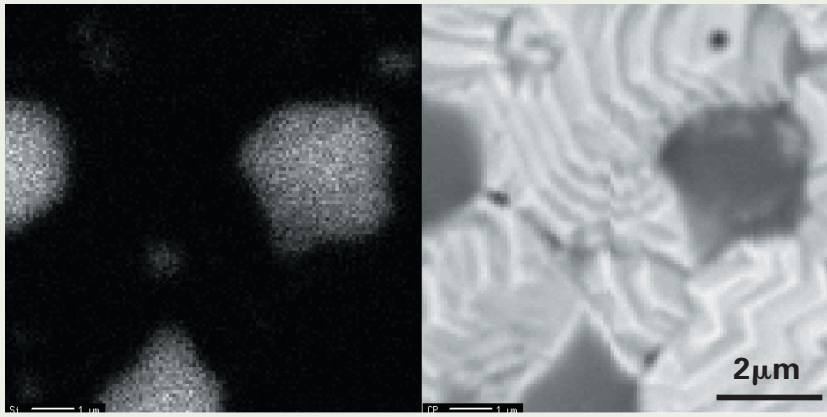


Fig.1. X-ray image (left) and BEI (right) of Si on an electrode-plate surface. The dark part of the X-ray image corresponds well to the bright part of the composition image.

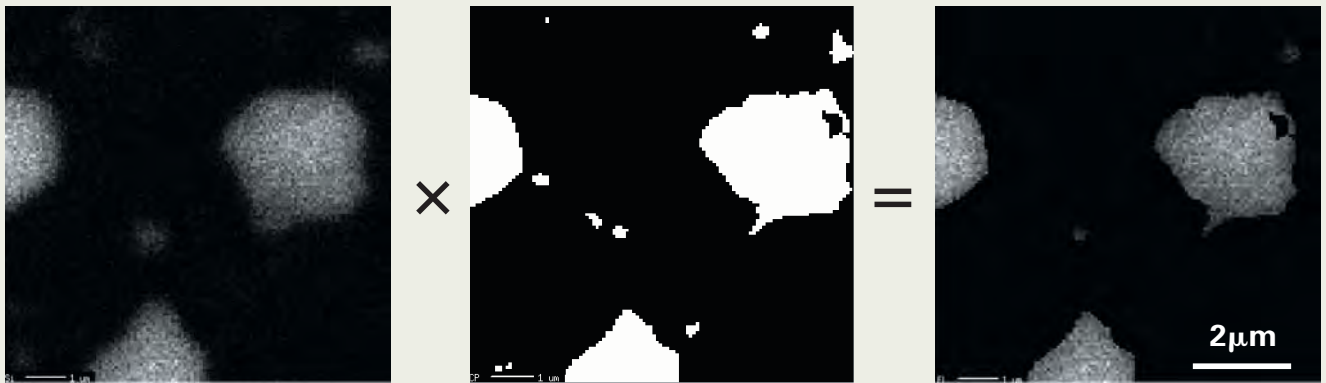


Fig. 2. Image with clear outlines(right) is synthesized by applying a mask (center) made from the BEI to the X-ray image (left).

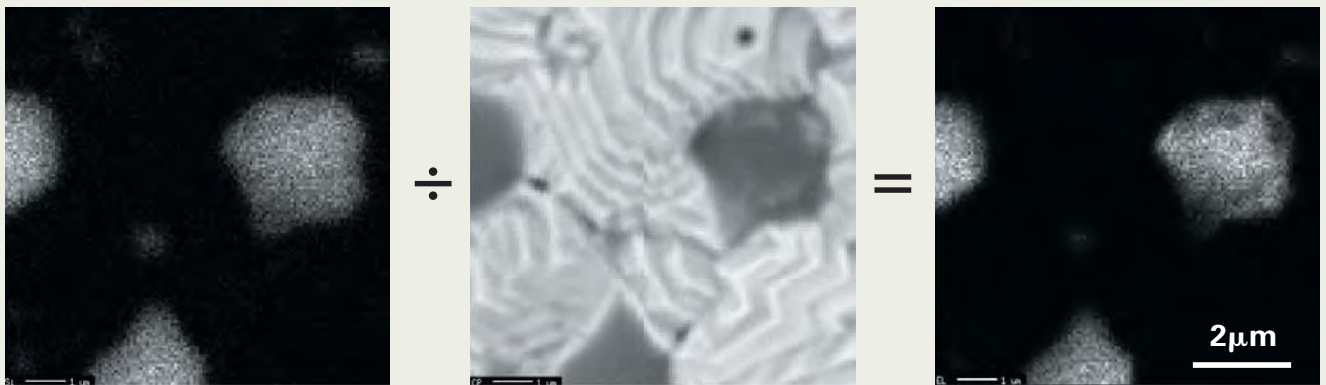


Fig. 3. Image with clear outlines (right) is synthesized by dividing the X-ray image (left) by the BEI (center).

cient number of analysis points for the map analysis. This lowers the resolution and degrades the appearance of the map. However, as long as the total measurement time is limited, even if the number of analysis points is increased, the analysis time per point is reduced and so the S/N ratio decreases, producing difficulty in seeing the data.

One of the causes of the difficulties in seeing the data is that each data point on the map is displayed as a square pixel, this is because, when the number of analysis points is small, the shape of the squares becomes conspicuous. As the distribution of constituent elements cannot be a group of squares, we have developed a method of displaying a clear map by the interpolation of analysis points (Fig. 4).

### Purpose

To convert an image data composed of square pixels, which produces an unsightly distribution due to a small number of analysis points, into a clear image by applying the bi-cubic method.

### Principles

In the image processing, there is a technique called the bi-cubic method, and it is used to improve the resolution of image (number of analysis points in analysis).

The bi-cubic method is a method of interpolating between data points with curved surfaces expressed piecewise by cubic polynomials. If this method is linked to a graph, the display of one analysis point with a square makes

a bar graph. The bi-cubic method converts it into a graph consisting of a curve passing through each data point (Fig. 5).

The bi-cubic method can be expressed as follows : Let  $f(x,y)$  be the source image data at the coordinates  $(x, y)$ ,  $F(x,y)$  the image data after the bi-cubic interpolation, and  $H_j(x)$  the one-dimensional cubic interpolation along the X-axis.

$$F(x, y) = H_{j-1}(x) C_3(y-j) + H_j(x) C_2(y-j) + H_{j+1}(x) C_1(y-j) + H_{j+2}(x) C_0(y-j),$$

$$\text{for } j \leq y < j+1$$

$$H_j(x) = f(i-1, j) C_3(x-i) + f(i, j) C_2(x-i) + f(i+1, j) C_1(x-i) + f(i+2, j) C_0(x-i),$$

$$\text{for } i \leq x < i+1$$

$$C_0(t) = -at^3 + at^2$$

$$C_1(t) = -(a+2)t^3 + (2a+3)t^2 - at$$

$$C_2(t) = (a+2)t^3 - (a+3)t^2 + 1$$

$$C_3(t) = at^3 - 2at^2 + at$$

a: Spline constant within the range of  $-1 < a < 0$

## Effects

The bi-cubic method allows the data with a small number of analysis points to be displayed clearly. As a result, its application is expected to bring the following two effects to the analysis:

### Reduction of analysis time

The bi-cubic method makes it possible to display the data with a small number of analysis points fairly clearly, thus enabling the researcher to shorten the analysis time. For example, if an analysis of  $500 \times 500$  points can be replaced by an analysis of  $125 \times 125$  points, the total measuring time is reduced to 1/16.

### Display of enlarged image

If a part of the map is enlarged, an unsightly mosaic-like image appears, reflecting the shape of square pixels. The bi-cubic method provides a smooth enlarged image (Fig. 6).

## 4. Sharpness of SEI and BEI (unsharp mask)

The image processing technology includes some methods for processing a defocused image to an apparently focused image. The unsharp mask, the 2D-FFT, and the Wiener method are its examples.

Among these techniques, the unsharp mask is incorporated in PhotoShop™, which is widely used image-processing software, and is useful for processing the SEI and BEI (Fig. 7 and Fig. 8).

### Purpose

To sharply display the blurred SEI or BEI as an apparently focused image by the use of the unsharp mask.

### Principles

The unsharp mask aims to sharpen the image. This may sound contradictory, but the name of the unsharp mask comes from its processing method.

When an original image is intentionally blurred and reversed, and then added to the original image, the image of edge is obtained (Fig. 9). Adding this image again to the original image results in an image with further emphasized edges (Fig. 10). In such a way, an image blurred is used for this masking technique. Therefore, it is named "unsharp mask".

### Effects

Unsharp masking displays the blurred image more clearly.

Although there are several other techniques for sharpening images, unsharp masking produces fewer artifacts (virtual images resulting from image processing), and so can be used with fairly high reliability. Also, the operation is easy. However, unsharp masking amplifies noise in the image, and significantly reduces the S/N ratio. Because of this, this techniques

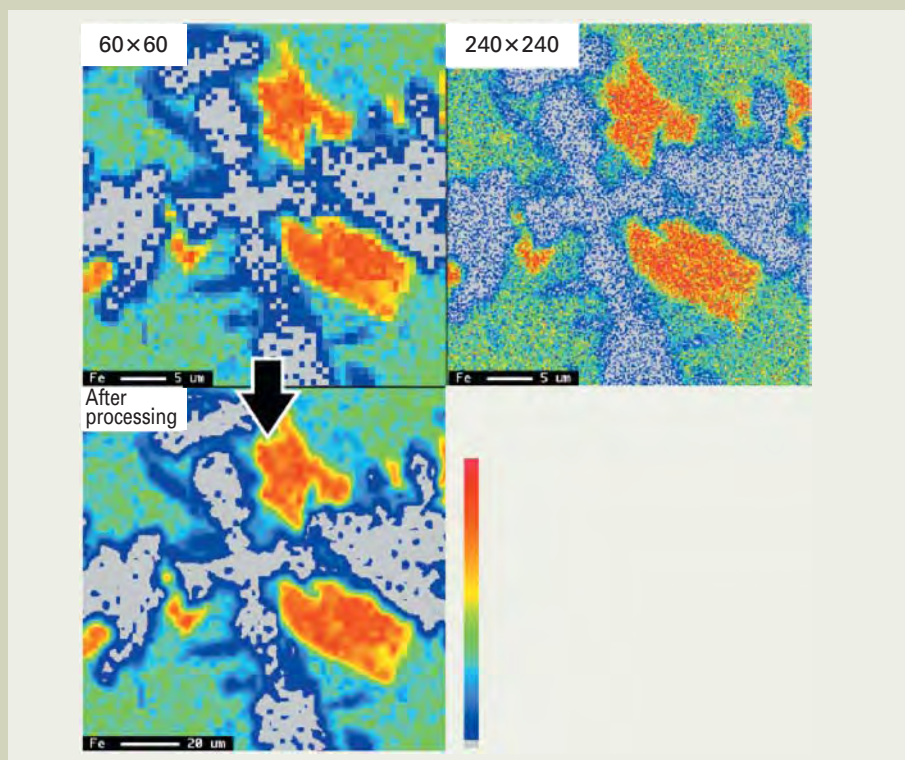


Fig. 4. Map of Fe in a ceramic.

● Analysis conditions: accelerating voltage 15 kV ● Probe current: 20 nA.

Top left:  $60 \times 60$  pixel map. Top right:  $240 \times 240$  pixel map.

The analysis time is the same as that for the top-left map. Bottom left:  $240 \times 240$  pixel map converted from the top-left map using the bi-cubic method.

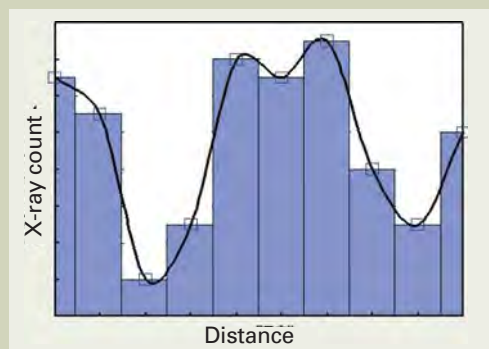


Fig. 5. Conceptual drawing of bi-cubic method.

If the conventional image-processing method that displays measured data points with squares is analogized to a graph, it is represented by a bar graph. The bi-cubic method converts the graph to a graph consisting of a curve passing through each measured data point.

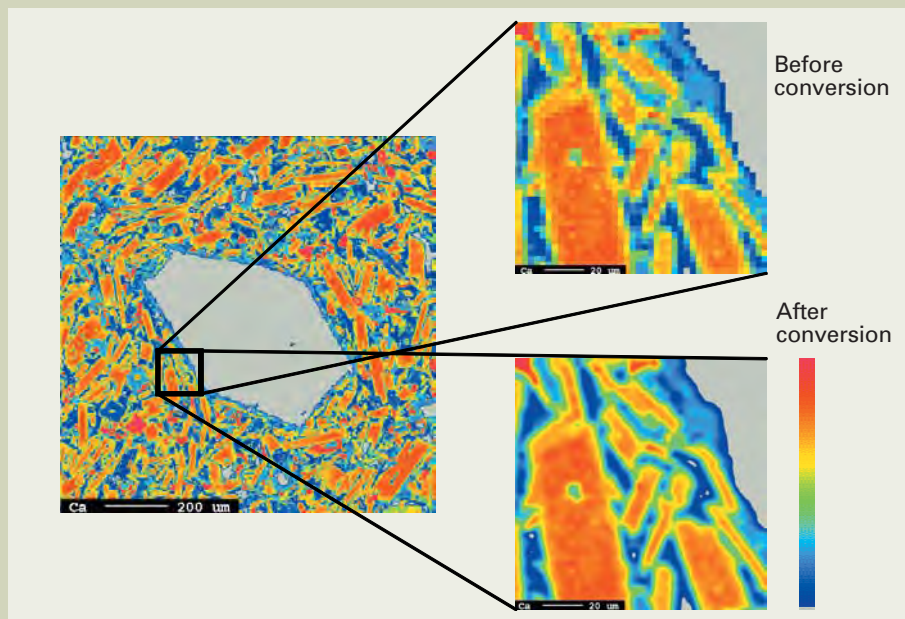


Fig. 6. Example of the bi-cubic interpolation applied to enlarged color-map data of a mineral.

is desirable to be applied to the case where raw data has a high S/N ratio.

## 5. Reduction of X-ray Image Blur due to Electron Scattering in the Sample (Filter to reduce the X-ray image blur)

The electron beam is scattered in a sample and spread in a region of approximately several micrometers in diameter and generates the characteristic X-rays (Fig. 11). For this reason, the X-ray is inevitably blurred, and the blur becomes remarkable in a highly magnified image.

If sharpening described in Section 4 is applied to image data such as a blurred X-ray image, various merits may be expected. Unlike the usual photographs, however, the X-ray image contains a lot of noises. Thus, if sharpening is made by the use of the ordinary image-processing software, the noise may be amplified to cause an image deterioration rather than improvement.

In consequence, when sharpening is applied to the X-ray image, its application must be carried in such a way that the process does not suppress the image deterioration. Accordingly, we have designed an image-processing filter capable of sharpening of the X-ray image taking the magnitude of electron beam scattering into consideration. We have named this filter "Filter to reduce X-ray image blur (FRX)", since it has been designed to obtain an image close to the image that might be obtained if the electron beam were not scattered in the sample.

By the use of FRX the X-ray image blur was noticeably reduced.

### Purpose

To reduce the X-ray image blur caused by the scattering of electrons, using FRX.

### Principles

#### Region of X-ray generation

The amount of X-ray image blur is determined by the size of the region of X-ray generation. So far, this size has been simply described as the region of scattering of the electron beam. However, to be precise, the sum of the diameter of the electron beam and the size of the electron beam scattering in the sample is the region of X-ray generation.

As a simple method of determining the expansion of electron beam in the sample, the use of a nomogram is recommended (Fig. 12).

Since the diameter  $d_0$  of an electron beam varies depending on the electron gun used, the use of actually measured data is necessary. For the JEOL EPMA, the data shown in Fig. 13 is available.

The expansion of the electron beam obtained from the analysis conditions (accelerating voltage, probe current, and sample) can be used as the parameters of the FRX.

### FRX

Generally, the value of measured counts in the X-ray image ranges from several to several hundreds of counts. It inevitably includes noise based on the statistical errors. The sharpening of an X-ray image applies the sharpening



Fig. 7. SEI of lead-free solder without image processing.

- Accelerating voltage: 15 kV
- Analysis area  $5\mu\text{m} \times 5\mu\text{m}$

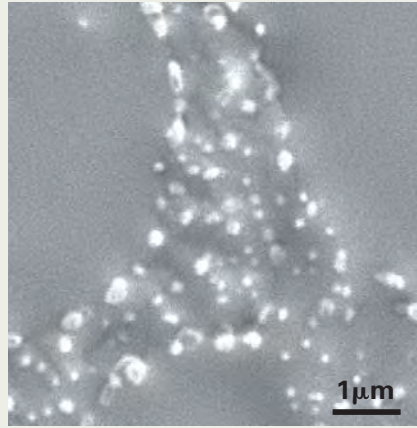


Fig. 8. SEI (Fig. 7) of lead-free solder, sharpened through an unsharp mask.

- Accelerating voltage: 15 kV
- Analysis area:  $5\mu\text{m} \times 5\mu\text{m}$



Fig. 9. Adding an intentionally blurred and reversed image (center) to the original image (left) provides a clear-edged image (right).



Fig. 10. Adding the clear-edged image (center) to the original image (left) results in an image with the edges further emphasized (right). Since the JEOL logo is originally not blurred, it becomes an image with each letter standing out.

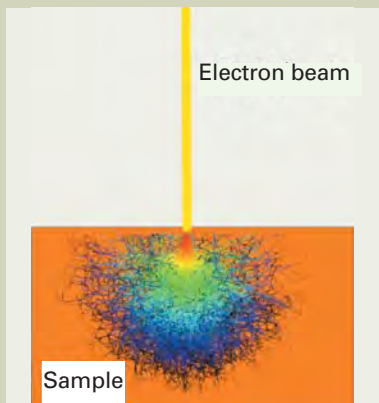


Fig. 11. Since the electron beam is scattered in the sample to spread the region of X-ray generation, a highly magnified X-ray image shows a noticeable image blur.

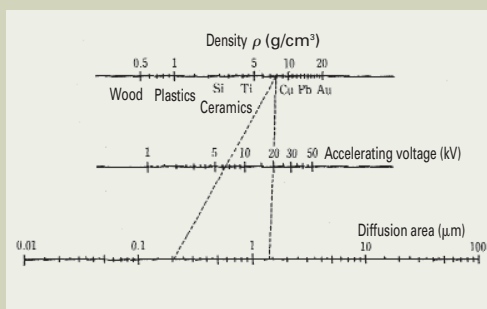


Fig. 12. Nomogram. It can be simply obtained from sample density  $\rho$  and the accelerating voltage to the sample.

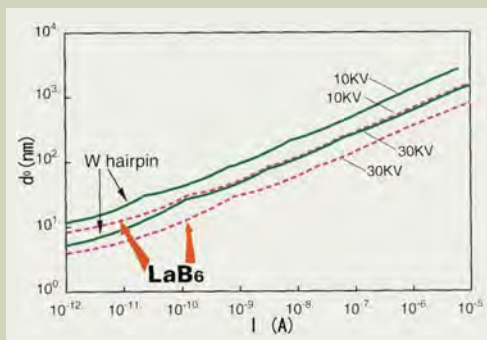


Fig. 13. Graph showing electron beam diameter  $d_0$  versus probe current  $I$  (JXA-8100/8200 series).

process to the noisy data with a low S/N ratio. For this reason, a simple application of the ordinary image processing to the X-ray image deteriorates the image quality significantly.

FRX is designed to minimize the deterioration of an image by taking into consideration the expansion of electron beam calculated from the analysis conditions as a parameter. In its application, a recursive calculation is carried out, and sharpening is made to remove only the blurring component predictable from the expansion of electron beams.

## Effects

Supposing that the X-rays image blur follows a Gaussian distribution, we tried to apply FRX to image sharpening. We found that such a simple model as a Gaussian distribution brought a great effect (Fig. 14).

When the line profiles before and after the processing are compared, the peaks after the processing are higher than those before the processing, while the valleys are deeper (Fig. 15).

We performed a simulation (Fig. 16) of line profiles of an image blurred with a Gaussian distribution, and reconstructed an image with FRX. Then, we could succeed in reducing the width of blur in the X-ray image to about half. Thus, if an appropriate model is made for the X-ray image blur caused by the scattering of electron beam, we can say that FRX may reduce the amount of X-ray blur apparently to about half.

## Verification of effects of FRX

The use of FRX can visually suppresses the X-ray image blur. To verify the reduction of X-ray image blur in actual measuring conditions, we took the X-ray images under three different conditions of the accelerating voltage, probe current and electron gun, and applied the image processing to them in order to investigate the effect of FRX.

## Experimental results

### ● Change in the accelerating voltage

When the accelerating voltage is changed, the electron scattering area in the sample also changes. Taking this into consideration, we investigated the removal of blur due to the scattering of electrons in the sample (Fig. 17).

The measured data shows that the image blurs are more remarkable with an increase in the accelerating voltage. Processing the image using FRX eliminates the blur and displays all the data more clearly and easily to look. The processed data proves that the image quality is equivalent to the data taken at an accelerating voltage lowered by about 3 to 5kV.

### ● Change in the probe current

When the probe current is changed, the diameter of electron beam also changes. Taking this into consideration, we investigated the reduction of the influence of a large-diameter beam on the blur of an image outline (Fig. 18).

It was found that as the probe current increases, particles appeared thicker. The possible cause is that the distribution of the probe current takes a shape closer to the cylindrical form rather than a Gaussian distribution with a broad skirt.

The data subjected to FRX had a clear

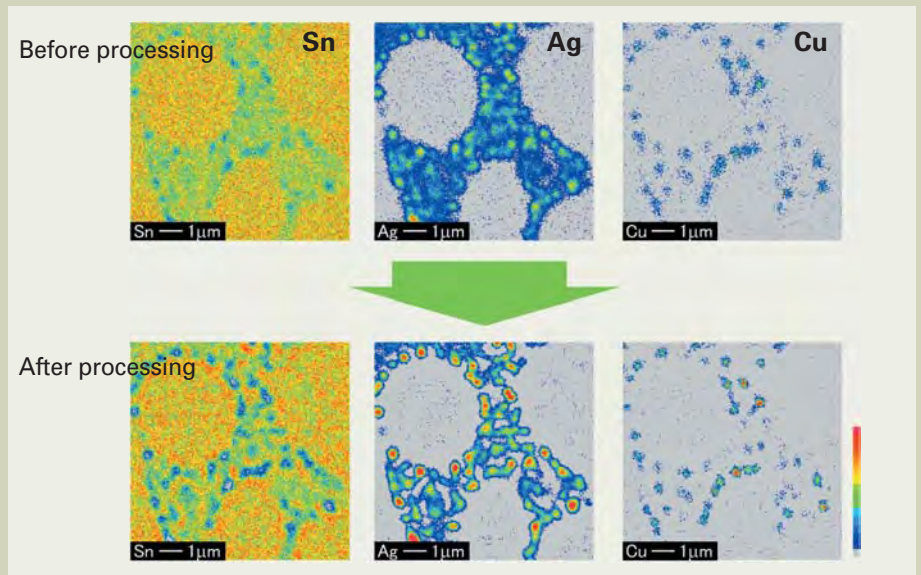


Fig. 14. Example of image processing of X-ray image of lead-free solder. The area of view is the same as that in Fig.7. When the top image is processed using FRX, the bottom image is obtained.

● Accelerating voltage: 8 kV ● Probe current: 10 nA ● Analysis area:  $5\mu\text{m} \times 5\mu\text{m}$

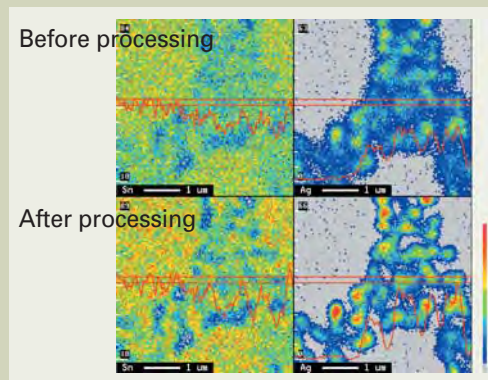


Fig. 15. Line profiles of data without image processing (top) and data subjected to FRX (bottom). The data subjected to image processing has higher peaks and deeper valleys.

● Accelerating voltage: 8 kV  
● Probe current: 10 nA  
● Analysis area:  $5\mu\text{m} \times 5\mu\text{m}$

## Simulation of a line profile using FRX

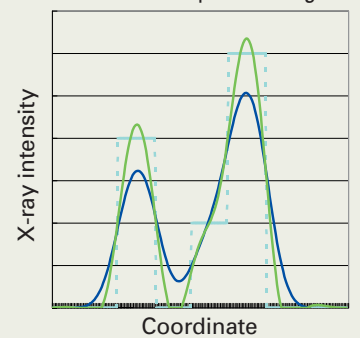


Fig. 16. Simulated data obtained by blurring an original data with Gaussian distribution. Compared to blurred data, the blur of the data after processing is reduced to about half.

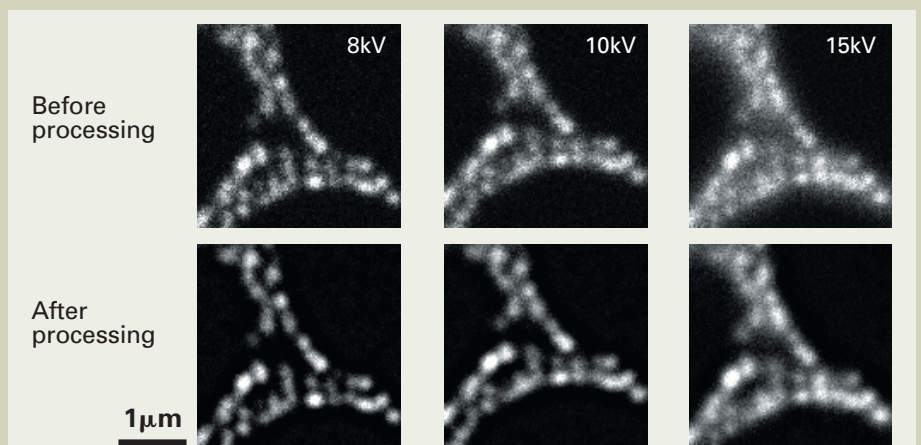


Fig. 17. Comparison between data measured with different accelerating voltage (top) and data processed with FRX (bottom).

● Probe current: 10 nA, analysis area  $5\mu\text{m} \times 5\mu\text{m}$

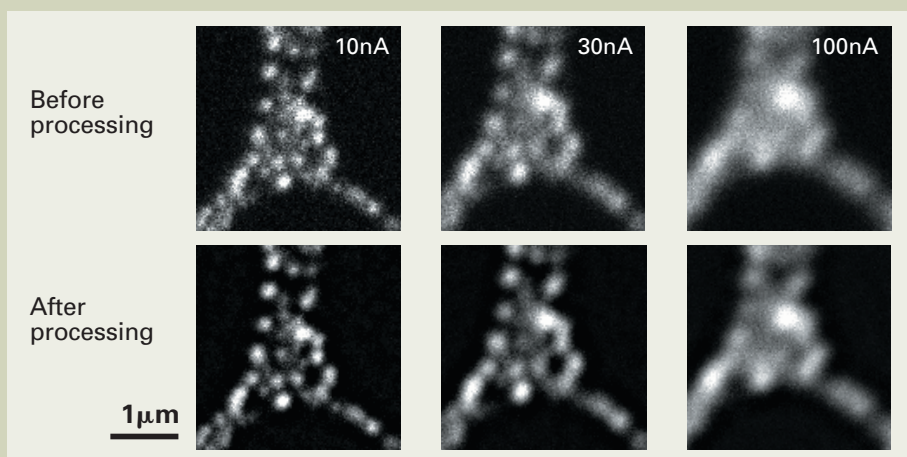


Fig. 18. Comparison between the data measured at various probe currents (top) and the data processed using FRX (bottom).  
 ● Accelerating voltage: 8 kV  
 ● Analysis area:  $5\mu\text{m} \times 5\mu\text{m}$

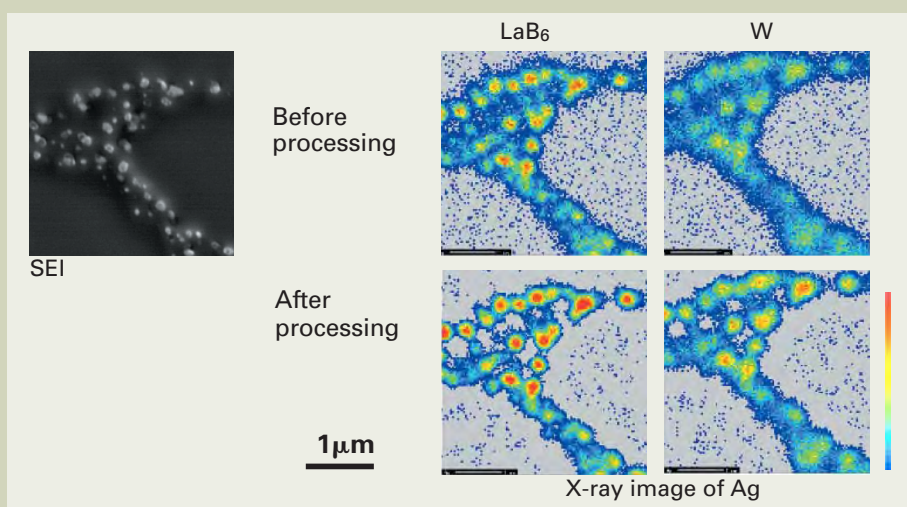


Fig. 19. Comparison among the data taken with LaB<sub>6</sub> tip and W filament.  
 ● Accelerating voltage: 8 kV  
 ● Probe current: 10 nA  
 ● Analysis area:  $5\mu\text{m} \times 5\mu\text{m}$

	Process	Effects
Image synthesis	An X-ray image is masked using a BEI. An X-ray image is synthesized with a BEI through multiplication or division.	It is easy to establish and understand the correspondence between the X-ray image and BEI.
Bi-cubic interpolation	Data points are interpolated between gaps to make the image conspicuous.	Dots of the X-ray image with fewer data points or enlarged image can be made less conspicuous. Since a conspicuous image can be obtained for data with fewer analysis points, the analysis time can be shortened.
Unsharp mask	A blurred image is sharpened.	An SEI or BEI can appear more focused when displayed.
FRX	Image blur due to the scattering of electrons or the expansion of the electron beam is removed from a highly magnified X-ray image.	The blur of an X-ray image is removed, ensuring ease of operation. Applying image processing to data obtained with a W filament makes the data close to one obtained with a LaB <sub>6</sub> chip.

Table 1.

shape free of image blur, but the particle shape was not reconstructed so nicely. This may come from the fact that the Gaussian distribution, which we used as the model of blur of the X-ray image, is not appropriate as the distribution model because of the expansion of an electron beam.

#### ● Comparison between the use of LaB<sub>6</sub> tip and the use of tungsten filament

The use of a LaB<sub>6</sub> tip in place of a tungsten (W) filament narrows the beam. We took the

data with a W filament (W data) and with a LaB<sub>6</sub> tip (LaB<sub>6</sub> data), and these data were processed with FRX (Fig.18.). In the filtered W data, the blur decreased, and the image becomes clear and easy to see, approaching the LaB<sub>6</sub> data. Of course, the best data is the filtered LaB<sub>6</sub> data (Fig. 19).

#### Prospects for FRX

At the present time, FRX calculates the amount of image blur and determines the parameters by inputting physical conditions

such as the accelerating voltage, current and information on the sample. When the FRX is built into an actual EPMA, the instrument can read the accelerating voltage and current from the measuring conditions. Accordingly, the only thing that the user should do is to input the information on the sample.

## 6. Summary

We conducted experiments on four kinds of image processing. The respective results are summarized in Table.1.

# Technology of Measuring Contact Holes Using Electric Charge in a Specimen

Shigemasa Ota, Tooru Ishimoto and Yukihiro Tanaka

Semiconductor Equipment Division, JEOL Ltd.

## Introduction

As a device yield-management technique, semiconductor mass-production plants carry out critical-dimension control of gate lengths and contact-hole diameters in lithography or etching processes using a critical-dimension measurement SEM (Scanning Electron Microscope), as well as process control by means of a visual-inspection SEM capable of detecting defects and classifying factors of the defects [1]. JEOL has developed the JWS series wafer-process inspection system as a visual-inspection SEM. The system has been practically used mainly in defect analysis through high-resolution observation based on defect-coordinate data obtained from a particle-inspection system, and also through element analysis using an Energy Dispersive Spectrometer (EDS). Initially, the system aimed at detecting defects on the wafer surface. Later, the industry began to demand that the system capability be expanded to the field of inspection of defects present inside the device. Along with this, research on the detection of contact-hole defects using secondary-electron images has also been implemented to meet increasing demands for inspection of contact-hole bottoms (residual film, hole diameter) [2]. Also, observation of internal defects, inspection of contact-hole openings, which have not been achieved by means of secondary-electron images, and the possibility for the method of extracting the etching conditions have been studied by utilizing the characteristics [3] of absorbed-current images.

In this study, researchers have faced a variety of problems. One is that slow scan is the only scan mode available due to the restriction of response speed since a direct-current amplifier circuit is used to form absorbed-current images. Another is that obtaining correct image information is difficult because signals are buried in various kinds of noise. The method of inspecting the level of the residual film in a contact hole was reported elsewhere. For example, the EB-Scope technique was developed to electrically inspect the level of the residual film in a contact hole [4]. This technique is based on the proportional relationship between the compensating current that is measured in a specimen when it is irradiated by an electron beam and the thickness of the insulating film deposited on the specimen, or between the former and the diameters of the contact holes (or the total number of contact holes).

In order to precisely detect signals buried in noise, JEOL has recently developed a wafer

process monitor, the i-Checker, that makes it possible to detect changes in electric charge inside a wafer (specimen) very accurately by improving the S/N ratio. The i-Checker gives us numerical information on how deeply and widely the contact hole is open or closed, instead of a mere binary judgment of 1 (open) or 0 (closed), since it can output a sequence of measured values as numerical data. As for information about the bottom of the contact hole, the i-Checker outputs differences in the diameters of contact holes or in the thicknesses of their residual films as the ratio of relative strengths. Therefore, JEOL has been promoting our i-Checker as a support tool for statistical process control (SPC) of etching systems and product wafers, and also for providing appropriate information on etching conditions.

This paper reports the results of stabilization of measured values, which was attempted with a focus on the electric field intensity of the specimen surface, and the applicability and possibility of the i-Checker viewed from the results of the fundamental experiments on this detection technique.

## Principle of Signal Detection

When an electron beam irradiates a specimen, secondary electrons, backscattered electrons, transmitted electrons and Auger electrons (referred to as secondary electrons or backscattered electrons) are generated as a result of the interaction between incident electrons and constituent material of the specimen. The potential changes due to the emission or accumulation of secondary electrons in the specimen as the number of electrons emitted from the specimen or accumulated in it exceeds the number of incident electrons depending on the accelerating voltage or the material of the specimen. When the specimen is grounded under this condition, an electron current flows into the wafer to offset the amount of emission of secondary electrons that occurred as a result of the interaction. **Figure 1** shows schematically the behavior of electrons. Supposing that the specimen is a conductive bulk specimen, the probe current  $I_p$  is expressed by equation (1):

$$I_p = I_{se} + I_{be} + I_{ae} \quad (1)$$

where  $I_{se}$  is the secondary-electron current,  $I_{be}$  the backscattered-electron current, and  $I_{ae}$  the absorbed-electron current that passes through the specimen. For reference purposes, it is reported that the changes in electric charge inside a specimen can be checked by

measuring  $I_{se}$  [5][6]. This principle of signal detection is being applied to semiconductor inspection systems. The i-Checker is a visual-inspection SEM that has a function for measuring  $I_{se}$ .

## Electric Field Intensity of Specimen Surface and Measured Value

**Figure 2(a)** shows schematically the i-Checker measurement model. The specimens to be measured are a 200 mm Si wafer and a 200 mm SiO<sub>2</sub> film/Si wafer. The specimen is regarded as a capacitor since its capacitance ranges from approximately 400 to 650 pF. When a specimen is irradiated by an electron beam, changes in electric charge occur on the specimen surface, and then corresponding changes in electric charge appear on the back of specimen. In our i-Checker system, the capacitance component is added to the underside of the specimen in which the changes in electric charge inside the specimen are accumulated. The i-Checker measures the changes in electric charge in the capacitance component to detect the changes in electric charge that occur on the specimen surface.

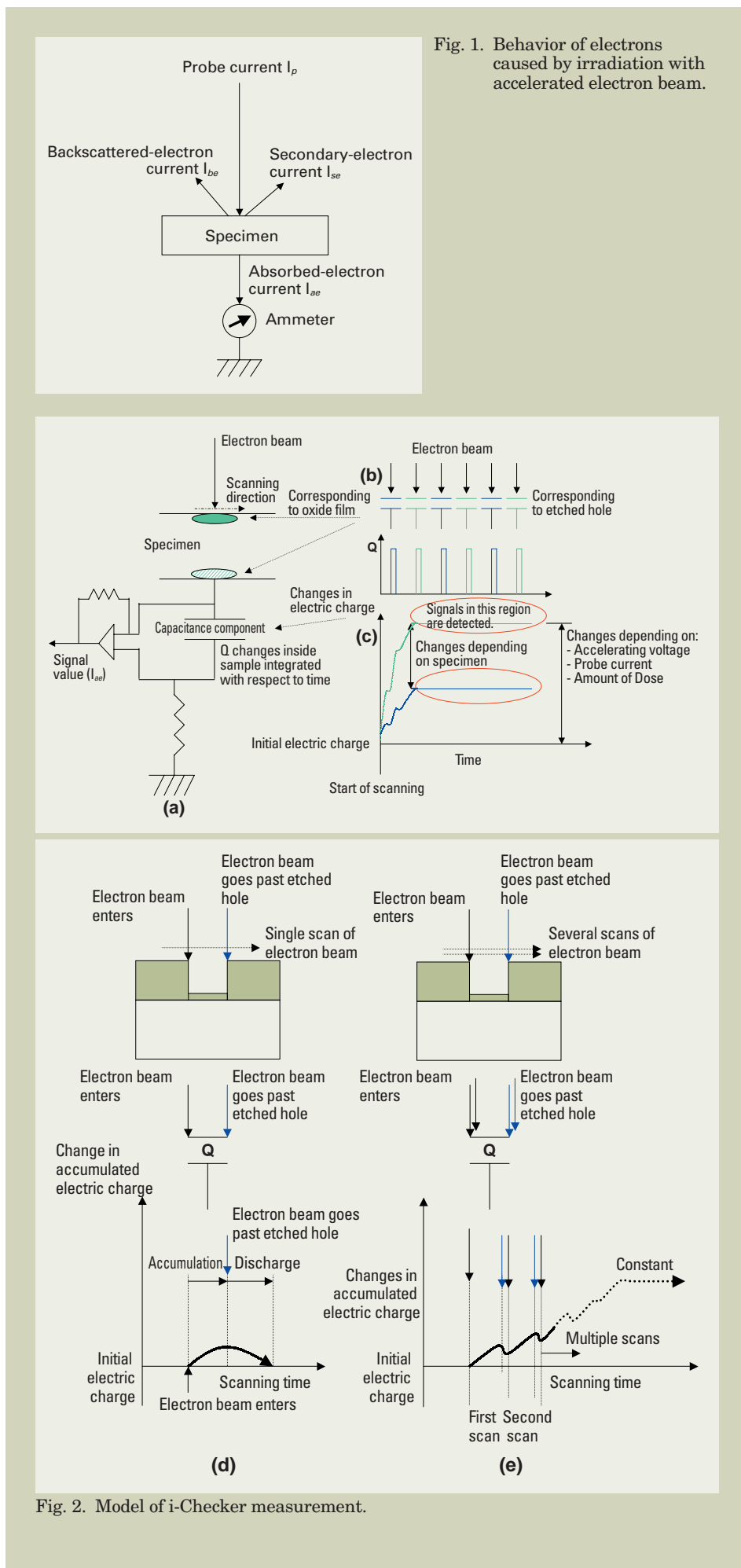
Here is detailed the change in electric charge that are caused by irradiation of an electron beam into the contact hole as the i-Checker irradiates the contact hole with the electron beam while scanning it. This is because the i-Checker is capable of inspecting the area under electron-beam irradiation using the SEM image. More explicitly, information such as the number of holes and their diameters and positions in the observation area can be effectively used as a means of controlling the amount of irradiation of the electron beam on the specimen by varying the scanning distance. Another reason is that the scanning approach is suitable for detecting stable signals at all times. As shown in **Fig. 2(b)**, every change in electric charge occurs at the irradiated point on the specimen surface as if the surface is irradiated by a pulsed beam, since electron-beam irradiation is based on the scanning method. **Figure 2(d)** shows a schematic diagram of these changes in electric charge. For example, when an electron beam enters a hole with a single irradiation, a change in electric charge occurs and the electric charge starts changing from the initial state, and when the electron beam goes past the hole as scanning proceeds, the electric charge returns to the initial state. In actual measurements, the electron beam is

scanned several times over the same area at a high speed. **Figure 2(e)** shows a schematic diagram of the changes in electric charge with this scanning time. In general, a change in electric charge at the contact hole increases from the initial value and returns gradually to the initial value in the case of the first scan. However, as the second scan is performed within a short period of time in high-speed scanning, another change in electric charge occurs before it returns to the initial value after the first scanning. As the scanning time increases, this phenomenon is repeated, and finally the electric charge reaches an equilibrium state. The amount of changes in electric charge when the equilibrium is reached, and the scanning time until the equilibrium is reached, depend on the specimen, the amount of beam dose, the scanning speed and the accelerating voltage.

As shown in **Fig. 2(c)**, by measuring signals from the area where the amount of electric charge integrated with respect to time changes in the capacitance component when the equilibrium is reached, the i-Checker detects the signals as the changes in electric charge on the specimen surface.

Changes in electric charge on the specimen surface influence the behavior of secondary electrons that are generated by the interaction of the irradiated electron beam and the material of a specimen. **Figure 3** shows schematically the behavior of secondary electrons emitted under the irradiation of an electron beam. As mentioned above, when an electron beam irradiates a wafer, secondary electrons are emitted from the hole and the oxide film. However, those secondary electrons, after being emitted, are brought back to the wafer due to the electric-charge balance inside the wafer. Therefore, the changes in electric charge in the equilibrium state shown in **Fig. 2 (c)** decrease, and then they finally go below the detection limit of the measuring instrument. Also, the difference in the changes in electric charge dependent on material becomes small. As a result, not only the difference between the contact holes and oxide film but also the difference in information on the bottoms of contact holes goes below the detection limit, making it impossible to obtain information about the minute differences of residual films in the contact holes with the etching conditions, for example. Besides, as the behavior of the secondary electrons emitted is uncertain, there are variations in measured values. This prevents us from obtaining stable measured values.

In solving these problems, we consider it important to control the emitted secondary electrons. As shown in **Fig. 3(b)**, an electrode plate is installed over the specimen surface in order to capture the emitted secondary electrons using the electric field of the specimen surface. Since this electrode plate can control the amount of secondary electrons that return to the specimen, it is expected that high-accuracy, high-stability measurement becomes practicable along with an increase in the amount of changes in electric charge and an increase in the amount of changes in electric charge due to the material of a specimen as well, as shown in **Fig. 2(c)**. We have verified that this measurement was



effective from the viewpoint of the relationship between the electric field intensity in the vicinity of the specimen surface and the measured values obtained from the i-Checker.

The i-Checker detected the signal corresponding to  $I_{ae}$  in equation (1). From equation (1),  $I_{ae}$  can be expressed as the following equation (1'):

$$I_{ae} = I_p - I_{se} - I_{be} \quad (1')$$

In this research, a 200 mm Si wafer and a 200 mm SiO<sub>2</sub> film/Si wafer were used as specimens to be measured. Therefore, the specimen surface becomes charged when an electron beam irradiates it. Thus,  $I_{ae}$  is expressed as in the following equation (2) by adding the term  $I_{ch}$  to equation (1'):

$$I_{ae} = I_p - I_{se} - I_{be} + I_{ch} \quad (2)$$

where  $I_{ch}$  is an electron current that affects electric charging. According to equation (2), the detecting signal  $I_{ae}$  becomes dependent on  $I_{se}$  and  $I_{be}$  that are generated by the interaction of the specimen and electrons, assuming that  $I_p$  is constant. The yields of secondary electrons and backscattered electrons vary with the accelerating voltage. Consequently, the amount of electrons to be emitted also varies with the accelerating voltage. When the collector electrode is installed in the vicinity of the specimen surface, it is presumed that the subsequent behavior of those secondary and backscattered electrons emitted becomes dependent on  $I_{ch}$  because the electrons are brought back to the specimen surface or captured by the collector due to the relationship between the surface potential of the specimen and the collector potential. Therefore, the detecting signal  $I_{ae}$  depends on  $I_{se}$ ,  $I_{be}$  and  $I_{ch}$ .

**Figure 4** shows the relationship between the electric field intensity on the specimen surface and  $I_{ae}$  as an example of experiment results. In this experiment, we used two types of wafers as specimens, which were irradiated with an electron beam under the following conditions: the accelerating voltage was 500 V, and  $I_p$  was 50 pA. One is a dry-etched wafer in which a contact hole with an aspect ratio of 10 was formed inside the SiO<sub>2</sub> film accumulated on the Si substrate with an SiO<sub>2</sub> film remaining on the bottom of the contact hole (under-etching condition). The other is also a dry-etched wafer; its contact hole passes through the SiO<sub>2</sub> film and reaches the substrate surface (over-etching condition). Measurement was performed on the following two regions: one is an oxide film region including a contact hole (referred to as the etched hole) and the other is an oxide film region where no contact hole is included (referred to as the oxide film). When a positive voltage was applied to the collector, the amount of  $I_{ae}$  at the etched hole shows a decrease in both the under- and over-etching conditions as the surface electric-field intensity increases. Although a similar tendency was recognized at the oxide film, the amount of decrease in  $I_{ae}$  was small compared to the etched hole when the surface electric-field intensity was high. Also, as the surface electric-field intensity increased, the difference in  $I_{ae}$  between the etched hole and the oxide film showed a tendency to widen. A similar

tendency was recognized when the accelerating voltage was raised to 1200 V. Therefore, it is presumed that the amounts of the signals that depend on a contact hole increase along as the electric field intensity on the specimen surface increase.

Next, we simulated the changes in electric charge inside an insulating material such as SiO<sub>2</sub> when an electric field is formed on the specimen surface. We will report the results of the calculations in detail elsewhere. The results indicate that positive holes accumulate on SiO<sub>2</sub>, and the number of accumulated positive holes shows a tendency to increase as the surface electric-field intensity increases (see **Fig. 5**). The results also suggested that positive charging progresses on the specimen surface as the surface electric-field intensity increases. In the experiment shown in **Fig. 4**, we presumed that the amounts of the signals that depend on contact holes increase as the surface electric-field intensity increases. This probably owes to the fact that secondary electrons emitted from the bottom of the etched hole can easily reach the etched hole opening on the wafer top. Thus, we consider that the reason why the amount of secondary electrons that emit outward from the bottom of the hole increases as the surface electric-field intensity and progressing positive charging on SiO<sub>2</sub> increase is the reduction of the potential barrier in the vicinity of the etched hole opening.

On the other hand, when a negative voltage is applied to the collector (see **Fig. 4**), the measured values obtained at the etched hole and the oxide film show a tendency to increase in both the under- and over-etching conditions as the surface electric-field intensity decreases. When a negative voltage is applied to the collector, secondary and backscattered electrons emitted are brought back to the specimen surface. Therefore, it is thought that the  $I_{ae}$  increases apparently since  $I_{se}$  and  $I_{be}$  in equation (2) decrease. Consequently, we consider that the i-Checker is capable of detecting information that originates in the changes in electric charge, which occurs on the specimen surface due to the irradiation by an electron beam.

**Figure 6** shows  $I_{ae}$  at the etched hole in the under- and over-etching conditions at an accelerating voltage of 500 V. We consider that a difference in  $I_{ae}$  depending on the etching conditions was recognized, and that changes in the residual-film on the bottom of the etched hole appeared as changes in  $I_{ae}$ .

## Comparison of Measured Values with Calculated Values

We clearly found that the changes in electron current in equation (2) depend on the charging of the specimen, which varies with the irradiation with an electron beam. In equation (2), assuming that the initial value (the value before the specimen is irradiated by an electron beam) is  $I_0$  and the rate of emission of secondary and backscattered electrons is  $\sigma$ ,  $I_{ae}$  is as expressed in the following equations:

$$I_{ae} = I_0 - (I_p - I_{se} - I_{be} + I_{ch}) \quad (3)$$

$$I_{ae} = \{I_0 - I_p \cdot (1 - \sigma) + I_{ch}\} \quad (4)$$

When measurement is performed on the etched hole,  $I_{ae}$  includes signals from the etched hole and the oxide film. In this measurement, simply assuming that the signal from the etched hole is  $I_{ae}^{hole}$  and the signal from the oxide film is  $I_{ae}^{matrix}$ , and that  $I_{ae}$  is the sum of  $I_{ae}^{hole}$  and  $I_{ae}^{matrix}$ ,  $I_{ae}^{hole}$  is as expressed in the following equation (6):

$$I_{ae} = I_{ae}^{hole} + I_{ae}^{matrix} \quad (5)$$

$$I_{ae}^{hole} = I_{ae} - I_{ae}^{matrix} \quad (6)$$

Assuming that the signals obtained by measuring the etched hole depend on the ratio of etched hole areas,  $I_{ae}^{hole}$  can be further expressed as in the following equation (7):

$$I_{ae}^{hole} = \frac{\left(\frac{D_h}{2}\right)^2 \cdot \pi \cdot N}{r_x \cdot r_y} \cdot I_{ae} \quad (7)$$

where  $D_h$  is the etched hole diameter,  $N$  is the number of etched holes in the irradiation area, and  $r_x$  and  $r_y$  are the lengths of the irradiation area along the X axis and Y axis respectively. We assume that the signal component from the etched hole when the etched hole undergoes measurement can be expressed as in equation (7) above.

Here, in order to verify equation (7), we prepared specimens that are believed to be of the same material and have the same etching conditions and measured their contact holes of different diameters. In this measurement, the accelerating voltage was set so that  $\sigma > 1$ , and the incident current and the scale factor were made constant. When verifying equation (7), we divided both sides of the equation by  $N$ , the number of contact holes in the irradiation area, and obtained an electron current from one hole as shown in equation (7') below.

$$\frac{I_{ae}^{hole}}{N} = \frac{\left(\frac{D_h}{2}\right)^2 \cdot \pi}{r_x \cdot r_y} \cdot I_{ae} \quad (7')$$

**Figure 7** shows the results of the measurement and the theoretical calculation. We used the value of  $\sigma$  taken from the literature [7]. In **Fig. 7**, a circle indicates the experimental value, and a solid line indicates the calculated values. When  $I_{ch} = 0$  (the influence of electric charging is disregarded) in equation (4), there is a big difference between the measured values and calculated values. Since it can hardly be thought in a practical situation that the specimen surface is not charged at all, we made calculations for various values of  $I_{ch}$ . As a result, we can see that the measured values show a tendency to match the calculated values as  $I_{ch}$  increments. According to this fact, although  $I_{ch}$  has a considerable influence on  $I_{ae}$ , we are confident that the utility of the model proposed in this report, which measures the changes in electric charge on the specimen surface, has been proved qualitatively.

Based on the results explained above, **Fig. 8** shows the results of measurement of contact holes, which was performed after the surface electric-field intensity had been optimized.

As a result of comparison of signals from a single contact hole, a difference in signals was recognized between the etching conditions A and B. The repeatability in this measurement was  $< 0.003 (3\sigma)$ . This suggests that signals from a single contact hole can be identified adequately, and that a stable measurement is attained by the optimization of the surface electric-field intensity.

We note that  $I_{ch}$  is a current generated by undergoing electric charging, and that any change of  $\sigma$  that depends on time and migrating components of electrons is ignored in this calculation. We are planning to extract and model these components for further developing the models proposed in this report.

## Application and Expansion of Current Images

Now,  $I_{ae}$  has shown a capability of capturing signals from the etched hole bottoms of wafers that undergo different etching processes. Initially, JEOL has researched and developed the technique of observing the bottom of an etched hole through images. The i-Checker can effectively obtain secondary electron images (SEI) because it was developed based on the visual-inspection SEM. By incorporating in it an additional function to obtain current images (i-Image) that shows the effects of  $I_{ae}$ , both secondary-electron images and current images can now be obtained.

Figure 9 shows a comparison of a cross-sectional secondary-electron image of a contact hole after FIB (focused ion beam) etching and an i-Image. This experiment was carried out at our Application Research Center. As is clear from the observation of cross-sectional images, when the brightness of a contact hole on an i-Image was low, there was an oxide film at the bottom of the hole. Therefore, this suggests that it is practicable to obtain information about the bottom of the contact hole by means of an i-Image as well.

For this purpose, we examined the interrelationship between the surface electric-field intensity and the i-Image using a variety of specimens that had been etched under

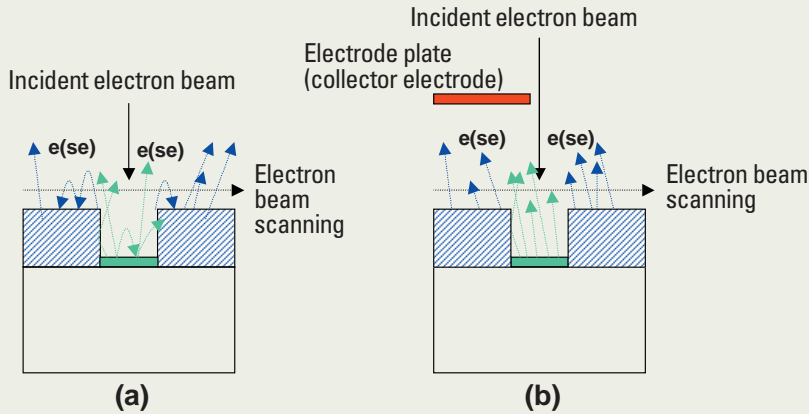


Fig. 3. Emission of secondary electrons under electron-beam irradiation.

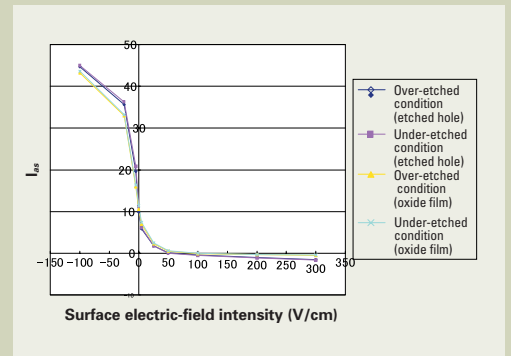


Fig. 4. Influence of surface electric-field intensity on  $I_{ae}$  (measured value) under the following conditions: Accelerating voltage: 500 V, incident-beam current: 50 pA

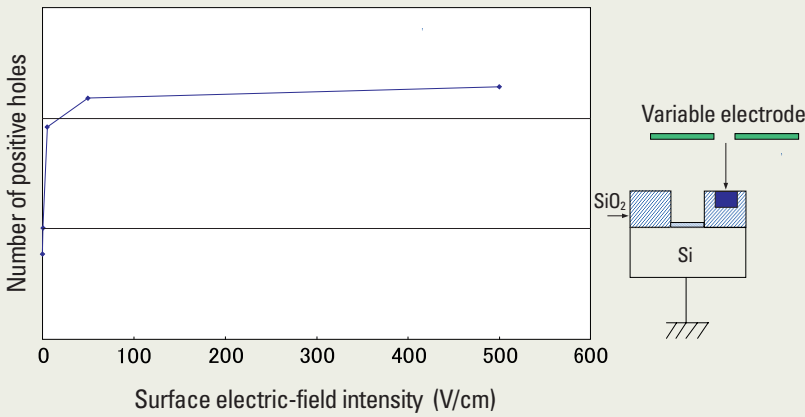


Fig. 5. Calculated number of positive charges near contact-hole opening and surface electric-field intensity.

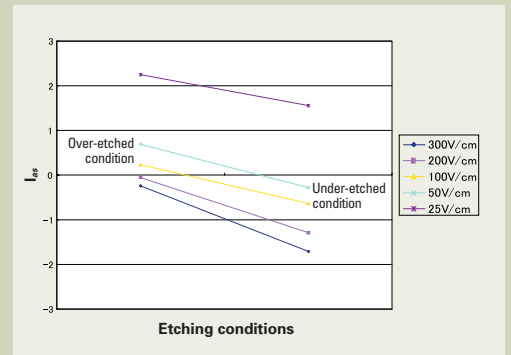


Fig. 6.  $I_{ae}$  (measured value) changing with etching conditions: Accelerating voltage: 500 V, probe current: 50 pA, aspect ratio: 10

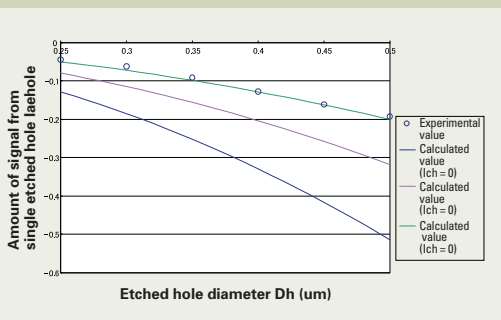


Fig. 7. Relationship between measured and calculated values of signals from an etched hole and etched hole diameter.

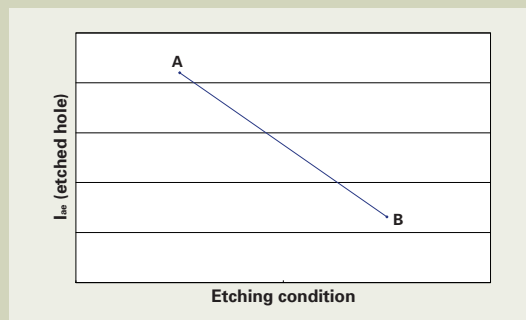


Fig. 8. Measured results of contact holes under optimized measurement conditions: Repeatability  $< 0.003 (3\sigma)$ .

different conditions. After the acquired i-Images were processed by brightness compensation and noise reduction, we obtained from the i-Image the data on the number of pixels and the gray scale for the contact hole bottom. **Figure 10** shows the dependence of the brightness from the area corresponding to the etched hole in the i-Image on the etching conditions for various surface electric-field intensities. The difference in the etching conditions was recognized as a difference of the mean brightness along with an increase in the surface electric-field intensity. We consider that the reason why the changes in electric charge took place at the etched hole bottom is that secondary electrons emitted from the etched hole bottom to the outside of the etched hole increased as the surface electric-field intensity increased. Therefore, it can be suggested that an i-Image makes it possible to obtain information about the bottom of the etched hole that underwent etching under different conditions and to obtain the information more sharply by further intensifying the surface electric-field intensity. In this experiment, a specimen with an aspect ratio of 10 was used. We think that it is feasible to obtain information about a larger aspect-ratio specimen by using the i-Image.

**Figure 11** shows an example of i-Image observation of contact holes. In this figure, the places A correspond to etched holes, but B seems to be affected by contrast from other areas. In observation using a secondary-electron image, no contrast that implies the existence of portion B was recognized. We presume that this is because the conditions of the changes in electric charge are different from those in the surrounding areas due to the presence of defects inside the oxide film. The cause of this has not been clearly determined yet. However, it is shown that use of an i-Image may make it practicable to obtain information on the inside of the oxide film, which cannot be observed through a visual inspection from the surface.

The results of this experiment show a possibility that an i-Image makes it possible to obtain differences in information on the bottoms of etched holes etched under different conditions. We will continue to develop the possibilities for collecting information on the bottoms of each hole one after another and observing high-aspect-ratio holes.

## Summary

Aiming at high-accuracy and high-stability measurement using the i-Checker, we have conducted this research, with an emphasis on the surface electric-field intensity. The results of the research are summarized as follows:

1. This research shows the capability of measuring, as an electrical signal dependent on the surface electric-field intensity, differences in information on the bottom of a contact hole, which vary with differences in etching conditions. This is due to the fact that the i-Checker detects signals caused by changes in electric charge that occur due to the interaction between the specimen and an electron beam.
2. This research shows that highly precise and stable measurement can be performed by optimizing the surface electric-field intensity.

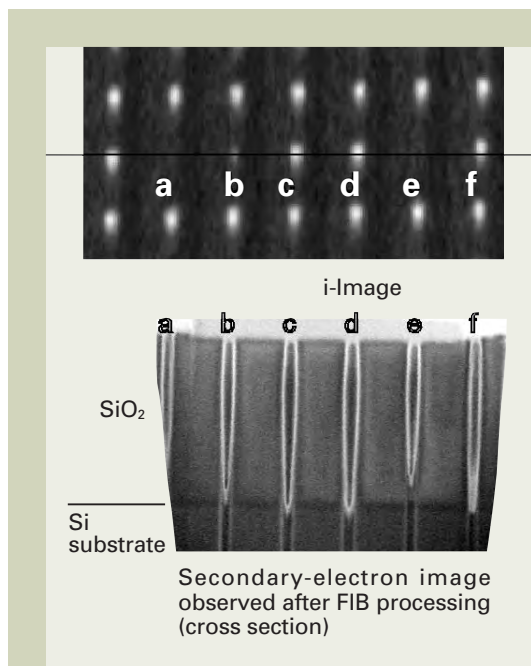


Fig. 9. Comparison of i-Image (top view) and secondary-electron image (cross-sectional view).

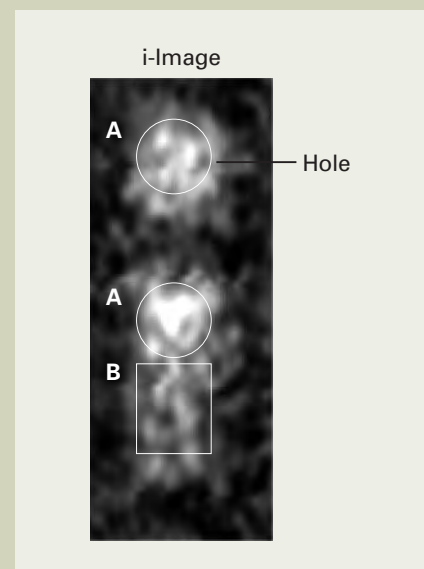


Fig. 11. Example of observation of a contact hole using the i-Image.

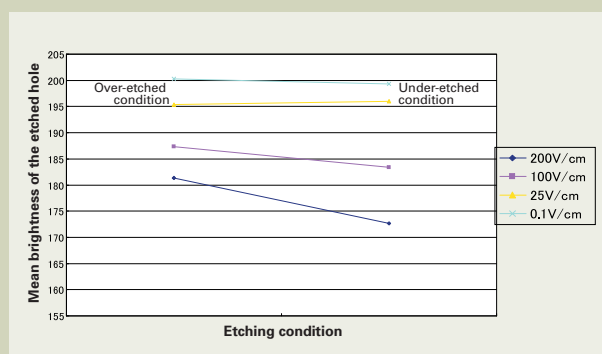


Fig. 10. Relationship between the mean brightness of a contact-hole bottom and etching conditions obtained using the i-Image: Aspect ratio: 10.

3. This research shows the capability of measuring, as an electrical signal dependent on the surface electric-field intensity, differences in information on the bottom of a contact hole, which vary with differences in etching conditions.
4. The measurement models I proposed show the capability of obtaining information on the bottom of a high-aspect-ratio contact hole owing to the surface electric-field intensity.

## Acknowledgement

This research is subsidized by the 2001 Assist Project for Industry Engineering Practical Development (Assistance Program for Development of High Technology Semiconductor Manufacturing Technique) of the New Energy and Industrial Technology Development Organization (NEDO). I express my gratitude to Mr. Tsutomu Negishi, Mr. Yuki Ono and Mr. Naoki Kikuchi of JEOL Application Research Center for excellent assistance for achieving this research.

## References

1. H. Fujioka, S. Okayama, J. Electron microscopy: Vol. 35, No. 1, 41-43 (2000).
2. K. Ono et al.: LSI Testing Symposium Minutes, 32-37 (1997).
3. Scanning Electron Microscope: Edited by Kanto Branch, Microscope Society of Japan, Kyoritsu Publishing Corporation (2000).
4. K. Yamada: IDEM Tech. Dig., 483-486 (1999).
5. H. Takahashi et al.: JEOL News, Vol. 33, No. 1, 38-42 (2001).
6. S. Ikeda et al.: OYO BUTURI, Vol. 56, No. 1, 97-105 (1987).
7. H. Seiler: *J. Appl. Phys.*, Vol. 54, No. 11, R1-R18 (1983).

# Organic EL Display Production Systems – ELVESS Series –

Yuji Yanagi

Tokki Corporation

## Introduction

Intensive research and development of organic electroluminescence (EL) displays in the industry started in 1987 when Kodak Company announced development of such display. As a result of concerted R&D efforts, organic EL displays have now reached the stage of practical applications. In 1997, Pioneer Corporation marketed organic EL displays used for car-mounted electronic equipment, and attracted attention of most of people. Since then, organic EL displays have also been incorporated in cellular telephones. Recently, the organic EL displays have gained more attention since they appeared as prototype full-color displays in both passive and active types presented at many exhibitions.

There are two types of light-emitting materials available for organic EL displays; one is small-molecular material, and the other is polymer material. The development of small-molecular materials has produced mono-color dot-matrix, and area-color type display panels in the market. Full-color display panels using small-molecular materials are also expected to appear in the market soon. In addition, display panels that employ polymer materials have come to the commercial stage.

Compared to LCDs, organic EL displays are self-emitted, featuring higher visibility and less thickness across the entire panel. Thus, great expectations are being placed on organic EL displays as the next-generation ultra-thin displays that will be utilized in a wide variety of fields. Especially, the cellular telephone market is considered to be very big. Development race in this sector is thus expected to intensify, as this market continues to have a growing future.

Since the organic EL display market has been enlarged, the development of organic EL materials has also made an outstanding progress. In this context, the display panel industry is increasingly demanding mass production systems of organic EL displays. To meet this demand, we, Tokki, have developed organic EL Vacuum Evaporation and Sealing System (abbreviated to ELVESS) in technical collaboration with a leading display panel

manufacturer. In this paper, the ELVESS, used for mass production of small-molecular organic EL displays, is presented in terms of system configuration, features, and future requirements and challenges for the system.

## Production of Organic EL Displays

The production process of commercial organic EL displays that employ small-molecular materials is outlined below.

High-density photolithographic patterning technique, used in semiconductor and LCD production, cannot be applied to the production of organic EL displays because moisture absorbed into organic layers and high-energy particles are hazardous to the organic light-emitting materials. Due to this limitation, vacuum-evaporation techniques using a mechanical shadow mask are still fully used to create organic light-emitting layers and metal-wiring network films. At present, it is therefore difficult to produce large-sized, high-precision, high-density, organic EL displays. As a result, the commercial production of these displays is limited to small displays.

A schematic diagram of organic EL display structure is shown in **Fig. 1**. Organic layers are vacuum-evaporated on a glass substrate on which an ITO film that functions as an anode is patterned. Then, a metal film serving as a cathode is vacuum-evaporated on the top of the organic layers via a shadow mask. After these processes finish, the vacuum-evaporated organic layers can emit light. However, as mentioned earlier, moisture in the air has a bad influence on organic layers. If such layers subjected to the adsorption of moisture are used as a display, the moisture causes dark spots to appear on the display, thus making a display screen faulty. To avoid making such a defective screen, it is necessary to seal off the organic layers to prevent the moisture adsorption. To achieve this, UV adhesive agent is used to firmly seal the organic layers with an adhesive encapsulation cap. At the same time, moisture absorbent must be included inside the encapsulation cap because moisture can pass through the sealing agent with the lapse of time.

**Figure 2** shows the flow of organic EL display production process. The production process consists of pretreatment (cleaning of substrates), organic-layer deposition, metal-

layer deposition, and encapsulation processes. Our research has shown that the continuous processing from layer deposition to encapsulation is the key system design for production of small-molecular organic EL displays. This design concept is integrally employed throughout the ELVESS Series; i.e. from prototype models to commercial mass production systems.

## Organic EL Display Production Systems

The Try-ELVESS shown in **Fig. 3** has the minimum requirements for continuous processing from layer deposition to encapsulation. This system was designed to meet demands of makers who need a trial production system. Although this system is compact, the concept to integrally perform the layer deposition to automatic encapsulation is realized with high reliability.

We have a system used for small-volume production and trial production called the Small-ELVESS whose external view is shown in **Fig. 4**. This system features a construction to separate the organic-layer deposition chamber and metal-layer deposition chamber, and provide a mask stock chamber, thus making it possible to perform both small-volume production and trial production. For trial production, it is essential to providing a stable automatic encapsulation. The Small ELVESS satisfies this criterion by using the multi-chamber layout.

**Figure 5** shows the block diagram of the mass production system. This system features a coupling of the vacuum-evaporation and encapsulation processing systems. These features achieve a multi-chamber layout that consists of two transfer chambers and several processing chambers. Each transfer chamber is located at the center of respective processing systems, and several processing chambers, such as the vacuum-evaporation chambers and the encapsulation chambers, surround each transfer chamber. Each processing chamber proceeds to a specific process and the finished works are transferred to the downstream chamber for the next process in accordance with tact time. The chambers for vacuum-evaporation system operate in the vacuum environment, while those for the encapsulation system function under the dry N<sub>2</sub> gas environment.

The key design features of the mass produc-

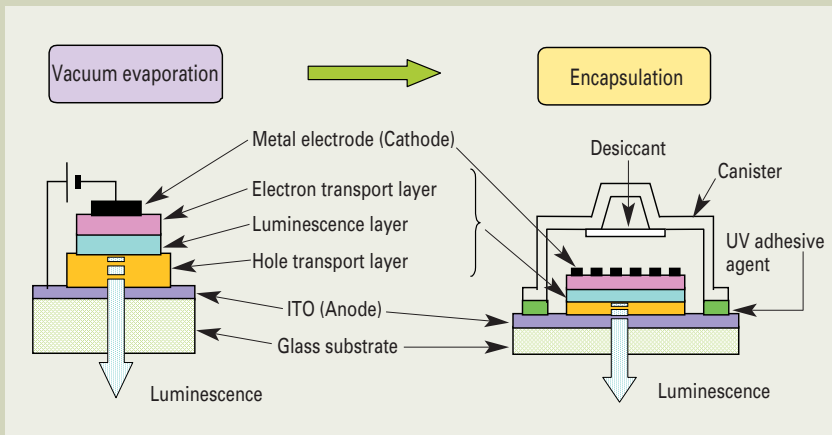


Fig. 1. Schematic diagram of organic EL display structure.



Fig. 3. Try-ELVESS.

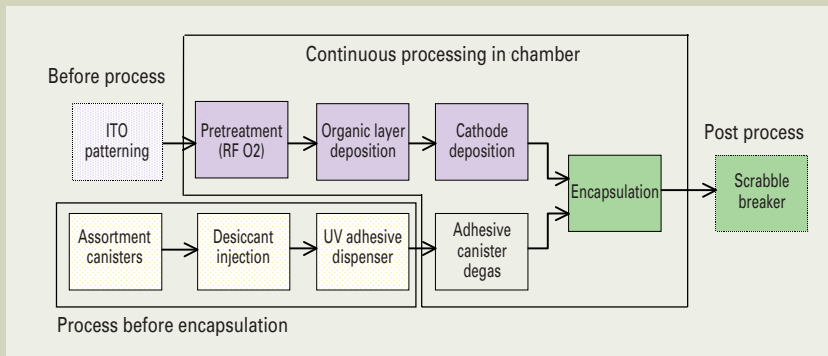


Fig. 2. Flow of organic EL display production process.



Fig. 4. Small-ELVESS.

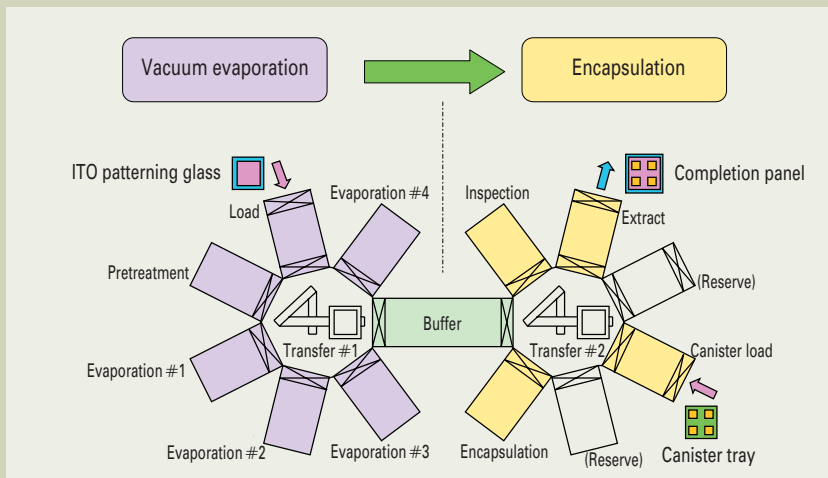


Fig. 5. Block diagram of the mass production system.



Fig. 6. Vacuum-evaporation system of ELVESS.

tion system is shown below:

- A full automatic continuous production line of integrated organic EL-layer deposition and encapsulation process.
- A completed display panel is produced one after another by simply supplying ITO-patterned glass substrates and encapsulation caps.
- The system is designed to carry out production for longer hours with an automatic feeding and a capacity to stock a large amount of starting materials.

This system has a multi-chamber layout designed for mass production with high productivity by integrated processing from vacuum-evaporation process to encapsulation. A stable quality control is achievable backed by this integrated mass production. The external

view of the vacuum-evaporation system is shown in Fig. 6.

In the commercial production of organic EL display panels, the improvement of the encapsulation process is the key factor, and all display panel manufacturers have focused their efforts on solving this issue. To establish know-how to enhance encapsulation technology is the key point to mass production of highly reliable, high-quality organic EL display panels.

In mass production, in addition to the deposition and encapsulation procedures, the process that was discussed in Fig. 2 for desiccant packing and adhesive coating process is highlighted as a unique technique for the organic EL display production, which are essential and very important to make reliable and quality display

panels.

## Requirements and Challenges for Organic EL mass production system

There are some specific requirements and challenges related to the production of organic EL displays and the countermeasures are mentioned below:

### Organic-layer deposition

The organic-layer deposition process is done at a low temperature under high vapor pressure. The deposition parameters are rather unstable where a slight temperature rise will rapidly increase the evaporation rate, causing bumping to easily take place. For a long time

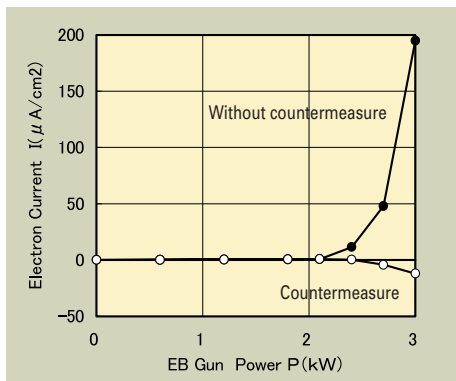


Fig. 7. Effect of the countermeasures against secondary electrons.

and continuous deposition run, a large-capacity evaporation source is required, and a special design is used to avoid the effect of bumping.

### Metal deposition

The metal-deposition process is done at a high temperature under low vapor pressure, where thick-film deposition is required. Since the deposition is done at a high temperature, the substrates, shadow masks and chambers receive strong thermal stress. As it consumes a large volume of evaporation material, an automatic material feeder is needed. In the ELVESH Series, a JEOL Electron Beam (EB) gun for vacuum evaporation is employed. The advantage of this device is to heat the material to be evaporated only, and give less thermal effect to adjacent provisions. The EB gun deposition provides an easy automation for material feeding in the long-term production.

However, the EB gun deposition brings a problem to cause degradation in the spectral characteristics of the organic light-emitting layer due to secondary electrons. Therefore, when the EB gun deposition is employed, it is necessary to provide enough measures against the secondary electrons. **Figure 7** illustrates

the effect of the countermeasures against the secondary electrons. From Fig. 7, it can be understood that, without the countermeasures, a large amount of electron current is generated during evaporation of the materials. This current is significantly reduced to a slight ion current level by adequate countermeasures.

### Encapsulation

It is important to continuously and integrally process the works from vacuum evaporation to encapsulation in a vacuum and low humidity environment. The key points in the process are non-exposure of the works into the air and elimination of humidity. In mass production, numerous display panels are batch-encapsulated under controlled-pressure application and highly accurate jig maneuver.

Currently, encapsulation by using thin film is still being under study. In the total evaluation, considering reliability, costs and productivity, we should adhere to the encapsulation using a solid structure like encapsulation caps or glass encapsulation plates in the commercial production of the display panels at the current stage.

As for the positional alignment between the glass substrate and encapsulation cap, a CCD alignment system is applied to meet the high accuracy positioning.

### Future Challenges for Organic EL Display Panel Production

At the present stage, the products of mono-color and area-color display panels have just placed in the market. However, the demand for mass production system of full-color displays is becoming stronger day by day.

In the production of the full-color EL displays, challenges to be solved include the miniaturization of patterning, and the development of large-sized substrates. In mass production, development of large-sized, high-accuracy shadow masks at reasonable costs is a stringent market demand. For the production of small-molecular organic EL displays, it is

essential to creating RGB layers by deposition that needs high-accuracy, microscopic shadow masks.

Since a glass substrate bends due to its own weight, a more accurate positioning system for alignment of the substrate and shadow mask is needed in accordance with the increasing trend of large-sized and thin lamination of the glass substrate.

At present, the organic materials are very expensive, and therefore, the improvement of usability of organic materials is also a hurdle to be cleared for cost reduction.

In addition, display panels are evolving toward larger size and thinner lamination. Also, the replacement of glass substrates with plastics plates or films is now under way. To meet this industrial trend, a film-encapsulation technology, which achieves highly sufficient reliability and durability, must be developed to replace the current techniques that use structure designs such as encapsulation caps and plates.

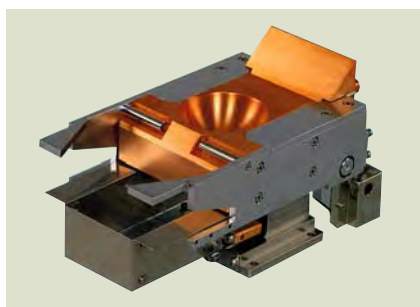
### Conclusions

Small-molecular organic EL production systems have been briefly reviewed. And, we have concluded that, for the organic EL mass production systems, the key point is to integrate automatic encapsulation unit into the system.

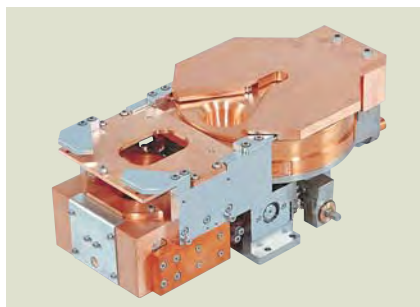
In the production of organic EL display panels, the film-encapsulation technology is indispensable and must be integrated into the system. We are focusing our manpower and resources on the development and establishment of film-encapsulation technology and systems to be integrated in our ELVESH Series.

Recently, prototype samples of polymer organic EL display panels have sequentially been announced, and their commercial production is also approaching. It is our positive commitment to develop mass production systems of polymer organic EL displays.

The photos on the right are JEOL electron beam guns for vacuum-evaporation and power supply. They are utilized for Tokki ELVESH series.



JEBG-163MB Electron beam gun.



JEBG-203UB Electron beam gun.



JST-10F EB power supply.

# In-Situ Observation of Freeze Fractured Red Blood Cell with High-Vacuum Low-Temperature Atomic Force Microscope

Keiichi Nakamoto<sup>†</sup>, C.B. Mooney<sup>††</sup> and Shin-ichi Kitamura<sup>†</sup>

<sup>†</sup>Electron Optics Division, JEOL Ltd.

<sup>††</sup>JEOL USA, Inc.

Freeze-fractured human Red Blood Cell (RBC) has been observed directly with a high-vacuum low-temperature Atomic Force Microscope (AFM). This AFM has an integrated vacuum system and a freeze-fracture mechanism inside the vacuum chamber. The AFM is able to observe the fractured RBC surface without exposing the ambient atmosphere. Then this AFM is possible to observe the fractured surface directly without making metal replica. Sandwich mount cleave and knife fracture techniques are used to obtain a freeze fracture surface, and therefore, after deep etching, a fine structure of membrane has been observed by both methods. This membrane bi-layer structure is obviously different from membrane surface structure. These methods are very rapid and easy ways for observation of freeze fracture surface without replica artifact. Also, we demonstrate the feasibility of these methods using AFM for freeze fracture in-situ observation.

Key words: AFM(Atomic Force Microscope), Freeze fracture, Red blood cell, high vacuum, low temperature, in-situ surface observation.

## Introduction

The Atomic Force Microscope (AFM) is of interest for imaging biological samples because of the extreme resolution in all three dimensions together with the ease of sample preparation [1 to 3]. Samples can be imaged directly without the need to coat or take thin sections of material as required routinely for Transmission Electron Microscopy(TEM) observation. It is also possible to image biological samples in physiological fluids [4]. TEM can be used to investigate the morphology of a variety of biological samples, but, the tissue must be frozen or/and dried [5]. More complicated techniques such as freeze-fracture, replication, etc. are necessary for the study of surface structure [6]. Surface information is thus obtained in an indirect manner and carries the risk of producing artifacts. In comparison with conventional TEM techniques, AFM has the advantage that the sample preparation procedures are relatively simple and convenient, and also staining and/or coating is not necessary. While many research groups have reported imaging of biological materials in air or in fluid, there have been few reports of freeze-fracture surface observations [7, 8]. This is very likely because there are few AFMs that are suitable for biological samples, i. e. that can operate under freezing without significant ice formation [9]. We will present an experimental setup of a freeze-fracture mechanism in an AFM chamber that is appropriate for the investigation of biological

freeze-fracture surfaces. We will also present results on the morphology of freeze-fracture surface of human red blood cells (RBC).

## Experiment

### Instrument General

**Figure 1** shows the schematic diagram and photograph of instrument. We modified a commercial AFM (JEOL JSPM-4210) for this experiment [10]. For the investigation of fine structures of a freeze-fracture surface with a low-temperature environment, it is critical to maintaining a high vacuum. For high-resolution imaging, the vibration of the vacuum pump must also be isolated from the imaging chamber. In order to avoid ice crystal formation from residual water in the chamber, the vacuum level should be less than  $1.0 \times 10^{-5}$  Pa. This is the vacuum level, in which the partial pressure of the water vapor is low enough to prevent water adsorption and formation of ice crystals. The vacuum must be maintained during AFM observation. The ultimate vacuum pressure measured with this instrumental configuration is  $8.7 \times 10^{-6}$  Pa.

### AFM head

The AFM head contains the following components, all of which are located inside the vacuum chamber: laser diode, four-quadrant photodiode and pre-amplifier. The cantilever's deflection is detected using the optical beam bounce technique. The laser is aligned before evacuation. Because the head

and the position of the cantilever are held constant during observation. The scanner is a piezoelectric tube with a maximum scan range of  $80 \mu\text{m} \times 80 \mu\text{m} \times 5 \mu\text{m}$ . The scanner is mounted on the XYZ coarse alignment stage. This stage is for positioning the sample under the tip. The stage can be adjusted from outside the vacuum chamber to locate a feature of interest other the sample has been freeze-fractured.

### Vacuum system and vibration isolation

Vacuum evacuation is performed with a 300 L/s magnetic bearing turbo molecular pump (TMP) and a rotary pump (RP). Gel isolators between the TMP and the chamber isolate the AFM from the TMP's vibration. Isolating the vibration of the TMP from the AFM is critical to high resolution imaging during vacuum evacuation. The noise reduction ratio of this configuration is more than -50 dB. The instrument can be baked with an internal heater at  $50^\circ\text{C}$  to  $60^\circ\text{C}$  to improve the vacuum. With this configuration, a vacuum pressure of  $1.0 \times 10^{-4}$  Pa is achieved after about 15 hours of baking. The ultimate vacuum pressure of  $8.7 \times 10^{-6}$  Pa was achieved with liquid nitrogen ( $\text{LN}_2$ ) cooling of the cold finger to cool the sample stage.

### Sample cooling

Sample cooling is performed with liquid nitrogen. We have achieved the sample temperature as low as  $-175^\circ\text{C}$ . In order to observe the sample with very low drift, it is important to maintain the temperature with

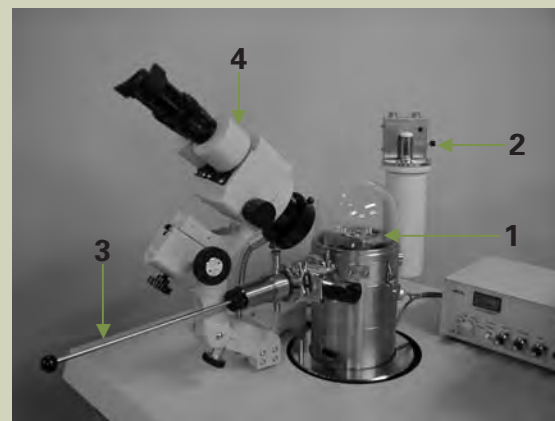
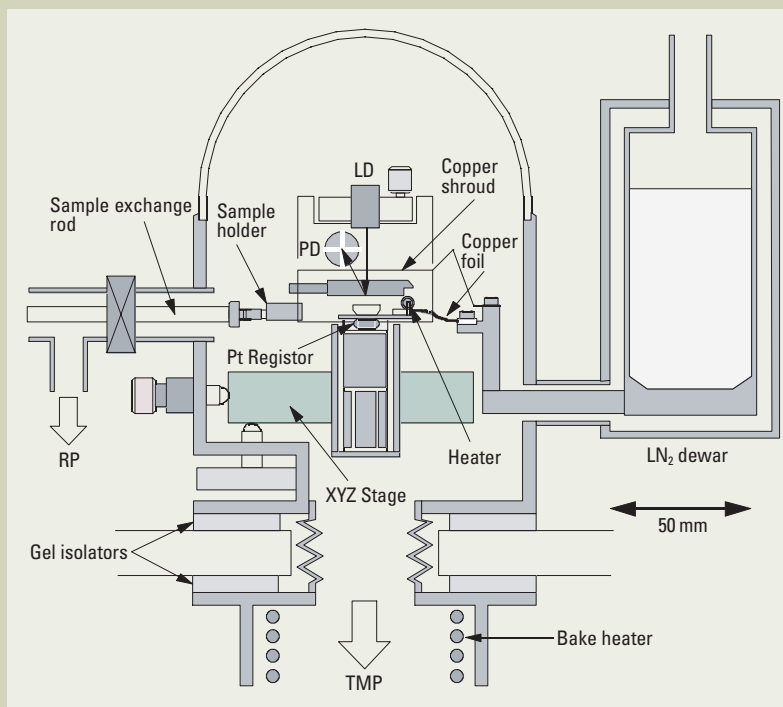


Fig. 1. Cross sectional drawing and photograph of a high-vacuum low-temperature atomic force microscope. (a) The sample holder is cooled via copper foils that are connected to a liquid nitrogen dewar. The atomic force microscope uses the optical beam bounce detection scheme and the piezoelectric tube scanner is located on the XYZ coarse stage. The sample holder stub is transferred by a sample exchange rod. The instrument is evacuated by a 300L/s turbo molecular pump. (b) 1: AFM head, 2: Liquid nitrogen dewar, 3: Sample exchange rod, 4: Optical microscope for sample position alignment.

very little fluctuation. Temperature control electronics are utilized to control the temperature from  $-175^{\circ}\text{C}$  to  $0^{\circ}\text{C}$  with less than  $0.1^{\circ}\text{C}$  fluctuation during observation. To freeze-fracture the sample successfully, the sample temperature needs to be  $-130^{\circ}\text{C}$  or less. After fracturing the sample surface, a deep etch is performed to sublime any ice by maintaining the sample temperature in the range from  $-60^{\circ}\text{C}$  to  $-80^{\circ}\text{C}$ . This experimental setup can also be used for the investigation of any materials at temperatures below  $0^{\circ}\text{C}$ .

A copper cold finger coupled to an  $\text{LN}_2$  dewar is mounted on the AFM chamber. The sample stage can then be cooled via a heat conductor fabricated from ultra-pure copper foils, where one end of the heat conductor is connected to the sample stage while the other end is coupled to the cold finger. The copper foils serve not only to transmit heat but also to decouple the vibration due to  $\text{LN}_2$  boiling. The copper foils also allow for the coarse stage motion as well as for scanning with the piezoelectric scanner. The sample stage can be heated from its terminal temperature of  $-175^{\circ}\text{C}$  to  $0^{\circ}\text{C}$  by a heating resistor (47 Ohm, 0.125 W). It is possible to heat the sample to room temperature with the heating resistor. The temperature of the sample stage can be monitored by a platinum thin film thermistor. The temperature of the sample holder can be controlled in a range from  $-175^{\circ}\text{C}$  to  $0^{\circ}\text{C}$  using a commercially available PID temperature controller that regulates the power dissipated in the resistor. The accuracy of the temperature adjustment is  $\pm 0.1^{\circ}\text{C}$ . The sample holder is thermally isolated from the piezoelectric tube by an epoxy pillar heat

shield.

### Anti frost

A gold coated copper shroud is mounted around the sample holder. The end of the copper shroud is coupled to the  $\text{LN}_2$  cooled cold finger. The shroud temperature is kept at  $-150^{\circ}\text{C}$  during cooling. This copper shroud is designed to prevent surface contamination due to the residual gas adsorption. In particular, water vapor adsorption and subsequent ice crystal growth must be prevented. The sample can be exchanged while the sample stage is cooled and the AFM chamber is evacuated. The sample holder is inserted into the AFM's vacuum chamber via a sample exchange rod that fits a small load-lock chamber. The load-lock is evacuated by the rotary pump.

### Sample preparation

Venous blood from healthy human was drawn and anticoagulated with heparin. The blood was then centrifuged at 2500 g for 10 minutes. Then the plasma supernatant was removed. The remaining red blood cells (RBC) were washed with phosphate-buffered saline (PBS) solution two times, and then centrifuged at 2500 g for another 10 minutes. Before rapid freezing, the glycerol is mixed about 30 vol. % of RBC [11].

### Experiment method

#### Sandwich cleave method

We have developed two methods for freeze-fracture. The first freeze-fracture method is sandwich mount cleave as shown in Fig. 2. A prepared RBC sample is put on a copper

sample holder, which is washed with acid ( $10\% \text{HNO}_3$ ). The sample holder is then rapidly frozen with over cooled liquid nitrogen. The sample holder is attached to the sample holder stub in the liquid nitrogen pool. The sample holder stub is then inserted into the AFM vacuum chamber and installed on the  $\text{LN}_2$  cooled sample stage using the sample exchange rod. Insertion of the sample holder is done as quickly as possible. Next, a hook is attached to sample exchange rod and the sample is fractured by pulling out the upper half of the sample holder. After fracture the sample is moved into position under the cantilever with XYZ coarse movement stage.

#### Knife fracture method

Another freeze-fracture method is knife fracture as shown in Fig. 3. A prepared RBC sample is deposited on an 18K gold sample holder. The sample is rapidly frozen utilizing over cooled liquid nitrogen. This sample holder is mounted on the sample holder stub in the liquid nitrogen pool. The sample holder stub is then inserted in the  $\text{LN}_2$  cooled sample stage via the load-lock and the sample exchange rod as quickly as possible. The sample is moved toward a cooled knife with the XYZ coarse movement stage and fractured with this knife. The fracture may be tried for several times to achieve a surface flat enough to observe with the AFM. After the fracture the sample is positioned under the cantilever with the XYZ coarse movement stage.

### Results and Discussions

In the both methods, the fracture is performed at  $-130^{\circ}\text{C}$ . After the fracture, the

sample temperature is kept at  $-80^{\circ}\text{C}$  for 5 seconds to make deep etching. AFM observation is performed using the slope detection mode at  $-110^{\circ}\text{C}$ . Commercial Si cantilevers are utilized, which have a resonance frequency of approximately 300 kHz. Images with a field of view of  $20 \times 20 \mu\text{m}$  and  $12 \times 12 \mu\text{m}$  with sandwich cleave method are shown in Fig. 4. The scan time is about 10 minutes per frame. A clear fractured RBC surface is observed with no ice crystals visible in the images. We observed the same area many times with no apparent ice crystal formation.

Figure 5(a) shows images with a field of view  $5 \times 5 \mu\text{m}$  and  $2.5 \times 2.5 \mu\text{m}$  with knife fracture method. The magnified P face of RBC is shown in Fig. 5 (b), and the surface RMS height was 2.3 nm. This surface roughness was obviously flat compared with membrane of RBC [11, 12]. A fluid mosaic model explains this structure [13].

Another convenient technique for in-situ observation is the appropriate determination of deep etching time. A fractured surface obtained by knife fracture method is shown in Fig. 6 (a). The image with a field of view  $10 \times 10 \mu\text{m}$  contains knife mark when fractured sample was prepared. The fracture was performed at  $-130^{\circ}\text{C}$ , and the observation performed at  $-110^{\circ}\text{C}$ . After retract the cantilever, the etching was done with  $-80^{\circ}\text{C}$  at 10 seconds. Figure 6 (b) shows the same area and same magnification image after etching, the observation temperature being  $-110^{\circ}\text{C}$  again.

## Conclusions

- 1). We have developed a practical high-vacuum low-temperature atomic force microscope with an in-situ freeze-fracture mechanism. The sample stage is cooled with a Cu foil heat conductor, which is connected to a liquid nitrogen dewar. The ultimate cold temperature is approximately  $-175^{\circ}\text{C}$ . The temperature can be controlled to  $\pm 0.1^{\circ}\text{C}$ . A cold shroud was developed to surround the sample holder for preventing the sample from the contamination due to the adsorption of residual gases and water vapor. The ultimate vacuum pressure of  $8.7 \times 10^{-6} \text{ Pa}$  was achieved with liquid nitrogen cooling.
- 2). We have developed two practical freeze-fracture methods for high-vacuum low-temperature atomic force microscope. A Sandwich cleave method is conventional method to get cleaved surface. A knife fracture method needs more technique, but it can easily get flat cleave surface. Both methods are suitable for AFM observation of freeze-fracture sample.
- 3). We have demonstrated in-situ observation of freeze-fractured red blood cell.

## References

1. Andreas Engel, Yuri Lyubchenko and Daniel Muller, trends in *CELL BIOLOGY*, **9**, 77 (1999).
2. Minoru Takeuchi, Hiroshi Miyamoto, Yasushi Sako, Hideo Komizu, and Akihiro Kusumi, *Biophysical Journal*, **74**, 2171 (1998).
3. Masamichi Aikawa, Shin-ichiro Kawazu,

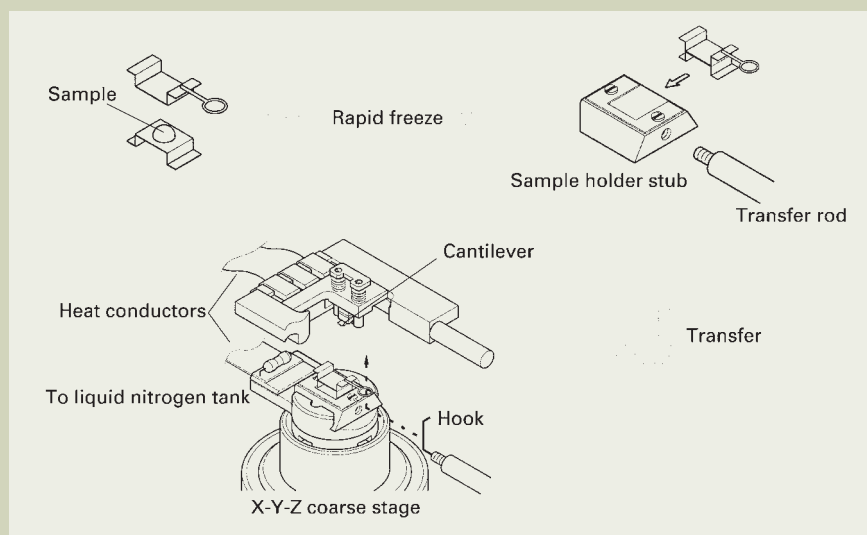


Fig. 2. Sample fracture method one. The sample is deposited on a copper sample holder. Then it is rapidly frozen using  $\text{LN}_2$  and transferred into the instrument with the sample exchange rod. A hook is attached to the sample exchange rod and the upper half of the copper holder is pulled free fracturing the sample.

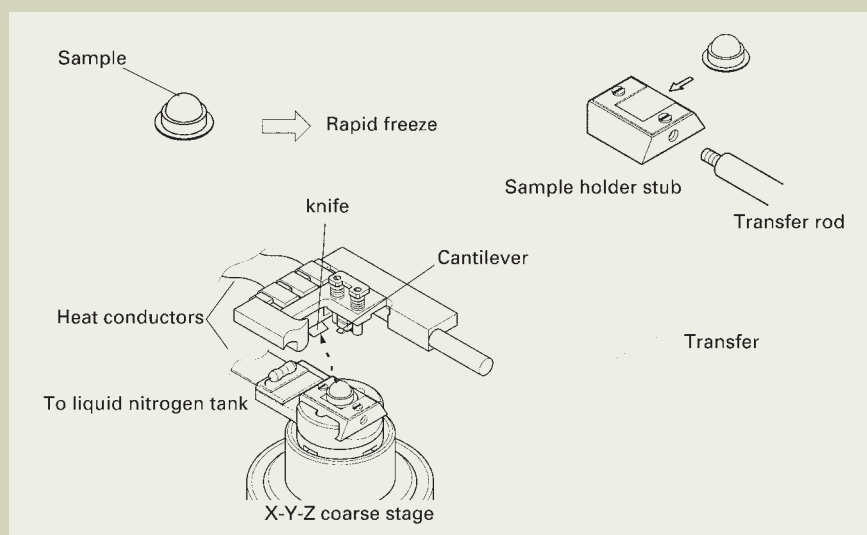


Fig. 3. The second sample fracture method. The sample is deposited on a gold sample holder and then rapidly frozen with  $\text{LN}_2$ . The sample holder is mounted on the sample stub and transferred into the instrument with a transfer rod. The sample is fractured with a pre-cooled knife using the XYZ coarse stage movement.

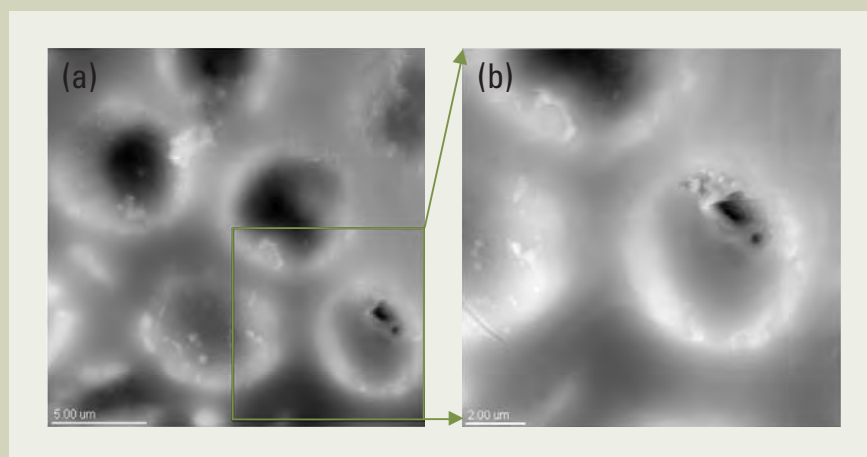


Fig. 4. (a) Topographic image observed using non-contact mode with  $20 \times 20 \mu\text{m}$  scan. The samples are fractured with sandwich cleave method. The temperature of the sample is  $-110^{\circ}\text{C}$ . (b) A zoom up scan image with  $12 \times 12 \mu\text{m}$  scan.

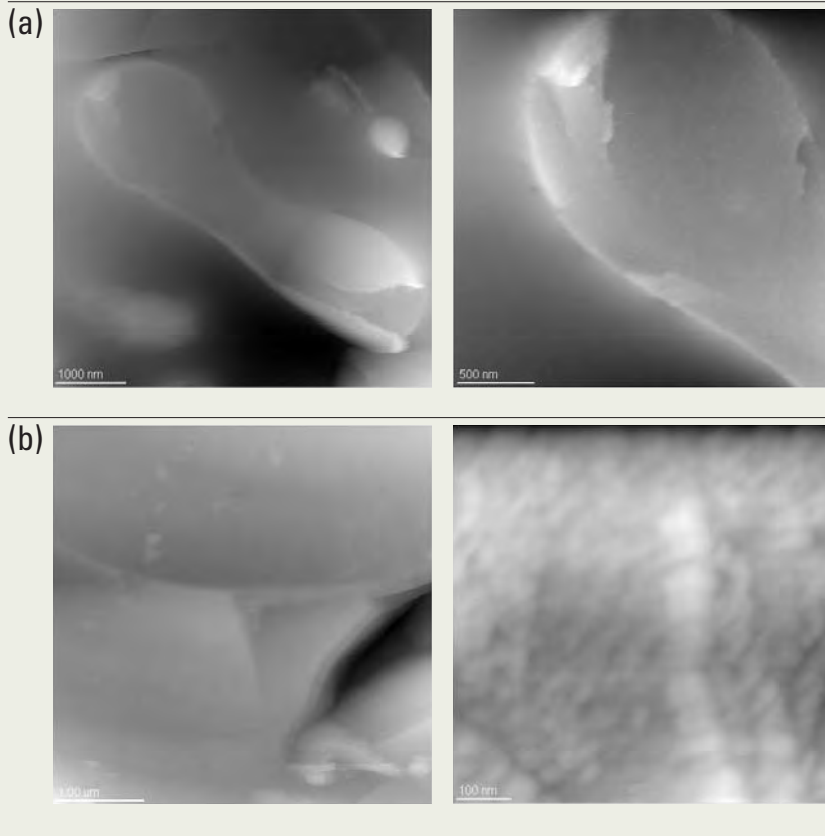


Fig. 5. (a) Topographic image observed using non-contact mode with  $5 \times 5 \mu\text{m}$  and  $2.5 \times 2.5 \mu\text{m}$  scan. The samples are fractured with knife fracture method. The temperature of the sample is  $-110^\circ\text{C}$ . (b) Another topographic image observed using non-contact mode with  $4.5 \times 4.5 \mu\text{m}$  and  $700 \times 700 \mu\text{m}$  scan.

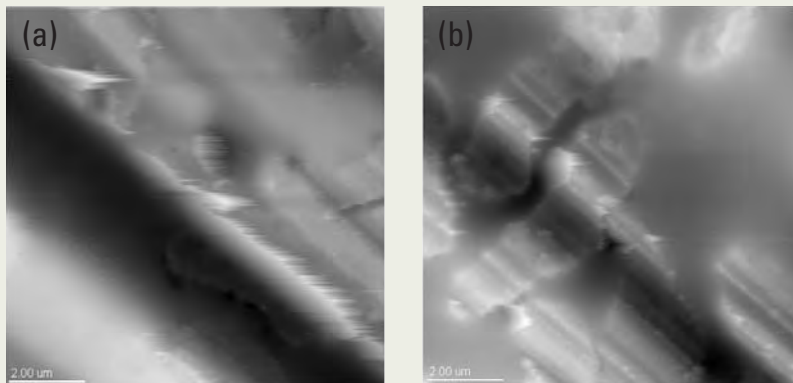


Fig. 6. (a) Topographic image observed immediately after the surface is fractured. The scan size is  $10 \times 10 \mu\text{m}$ . (b) Topographic image after etching at  $-80^\circ\text{C}$  at 10 seconds, scanned area and magnification are the same as Fig. 6(a).

- Tujihiko Kamio, Yoshitsugu Matsumoto, Toshimitsu Naya, Motomi Torii, Yoshihiro Ito, Bernard Tandler, Yamaji Nakano, Tsutomu Takeuchi, Soshi Shiraishi, Kiyoshi Kanamura, *Parasitology International*, **46**, 241 (1997).
4. Achim Linder, Ulrich Weiland, and Hans-Jurgen Apell, *Journal of Structural Biology*, **126**, 16 (1999).
  5. LIU Zhenxia, ZHOU Meiyun, XIE Hengyue, QIAN Ruolan, ZHANG Yi, HU Jun and LI Minqian, *Chinese Science Bulletin*, **43**, 289 (1998).
  6. Rapid freezing, Freeze fracture, and Deep etching, edited by Nicholas J. Severs and David M. Shotton (Wiley-Liss, Inc. New York 1995) p. 32.
  7. Jianxun Mou, Jie Yang, and Zhifeng Shao, *Rev. Sci. Instrum.*, **64**, 1483 (1993).
  8. Zhifeng Shao, Yiyo Zhang, *Ultramicroscopy*, **66**, 141 (1996).
  9. H. Bluhm, S. H. Pan, L. Xu, T. Inoue, D. F. Ogletree, and M. Salmeron, *Rev. Sci. Instrum.*, **69**, 1781 (1998).
  10. Keiichi Nakamoto, C. B. Mooney, and Masashi Iwatsuki, *Rev. Sci. Instrum.*, **72**, 1445 (2001).
  11. P.-C. Zhang, C. Bai, Y.-M. Huang, H. Zhao, Y. Fang, N.-X. Wang, Q. Li, *Scanning Microscopy*, **9**, 981 (1995).
  12. V. Tsai, X.-S. Wang, E. D. Williams, J. Schneir and R. Dixon, *Appl. Phys. Lett.*, **71**, 1495 (1997).
  13. S. J. Singer and Garth L. Nicolson, *Science*, **175**, 720 (1972).

# Peak Deconvolution Analysis in Auger Electron Spectroscopy

Kenichi Tsutsumi, Nobuyuki Ikee and Yuji Nagasawa

Application & Research Center, JEOL Ltd.

## Introduction

Among many methods of analyzing solid surfaces, Auger Electron Spectroscopy (AES) is available to and used in many academic and industrial fields. AES allows analysis of the very top surface less than 5 nm in depth of minute area (a few 10 nm in diameter). However, it is difficult to analyze measured Auger spectrum because the energy of Auger electrons is greatly influenced by the bonding state of atoms. In the case of AES, the spectrum generated by the Auger transition has a complex shape, and it is unable to be obtained by the convolution with the use of Gaussian function and the Lorentzian function unlike in the case of XPS. If Auger spectra were analyzed in detail, the evaluation of the chemical state can also be performed with the elemental analysis, like XPS [1][2][3]. Under the present circumstance, the use of AES is limited to identification and the rough quantitative analysis of elements, and the chemical state analysis in AES is only performed for limited number of elements, actually.

Our Auger electron analyzer (JAMP-7800 series) can measure whole AES spectrum with the energy resolution of 0.6% and up to 0.06% in maximum. As a result, the intensity change and the shape change of the spectrum can be detected more remarkably to show the chemical state change of atoms. In this paper, we introduce some experimental results obtained by the use of this analyzer, which includes quantitative analysis and chemical state analysis based on the detailed peak deconvolution method.

## Importance of Peak Deconvolution Methods in AES

### Isolation of individual spectra from overlapped AES spectra

Auger electrons are a part of a large amount of secondary electrons emitted from the solid surface. Auger spectrum appears as a smaller peak on a large background. In the case of the low concentrated element, its Auger peak is

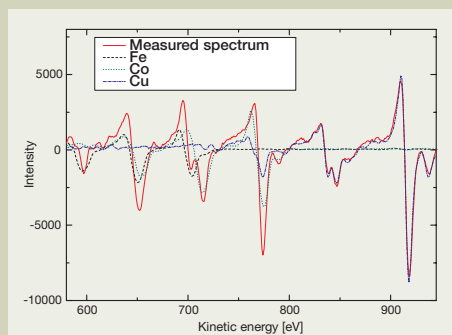


Fig. 1. Spectrum of Fe-Co-Cu alloy and results of deconvolution using the respective standard spectra. (energy resolution: 0.6%)

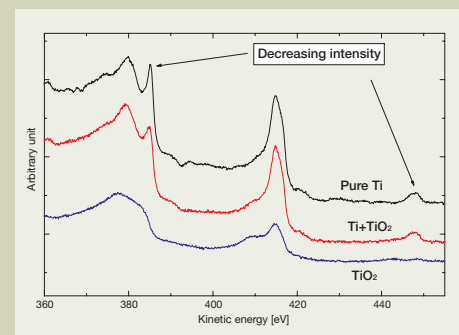


Fig. 2. Changes in Ti spectrum due to the bonding with oxygen (O). (energy resolution: 0.15%)

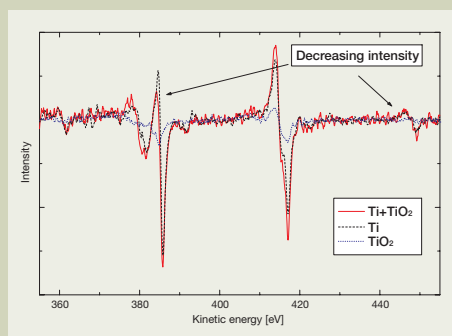


Fig. 3. Result of deconvolution of (Ti + TiO<sub>2</sub>) spectrum using the respective standard spectra.

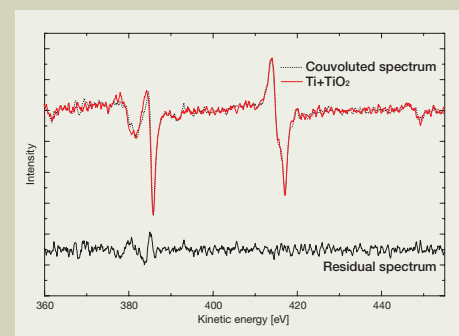


Fig. 4. (Ti+TiO<sub>2</sub>) spectrum, convoluted spectrum and residual spectrum.

	Ti	Ti <sup>4+</sup>	O <sup>2-</sup>	Total
Coefficient to multiply standard spectrum (atomic%)	0.677	0.149	0.283	1.109
Shift amount of standard spectrum	0.0	0.0	0.0	—

Table 1. Results of Fitting (Ti+TiO<sub>2</sub>) by K-value method.

small, and occasionally buried in a big Auger peak of another element or a big noise due to statistical fluctuation. On the other hand, measured Auger spectrum is often different from its original one because of multiple overlapping spectra. These are reasons why qualitative/quantitative analysis is difficult and complicated. With the peak deconvolution method, it is possible to isolate individual Auger peaks and perform the qualitative/quantitative analyses for every component elements accurately.

As an example, **Fig. 1** shows an Auger spectrum obtained from an Fe-Co-Cu alloy and the results deconvoluted to each spectra. Even if the measured spectrum were very complex, it is possible to isolate it to respective spectra by the use of the peak deconvolution method based on the standard spectra.

### Detection of the change in Auger spectrum due to chemical state difference

Auger spectrum is often different from the original one as a result of spectrum overlap-

ping not only with the spectrum of another element but also with that of the same element in a different chemical state. The deconvolution allows a more detailed analysis in such a case, too. **Figure 2** shows an example of the spectrum of a specimen made of a mixture of Ti and TiO<sub>2</sub> (Ti+TiO<sub>2</sub>), and its deconvoluted results.

As shown in **Fig. 3** and **Fig. 4**, in the Auger spectrum of Ti, the increased percentage of TiO<sub>2</sub> causes the reduction of two peak heights and the peak broadening over the whole spectrum. **Fig. 3** and **Fig. 4**, and **Table 1** shows the results of application of the peak deconvolution method with the use of spectra of metallic Ti and TiO<sub>2</sub> as standards.

It is apparent in **Fig. 4** that the fitting is satisfactory with respect to the shapes of the standard spectra of Ti and TiO<sub>2</sub>, although a little residual remains near 385 eV. It is possible for the spectrum of many elements to be deconvoluted with high energy resolution (dE/E= 0.15%) into a few standard spectra in different chemical states. As shown in **Table 2**, the component of these standard spectra correspond to the atomic% of metallic Ti (67.7%)

and oxidized Ti<sup>4+</sup> (14.9%). Similarly, the atomic% of oxygen (O<sub>2</sub>) is calculated to 28.3% by using the oxygen spectrum in TiO<sub>2</sub> as standard one. These results give that the oxygen content is the approximately twice of that of Ti<sup>4+</sup>, suggesting that Ti exists as TiO<sub>2</sub>. However, the total atomic% amounts to over 1. This reason may be attributed, as shown in the residual in **Fig. 4**, to the presence of Ti having a different oxidation number. The residual of these spectra requires a future research.

The peak deconvolution method is very useful not only to analyze elements but also to distinguish the chemical states of respective atoms.

## Application of Peak Deconvolution Method

### Auger spectra of Si-KLL in SiO<sub>2</sub>/Si<sub>3</sub>N<sub>4</sub>/Si multi-layer film

Si is one of the elements whose chemical states and the shapes of peaks change significantly depending on the bonding state. As a specimen, a thin film consisted of a few tens of

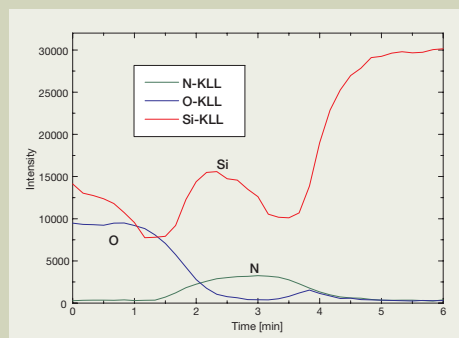


Fig. 5. Depth profiles of SiO<sub>2</sub>/Si<sub>3</sub>N<sub>4</sub>/Si.

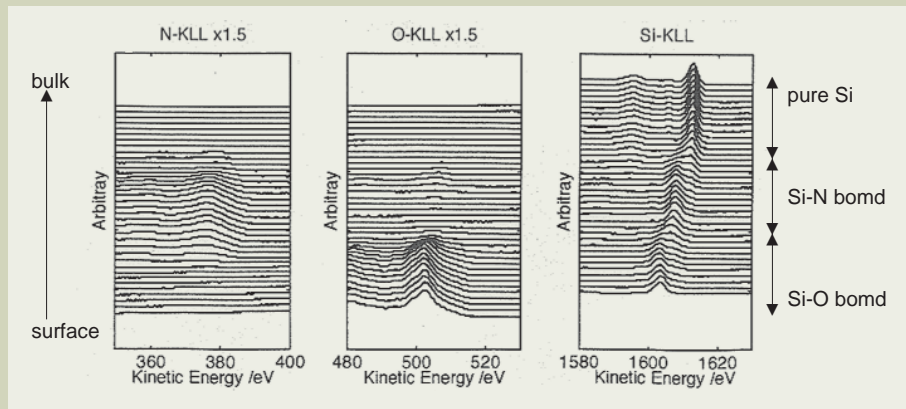


Fig. 6. Auger spectra obtained from depth profiles.

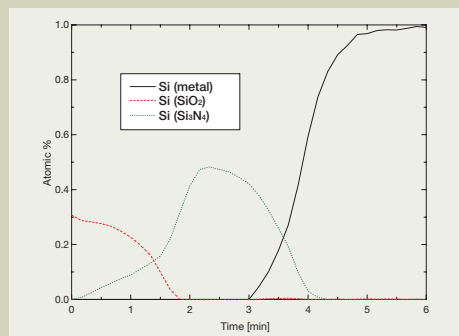


Fig. 7. Results of peak deconvolution using Si, Si (Si<sub>3</sub>N<sub>4</sub>) and Si (SiO<sub>2</sub>) as standard spectra.

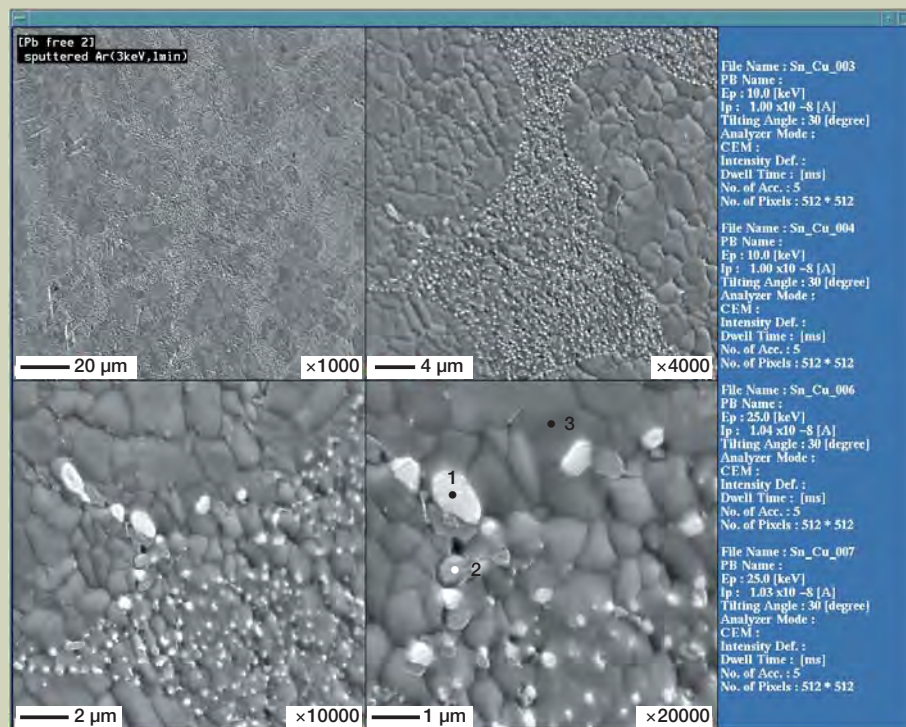


Fig. 8. Secondary electron images of Cu-Ag-Sn-Bi-based solder (points 1 to 3). (accelerating voltage: 10 keV, probe current: 10 nA)

nm thick SiO<sub>2</sub> and Si<sub>3</sub>N<sub>4</sub> films laminated on a Si substrate was used, and the depth profiles of N, O and Si were measured with high energy resolution (dE/E=0.15%). **Figure 5** shows the depth profiles of their respective Auger spectrum intensities, and **Fig. 6** shows the spectra measured at that time.

The depth profiles in Fig. 5 show that the intensity of the Si-KLL spectrum fluctuates along with the changes of O and N. When the spectra measured with the depth profiles were observed, as shown in Fig. 6, to know the reason, it was discovered that the peak energy shifted and the peak shape changed also as the bonding states with O and N or the respective percentages changed. Therefore, a peak deconvolution was conducted using Si, Si (Si<sub>3</sub>N<sub>4</sub>) and Si (SiO<sub>2</sub>) as standard spectra.

**Figure 7** shows the results.

The Si-KLL depth profiles could be converted to the Si chemical state profiles by applying the peak deconvolution. In other words, the evaluation of the respective thin films presented a possibility to evaluate not only the percentage of O and N but also the state of their bonding with Si from the measured Auger spectra.

### Analysis of precipitated elements in Pb free solder

As an attention has increasingly been focused on the environmental issues in recent years, activities or projects such as ISO-14000 positively taking the environment into account are now underway in the industrial fields.

Especially, Pb free solder consisted of dissolved metals such as Ag and Cu instead of Pb has began to be used in the electronics industry. Here, an example of analysis of a commercially available Pb free solder is presented.

The specimen is a commercially available Cu-Ag-Sn-Bi-based Pb free solder. It was polished to have a planer surface, and cleaned using Ar ions at 3 keV in an ultrahigh vacuum for one minute. The SEM images in **Fig. 8** show that crystalline particles with sizes of a few μm have grown due to Ar etching and that those crystalline particles gather together to form two phases. One phase is composed of particles with bright spots of 1 μm or less in size and relatively dark gray particles, and the other phase is free of such particles.

The results of point analyses of these phases

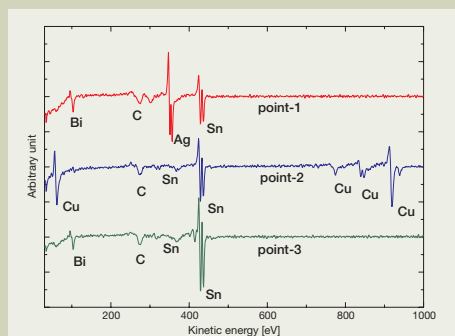


Fig. 9. Result of point analysis of Cu-Ag-Sn-Bi-based solder (points 1 to 3). (accelerating voltage: 10 keV, probe current: 10 nA, energy resolution: 0.6%).

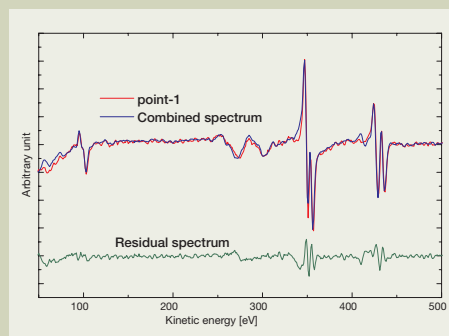


Fig. 11. Result of fitting of Auger spectra at point-1.

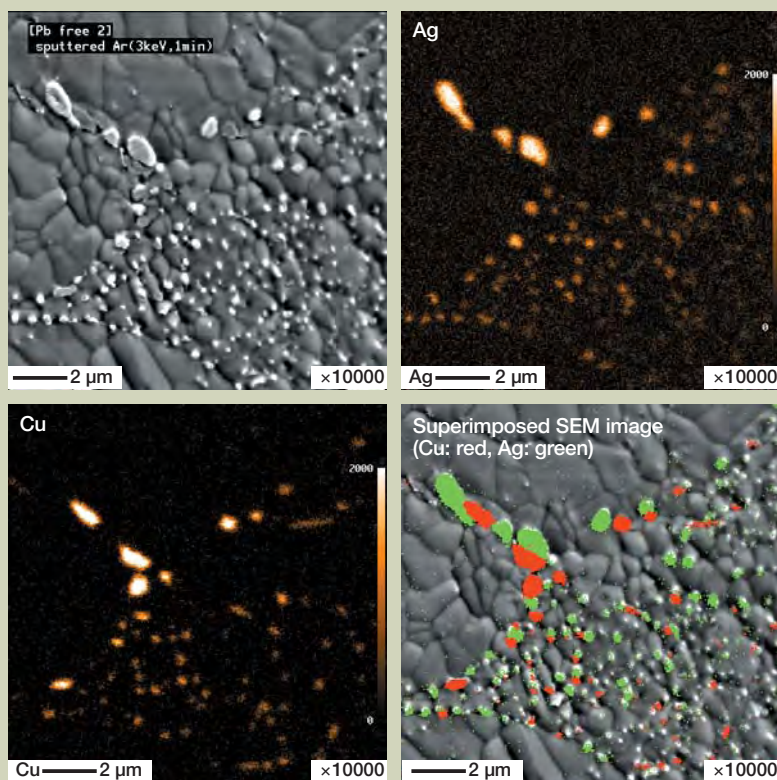


Fig. 10. Results of Auger mapping of Cu-Ag-Sn-Bi-based solder. (accelerating voltage: 10 keV, probe current: 10 nA)

	point-1	point-2	point-1
C	0.464	0.479	0.528
Cu	0.0298	0.681	0.0112
Ag	0.487	0	0
Su	0.355	0.436	0.658
Bi	0.302	0	0.248
sum	1.638	1.596	1.445

Table 2. Result of Auger spectra (before correction).

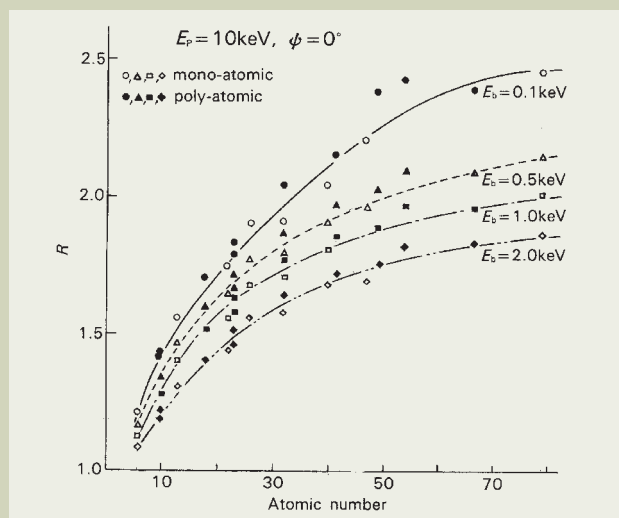
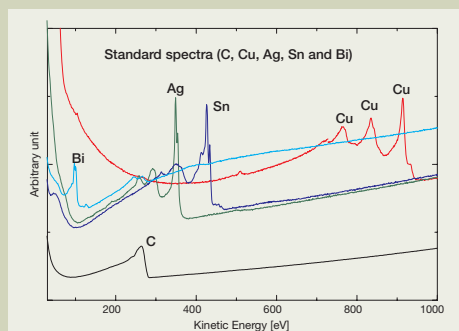


Fig. 12. Backscattered electron generation coefficient.

are shown in **Fig. 9**. From these spectra, it can be seen that the small bright particles are consisted of Ag, Sn and Bi, and the gray particles are consisted of Cu and Sn, while the matrix is consisted of Sn and Bi. Auger mapping makes these differences more noticeable (**Fig. 10**).

The result of above mapping is perfectly identical to the result of point analysis in **Fig. 9**, and clearly shows an uneven segregation state in solder. The Cu-Ag-Sn-Bi-based solder is often considered to have a uniform composition, but this result shows that, not only crystalline particles of Sn and Bi of a few  $\mu\text{m}$  in size, but also Ag, Sn, Bi, Cu and Sn particles of 1  $\mu\text{m}$  or less in size, are unevenly segregated.

Almost all the Ag peaks are detected to be



**Fig. 13.** C, Cu, Ag, Sn and Bi standard spectra.

Standard spectrum	Correction coefficient*
C	1.82
Cu	1.12
Ag	1.02
Su	1.0
Bi	0.908

**Table 3.** Backscattered electron correction coefficients of respective standard spectra when backscattered electrons are generated from Sn substrate.

\*Assumed to be detected from Sn substrate.

	point-1	point-2	point-3
C	0.252	0.262	0.233
Cu	0.014	0.605	0.012
Ag	0.475	0	0
Su	0.352	0.435	0.647
Bi	0.327	0	0.252
SUM	1.420	1.302	1.144

**Table 4.** Result of fitting of Auger spectrum (after correction of amount of backscattered electrons generated).

higher than the original Ag peak in these spectra as a result of overlapping on Sn peak at 350 eV. We tried a quantification of trace particles of 1  $\mu\text{m}$  or less in size using the K-Value method more exactly than the quantification using the relative sensitivity factor method. The peak deconvolution method was applied using C, Cu, Ag, Sn and Bi as the standard spectra. **Figure 11** and **Table 2** show the results of peak deconvolution applied to the Auger spectra at the point-1 in **Fig. 8**. In the residual spectrum, some fitting fail points are seen.

Table 2 shows the result of quantification by the peak deconvolution methods and the list of component ratios of the respective standard spectra. As described in the previous section, these components directly correspond to the atomic concentration in the K-Value method. Therefore, these coefficients can be regarded as the respective atomic concentrations. However, the total of those quantification exceed 1 greatly. The magnitude of this error is attributable not only to the changes in the chemical state of each element as was shown in the residual spectra, but also to some other factors not taken into consideration.

For the quantitative discussion of the amount of Auger electrons generated, it is necessary to consider the following three factors in principle:

- (1) Amount of secondarily excited Auger electrons due to backscattered electrons in bulk
- (2) Atomic density of materials to be measured
- (3) Mean free path of electrons in materials to be measured

In the following experiment, the atomic density described in (2) and the mean free path described in (3) were not taken into consideration, because the components of trace particles in the solder could not be measured exactly. Now, a correction was made only for the amount of secondarily excited Auger electrons due to backscattered electrons in bulk described in (1).

Backscattered electrons coming out of the specimen surface excite atoms near the surface and generate more Auger electrons. For this reason, the intensity of Auger electrons needs to be corrected according to the amount of backscattered electrons in bulk. This intensity may vary depending on the main element in the bulk to be analyzed. For example, the Auger spectrum of C existing on the surface of a substrate made of the heavy metal has a higher intensity than that of C existing on the surface of a substrate made of C, sometimes amounting to double the intensity ratio. Here, the correction coefficients of the respective standard spectra were calculated based on the backscattered electron generation coefficient [4] [5] shown in **Fig. 12**.

**Figure 13** shows the standard spectra of the respective elements used in this measurement, and **Table 3** shows the backscattered electron correction coefficients calculated from the backscattered electron generation coefficients. These backscattered electron correction coefficients are calculated in the case of C on an Sn substrate, where the intensity of the C spectrum is 1.82 times stronger than the intensity of the C spectrum on a C substrate. The actual standard spectrum in **Fig. 13** clearly shows that the C background is smaller than the back-

grounds of other elements.

**Table 4** shows the result of quantification performed again using these coefficients. Although the total of atomic concentrations exceeds 1, the value apparently comes closer to the true value than the value in **Table 2**. The error in this quantitative analysis should be further investigated with taking (2) the atomic density and (3) the mean free path into consideration.

## Summary

Auger Electron Spectroscopy (AES) can be applied not only to element analysis in minute areas, but also to the chemical state analysis. In the actual situation, the Auger spectral analysis is mostly performed for the element analysis and the rough quantitative analysis because of the complicated Auger transitions. The theory of AES measurement has not established completely yet. Accordingly, so many applications exist for the use of AES to the detailed chemical-state analysis.

In the experiments described in this paper, we showed some examples of the application of chemical-state analysis and quantitative analysis using the peak deconvolution method. Through the exact investigation of spectra, we stated on the possibility of AES application to the evaluations of chemical states and the exact quantitative analysis. Especially, with respect to the quantitative analysis, we conducted the detailed study of Auger spectra by use of the peak deconvolution method instead of the relative sensitivity factor method. However, errors in this quantitative analysis in this paper need to be further studied in the future.

As shown above, the analysis of Auger spectra still has plenty of room for investigation. It is sure that new applications of AES will be discovered through continuing research and development of analytical methods.

## References

1. N. Ikee, T. Negishi: JEOL EPMA Surface Analysis User's Meeting Material (AP61) (in Japanese)
2. Y. Nagasawa, N. Ikee: JEOL EPMA Surface Analysis User's Meeting Material (AP66) (in Japanese)
3. Y. Nagasawa: JEOL EPMA Surface Analysis User's Meeting Material (AP78) (in Japanese)
4. S. Ichimura and R. Shimizu: *Surface Science* **112** (1981) p.368
5. S. Ichimura, R. Shimizu and J. P. Langeron: *Surface Science* **124** (1983) L49

# JEOL's Challenge to Nanotechnology

Sadao Aoyagi

Engineering Management Division, JEOL Ltd.

## What is Nanotechnology?

Nanotechnology is attracting an increased attention in the world today. Encouraged by the National Nanotechnology Initiative (NNI) established by former US President Clinton in 2000, research and development on nanotechnology has accelerated as a national strategy of many countries.

The author attended the Micro & Nano Engineering (MNE) Conference 2001 in Grenoble, France, in September 2001. Since the first meeting held at the University of Cambridge in 1975, this annual meeting has been held in various European countries and marked the 27th last year. At the meeting, more than 450 scientists from around the world discussed and exchanged information on nanoscience and nanoengineering. Researchers also presented numerous reports on the creation, analysis, and evaluation of nanostructures. In October 2001, the author attended the 14th International Microprocesses & Nanotechnology Conference 2001 in Matsue, Japan, which drew more than 300 participants from throughout the world. Researchers here have also presented and exchanged information on nanotechnology. Although the word "nanotechnology" has become popular recently, it is not an entirely new field as one can see from these conferences.

What is meant by "nano"? "Nano" is a prefix that means one billionth of something like a second or a meter. One nanometer is one billionth of a meter ( $10^{-9}$  m). **Figure 1** shows the scale of lengths. We can see how small one nanometer is.

We often use a phrase used to express an industrial trend by referring to a specific field. As an example, "the information technology (IT) revolution" is a revolution in communication technology. In contrast, the word "nano" does not refer to a specific field. This means that everything in the cosmos can be the target for nanotechnology. "Nanotechnology" means nanostructure engineering, research, and development in creation of useful materials, devices, and systems at nanometer-size

scale.

The smallest unit of substances known to us is the atom, but it is not functional by itself. We may say that nanotechnology produces the smallest functional unit (approximately one nanometer in size) by building groups of atoms.

### Approaches to nanotechnology: "Bottom up" and "Top down"

Approaches to nanotechnology research and development are grouped into two categories, "bottom up" and "top down". The bottom-up approach ingeniously controls the building of nanoscale structures. This approach shapes the vital functional structures by building atom by atom and molecule by molecule. The bottom-up approach researchers are working to find the mechanism of "self-assembly". "Self-assembly" is like the most basic ingredients of a human body reproducing the most basic structures by themselves. "Self-assembly" covers the creation of the functional unit by building things using atoms and molecules, growing crystals and creating nanotubes.

"Top down" is an approach that downsizes things from large-scale structures into nanometer-scale structures. As an example, vacuum tubes yielded to transistors, they then gave way to ICs (integrated circuits) and eventually LSIs (large scale integrated circuits). The way of creating things by downsizing from millimeter size to micrometer size is called "microtechnology". The top-down approach is an extension of microtechnology. The narrowest line pattern on a semiconductor device is now coming to the 50 nanometer level. This is an achievement of the top-down approach.

The word "micro electro mechanical system" (MEMS) is not so popular as nanotechnology, but is well known to nanoscience and nanotechnology researchers. MEMS is a system assembled at micrometer size by a combination of electrical and mechanical technology. MEMS technology has already provided many things of practical use to society. **Figure 2** shows an example of MEMS. It is a

scanning electron microscope (SEM) micrograph showing part of a gear wheel made using lithography technology (field of view: 300 micrometers).

In my understanding, the final goal of MEMS is to create nanoscale structures (NEMS: nano electro mechanical system). There are, however, many hurdles to overcome in its research and development, and many scientists around the world are continuing to make hard efforts.

### Nanotechnology will make our life more comfortable

Why is nanotechnology so important? Former President Clinton said, "In the future, all information in the Library of Congress can be stored in the size of one sugar cube". There are many practical issues to overcome before reaching this target even if it is theoretically possible.

Thinking of our daily life, for example, since the outer diameter of a gastroscope, 15 mm in the past, was downsized to 2 to 3 mm, the patient's pain has been greatly decreased during a stomach examination. Let us recall the 1966 movie "Fantastic Voyage". This is a science-fiction movie in which four miniaturized doctors entered a human body to conduct a brain surgery. Today, a technique similar to this movie, called a "drug delivery system", has become a reality. This application of nanotechnology delivers medicine to a specific body part, allowing us to use the minimum amount of medicine necessary. Nanotechnology makes our life more convenient and comfortable.

ICs are already incorporated in most of our daily-use appliances and exhibit a variety of capabilities. ICs and LSIs are greatly downsized and multifunctional, making our daily life more efficient. These chips enable us to use handy cellular phones, and automatically pay for train tickets and commodities. Microtechnology has brought about such achievements.

Now, nanotechnology has emerged. In the upcoming years when practical applications of

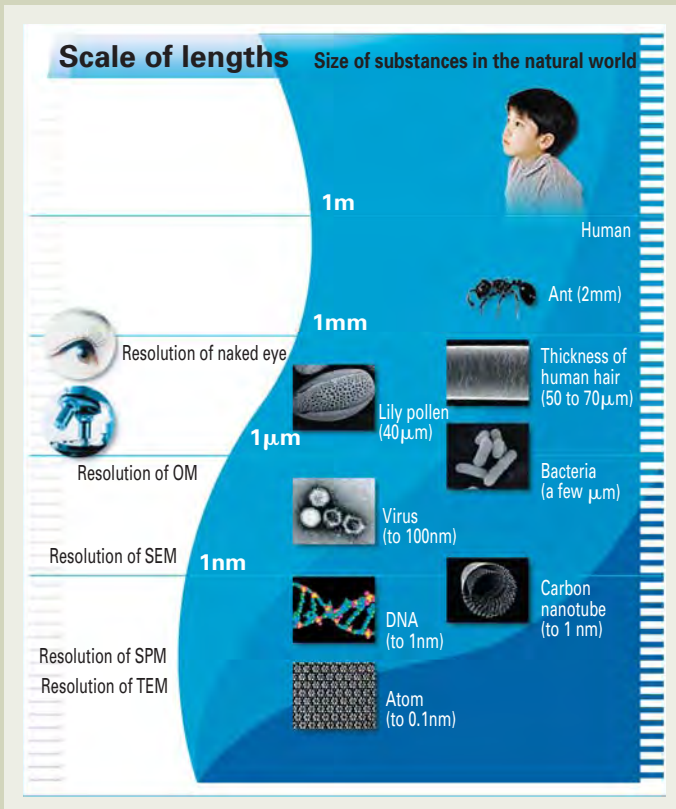
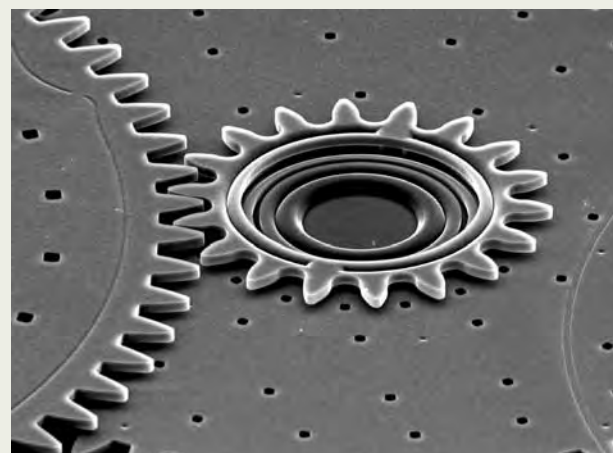


Fig. 1. Scale of lengths.



×300



×700

Fig. 2. SEM micrograph of a micromachine. Courtesy of Professor Fujita of the Institute of Industrial Science, University of Tokyo.

nanotechnology prevail, our daily life will become much more convenient and comfortable.

## Development of Nanotechnology

### Nanomaterials are in the production stage

The following is a comment made by a professor at Nagoya University when the author visited him in August 2001. “We have nanomaterials, but no nanotechnology”. “We have techniques to produce nanomaterials like carbon nanotubes (CNT: carbon tubes 1 nm in diameter and several micrometers in length) and nanofullerene (spherical carbon approximately 1 nm in diameter) with a production yield of approximately 90%, but we have no techniques to cut and assemble these nanomaterials”.

Scientists engaged in materials research have been using the transmission electron microscope (TEM) for more than 30 years to observe nanometer-size materials. The professor pointed out that observing nanomaterials is not new, but the technology needed to manipulate and control nanoscale substances is

not yet fully developed.

The author will introduce two examples of nanomaterials research. **Figures 3a to 3c** are TEM images that show the creation process of xenon (Xe) nanoparticles. When injecting Xe ions into an aluminum (Al) substrate, Xe microcrystals combine with each other to form Xe nanoparticles. **Figure 3a** shows the state before the microcrystals combine: **Figure 3b** shows the state during the microcrystals merge: and **Figure 3c** shows the state after the microcrystals have combined. The resulting Xe nanoparticles are arranged in the Al substrate in the form of solid octahedrons. When viewed from a certain direction, they look hexagonal. The two microcrystals isolated from each other (**Fig. 3a**) combine with each other to form a single large solid octahedron (**Fig. 3c**). The TEM images clearly visualize a nanoscale change of a nanomaterial.

The next example is a nanowire. **Figure 4** shows a schematic diagram of a helical multi-shell gold nanowire and a micrograph taken with a TEM (magnification: 20,000,000). This micrograph shows the gold nanowire approximately 1 nm in diameter.

We have great expectations for the fabrication and creation of nanodevices, which will contain nanotubes, nanoparticles, nanowires,

and other materials.

### Nanotechnology is in the development stage

The suggestion of the professor at Nagoya University has provided a hint to what instrument suppliers must do. Namely, we have to meet the demands from top-level researchers engaged in nanotechnology. To achieve this objective, we have to further improve the performance and capabilities of our products by enhancing our technology. After attending several meetings on nanotechnology, the author also recognized that in addition, scientists have many issues for the creation of nanostructures.

A leading industry employing the top-down approach is the semiconductor industry. Integration of semiconductor devices is an application of nanotechnology. The narrowest line pattern of a semiconductor device now reaches below 100 nm; therefore, controlling the patterns at the nanometer level is essential. In addition, the semiconductor roadmap (International Roadmap for Semiconductor Technology) projects the miniaturization of the semiconductor design rule in the future.

However, many difficulties confront us, and research and development are being pushed

forward aggressively to solve these problems. When downsizing a large substance, the function of this substance also changes. Therefore, we must overcome many challenges that take place.

From the viewpoint of the bottom-up approach, research and development efforts are made based on the following mechanism: A single atom has no function on its own, but when atoms gather together to become the size of DNA (approximately 1 nm), they suddenly have novel functions. In research on metals, ceramics, semiconductors, polymers, and biology, scientists are now evaluating physical properties of aggregates of atoms and molecules. However, we still have a wide range of unknown obstacles, which have to be overcome.

### Nanotechnology is making progress in various fields

Nanotechnology is now regarded as the core scientific technology. Many researchers have reported that ceramic, metallic, and other materials enhance their physical properties when created using nanoscale control. We can expect that materials can be improved in many ways, and large devices become compact while improving their capabilities. For example, many people are tackling the creation of single electron devices using a single CNT. Utilizing nanotechnology, we can downsize and enhance devices. Nanotechnology is expected to progress in various fields, including information/communication, life science, environmental conservation, energy saving and medical care.

**Figure 5** shows an example of the applications of “nanotube tweezers” that are created by means of CNTs. The schematic diagram at left shows the construction of a molecular device using the nanotube tweezers, and the SEM micrograph at right makes the nanotube tweezers visible. The tips of the nanotube tweezers can be opened and closed by switching on and off a voltage between the two CNT probes. Nanotube tweezers are expected to be applied in various fields of research and development on nanoscience and nanotechnology, in terms of the bottom-up approach.

In biological studies, TEM and SEM have contributed to the progress of medical care by offering imaging of virus particles several nanometers in size. Worldwide efforts are being made to create artificial human organs including eyes and ears. We may say that good news will be brought to people with visual or hearing difficulties in the near future.

Many efforts in leading research and development start with the development of new technology and products. This is where JEOL’s challenge to nanotechnology lies ahead.

## JEOL’s Challenge to Nanotechnology

### JEOL’s continuing challenge to nanoscience and nanotechnology

**Figure 6** shows a composite of a TEM micrograph (replica of a single crystal aluminum surface) and a photograph of mountain climbers, taken in the 1960s. This photograph is a message depicting JEOL’s challenge to the microworld. Since its establishment, JEOL

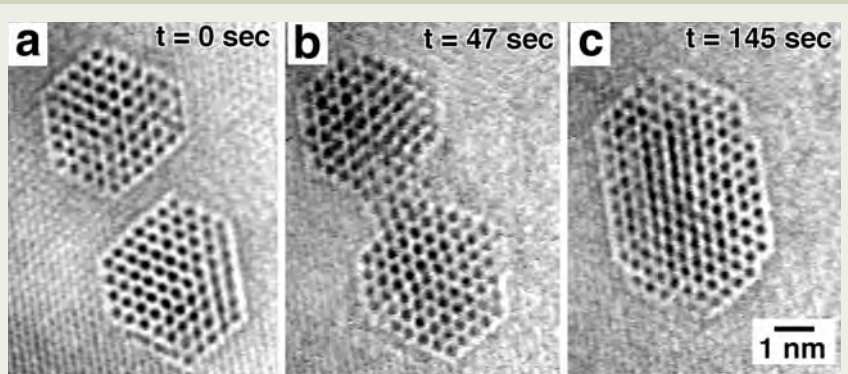


Fig. 3. Creation of xenon nanoparticles. Courtesy of Dr. Furuya of the Nanomaterials Laboratory, National Institute for Materials Science.

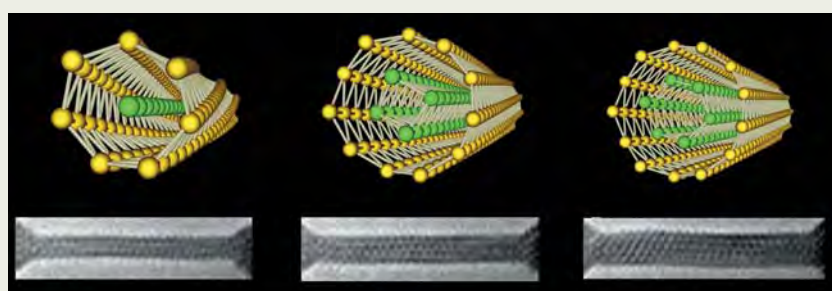


Fig. 4. Helical multi-shell gold nanowire. Courtesy of the Takayanagi Particle Surface Project, Japan Science and Technology Corporation.

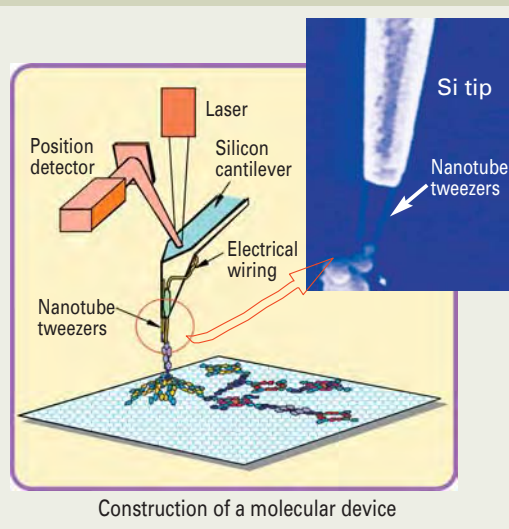


Fig. 5. Application of nanotube tweezers mounted on nanomanipulator. Courtesy of Professor Nakayama of Osaka Prefecture University.



Fig. 6. Composite of a TEM micrograph (replica of a single crystal aluminum surface) and a photograph of mountain climbers.

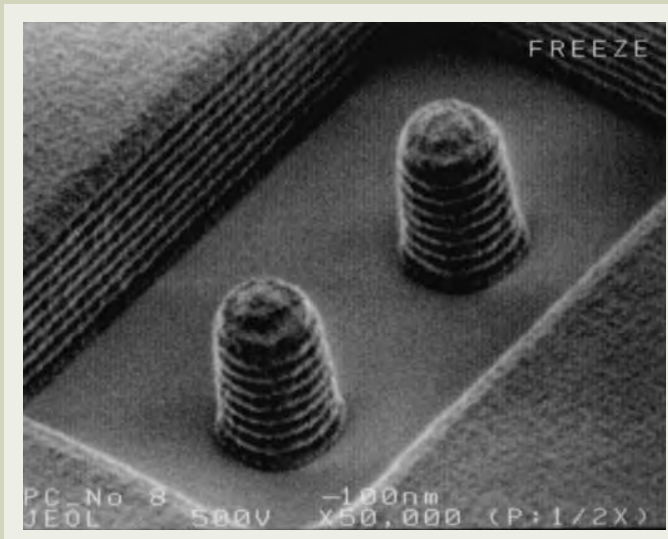


Fig. 7. LSI's nanostructures.



Fig. 8. "Nanopanda" figure.

has been actively engaged in research and development of products for research at the micro and nano level. Our variety of products has contributed to nanoscience research around the world. Many JEOL customers have been awarded the Nobel Prizes, and six Nobel Prize laureates planted commemorative trees when they visited our company. The information boards placed at these trees convey their outstanding accomplishments.

The author will explain some examples of applications of JEOL products related to nanotechnology.

### "Characterization": Observation of nanomaterials and nanostructures

**Figure 7** shows a defect-review SEM (DRT-SEM) micrograph of nanostructures of an LSI. JEOL's DRT-SEM is used as a tool for monitoring processes and detecting defects in the semiconductor production lines. This is an example of the image of surface nanostructures. Accurate observation of nanoareas is the starting point to understand substances, just as "seeing is believing". JEOL's TEM, SEM, scanning probe microscopes (SPM), electron probe microanalyzers (EPMA) and other instruments can observe and analyze nanostructures of materials. These instruments are used for structural characterization and materials research at the microscale and nanoscale.

### "Nanometrology": Metrology and analysis of materials at the nanoscale

We use a ruler to measure the size or length of visible substances. If the substance to be measured is too small, we cannot measure it with our eyes or using an optical microscope. The TEM, SEM, and SPM are powerful tools for measuring such small substances.

Our EPMA, nuclear magnetic resonance spectrometers (NMR), mass spectrometers (MS), and other instruments are used for the analysis of substances. Professor Noyori at Nagoya University, the Nobel Prize laureate in

2001, used JEOL's NMR in the development of catalysts and evaluation of synthesis results, as an important tool in his research of asymmetric synthesis. NMR is used in three-dimensional structure analysis and molecular movement evaluation at a molecular level. The NMR allows us to evaluate the distance between atoms at the 0.1 nm level and the movement of atoms inside molecules. This clarifies the three-dimensional structures of proteins.

JEOL's MS is an effective tool for mass analysis and chemical structural analysis of trace components at the picogram (pg) or femtogram (fg) level. The pico level or femto level is below the nano level. In recent years, the mass spectrometer combined with electrophoresis has been used for structural and functional analysis of genes, genomes and proteins.

### "Fabrication": Creation of nanostructures and nanodevices

One of the cutting-edge technologies for "creation" in the nanoworld is pattern writing using a SPM. **Figure 8** shows a "nanopanda" figure fabricated by moving atoms one by one on the silicon substrate surface, using an ultra-high-vacuum scanning tunneling microscope (UHV-STM). Nanotechnology offers such fine fabrication and creation.

Semiconductor-device fabrication is a leading technology for creating nanodevices. To produce semiconductor devices, 200 to 300 processes are necessary. The production of photomasks is very important in the front-end process. JEOL has been supplying electron beam lithography systems (EBX) that are indispensable tools for the fabrication of photomasks. These systems are also used for writing micropatterns for MEMS and system on a chip (SOC). In the ultra-microscopic world, defects or foreign matter of nanometer scale can cause fatal defects in semiconductor devices. JEOL also offers systems that detect, classify and analyze defects that occur in the

semiconductor fabrication process.

Today, large-volume information, including images and motion pictures, is being transferred via networks at high speed. Conventional electronic-transfer becomes difficult at such large volume and high speed. As a replacement, optical communication technology that utilizes the high speed of light is being developed. In developing a variety of optical communication devices such as band-pass filters, highly sophisticated deposition technology is required to form thin films on surfaces of glasses and metals at the nanometer level. JEOL's high-density reactive ion plating systems (HDRIP) can meet this requirement and contribute to the creation of nanoscale, high-quality, multi-layer thin films.

### JEOL's contribution

On the basis of "Creativity" and "Research and Development", JEOL positively challenges the world's highest technology, thus forever contributing to the progress in both Science and Human Society through its products.

This is JEOL's company philosophy. Based on strong determination, our challenge continues to offer advanced technologies and products, which are useful for characterization, metrology, and fabrication of nanomaterials and nanostructures. JEOL's integrated technology of "Characterization, Nanometrology and Fabrication" will contribute to a variety of solutions in nanoscience and nanotechnology.

### References:

The author has written this paper by referring to the following articles.

1. Nanotechnology (Shaping the world atom by atom): National Science and Technology Council of USA.
2. Nanotechnology Research Directions: M. C. Roco, R. S. Williams and P. Alivisatos
3. Micro & Nano Engineering 2001 abstracts: 9/16-9/19 2001, Grenoble, France.
4. Microprocesses and Nanotechnology 2001 digest of papers: 10/31-11/2 2001 Matue, Japan.

# Progress in Development of High-Density Reactive Ion Plating

Yasushi Shimizu

Industrial Equipment Division, JEOL Ltd.

## Introduction

With the increasing trend toward higher quality and commercial supply of information/communication-related and audio/visual equipment, numerous optical components that incorporate thin films have been commercialized. In this context, the highest possible quality of thin films is becoming a stringent market need.

The current vacuum-deposition systems have difficulty meeting this need depending on their applications, and the ion- or plasma-assisted deposition systems are now being supplied by various coating equipment manufacturers.

We succeeded in the development of the JEIP high-density reactive ion-plating (HDRIP) system that utilizes the electron-beam excited plasma in 1991. Recently, we have commercialized the JBS-1130FA, an upgraded model of the conventional JEIP series. The external view of the JBS-1130FA is shown in Fig. 1.

As the development concepts for high-density plasma process technologies, we defined the following three targets.

- Deposition of high-quality multi-layer optical films (those films with no wavelength shift)
- Deposition at lower temperatures (substrate heated to less than 200°C)
- Compatible with large deposition equipment (in order to gain uniform distribution of optical film thickness, nd)

We added the following two development targets with special emphasis on the productivity of film deposition.

- Improving reproducibility of film deposition
- Increasing the film-deposition rate.

In this paper, we will report the history of development and outline the major elemental technologies of the HDRIP system.

## Requirements for Plasma Source

### Generation of high-density plasma

We decided that the high-density plasma is a key factor for accelerating the reaction of plasma ions and forming films with better stoichiometry.

We judged that the high-density plasma is essential to form high-quality thin films under low-temperature substrate heating and increased deposition-rate conditions.

### Stable generation of plasma and exclusion of impurities

To maintain stable plasma generation and prevent impurities from mixing into the film, we thought of a new structural design where the plasma source and the discharge electrodes are not placed inside the deposition chamber.

The changes induced by the adhesion of insulating film to the electrodes and impurities mixing into the film due to evaporation or sputtering will be not negligible factors in the formation of high-quality films. Rather, these factors will adversely affect the film quality, film-thickness distribution, and reproducibility of film deposition.

### Plasma-output conditions independent of film-deposition conditions

We judged that diversified coating conditions are advantageous to set deposition parameters and ensure the reproducibility of film deposition. Also, these broader conditions are expected to contribute to controlling the film quality.

Based on this concept, we thought the introduction of new design in order that operators can specify the plasma output independent of the film-deposition conditions and minimize the restrictions on the evaporation materials (any materials can be used irrespective of their beings: conductive or dielectric).

### Other requirements

We increased the efficiency of plasma generation (minimized discharge power) to adapt to the design for a highly durable, long-life plasma source that does not require frequent exchange of parts.

## Generation of High-Density Plasma

The electron-beam excited plasma (EBEP) technique, which was developed under the technical guidance of the Institute of Physical and Chemical Research, is applied to the plasma source for the ion-plating process.

In this plasma source, argon (Ar) gas is introduced to a discharge chamber equipped with a hot cathode to induce discharge and thereby generate an electron beam from this argon plasma. By introducing a reactive process gas such as oxygen (O<sub>2</sub>) into the deposition chamber, a reactive plasma is formed. Since the electron beam has an energy determined by the accelerating (extracting) voltage, it is possible to select a voltage suitable for the ionization (generally about 100 eV). By this technique, we can generate high-density plasma at higher ionization efficiency and specify the film-deposition conditions that can achieve the requirements for the films.

Figure 2 shows the characteristics of the plasma generated in the oxygen process gas environment (Ar gas feed rate: 50 mL/min) by the Langmuir probe method.

By examining the new design from the viewpoint of the HDRIP process, the following facts have become clear:

In the formation of high-quality films with the HDRIP system, the most important point is to increase excitation and ionization efficiencies of the evaporated particles as well as to ionize reactive process gas. Figure 3 shows the plasma discharge observed near the evaporation source in the Ta<sub>2</sub>O<sub>5</sub> film deposition process. The emission spectrochemical analysis was used to identify the characteristics of the plasma (such as luminescence intensity) in the film-deposition process space.

To achieve high-excitation-and-ionization efficiencies, it has become necessary to develop a special-purpose electron-beam deflection gun and power supply for the use with the HDRIP system, and to examine appropriate deposition conditions.

To achieve high-excitation-and-ionization efficiencies, it has become necessary to develop a special-purpose electron-beam deflection gun and power supply for the use with the HDRIP system, and to examine appropriate deposition conditions.

## Special-Purpose Electron-Beam Deflection Gun and Power Supply

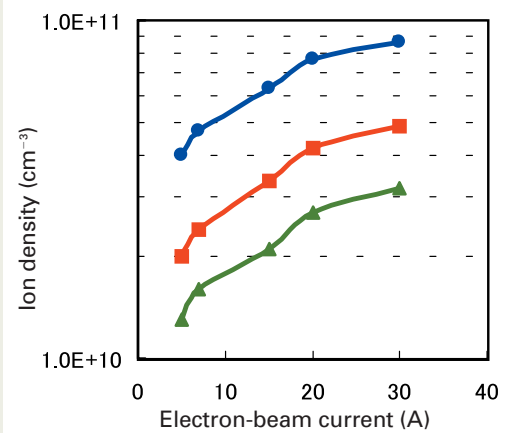
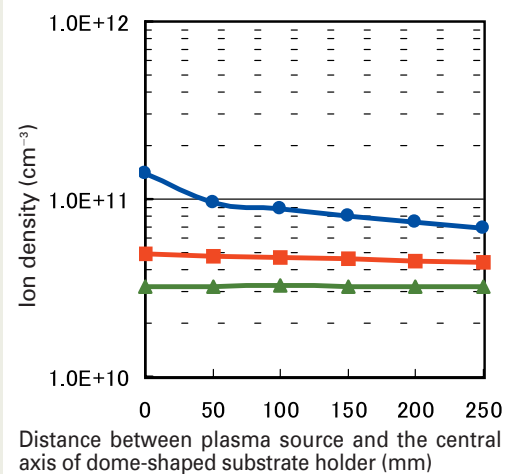
We have improved the electron-beam deflection gun (JEBG-203UA0)/power supply (JST-10F), both of which are among our major products, so that they can be effectively used with the new HDRIP system. In other words, the HDRIP system is a result of the integrated



Fig. 1. JBS-1130FA High-Density Reactive Ion-Plating System.



Fig. 3. Plasma discharge in Ta<sub>2</sub>O<sub>5</sub> deposition process.



**Measurement conditions**

Plasma generation conditions: Beam current: 30 A, Accelerating voltage: 120 V  
 Distance between the plasma source and the central axis of the dome-shaped substrate holder: Approx. 350 mm  
 The measurements were performed by moving the Langmuir probe away from the central axis of the dome-shaped substrate holder.  
 Vertical distance from the top of the evaporation source:  
 ● 200 mm, ■ 300 mm, ▲ 400 mm

Note: It was difficult to measure the plasma near the plasma source due to the effect of the high-energy electron beam. Therefore, the measurement positions were separated from the electron beam source.

Fig. 2. Characteristics of the plasma generated in the oxygen process gas environment (Langmuir probe method).

technology of electron-beam excited plasma and the electron-beam deflection gun and power supply.

Since the standard electron-beam deflection gun and power supply are designed based on the use for vacuum deposition, we judged it necessary to think new structure and design conditions compatible with the high-density plasma process. If the standard gun and power supply are used with the HDRIP process, problems will occur. Some of these problems and measures to solve them are listed below.

- The energy of the high-density plasma heats the electron beam gun and weakens the

gun's magnetic field to appropriately deflect an electron beam generated by the gun, thus causing the displacement of the beam position from the target position.

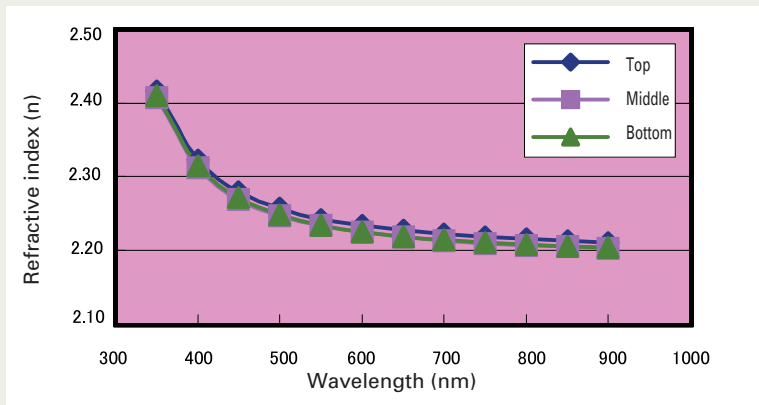
- It is necessary to design a heat-shield structure to improve water-cooling performance.
- The plasma cannot maintain a stable state when different evaporation materials are used and, as a result, the high-speed deposition is restricted. This problem not only adversely affects the quality, distribution, and reproducibility of the film deposition, but also restricts setting of a wide range of film-deposition conditions.

- It is necessary to introduce a new design structure that will improve the ionization efficiency and reaction of the evaporated particles and reactive gas.

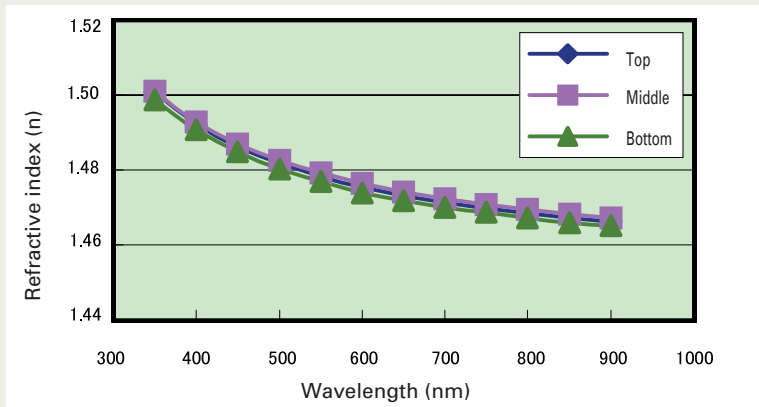
- It is necessary to optimize the beam scan conditions so that they will be compatible with the shape of the hearth and the special structure of the HDRIP system.

**Examination of Film-Deposition Conditions**

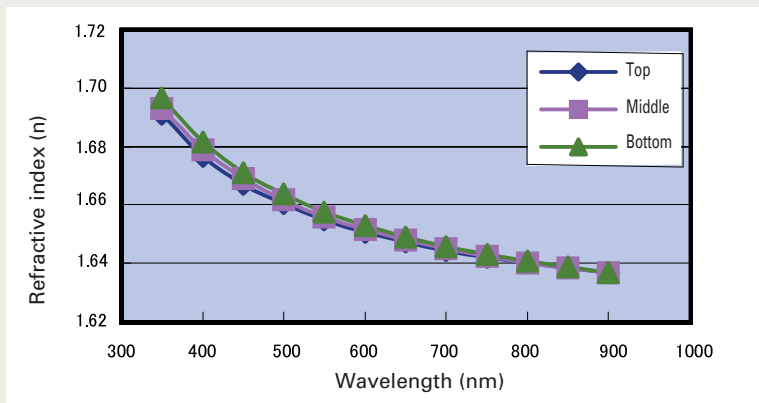
High-density plasma process was established as one of elemental technologies of the



Dispersion of refractive index of Ta<sub>2</sub>O<sub>5</sub> film.



Dispersion of refractive index of SiO<sub>2</sub> film.



Dispersion of refractive index of Al<sub>2</sub>O<sub>3</sub> film.

Fig. 4. Refractive indices of three different films.

In each graph, the refractive index of the top is obtained from the film deposited on the glass substrate placed at the center of the dome-shaped substrate holder, middle from the substrate at the position midway between the center and the periphery, and bottom from the substrate at the periphery. Our JEIP-900FA HDRIP system was used for the measurements. The absorption level of each film is negligible.

HDRIP system, but this achievement was not enough to form high-quality films. Another important factor is to appropriately apply high-density plasma process to the new, ion-plating deposition method.

We examined various film-deposition conditions for the HDRIP system. Listed below are our major efforts.

### Evaporation material

We selected Ta<sub>2</sub>O<sub>5</sub> to form the film with high refractive index and SiO<sub>2</sub> for low refractive index. Since we first judged that conductive evaporation materials would be the best choice from the viewpoint of stable generation of plasma, Ta<sub>2</sub>O<sub>5</sub> based materials and silicon were used. However, it was shown that the silicon could not increase the film-deposition rate

(due to splashing) and also was not suitable for the deposition through a hearth with multiple points. Therefore, we reviewed the materials.

We reexamined the film-deposition conditions using SiO<sub>2</sub> (insulating material) and successfully achieved the satisfactory film performance of this material. This achievement enabled us to increase the number of available evaporation materials. We believe that this success has been brought about by the special-purpose electron-beam deflection gun and power supply, which are compatible with the high-density plasma process.

### Film-deposition pressure and rate

A simple method of raising the plasma density in the deposition chamber is to increase the pressure in the chamber (increase the

process gas flow). However, since the ratio of active species (excitation species including ions) in the process gas particles is increased, the reactivity of the plasma ions does not always become high.

The electron-beam excited plasma used for the HDRIP system can maintain the stable state even at pressures of the order of the 1 to 5 × 10<sup>-2</sup> Pa. Therefore, it is now possible to set the pressure suitable for the reaction between reactive process gas and evaporation materials.

Evaluations of ion-plated films indicated that the HDRIP system's pressure conditions could be set comparable to that of the vacuum-deposition system (low pressure even for ion plating). We judged that this feature would contribute to enhanced film quality and distribution characteristics.

Film material	Proper rate (nm/s)
High refractive-index film (Example: Ta <sub>2</sub> O <sub>5</sub> or TiO <sub>2</sub> )	0.2 to 1.0 Conventional rate: approx. 0.6
Medium refractive-index film (Example: Al <sub>2</sub> O <sub>3</sub> )	0.2 to 1.5 Conventional rate: approx. 1.0
Low refractive-index film (Example: SiO <sub>2</sub> )	0.5 to 3.0 Conventional rate: approx. 2.0

Note : The film-deposition rate is determined from film material and deposition conditions.

Table 1. Example of film-deposition rates.

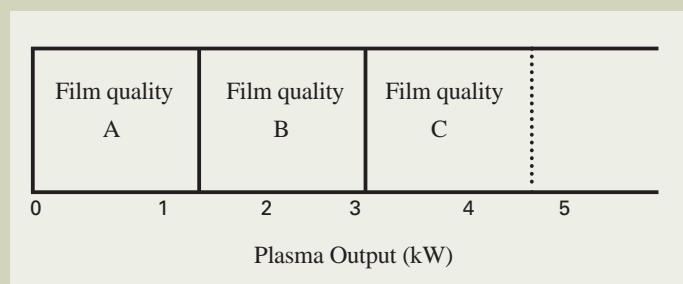


Table 2. Film quality depending on plasma output.

Film quality	Description
A	The film has the same quality level as that made in vacuum deposition.
B	The film has higher quality level than that made in vacuum deposition. However, the quality level may be classified as rank A or C depending on the deposition conditions. The film quality parameters (such as internal stress) can be adjusted within an arbitrary range in this output level.
C	The film has excellent quality level with respect to the resistance to heat and environmental change. The film can always maintain a given quality level in this output level.

Table 3. Definition of film quality.

Film material	Vacuum deposition	Film quality B	Film quality C
SiO <sub>2</sub>	-1	-0.9	-2.8
Ta <sub>2</sub> O <sub>5</sub>	-0.5	-1.0	-2.0
TiO <sub>2</sub>	+0.25	-0.3	-0.6

+: Tensile stress,

-: Compressive stress

Other parameters are also changed to define proper film-deposition conditions.

Note : The internal stresses of the ion-plated films using the HDRIP system and vacuum-deposited films will differ from those listed in the table depending on the film-deposition and measurement conditions.

Table 4. Relative comparison of internal stress of ion-plated films and vacuum-deposited films.

Since the HDRIP system was able to generate the plasma under low-pressure (high-vacuum) conditions, better optical film thickness distribution (nd) and reproducibility of film deposition were achieved. **Figure 4** shows the refractive indices of three different films.

The film-deposition rate is another important parameter and we think that the deposition of one layer at a low rate is necessary to form a high-quality film on the substrate. It is necessary to set an upper limit of this rate to maximize the effect of energies, such as heat energies and ion energies, over the substrate. Therefore, we determined that our goal is to raise this upper limit.

We judged that only supplying the energy to the substrate would have a limitation, and therefore, we examined a design that makes possible the generation of high-density plasma in the space between the evaporation source and the substrate. That is, we focused our efforts on creating the conditions in this space that promotes the reaction of activated particles of process gas and vapors. The conditions listed in **Table 1** were established to increase the activation, excitation, and ionization of the evaporated particles on the evaporation source.

## Plasma output

In the HDRIP system, high-density plasma process is utilized as a means for the creation of high-quality optical films. As the next step, we investigated the relationship between the film quality and plasma output.

Under arbitrary conditions, the film quality and plasma output have the relationship as shown in **Table 2** and **3**. Note that the relationship may remarkably differ from these tables depending on the film material and film-deposition conditions.

The following definitions are used to express these film quality levels.

The film classified as C or B has dense structure (amorphous structure) with superior resistance to the environmental change. It also features high refractive index and internal stress. The internal stress will be a problem depending on the required film specifications. We investigated the conditions that could reduce the internal stress, using the film with quality level B.

**Table 4** shows the relative comparison of internal stresses in the films formed using the HDRIP system and those using a vacuum-dep-

osition system. In this table, the internal stress of the SiO<sub>2</sub> film deposited with the vacuum-deposition system is defined as "Reference value 1".

## Conclusion

We discussed the development concepts, history of success, and elemental technologies for the HDRIP system, using concrete examples.

Now, high-quality optical films are created by means of various deposition methods. In addition, much higher qualities are increasingly required for those thin films. In order to meet this demand, we believe that the best way to make the required high-performance, high-quality thin films is to select the film-deposition process suitable for the intended applications and objectives and draw the full performance from the selected process.

We expect this report will help all of readers understand features and capabilities of our new HDRIP process.

# Applications of High-Power Built-in Plasma Gun

Tohru Takashima

Industrial Equipment Division, JEOL Ltd.

## Introduction

Recently, in the optical thin-film market, customers are increasingly demanding low price and high quality in optical components incorporated in home electric and electronic appliances. To meet these demands, advanced equipment such as our high-density reactive ion-plating system has started to contribute greatly to forming high-quality thin films in a wide variety of industrial areas.

In addition to the demands for introduction of new systems, there has been a gradual increase in another need to modify the existing vacuum-deposition systems to enhance the film qualities (resistance to environmental change, adhesion, and hardness). In this context, the recognition that the ion/plasma technology is indispensable for creating high-added-value thin films is widening.

Achieving both low-price and high-quality optical components is a hard challenge. However, if the technology that adds high value to films is combined with large equipment that provides an enormous throughput per batch (for example, 1800 mm diameter equipment), it is possible to meet the market needs for low-price and high-quality optical components to a considerable extent.

In this context, JEOL has developed a new, built-in plasma gun, the BS-80010 (**Fig. 1**). The BS-80010, designed based on our existing 3 kW built-in plasma gun EPG-3010, features 6 kW plasma output. This development was done with a view to finding applications for large equipment.

## Outline of High-Power Built-in Plasma Gun

The new, high-power built-in plasma gun uses the same operating principle as the existing EPG-3010 that has a 3 kW plasma output. **Figure 2** shows a schematic diagram of the BS-80010. First, the argon plasma is generat-

ed inside the plasma gun by the direct-current discharge of thermoelectrons emitted from the tungsten filament. The electrons in the plasma are accelerated by the electric field generated by the extracting electrode (anode) and introduced into the vacuum chamber. These electrons irradiate evaporated particles and the introduced argon gas inside the vacuum chamber, efficiently exciting and ionizing them. At the maximum power output rating, the discharge voltage and current are 160 V and 38 A.

Introducing the electron beam into the vacuum chamber diffuses the plasma widely inside the chamber and thereby high-density plasma is generated over the chamber interior. In addition, it is possible to select the direct-beam method or spiral-beam method by changing resistors A and B, which are connected between the chamber walls and extracting electrode.

### Irradiation-beam method

In this method, electrons flow into grounded surfaces of the vacuum chamber walls. It can achieve highly efficient ionization. This method is useful for ion-plating substrates with metallic films because it can continue to provide stable discharge while maintaining the conductivity of the grounded surfaces of the chamber walls.

### Reflection-beam method

In this method, the reflected electrons flow to the extracting electrode (anode) (**Fig. 3**). That is, the electrons are not only introduced into the vacuum chamber, but also returned to the electrode. During this process, the extracting electrode heats due to the current that flows to it, and this heat cleans its surface. This process can maintain the conductivity of the extracting electrode and stable discharge even in an environment where the grounded surfaces of the vacuum chamber walls are covered with insulating materials. Thus, this

method expands the applications of ion plating.

## Specifications of Built-in Plasma Gun BS-80010

This built-in plasma gun features the following specifications.

- Plasma output: Up to 6.08 kW  
(discharge voltage: 160 V, discharge current: 38 A)
- Operating pressure:  $1 \times 10^{-2}$  to  $1 \times 10^{-1}$  Pa
- Discharge gas: Up to 20 mL/min (argon gas)  
Cooling water: 7 L/min or more  
(temperature: 25 °C or less)

## Applications of BS-80010

The high-power built-in plasma gun BS-80010 is a special-purpose component developed for use as a plasma generator in the optical thin-film industry. In its major applications, this gun is incorporated into existing or new vacuum-deposition systems. It generates high-density plasma in the vacuum chamber and forms thin films by means of the ion-plating method to add high value to those films.

We show examples of the applications using this new BS-80010 gun. Thin films were deposited in an 1800 mm diameter vacuum-deposition system by using the ion-plating method, and the effectiveness of the gun was evaluated. The experiments were carried out with support from an optical-systems manufacturer.

### Experimental conditions

The built-in plasma gun BS-80010 was installed on the floor of an 1800 mm diameter vacuum-deposition system. The beam irradiation angle was appropriately adjusted to direct the plasma beam toward the film-deposition space. Then, various film-forming experiments were performed. The experimental conditions such as ultimate pressure, substrate temperature, and film-deposition rate were the

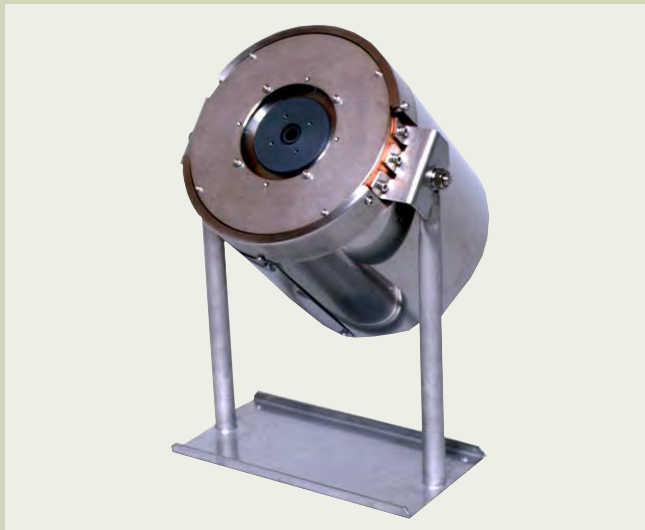


Fig. 1. External view of built-in plasma gun BS-80010.



Fig. 3. Spiral beam of High-Power Built-in Plasma Gun.

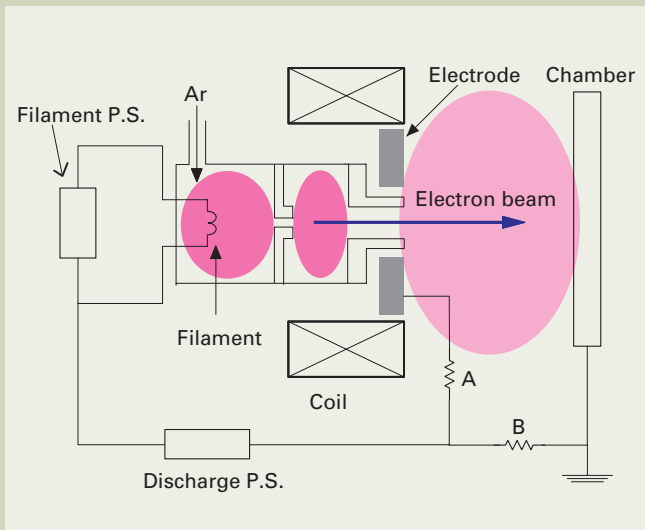


Fig. 2. Schematic diagram of High-Power Built-in Plasma Gun.

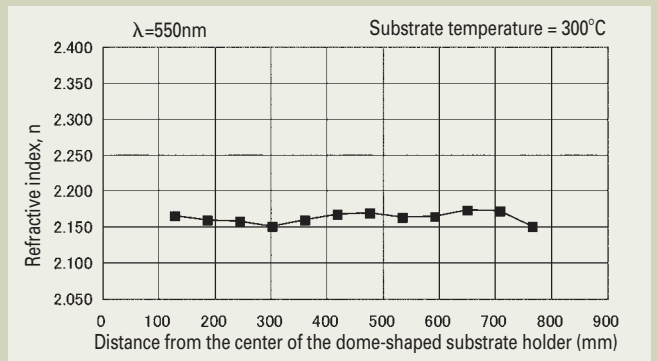


Fig. 4. Refractive indices and distribution of twelve single-layer Ta<sub>2</sub>O<sub>5</sub> films.

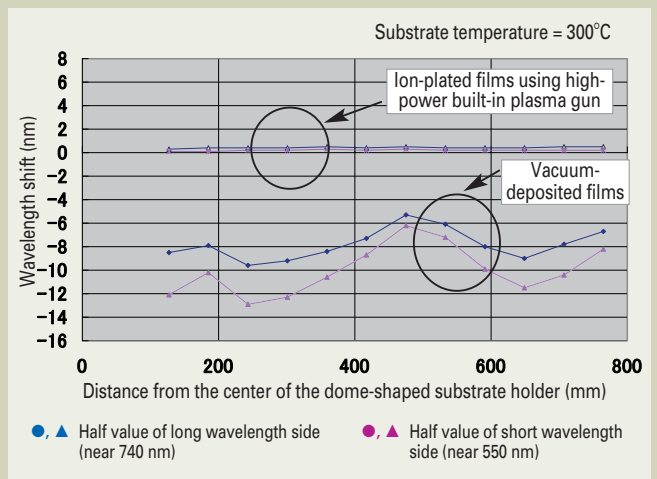


Fig. 5. Wavelength shifts of twelve multi-layer SiO<sub>2</sub>/Ta<sub>2</sub>O<sub>5</sub> films (19 layers).

same as those used in the vacuum-deposition method.

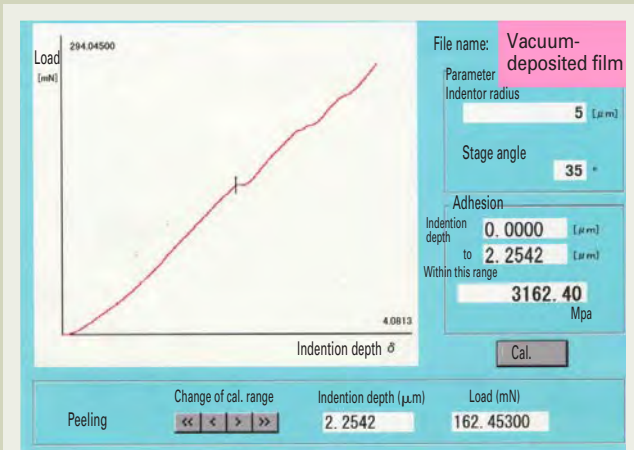
### Refractive indices of single-layer films

Twelve glass substrates were arranged in a dome-shaped substrate holder, from the center toward the periphery, spaced equally apart. Then, single-layer Ta<sub>2</sub>O<sub>5</sub> films were deposited on the glass substrates. **Figure 4** shows the measured results of the refractive index of

each Ta<sub>2</sub>O<sub>5</sub> film versus the location, although the results do not show the comparison with the data obtained from the vacuum-deposition method. The ion-plating method using the built-in plasma gun BS-80010 can offer refractive indices higher than those obtained from the vacuum-deposition method, and also provide distribution almost the same as vacuum deposition, verifying the high quality of ion-plated films.

### Wavelength shift of multi-layer films

**Figure 5** shows the wavelength shifts of twelve multi-layer SiO<sub>2</sub>/Ta<sub>2</sub>O<sub>5</sub> films (19 layers each). The wavelength shift, in terms of the uniformity across the dome-shaped substrate holder of the wavelength of the 50% transmittance point of the long-wave edge, was evaluated by comparing that at room temperature and that obtained under 100°C heating with



Adhesion of vacuum-deposited film: 3162.40 MPa



Adhesion of ion-plated film: 4798.57 MPa

Fig. 6. Adhesion of multi-layer  $\text{SiO}_2/\text{Ta}_2\text{O}_5$  films (19 layers).

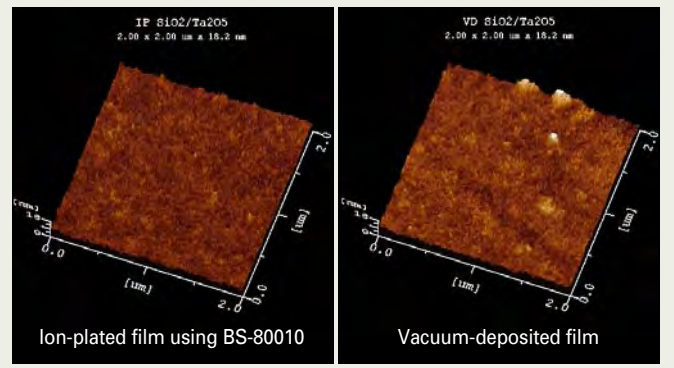


Fig. 7. AFM images of multi-layer  $\text{SiO}_2/\text{Ta}_2\text{O}_5$  Film (19 layers).

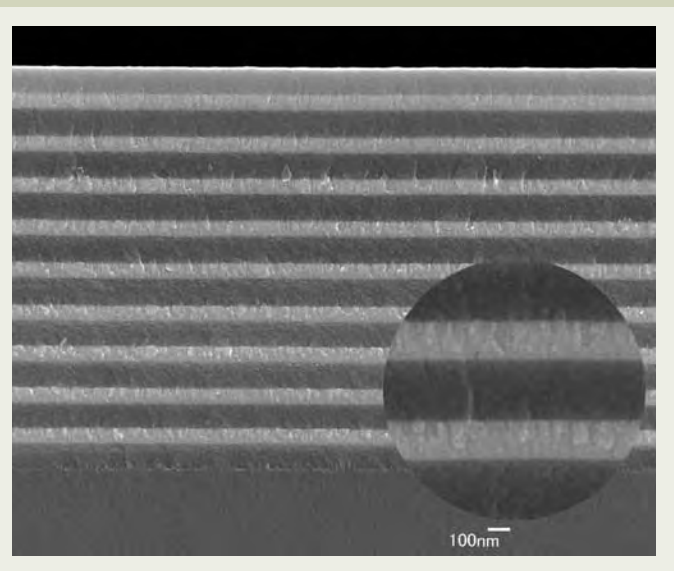


Fig. 8. Cross-sectional SEM image of multi-layer  $\text{SiO}_2/\text{Ta}_2\text{O}_5$  film (19 layers).

hot air. This evaluation shows that the wavelength was shifted toward the short wavelength side by 6 to 13 nm for the vacuum-deposited films, while the wavelength shift was minimal over the entire area of the dome-shaped substrate holder for the ion-plated films using the built-in plasma gun BS-80010.

### Adhesion of multi-layer films

The adhesions of the multi-layer film samples discussed were measured with NEC Sanei Instruments Thin Film Physical Property Test Equipment MH4000. **Figure 6** shows the test results. They prove that the ion-plated film using the built-in plasma gun BS-80010 has adhesion higher than that of the vacuum-deposited film.

### AFM images

The surfaces of the film samples discussed were observed with a JEOL scanning probe microscope (JSPM-4210). **Figure 7** shows the AFM images of a  $2\mu\text{m}$  square. Several protrusions are visible on the vacuum-deposited film, while no conspicuous protrusions were observed on the ion-plated film using the built-

in plasma gun BS-80010. The BS-80010 can offer improved smoothness of the film surface.

### Cross-sectional SEM image

The cross section of the ion-plated film sample discussed was observed with a JEOL field emission scanning electron microscope (JSM-6700F). **Figure 8** shows the resulting SEM image. When the vacuum-deposition method is used, the film is likely to grow in a columnar form caused by the adsorption of water into and desorption from the gaps between the columns, thus causing the wavelength shift. On the other hand, Fig. 8 shows that the built-in plasma gun BS-80010 can create a highly dense ion-plated film with a flat interface.

## Conclusion

In the evaluations of ion-plated films that were deposited using the high-power built-in vacuum-deposition system, it was verified that thin films, which have higher quality (for example, reduced wavelength shift and higher adhesion) compared to the conventional vacuum-deposition method, can be formed. Based on the experimental results, we expect that the new, built-in plasma gun will contribute to creating the films which meet the needs of the optical thin film industry.

In the future, we will explore possibilities for new applications of our built-in plasma guns and continually pursue the improvement and development of these guns so that the products will be used more widely in the industrial fields, together with timely report of our research activities. In closing, we would like to express our sincere appreciation to the optical-systems manufacturer who supported us in the experiments of film formation with their 1800 mm diameter vacuum-deposition system.